

**Department of Physics and Astronomy  
University of Heidelberg**

Bachelor Thesis in Physics  
submitted by

**Anna-Maria Elisabeth Glück**

born in Horb am Neckar (Germany)

**2020**



# **The Production of Neutron-Rich Isotopes by Laser-Driven Neutron Sources**

This Bachelor Thesis has been carried out by Anna-Maria Elisabeth Glück at the  
Max Planck Institute for Nuclear Physics in Heidelberg  
under the supervision of  
Honorarprofessor Dr. Christoph H. Keitel and Dr. Yuanbin Wu



# Abstract

In this work, the production of neutron-rich isotopes via neutron capture cascades in a single-component target irradiated by pulsed laser-driven neutron sources is theoretically investigated. Two sets of nuclides are considered as the seed nuclei, the first set consisting of  $^{75}_{33}\text{As}$ ,  $^{126}_{51}\text{Sb}$ ,  $^{176}_{71}\text{Lu}$ ,  $^{187}_{75}\text{Re}$ ,  $^{192}_{76}\text{Os}$ ,  $^{226}_{88}\text{Ra}$ ,  $^{233}_{91}\text{Pa}$ , and  $^{244}_{95}\text{Am}$ , and the second set comprising  $^{171}_{69}\text{Tm}$ ,  $^{193}_{77}\text{Ir}$ ,  $^{197}_{79}\text{Au}$ ,  $^{227}_{89}\text{Ac}$ , and  $^{255}_{99}\text{Es}$ . The laser-driven neutron sources used in our calculations are modeled after those proposed for Petawatt-class laser facilities and currently running inertial confinement fusion facilities. By investigating the enrichment of target nuclei with these two neutron sources in one and multiple pulses, we study the effects different numbers of neutrons per pulse and different repetition frequencies have on the resulting populations of neutron-rich isotopes. We also study the maximal abundances that can be produced with such neutron sources by investigating different saturation conditions. The calculations are performed using cross section data from the ENDF/B-VIII.0 and the TENDL-2019 library, and the precision of our results, as well as the influence of different cross section data taken from NON-SMOKER on our results is studied too. Our results show that successive neutron capture of up to 4 neutrons are possible. This promises new experimental possibilities to produce neutron-rich isotopes and simulate neutron capture nucleosynthesis in the laboratory.

In dieser Arbeit wird die Produktion von neutronenreichen Isotopen über Neutroneneinfangskaskaden in einem Target, das aus Atomen eines einzelnen Isotops besteht und das mit Neutronenpulsen aus lasergetriebenen Neutronenquellen bestrahlt wird, theoretisch untersucht. Als Ausgangskerne werden zwei Sätze von Nukliden betrachtet: Der erste Satz besteht aus  $^{75}_{33}\text{As}$ ,  $^{126}_{51}\text{Sb}$ ,  $^{176}_{71}\text{Lu}$ ,  $^{187}_{75}\text{Re}$ ,  $^{192}_{76}\text{Os}$ ,  $^{226}_{88}\text{Ra}$ ,  $^{233}_{91}\text{Pa}$  und  $^{244}_{95}\text{Am}$  und der zweite aus  $^{171}_{69}\text{Tm}$ ,  $^{193}_{77}\text{Ir}$ ,  $^{197}_{79}\text{Au}$ ,  $^{227}_{89}\text{Ac}$  und  $^{255}_{99}\text{Es}$ . Die laserbetriebenen Neutronenquellen, die in unseren Berechnungen verwendet werden, sind denen nachempfunden, die entweder für Petawatt Lasereinrichtungen geplant sind oder die momentan in Trägheitsfusionseinrichtungen betrieben werden. Indem wir die Anreicherung von Targetkernen in einem und mehreren Pulsen dieser beiden Quellen untersuchen, erforschen wir die Effekte, die unterschiedliche Anzahlen an Neutronen pro Puls und verschiedene Pulsfrequenzen auf die Populationen an neutronenreichen Isotopen haben. Weiterhin untersuchen wir die maximal möglichen Populationen von mit Neutronen angereicherten Isotopen, die mit solchen Neutronenquellen produziert werden können, indem wir zwei verschiedene Sättigungsbedingungen betrachten. Für unsere Berechnungen verwenden wir Wirkungsquerschnitte aus den Bibliotheken ENDF/B-VIII.0 und TENDL-2019, und wir untersuchen auch die Präzision unserer Resultate und den Einfluss, den die Verwendung von anderen Wirkungsquerschnitten aus den NON-SMOKER Datensätzen auf die Ergebnisse hat. Unsere Resultate zeigen, dass sukzessive Neutroneneinfangsreaktionen von bis zu vier Neutronen möglich sind. Damit offenbaren unsere Ergebnisse neue experimentelle Möglichkeiten, um neutronenreiche Isotope zu produzieren und die Nukleosynthese von schweren Elementen über Neutroneneinfangsreaktionen im Labor zu simulieren.

# Contents

<b>1</b>	<b>Introduction</b>	<b>9</b>
<b>2</b>	<b>Nuclear Reactions and Cross Sections</b>	<b>13</b>
2.1	Types of Neutron Reactions and Cross Sections . . . . .	14
2.1.1	Scattering Reactions . . . . .	14
2.1.2	Nuclear Transmutation . . . . .	15
2.1.3	Nuclear Reaction Mechanisms . . . . .	15
2.1.4	Types of Nuclear Transmutation Reactions . . . . .	16
2.2	Experimental Data and Codes Used in this Work . . . . .	18
2.2.1	The ENDF/B-VIII.0 Library . . . . .	18
2.2.2	The NON-SMOKER Code . . . . .	20
2.2.3	The TENDL-2019 Library and the TALYS Code . . . . .	25
<b>3</b>	<b>Neutron Capture Nucleosynthesis</b>	<b>33</b>
3.1	The S-Process . . . . .	36
3.1.1	Models, Conditions and Sites of the S-Process . . . . .	36
3.2	The R-Process . . . . .	39
3.2.1	Models and Conditions for the R-Process . . . . .	39
3.2.2	Astrophysical Sites of the R-Process . . . . .	42
<b>4</b>	<b>Laser-based Neutron Sources</b>	<b>47</b>
4.1	Conventional Neutron Sources . . . . .	47
4.2	Neutron Production with Light Ion Beams . . . . .	50
4.3	Neutron Production via Photonuclear Reactions . . . . .	52
4.4	Neutron Production in Thermonuclear Fusion Reactions . . . . .	54
<b>5</b>	<b>Theoretical Approach of the Present Work</b>	<b>56</b>
5.1	Neutron Capture in Beam-Target Interaction . . . . .	56
5.1.1	Neutron Captures During One Neutron Pulse in a Thin Target . . . . .	57
5.1.2	Neutron Captures During One Neutron Pulse in a Thick Target . . . . .	60
5.1.3	Neutron Captures for Multiple Neutron Pulses in a Thick Target . . . . .	61
5.1.4	Total Number of Produced Nuclides . . . . .	63
5.2	Neutron Sources and Targets . . . . .	65

5.3	Cross Section Data . . . . .	69
<b>6</b>	<b>Numerical Results</b>	<b>71</b>
6.1	Numerical Results for Neutron Source 1 . . . . .	71
6.1.1	Results after 1 Pulse . . . . .	71
6.1.2	Results after $10^4$ Pulses . . . . .	74
6.1.3	Saturation Condition 1 . . . . .	81
6.1.4	Saturation Condition 2 . . . . .	97
6.2	Numerical Results for Neutron Source 2 . . . . .	107
6.2.1	Results after 1 Pulse . . . . .	107
6.2.2	Results after 100 Pulses . . . . .	109
6.2.3	Saturation Condition 1 . . . . .	112
6.2.4	Saturation Condition 2 . . . . .	116
<b>7</b>	<b>Comparisons</b>	<b>121</b>
7.1	Comparing the 1 Pulse $N_1$ for TENDL and ENDFB Data . . . . .	121
7.2	Comparing the 1 Pulse $N_1$ for NON-SMOKER and ENDFB Data . . . . .	123
7.3	Comparison of the Results for Different Cross Section Datasets . . . . .	125
7.3.1	Comparison of the Original Results with the Results Calculated From Dataset A . . . . .	127
7.3.2	Comparison of the Original Results with the Results Calculated From Dataset B . . . . .	136
<b>8</b>	<b>Summary and Conclusion</b>	<b>144</b>



# 1 Introduction

The production of heavy elements in the laboratory has always been a goal of humankind. While in the mid-ages, alchemists were aiming to produce gold in, admittedly, unscientific ways, modern scientists have developed countless methods [1] of producing heavy isotopes that have either never been produced before in the laboratory to study their nuclear quantities, or that have applications in medicine or industry. Still, about half of all predicted isotopes are currently not experimentally accessible [1–3]. While most proton-rich nuclides up to the proton drip line have been produced, neutron-rich isotopes are not as easily created in the laboratory [1–4], and the neutron drip line has only been investigated until Neon [4].

Therefore, the experimental production of neutron-rich isotopes is subject to extensive research [3], as they are scientifically relevant in many different ways. Firstly, the access to very neutron-rich nuclides in the laboratory could make it possible to improve our understanding of the nuclear structure and strong interaction, as well as to test and improve nuclear models [2, 5–8], by measuring quantities like the nuclear mass or investigating low-lying nuclear states spectroscopically. Furthermore, neutron-rich isotopes are important for applications in nuclear medicine and cancer therapy [9–12], as well as in the industry [13, 14].

Moreover, producing neutron-rich isotopes in the laboratory and investigating their mass,  $\beta$ -decay rates, and cross sections is crucial for a better understanding of the astrophysical slow and rapid neutron capture processes of nucleosynthesis [15, 16], which are each responsible for the production of about 50% of all heavy elements found in the universe. Despite the fact that these processes have been studied extensively since the 1950s [17], there are still numerous open questions. In fact, the origin of heavy elements in the cosmos was on the list of the "Eleven Great Questions for the 21st Century" that the US National Research Council published in 2003 [18]. Among the greatest uncertainties is the astrophysical site of the r-process [16, 19–22]. However, also the stellar models for the s-process are under investigation, for which research is carried out especially on the s-process branching point nuclides [15, 23, 24]. Furthermore, because the current models for the nucleosynthesis of heavy elements do not yet reproduce the abundances of heavy nuclides everywhere in the universe perfectly, there have been several new processes proposed [15, 25–29] to account for differences, which could also be tested better if data was available for more neutron-rich nuclides relevant to these processes.

## 1 Introduction

Currently, most neutron-rich nuclides are produced in reactors or accelerator-based facilities, with the most important production processes being neutron capture, fusion, spallation, fragmentation, and fission. Projectile fragmentation and fission, as carried out at the leading facilities like the Rare Ion Beam Facility at RIKEN in Japan [30, 31], are currently the most promising way of producing extremely neutron-rich nuclides [2–4]. Such facilities, however, are very expensive and space-consuming [32–34]. As in the last decades, there have been many advancements in laser technology, high-power lasers are now able to generate highly intense neutron beams, offering the opportunity to produce neutron-rich isotopes via neutron capture [35–46]. The neutron production mechanisms in such facilities vary from interactions of laser-accelerated light ions [35–37, 46] or electrons [38] with a secondary target (beam-target interaction) to neutron production via thermonuclear reactions [40–45]. At the National Ignition Facility (NIF) at Lawrence Livermore National Laboratory (LLNL) in the USA, it is currently possible to produce neutron pulses with over  $10^{16}$  neutrons per pulse by inertial confinement fusion [41], and studies for neutron beams produced in beam-target interactions [35, 38] suggest that with Petawatt-class lasers at future facilities such as ELI-NP [47], neutron beams with up to  $10^{12}$  neutrons per pulse will soon be possible. Though these pulse numbers are lower than for accelerator-based spallation sources [32], for instance, the sub-nanosecond durations of the neutron pulses generated with the considered neutron sources lead to peak neutron fluxes of up to  $10^{26} \text{ cm}^{-2} \text{ s}^{-1}$  [41] at the NIF, and at ELI-NP, fluxes up to over  $10^{20} \text{ cm}^{-2} \text{ s}^{-1}$  [38, 47] are proposed. Therefore, laser-driven sources promise the production of neutron fluxes higher than accessible for any conventional neutron sources [32] at comparably small facilities, which, hence, make the production of neutron-rich nuclides accessible also at hospitals or universities. Furthermore, because of the high neutron fluxes, it is possible to study neutron capture cascades similar to those in nucleosynthesis. Therefore, experiments with such neutron sources would allow for the first time to study nucleosynthesis processes in the laboratory, giving us the chance to understand the r- and s-process of nucleosynthesis better [38, 45, 48].

In this thesis, starting from the work of Hill and Wu in Ref. [49], we investigate the production of neutron-rich nuclei via successive neutron capture reactions for pulsed laser-driven neutron sources irradiating a solid-state target made out of nuclei of a single seed nuclide. In Ref. [49], Hill and Wu have studied the production of neutron-rich isotopes of 95 of the heaviest nuclides available in the ENDF/B-VIII.0 library [50] from  $Z = 3$  to  $Z = 100$ . A laser-driven neutron source with  $10^{12}$  neutrons per pulse and a repetition rate of 1 Hz for 1 pulse and for  $10^4$  pulses has been considered. Especially good performances in these calculations have been found for two sets of seed nuclides, with the first set consisting of  $^{75}_{33}\text{As}$ ,  $^{126}_{51}\text{Sb}$ ,  $^{176}_{71}\text{Lu}$ ,  $^{187}_{75}\text{Re}$ ,  $^{192}_{76}\text{Os}$ ,  $^{226}_{88}\text{Ra}$ ,  $^{233}_{91}\text{Pa}$ , and  $^{244}_{95}\text{Am}$ , and the second set comprising  $^{171}_{69}\text{Tm}$ ,  $^{193}_{77}\text{Ir}$ ,  $^{197}_{79}\text{Au}$ ,  $^{227}_{89}\text{Ac}$  and  $^{255}_{99}\text{Es}$ . The results in Ref. [49] show that for the chosen parameters, the production of isotopes enriched

with up to 2 neutrons is possible already for one pulse, and in  $10^4$  pulses, neutron capture cascades with up to 4 neutrons can be observed. Furthermore, their results show that the total number of nuclei with  $i$  more neutrons  $N_i^{\text{tot}}$  than the seed nuclide scales approximately with the number of pulses applied to the power of  $i$  as long as saturation does not occur due to competition among neutron capture, radioactive decay, and loss of neutron-rich nuclides due to nuclear transmutations. Moreover, studies with different numbers of neutrons per pulse  $N_p$  have shown that the abundances  $N_i$  left after a specific number of pulses scale with  $N_p^i/A^{i-1}$ , where  $A$  is the target area, before saturation occurs.

In the present work, we implement the TENDL-2019 [51] cross section data for the neutron-rich isotopes to the calculation, as in TENDL-2019 more reaction channels, models and experimental data are included in this library than in the NON-SMOKER data [52, 53] used in Ref. [49]. In Ref. [49], a target area of only  $A = 25 \mu\text{m}^2$  has been assumed. In a realistic laser facility, however, only a significant fraction of the emitted neutrons could hit such a small target if it were placed directly at the neutron source, which, in reality, is not the case. Therefore, in this work, we study the irradiation of a larger, more realistic target of seed nuclides ( $A = 10^4 \mu\text{m}^2$ ) with laser-driven neutron sources. As target materials, we use the two sets of seed nuclides that have been found to perform well in Ref. [49]. Furthermore, we do not only investigate a neutron source delivering  $10^{12}$  neutrons per pulse at a repetition rate of 1 Hz, but we also study the same neutron source operating at repetition rates of 10 Hz, and one pulse per minute. Therefore, all repetition rates proposed for the laser-driven neutron source at Petawatt-class laser facilities such as ELI-NP in Romania, after which the neutron yield of  $10^{12}$  neutrons per pulse is modeled, are investigated. Moreover, we study another neutron source generating pulses of  $10^{16}$  neutrons three times per day, which is based on the inertial confinement fusion source at the NIF. For these two neutron sources and the 13 seed nuclides, we study the neutron-enrichment of the target after 1 and multiple pulses of neutrons, as in Ref. [49]. However, our larger target allows us to make more accurate estimations of the possibilities in the current and planned laser sources under investigation, and for multiple pulses, the influence of different repetition rates and, therefore, the effect radioactive decay in between pulses has on the results can be investigated systematically. Moreover, the saturation due to competition between the gain of nuclei of a specific isotope with the loss of such nuclei due to radioactive decay and nuclear transmutation is thoroughly investigated in the present work by studying two saturation conditions, i.e. when the maximal populations of each isotope are reached, and when the differences between the populations after  $s$  and  $s - 1$  pulses is smaller than the population after 1 pulse. Even though the yields of neutron-enriched nuclei for the first neutron source considered that are calculated in this work are smaller than those in Ref. [49], as we are using more realistic target dimensions, our calculations show that the observation of neutron capture cascades with up to 4 neutrons are still possible. In fact, the analysis of the maximal

## 1 Introduction

abundances shows that for the first neutron source considered and a repetition rate of 10 Hz, such cascades can be observed for all of the considered seed nuclides, and that nuclei enriched by 4 neutrons can be produced in quite high abundances for some seeds.

The thesis is structured as follows. In chapter 2, the basic quantities and reaction processes involved in the calculations are explained. An overview about the three nuclear data libraries ENDF/B-VIII.0, TENDL-2019, and NON-SMOKER that we use the cross section data of for our calculations is also given. In Chapter 3, the astrophysical processes involved in neutron-capture nucleosynthesis in the s- and r-process are addressed. The main purpose of this chapter is to show the astrophysical conditions under which these processes occur and illustrate the issues of current research on neutron-capture nucleosynthesis, for the motivation in astrophysics of the present study. Chapter 4 presents an overview on the laser-driven neutron sources, including neutron production mechanisms in the laser-driven neutron sources, comparisons with reactor- and accelerator-based neutron sources, and comparisons with the neutron fluxes during the r- and s-process. In chapter 5, the theoretical approach employed in the present work, which is taken from Ref. [49], and the approximations made in the calculations are explained and discussed. Chapter 6 focusses on the discussion of the numerical results for the two neutron sources. Results after one pulse, as well as multiple pulses are presented, and the saturation of neutron-enrichment is investigated on the basis of two saturation conditions. In chapter 7, we make comparisons of the results we achieve with our calculations when using cross section data from different nuclear data libraries, including ENDF/B-VIII.0, TENDL-2019 and the NON-SMOKER data to check the precision of our results. Finally, the present work concludes in chapter 8 with a summary of the most important results and an outlook.

## 2 Nuclear Reactions and Cross Sections

Generally, nuclear reactions can be described as a process in which a projectile  $a$  reacts with a target nucleus  $A$  to the (possibly changed) nucleus  $B$  and one or several particles  $b_i$ . Such a reaction will in the following be written as



If for a certain reaction all quantum numbers are defined (e.g. types of the particles, relative wave vector, energy for the relative movement of the particle and the nucleus, angular momenta of the particle, the nucleus and their coupling...), it is common to speak of a "channel" over which the reaction occurs [54]. In the same way, the entrance channel and exit channel of a nuclear reaction are defined. For these channels, it is important that some nuclear quantities are conserved during the reaction, i.e. the total electric charge, the total energy of the system, if it is isolated, the total angular momentum and its projections on the  $z$ -axis, and, lastly, the isospin for strong interaction.

The incoming particle  $a$  can generally be any kind of charged particle, nucleus, nucleon or photon, but as we will be focusing on processes induced by a laser-driven neutron source hitting a target of seed nuclides, the focus in the following will lie on neutron-nucleus reactions that will be further addressed in this chapter.

It has been proven that for incoming neutron energies greater than 1eV, the atoms in a target do not affect each other in neutron-nucleus interactions, so that even though only one target nuclide will be assumed in the following considerations, they can be transferred to the situation of a neutron beam bombarding a target made out of many nuclides [55]. Also, for such energies, the cross section is dominated by the interaction of the neutron with the nucleus and not the atom as a whole.

To classify the probability of a nuclear reaction, nuclear cross sections  $\sigma$  are used. A cross section of a nuclear reaction is given in units of area, more specifically in barns with  $1\text{b} = 10^{-24}\text{cm}^2$ . Therefore, the so-called total cross section  $\sigma_{\text{tot}}$  indicating the probability for any reaction to occur can intuitively be regarded as the area that the neutron "sees" when being shot at a specific nuclide [55], even though this picture is not physically correct. However, the total

cross section  $\sigma_{\text{tot}}$  is not the only one that is interesting to us. Because neutrons are uncharged particles, they do not face a Coulomb barrier upon interacting with the nucleus of an atom, so that neutron-nucleus reactions can occur at virtually any energy from thermal energies to a few hundred MeV [55], [54]. Therefore, abundant reaction mechanisms are possible, which are represented with so-called partial cross sections  $\sigma_p$  that make up the total cross section at a given energy [55] and that dominate at different energy ranges.

$$\sigma_{\text{tot}} = \sum \sigma_p \quad (2.2)$$

The most important of these will be addressed in the following, with a focus on reactions that can occur in the energy range regarded in the calculations carried out in the present work, i.e. 50 keV - 10 MeV.

## 2.1 Types of Neutron Reactions and Cross Sections

### 2.1.1 Scattering Reactions

The first class of possible neutron-nucleus reactions are scattering reactions. These reactions include all reactions in which the only particle  $b$  emitted from the nucleus during the reaction is a neutron [55]. Scattering processes can, again, be divided into elastic and inelastic scattering. The former is characterized by the fact that during an elastic process (which defines the elastic cross section  $\sigma_{\text{el}}$ ), the sum of the kinetic energies of target and projectile remains constant, as does the outer and inner configuration of the particles. It can therefore be described as a  $A(n, n)A$  reaction, and will be referred to as  $(n, n)$  in the following. Elastic Scattering processes usually dominate at energies lower than 200 keV [56].

A cross section commonly used in describing nuclear processes is the so-called non-elastic cross section, describing all processes in which the energies and inner structure of the particles before and after the reaction is changed in some way. This cross section can, therefore, be calculated via

$$\sigma_{\text{non-el}} = \sigma_{\text{tot}} - \sigma_{\text{el}}. \quad (2.3)$$

This cross section therefore also includes inelastic scattering processes with the inelastic cross section  $\sigma_{\text{inel}}$ , for which the sum of the kinetic energies of the nuclides in the entrance and exit channel is not the same and which occur dominantly in an energy range between 0.2 and 4 MeV [56]. In this kind of process, the incoming neutron enters the nucleus and transfers part of its energy either to a single nucleon inside the target nucleus or to the whole nucleus, exciting a

collective movement (e.g. vibration or rotation) and thereafter leaves the nucleus with changed energy [54]. Therefore, inelastic scattering can be described as  $A(n, n')A^*$  or, in short,  $(n, n')$ .

### 2.1.2 Nuclear Transmutation

In contrast to the scattering reactions, all other reactions of neutrons with nuclei do not preserve the initial nuclide, but it is changed during the process - nuclear transmutation occurs. The cross section for these will, therefore, be referred to as the transmutation or species-loss cross section  $\sigma_{\text{tr}}$  in the following.

$$\sigma_{\text{tr}} = \sigma_{\text{tot}} - \sigma_{\text{el}} - \sigma_{\text{inel}} \quad (2.4)$$

$$= \sigma_{\text{non-el}} - \sigma_{\text{inel}} \quad (2.5)$$

### 2.1.3 Nuclear Reaction Mechanisms

Before going into detail on the types of nuclear transmutation reactions that exist, the different nuclear reaction mechanisms shall be addressed that each contribute to all processes but dominate at different energy ranges. Generally, it would be best to describe every nuclear reaction in ab-initio calculations. However, such calculations accounting for the strong interaction between the incoming neutron and all nucleons have only been achieved for very simple reactions and target nuclei (see, for example, Refs. [57, 58]). Therefore, models describing the reaction dynamics in a more simple way had to be developed based on the observations of the cross section values. Historically, reactions were first differentiated by the typical reaction time, and a classification in direct and compound nuclear statistical reactions was made [59].

For direct reactions, the interaction time is on the order of the time of transit of the incident particle, in our case a neutron, across the nucleus, which amounts to about  $10^{-23} - 10^{-22}$  s [54]. With that short reaction time also comes a weak dependence of direct cross sections on energy [59]. Such direct reactions can be described to occur in only a few steps in which the nucleus transfers part of its energy to the nucleus, either to collectively excite all nucleons in the nucleus like in a giant resonance or to transfer its energy to a specific nucleon or particle in the nucleus. Therefore, for only a few steps to suffice for reactions to occur, direct processes dominate for relatively large incoming neutron energies.

In contrast to the direct processes, the reaction time for so-called compound nucleus reactions is several orders of magnitude higher as it totals  $10^{-19} - 10^{-15}$  s [60]. Therefore, the compound nucleus cross section also heavily depends on the energy of the incoming particle. In fact, the cross sections for neutron-nucleus interactions exhibit considerable resonance structures for

energies between 1 eV and 1 keV. These resonances also indicate that for compound nuclear reactions, nearly bound states of the nucleus consisting of the incoming particle and the target nucleus with well-defined quantum numbers must exist. Therefore, unlike the direct reactions, compound reactions cannot be described as occurring in only a few steps. Instead, numerous internuclear interactions take place and in complicated process, the energy is distributed between the nucleons in the nucleus, resulting in thermal equilibrium of the neutron and the nucleons of the target nucleus that by that time are assumed to have become indistinguishable. The neutron and the nucleus then form a highly excited so-called compound nucleus. This concept was first introduced by Bohr in 1936 in Ref. [61], who also formulated the hypothesis that for a reaction in which such a compound nucleus is created, the process leading to the forming of the compound nucleus and the process of its decay can be assumed as independent (apart from the one condition that conservation laws have to apply). Usually, the lifetime of such a compound nucleus state is finite and after its formation, it can either undergo a  $\gamma$ -decay to a lower-energy state, split in two smaller nuclei (nuclear fission) or, if by chance enough energy is transferred to one or several nucleons or other kinds of nuclear fragments, emit one or several particles. The emitted particle can, of course, be a neutron again, so that elastic or inelastic scattering can occur via compound nucleus reactions [62] as well as direct processes. Else, nuclear transmutation occurs. Generally, compound nuclear reactions dominate for relatively low energies of up to 20 MeV. It is also only for a small energy window that single resonances of the compound nucleus can be found in the nuclear cross section, which is due to the fact that with increasing energy, the spacing between the nuclear levels gets tighter and exit channels become available, so that an isolated resonance being present becomes unlikely and instead, averages over the fluctuations must be taken in the statistical theory of compound reactions [59].

In between the direct and the compound nucleus reactions, there is another reaction mechanism, in which the reaction occurs neither after only a few interactions of the neutron with the nucleus nor after the statistical equilibrium is fully developed and, therefore, the compound nucleus is fully formed, but during the process of establishing said equilibrium [54]. This type of reaction is, hence, called a pre-equilibrium reaction. Such reactions significantly contribute to nuclear cross sections for energies above 4 MeV, and at energies above 10 MeV already a significant part of reactions take part in pre-equilibrium processes [56].

### 2.1.4 Types of Nuclear Transmutation Reactions

Finally, types of nuclear transmutation reactions that are of importance to the present work shall be addressed. The transmutation process that is most important for our calculations is the neutron capture reaction  $(n, \gamma)$ , in which a neutron is captured by the nucleus, which there-

## 2.1 Types of Neutron Reactions and Cross Sections

after undergoes a  $\gamma$ -decay. After such a reaction, the target nucleus is, hence, enriched with one neutron, so that this nuclear interaction is the foundation of the formation of heavy and/or neutron-rich isotopes during stellar nucleosynthesis and in the experiments with laser-driven neutron sources that are simulated in this work. Therefore, it makes sense to attribute a specific neutron capture cross section  $\sigma_{n\text{-cap}}$  to those reactions. Neutron capture can occur at very low energies because the energy does not have to suffice for the ejection of any nucleon and, as already explained, neutrons do not have to overcome the Coulomb barrier of the nucleus as they carry no charge. In fact, neutron capture dominates especially for low energies and, together with elastic scattering, is the preeminent reaction for energies lower than 200 keV, while for increasing energy, the neutron capture cross section generally decreases as other reaction channels become available [56]. At these low energies, neutron capture for medium to heavy nuclei near the valley of nuclear stability is dominated by compound nuclear neutron capture in which a compound nucleus is formed first of the neutron and the target that then undergoes a subsequent  $\gamma$ -decay [63]. However, especially for nuclides with a very limited number of compound nucleus states, direct capture also plays a dominant role in which a direct electromagnetic transition to a bound final state occurs instead of the formation of a compound nucleus. For higher incident energies of around 4 MeV, neutron capture can also happen via pre-equilibrium processes.

If the energy transferred from the incident neutron to another particle in the nucleus, like a nucleon or an  $\alpha$ -particle, either directly or via the statistical equilibrium of a compound nucleus, is large enough, it can be ejected [54]. Generally, reactions in which a particle is emitted, though they can happen at lower energies, are generally suppressed at energies below a few MeV and they only begin to dominate above approximately the separation energy of this particle. For direct particle emission reactions, it makes sense to classify so-called pick-up reactions, in which the incident neutron "picks up" another nucleon or particle from the nucleus to form the ejectile because the projectile does not lose its identity as it is the case for compound nuclear reactions [60]. If the projectile consisted of several particles, also so-called stripping reactions could occur, in which the projectile transfers one or more nucleons to the target. Furthermore, knock-out reactions can occur as direct reactions, in which the projectile knocks out an additional particle from the target nucleus. Such reactions, in which three or more nucleons or nuclei are present after the collision, can also occur via compound or pre-equilibrium reactions. After a binary particle emission, either in pre-equilibrium or after the formation of the compound nucleus, the residual nucleus could contain enough excitation energy to emit a second particle in a so-called multiple emission [51]. This is only possible for incident energies above the neutron separation energy, i.e. 7-10 MeV for nuclides near the valley of stability. For energies lower than 40 MeV, this secondary emission only happens after a statistical equilibrium of the nucleons is established in the residual nucleus, but for higher energies, such a

secondary emission could even occur in a pre-equilibrium process if the residual nucleus' excitation energy is so high that further fast particles inside this nucleus, which can be imagined as strongly excited particle hole-pairs that result from the primary emission, become possible [56].

Finally, nuclear fission could occur when a heavy nucleus is bombarded with a neutron. This process occurs via the formation of a compound nucleus, which splits into two lighter nuclei [62]. For fissile nuclides, for which the change in binding energy due to the addition of a neutron alone is sufficient for the nucleus to overcome the energy barrier for fission, this is possible even with thermal neutrons. Fissionable nuclides, on the other hand, also include those for which generally higher energy neutrons are required as the binding energy of the neutron is lower than the critical energy needed for fission, so that extra kinetic energy of the neutron is needed to overcome the barrier.

## 2.2 Experimental Data and Codes Used in this Work

For the calculations of neutron-capture processes with laser-driven neutron sources, three different sets of cross sections are used and compared. Those are the ENDF/B-VIII.0 library[50], the TALYS-based TENDL-2019 library[51, 56, 64, 65] and the cross section library based on the NON-SMOKER code[52, 53, 66]. Those libraries, as well as the way the cross sections in each are obtained will be discussed in the following.

### 2.2.1 The ENDF/B-VIII.0 Library

The ENDF/B-VIII.0 library is the latest release of the US-American ENDF (Evaluated Nuclear Data File) library project and has been published in 2017 [50]. It consists of experimental nuclear data that has undergone an evaluation, in which the measured data (for instance nuclear cross sections) are combined with the forecasts of nuclear model calculations to ultimately try to find the "true" values [67], which then are parametrized, reduced to tabular form and saved in the evaluated nuclear data files. The ENDF library project, which started in 1968, is coordinated by the Cross Section Evaluation Working Group (CSEWG) and includes experimental nuclear data from the US and from all over the world, with notable contributions from libraries like the European JEFF (Joint Evaluated Fission and Fusion) file, the Japanese JENDL (Japanese Evaluated Nuclear Data Library), and from South Korea [50]. Since the release of the first ENDF/B-I file in 1968, the library has been improved frequently with data that has become newly available as well as newer nuclear models, but only after rigorous extensive testing of the new data [67], so that today, it is often used as a standard reference library of nuclear data. The ENDF/B-VIII.0 library itself is structured in different sublibraries for various

projectiles<sup>1</sup> as well as special libraries for e.g. radioactive decay data. These sub-libraries each contain separate evaluated nuclear data files for different target nuclides. The single incoming particle - target nuclide files in the ENDF/B-VIII.0 library are provided in the standard ENDF-6 format for nuclear data, which is one data file separated in different sub-files, with e.g. the MF1 subfile giving general information, MF2 containing resonance parameters and MF3 listing the tabulated cross sections in a minimal energy range of  $10^{-5}$  eV to 20 MeV for the available reaction branches [67]. These three first files are also the most important for the data needed in this work.

Especially for low energies and incident neutrons, resonances have a high impact on nuclear cross sections. Therefore, the resonance contributions to the cross sections for both the resolved and the unresolved energy range are stored in MF2 [67]. These contributions, however, are not stored as pointwise cross sections, but as parameters of different models and self-shielding factors, with which the resonance contributions to the cross sections can then be calculated. For the resolved energy range, in which the level density is not high enough for the resonances to overlap and the individual resonances can also be resolved in experiments, the parameters for individual resonances are preferred to be stored for a single-level or multilevel Breit-Wigner representation, but if the agreement with the experimental data is significantly better, the Adler-Adler or Reich-Moore model or an R-Matrix representation in limited format is used [67]. For the unresolved energy range, in which the resonances still do not overlap but the resonances cannot be resolved due to experimental constraints, only the single-level Breit-Wigner representation is used and the resonance self-shielding has to be treated statistically. For details on these models, regard Ref. [67].

However, not even in the resonance ranges are the cross sections calculated from the parameters stored in MF2 the only contributions to the cross sections values, which is mostly due to resonances outside the range, inadequacies of the representation or competing cross sections. Therefore, the experimental values of the cross sections without the explicit resonance contributions and self-shielding factors are stored in MF3. Because it is usually not possible to experimentally determine absolute cross section values, they are measured relative to cross section standards, of which the IAEA has published new ones in 2017 [68] and which are mostly incorporated in ENDFB-VIII.0 as well [50]. The measured cross sections are then saved as a function of energy at only so many energy points in an energy range of at least  $10^{-5}$  eV until 20 MeV as needed to represent the cross section accurately [50]. For intermediate energy points, an interpolation scheme is specified in the data file. The experimentally most well-known cross section is the total cross section [67]. However, next to the total cross section, the partial cross sections of most important reactions and sums of reactions are stored

---

<sup>1</sup>i.e. photons, neutrons, protons, deuterons, tritons, <sup>3</sup>He,  $\alpha$ -particles and electrons

in the ENDF/B-VIII.0 library as well. For these, it is made sure that the elastic and non-elastic type cross sections from MF3 add up to the total one. However, the partial cross sections have higher inaccuracies than the total one [67].

In the current library ENDF/B-VIII.0, which, according to the paper published with the release "represents the biggest change to the ENDF library in years"[50], the neutron sub-library that we work with in our calculations contains data for as much as 557 isotopes as target nuclei, which is an improvement of 32% compared to the former release ENDF/B-VII.1. This major growth is, however, not only due to the availability of new experimental data, but in the current version of the library, there are also nuclides for which data has been obtained from the TENDL-2015 [69] library in combination with the EMPIRE code, which both use theoretical models for the calculation of nuclear cross sections. This is the case for all unstable nuclides with  $T_{1/2} > 1$  h that have no experimental data available, but also some data for As, Au and Pt was adapted from TENDL-2015. For a detailed description and analysis of the origin of the data for each target nuclide, please refer to the release note Ref. [50] of the ENDF/B-VIII.0 library.

To be able to use data in an ENDF format for evaluation, the files have to be preprocessed first. In our case, we are using the PREPRO 2018 codes[70] for this task. These codes consist of 18 codes dedicated to preprocessing ENDF format data files and make the data available for evaluation in all kinds of programming languages [71]. For this, the data is first converted to C, C++ and FORTRAN readable form with the ENDF2C code. Subsequently, the PREPRO codes are used to interpolate between the energies at which the cross sections are defined in the ENDF-6 file. Another important code is RECENT, which reconstructs the true cross sections by adding the MF3 cross section values to the resonance contributions from MF2. If only a self-shielding factor was stored in MF2 for a specific energy range, the cross sections from MF3 are simply multiplied with it [67]. Furthermore, the cross sections are doppler-broadened, the activation cross sections are calculated and the angular distributions of the cross sections are calculated or corrected [71]. Finally, it is made sure that the cross sections consisting of different contributions are exactly the sum of all subchannel cross sections and the general information is updated.

### 2.2.2 The NON-SMOKER Code

The second set of nuclear cross sections that are used in this work are those calculated with the NON-SMOKER code [52, 53, 66] and stored in the NON-SMOKER database. Contrary to the ENDF/B-VIII.0 library, which consists mainly of experimentally determined nuclear data, the cross sections and reaction rates of this dataset are of purely theoretical nature, with the only experimental data going into the calculations being nuclear masses and information about the ground and excited state levels, where they are available. That only little experimental data is

used is due to the goal of the NON-SMOKER code to provide consistent cross section data for all nuclides from the valley of stability to the neutron and proton drip lines. To achieve this global description, locally larger deviations from experimental values are accepted than if all possible experimental data was used. Furthermore, because many quantities like separation energies or the  $Q$ -values of reactions depend on and are sensitive to mass values, which, for heavy nuclides are mostly unknown, two different theoretical mass models were implemented in the code, the Finite Range Droplet Model (FRDM) [72] and the extended Thomas-Fermi approach with Strutinski integral (ETFSI-Q) [73]. These mass values are used if no experimental data is available, and the different models lead to two different sets of calculated cross sections.

The focus in the NON-SMOKER code lies on the theoretical calculations of nuclear quantities relevant to the investigation of stellar nucleosynthesis and astrophysical energy generation processes, as most of the relevant nuclides for these processes are not accessible in the laboratory for experimental investigations. Therefore, it calculates nuclear reaction cross sections, astrophysical reaction rates, maxwellian averaged cross sections and nuclear partition functions for an astrophysical energy range [74] of thermal energies up to a few MeV. For the cross sections specifically, all kinds of capture cross sections as well as cross sections for all processes with  $Q > 0$  involving neutrons, protons and  $\alpha$  particles as pro- or ejectiles are calculated.

All calculations performed with the NON-SMOKER code base on the Hauser-Feshbach statistical model [75] for compound nucleus reactions. Therefore, for the cross sections calculated with this model to describe reality sufficiently, the compound framework has to be applicable, i.e. the reaction has to occur via the formation of a compound nucleus that must reach the equilibrium before breaking apart, and the level density of the target nucleus at the energy of the incoming particle has to be high enough so that the resonances overlap completely. In this case, instead of describing the single resonances, averaged transmission coefficients  $T$  can be introduced to describe absorption via the imaginary part of optical nucleon-nucleus potential.

### **The Optical Model Potential**

Measured neutron cross sections  $\sigma$ , especially for low energies, can fluctuate heavily with even small changes in the energy because of resonances that occur due to complicated interactions with the nucleons in the target nucleus [54]. However, when averaging over energy, the reactions and corresponding cross sections can be described as the interaction of the incoming particle with a mean-field potential  $U$  in the so-called optical model, which introduces a potential  $U = V + iW$  consisting of a real and an imaginary part with which the average cross sections can be calculated. The imaginary part  $W$  is introduced to account for the "absorption" of the incoming particle into the potential of the target nucleus and, therefore, all nuclear reactions other than shape-elastic scattering [54], [76]. In the NON-SMOKER code, optical po-

tentials are used to determine the average transmission coefficients for the compound nucleus decay.

To achieve consistency for all nuclides, the optical potentials implemented in the NON-SMOKER code are all global. For incoming (and exiting) neutrons and protons, the microscopic potential developed in Ref. [77] is used with corrections to the imaginary part [53]. For  $\alpha$ -particles, the optical potential used is the one that was introduced in Ref. [78], even though this approach introduces uncertainties, especially for heavier nuclei [53], because of its phenomenological nature. Lastly, for deformed nuclei, an effective spherical potential of equal volume is used that is based on averages of the deformed potential over the angles between the nucleus' orientation and the incoming particle.

### The Hauser-Feshbach Statistical Model

The calculation of the cross sections in NON-SMOKER is carried out in the Hauser-Feshbach formalism for compound nuclei [53]. In this model, the cross section for the reaction  $A_0^\mu(a, a')A_f^\nu$  of the nucleus  $A_0$  in an excited state  $\mu$  with the excitation energy  $E_0^\mu$  with the projectile  $a$  over a compound nucleus to the nucleus  $A_f$  in an excited state  $\nu$  with excitation energy  $E_f^\nu$  and the ejectile  $a'$  can be calculated via

$$\sigma^{\mu\nu}(E_{\text{CM}}) = \frac{\pi}{k^2} \sum_J \sum_{\Pi=-1}^1 \frac{2J+1}{(2s+1)(2I_0^\mu+1)} \quad (2.6)$$

$$\times \frac{T_a^\mu(E_{\text{tot}}, J, \Pi, E_0^\mu, I_0^\mu, \Pi_0^\mu) T_{a'}^\nu(E_{\text{tot}}, J, \Pi, E_f^\nu, I_f^\nu, \Pi_f^\nu)}{T'_{\text{tot}}(E_{\text{tot}}, J, \Pi)}. \quad (2.7)$$

Here,  $E_{\text{CM}}$  is the center of mass energy,  $E_{\text{tot}}$  is the total energy of the compound nucleus,  $k$  the wave number for the relative motion of projectile and target nucleus,  $s$  is the spin of the projectile,  $I_0^\mu$  the spin of the target nucleus and  $\Pi_0^\mu$  the parity of the excited target nucleus state  $\mu$ . For the exit channel, the quantities  $I$ ,  $E$  and  $\Pi$  have a subscript  $f$  and a superscript  $\nu$  instead, indicating the remaining nucleus  $A_f$  and its energy state  $\nu$ .  $E_{\text{tot}}$ ,  $J$  and  $\Pi$  are the total energy, the total angular momentum and the parity of the compound nucleus state via which the reaction occurs, and  $E_{\text{tot}}$  is defined by  $E_{\text{tot}} = S_{\text{projectile}} + E_{\text{CM}} + E_0^\mu$  with the separation energy  $S_{\text{projectile}}$  of the projectile in the compound nucleus [56]. The total transmission coefficient is the sum of the transmission coefficients for all possible ejectiles and energies of the residual nucleus  $T'_{\text{tot}} = \sum_{a', \nu} T_{a'}^\nu$ .

In Eq. (2.7), the concept of compound nucleus reactions is illustrated quite well. The fact that the transmission coefficients of the projectile entering the target nucleus and forming a compound system,  $T_a^\mu$ , and the transmission coefficient of the ejectile leaving the compound

nucleus in the exit channel,  $T_{a'}^\nu$ , are decoupled, is due to Bohr's independence hypothesis of the formation and the decay of the compound nucleus being independent. That conservation laws apply despite this independence hypothesis is indirectly included in the formula via the dependences of the transmission coefficients on the quantities  $E_{\text{tot}}$ ,  $J$  and  $\Pi$  which all have to be conserved during the reactions.

Because in an experiment, usually the cross section with  $\mu = 0$  and every possible  $\nu$ ,  $\sigma^{lab} = \sum_{\nu} \sigma^{0\nu}$  are measured, the laboratory cross sections in the NON-SMOKER data that we use in our calculations are computed via Eq. 2.7 with the transmission coefficient  $T_{a'}^\nu$  replaced by a transmission coefficient  $T_{a'}$  including all states  $\nu$  of  $A_f$ .

$$T_{a'}(E_{\text{tot}}, J, \Pi) = \sum_{\nu=0}^{\nu_f} T_{a'}^\nu(E_{\text{tot}}, J, \Pi, E_f^\nu, I_f^\nu, \Pi_f^\nu) + \int_{E_f^{\nu_f}}^{E-S_{f,a'}} \sum_{J_f, \Pi_f} T_{a'}(E_{\text{tot}}, J, \Pi, E_f, J_f, \Pi_f) \rho(E_f, I_f, \Pi_f) dE_f \quad (2.8)$$

where  $S_{f,a'}$  is the channel separation energy,  $E$  the excitation energy of the compound nucleus and  $\nu_f$  is the highest experimentally known state. In the NON-SMOKER code, up to 19 experimentally known levels are employed for each nuclide, using experimental data from Ref. [79], before the sum turns into an integral over the coefficients multiplied with a continuous level density.

The transmission coefficients  $T_a^\mu$  are calculated by summing over all partial waves that are quantum mechanically allowed,  $T_{als}$ , with the orbital angular momentum  $l$  and the channel spin  $s$  [53]. In case  $a$  or  $a'$  are particles, which for neutron-nucleus interactions is definitely true for  $a$ , the transmission coefficients  $T_{als}$  (or  $T_{a'l's'}$ , respectively) are calculated by solving the Schrödinger equation with the optical potentials introduced in a former paragraph of this section. For radiative transmission coefficients, i.e. transmission coefficients if  $a$  or  $a'$  are  $\gamma$ -rays, only the dominant transitions of electric and magnetic dipole transitions (E1 and M1) are taken into account when calculating the cross sections. For the M1 transition coefficients, the simple single particle approach is used [53, 80]. For E1 transitions, the transmission coefficients are calculated using the Lorentzian representation of a giant dipole resonance, which is caused by the protons and neutrons in the compound nucleus oscillating against each other [53], with the resonance parameters calculated by global models. In the models used, it is assumed that the  $\gamma$ -ray transmission coefficients are independent of spin and parity, an approximation that is valid as long as the wave functions of the highly excited states show a high degree of mixing [81].

The Hauser-Feshbach formula is based on the assumption that forming and decay of a compound nucleus are independent processes. However, the decay is actually not fully statistical, but there is some memory left in the compound system on the way it was formed. Especially the elastic channel has to be enhanced compared to the formula (2.7) because the particle can be immediately emitted before the equilibrium in the compound nucleus is formed [53]. This enhancement of the elastic reaction channel is taken account of in the NON-SMOKER code with width fluctuation corrections  $W(a, a', J, \Pi)$  with which the elastic channel is multiplied and to which the other transmission coefficients are renormalized [53].

The level densities used for the calculations in (2.8) in NON-SMOKER are calculated with the phenomenological back-shifted Fermi-gas model combined with the constant temperature formula [82] at very low excitation energies, as the back-shifted Fermi-gas model diverges at low energy [83]. For the back-shifted Fermi-gas model, an energy-dependent level density parameter  $a$  as well as microscopic corrections from nuclear mass models are moreover applied [83]. The level densities present one of the biggest uncertainties in the calculation of cross sections in the Hauser-Feshbach model with width fluctuation corrections [53], because extrapolating the phenomenological models used in NON-SMOKER for nuclei far off stability is highly uncertain [81] as well.

### Corrections to the NON-SMOKER data

Due to deficiencies in the estimates of the nuclear structure in the global model parameters employed for the Hauser-Feshbach models in the NON-SMOKER code, especially the microscopic correction factor of the FRDM model in the level density calculations, the cross sections exhibit a systematic deviation from experimental values depending on the neutron number, with the greatest deviations for magic numbers [84]. Therefore, correction factors depending on the neutron number have been derived in Ref. [84] for the nuclides for which experimental values were available and that can also be applied for neutron far off stability for which no experimental values are present.

### Applicability of the NON-SMOKER Code

As described above, the NON-SMOKER code provides two different mass models, and, therefore, also two sets of cross sections. For the first dataset, the FRDM is used for the cross section calculations for all nuclides with  $9 < Z < 84$ , from the proton drip line to the neutron drip line. For the second dataset, the ETFSI-Q model is used, and the range of atomic numbers of nuclides for which the calculations are performed is smaller with only  $23 < Z < 84$ . Even though the FRDM range is higher, this model suffers inconsistencies around shell closures, so that the cross sections for isotopes in these areas suffer higher inaccuracy.

For the calculations with the NON-SMOKER code, the Hauser-Feshbach statistical model for nuclear reactions is used, as for most astrophysical reactions, this model is applicable. However, one has to proceed with caution when using the NON-SMOKER cross sections in simulations of experiments because this model is only applicable if the level-density of the target nucleus around the peak of the incoming particle's energy is high enough to be treated statistically [53] and the resonances are completely overlapping [52]. Furthermore, the compound nucleus picture on which this model is based on only dominates for relatively low energies smaller than 20 MeV.

While the second condition is fulfilled for our calculations as we only consider an energy range of 50 keV to 10 MeV for the incident neutrons, the first condition causes problems for very light nuclei, nuclei with many neutrons and, thus, low separation energies, and nuclei near shell closures, as the level densities of these nuclei are too low to be assumed as statistically distributed. To describe the cross sections of these nuclei correctly, single resonances and direct capture contributions would have to be considered.

However, even with those inaccuracies in the statistical assumption and the FRDM model, the cross sections calculated with NON-SMOKER only deviate from experimental data by a factor of up to 1.5-2 with an even lower average deviation or 1.3-1.4 on average for neutron capture cross sections [52].

### 2.2.3 The TENDL-2019 Library and the TALYS Code

The last reaction data library used in the present work is the TENDL-2019 [65] (TALYS Evaluated Nuclear Data Library) library based on the TALYS code. Just like the ENDF/B-VIII.0 library, it is provided in the ENDF-6 format and, therefore, also has to be preprocessed with the PREPRO 2018 [70] codes. In contrast to the ENDF/B-VIII.0 library and the NON-SMOKER data, however, TENDL has the ambition to be a complete nuclear data library, as the philosophy behind this collection of data is that "every nuclear reaction process which is expected to take place in reality should be present in a nuclear data library, measured or not measured"[64]. While the ENDF/B-VIII.0 library consists of incomplete experimental data from different eras of nuclear data evaluation since the 1960s, therefore causing big quality differences even for different reaction channels of the same isotopes, and the NON-SMOKER data only comprises data important for astrophysical nuclear processes, the TENDL-2019 library is based on complete theoretically calculated nuclear reaction data for neutrons, photons, protons, deuterons, tritons, He-3 particles and  $\alpha$ -particles as projectiles and all 2813 isotopes from Hydrogen to Moscovium that are either stable or have a half-life longer than 1 second as target nuclides [65]. With this complete basis of nuclear reaction data, the TENDL library is improved by the

incorporation of experimental data, either by directly including the data from ENDF/B-VIII.0 as it is the case for very light or very well-examined nuclides<sup>2</sup> or by adjusting the input parameters of the TALYS code, which are by default taken from the Reference Input Parameter Library RIPL [85], until the calculated cross sections agree with the experimental data [64]. The mass values stored in this library are primarily the experimental values from the 2003 Audi Waspra table [86] and, therefore, a new version of the table used in NON-SMOKER. In case there are no experimental values, however, the values come from Goriely’s mass table based on Skyrme-Hartree-Fock-Bogoliubov calculations [87].

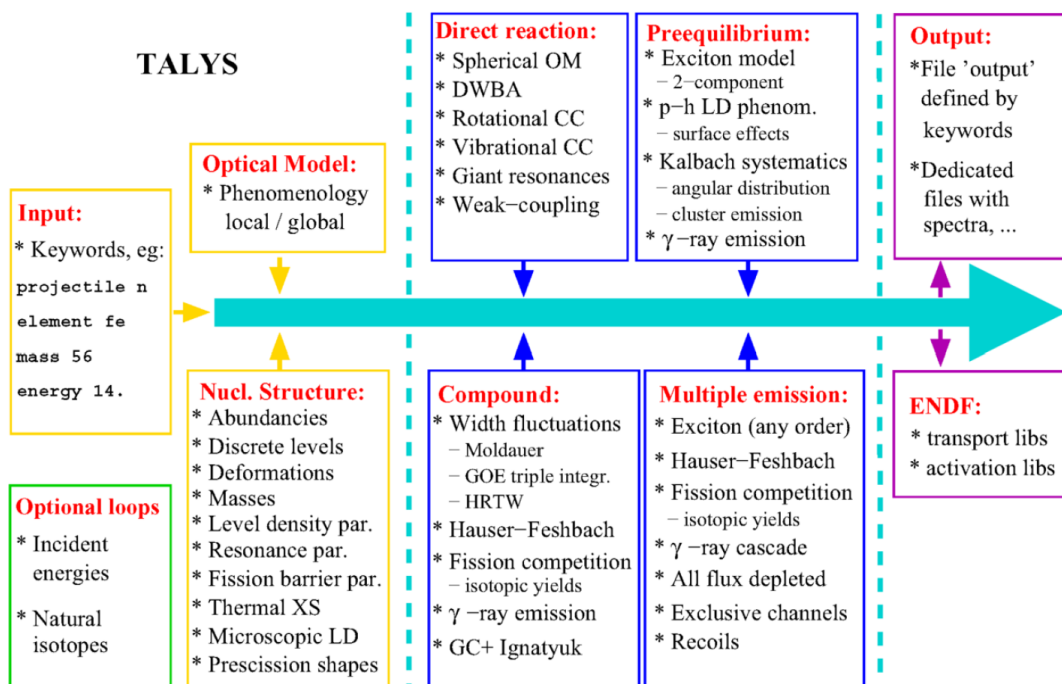


Figure 2.1: Theoretical models the TALYS code is based on [51].

The theoretical calculations for the TENDL library are mainly executed with the TALYS code. However, TALYS does not provide resonance information, the average number of neutrons from fission, prompt fission neutron spectra and complete covariance information. Therefore, to generate data for these processes and quantities, the codes TARES, TAFIS, TANES and TASMAN have to be used, respectively. Finally, the TEFAL code takes all of the information computed by the other codes and converts it into the ENDF-6 format.

TALYS is a code for analyzing and predicting nuclear reactions with the projectiles  $n$ ,  $\gamma$ ,  $p$ ,  $d$ ,  $t$ ,

<sup>2</sup>For the TENDL-2019 neutron sublibrary, this is the case for  ${}^1,2,3\text{H}$ ,  ${}^{3,4}\text{He}$ ,  ${}^{6,7}\text{Li}$ ,  ${}^{10,11}\text{B}$ ,  ${}^{7,9}\text{Be}$ ,  ${}^{12,13}\text{C}$ ,  ${}^{14,15}\text{N}$ ,  ${}^{16,17,18}\text{O}$ ,  ${}^{19}\text{F}$ ,  ${}^{232}\text{Th}$ ,  ${}^{233,235,238}\text{U}$  and  ${}^{239}\text{Pu}$ [65].

$^3\text{He}$  and  $\alpha$  for energies from 1 keV to 200 MeV and target nuclides with  $A > 5$ , enabling the calculation of nuclear reaction cross sections from the unresolved energy range up to intermediate energies and, thus, for the neutron energies considered in this work [51]. The TALYS code itself is based on various nuclear physics models illustrated in Fig. 2.1 the predictive abilities of which the calculations heavily rely on. Because the Hauser-Feshbach statistical model with width fluctuation corrections is used here as well for many calculations, the TALYS code - just like the NON-SMOKER code - suffers from inaccuracies for lighter nuclides. However, for those light nuclei, the TENDL-2019 library incorporates nuclear data directly from ENDF/B-VIII.0, therefore making it sufficiently reliable also for lighter nuclides. Another difference to the NON-SMOKER data is that for TENDL-2019, some direct capture processes, pre-equilibrium processes, fission as well as single resonances are actually calculated or adapted from experimental data [64] so that instead of just averaged cross sections with only the most important effects in the astrophysical energy range, TALYS accounts for most physically possible processes for the regarded projectiles and target nuclei. For neutron capture, for example, not only calculations with the Hauser-Feshbach model are performed, but also pre-equilibrium and direct capture is taken account of, and for low energies, single resonances are calculated as well.

In the following, the nuclear models for calculating the nuclear data available in TENDL-2019 will be illustrated, with the focus lying on the calculation of processes that are actually relevant to our work. Generally, more phenomenological models are used in the TALYS code than in NON-SMOKER because there is more experience in fitting these parameters to experimental data than for microscopical models. However, as explained for the NON-SMOKER level densities, such models are quite uncertain when extrapolating them to nuclei for which little to no experimental data is available.

### **The Optical Model Potential**

In TALYS, not only the particle transmission coefficients for the Hauser-Feshbach formula, but also quantities like the total cross section, the reaction cross section and the shape elastic angular distribution [64] are calculated with the optical model. Furthermore, the direct reaction formalisms employed in TALYS also based on this model.

In contrast to NON-SMOKER, where a global, microscopical OMP is employed, the optical potentials used in the TALYS code for the computation of the TENDL library are of phenomenological nature, meaning that instead of the potentials basing on microscopical calculations of nucleon-nucleon interactions, a Wood-Saxon potential is adapted and fitted to experimental data. Specifically, for non-actinide targets and nucleons as projectiles, the optical model potential of Koning and Delaroche [88] is used, for which different potential terms representing

the volume-central, the surface-central and the spin-orbit potential, as well as the Coulomb term for charged projectiles are fitted to experimental data for each target nucleus individually, therefore constructing a so-called local OMP. If, however, not enough data is available, a global parametrization developed in Ref. [88] is employed, calculations with which, however, are subject to relatively high uncertainties since it is not possible to describe the differences in the nuclear structure even between adjacent nuclei adequately in a smooth function of  $Z$  and  $A$  [88].

For actinides, the global optical potential developed in Ref. [89] is used. Lastly, for deuterons, tritons and Helium-3 particles as ejectiles or projectiles, a simplification of the folding approach of Watanabe [90] is used on the Koning and Delaroche potential to determine the OMP, and for  $\alpha$ -particles, the optical potential is that of Avrigeanu et al. [91].

### Direct Reaction Calculations with TALYS

In TALYS, direct reaction calculations are performed for each nuclide. For these calculations, several different methods are implemented in TALYS: (1) the Distorted Wave Born Approximation (DWBA) for (almost) spherical nuclides [51, 92], (2) coupled-channels calculations [51, 93], (3) the weak-coupling model for nuclei with an odd mass number [51], and (4) a model to include giant resonance contributions in the continuum [51]. For details on these models and their implementation in TALYS, see Refs. [92], [93] and [51, 56]. Furthermore, while with the other models prevalingly inelastic cross sections are calculated, it is also possible to estimate the direct neutron capture contribution with TALYS, which is important for light nuclides, nuclides near shell closures, and heavy neutron-rich nuclides with no resonance states available [94]. The used framework for this is the perturbative approach of the potential model, which is further described in [95] and [63].

### Level Densities used in TALYS

For most nuclides, the level density model used in calculations with TALYS is the back-shifted Fermi-gas model that has already been introduced in the section about the NON-SMOKER code [64]. However, there are some differences in the implementations of this model, as explained in Ref. [51], i.e., slightly different Fermi gas spin distributions and different choices of parameters as compared with the NON-SMOKER code. Moreover, instead of combining this model with the constant temperature model as it is done in NON-SMOKER, the divergence of the density at low energies is handled by introducing a density  $\rho_0$ . For more details, see Ref. [96].

While for most nuclides, the back-shifted Fermi-model is used, the ordinary Fermi-gas model is applied for some nuclei in combination with the constant-temperature model [51]. Further-

more, for very low energies, the Generalized Superfluid Model (GSM) is implemented. For more details on this, see Refs. [51, 96]. Moreover, for deformed nuclides, correction terms describing collective effects of the level densities, for which the expressions can be found in Ref. [51], can be applied as well. The parameters of all level density models have been adjusted to the discrete level data in the RIPL database [85], as well as average neutron resonance spacings. With that, the parameters are the same as in Ref. [96]. In addition to these phenomenological models, microscopic models for level densities are also implemented in TALYS for some nuclides [51].

### Gamma-Ray Transmission Coefficients

The  $\gamma$ -ray transmission coefficients for a  $Xl$  transition, which enter the Hauser-Feshbach as well as the pre-equilibrium model for several  $l$  to calculate cross sections with  $\gamma$ -emission, are calculated in TALYS according to

$$T_{Xl}(E_\gamma) = G_{\text{norm}} 2\pi f_{Xl}(E_\gamma) E_\gamma^{2l+1} \quad (2.9)$$

for the photon energy  $E_\gamma$  and the so-called gamma-ray strength function  $f_{Xl}(E_\gamma)$ . The factor  $G_{\text{norm}}$  is a normalization factor determined by the radiative capture width  $\Gamma_\gamma$ .

For the calculation of these  $\gamma$ -ray strength functions, two phenomenological models are used for the computation of the TENDL library, which, as already mentioned for the NON-SMOKER data, also assume the independence of the transmission coefficient of parity and spin. For most  $El$  and  $Ml$  transitions, the underlying form of the function used in TALYS is the Brink-Axel option with a standard Lorentzian describing the giant dipole resonance shape, which is also used in the NON-SMOKER code for E1 transitions. Only for E1 giant resonances  $f_{Xl}(E_\gamma)$  is assumed to have another shape, that of a generalized Lorentzian developed by Kopecky and Uhl [97]. For E1, there are also experimental GDR parameters stored in the RIPL library, while for the other transitions, global parameter formulas are used for the calculations [51]. Finally, there are microscopic strength-functions for E1 transitions implemented in TALYS [51].

### Fission

The last quantities left entering the TALYS compound nucleus reaction cross sections are the transmission coefficients for nuclear fission. In TALYS, the calculation of those is based on the transition state hypothesis formulated by Bohr and the Hill-Wheeler expression for the the probability of tunneling through the fission barrier [51]. According to Bohr, when fission occurs, the nucleus goes through a transition state which can be described by nuclear levels on the fission potential barrier. Furthermore, it is assumed that at each point of the process, the system equilibrates [98]. The Hill-Wheeler expression then gives the transmission coefficient for tunneling through the fission barrier with height  $B_f$  and the width  $\hbar\omega_f$  via a transition state

with energy  $\varepsilon_i$  above the barrier if the compound nucleus has an excitation energy  $E$  [51]:

$$T_f(E, \varepsilon_i) = \frac{1}{1 + \exp\left(-2\pi \frac{E - B_f - \varepsilon_i}{\hbar\omega_f}\right)}. \quad (2.10)$$

Even though experimental values for the fission barrier parameters are taken from the RIPL database [85], the fission transmission coefficients are oftentimes further normalized to experimental results from other nuclear data libraries [64]. This is due to the fact that fission channel calculations are difficult so that the theoretical fission calculations are a weak point of TENDL.

### Compound Nucleus Reactions

Now that the computation of all transmission coefficients entering the Hauser-Feshbach formula for compound nucleus reactions - particle emission,  $\gamma$ -emission and fission - and all other important quantities for the calculation of those cross sections like level densities and the optical model potentials have been explained, the TALYS calculations for binary compound nucleus reaction cross sections will be addressed in the following. Besides the variations of the quantities entering Eq. (2.7), the compound nuclear cross section in the laboratory is calculated very similarly in TALYS as in the NON-SMOKER code. However, because many more transmutation coefficients are calculated in TALYS than in NON-SMOKER, there are not only transmission coefficients for particle emissions as well as M1 and E1  $\gamma$ -emissions, but also for nuclear fission and  $\gamma$ -ray transmission coefficients of higher polarity. Therefore, when calculating  $T_{\text{tot}}$ , more processes have to be accounted for. In addition, the Moldauer model [99] is used in TALYS for the width fluctuation corrections.

Furthermore, TALYS takes into account that the Hauser-Feshbach model is not fully applicable when direct reactions and pre-equilibrium reactions are present [100] by multiplying the cross sections for single reactions from a specific entrance channel to a specific exit channel calculated with Eq. (2.7) with a so-called depletion factor  $D^{\text{comp}}$ . Therefore, instead of integrating over the transmission coefficients as in Eq. (2.8) to determine the laboratory cross sections, the integral has to be carried out over the single cross sections for TALYS. The factor  $D^{\text{comp}}$  reduces the cross section for the formation of a compound nucleus by subtracting effects based on direct and pre-equilibrium processes [51]:

$$D^{\text{comp}} = (\sigma_{\text{reac}} - \sigma_{\text{direct}} - \sigma_{\text{pre-eq}}) / \sigma_{\text{reac}}. \quad (2.11)$$

The underlying assumption that direct, pre-equilibrium and compound cross sections can be added incoherently is technically not quite correct [100], however, it reduces computational effort.

### The Preequilibrium Model

Apart from cross section calculations for direct and compound nucleus processes, TALYS also performs computations of cross sections for pre-equilibrium reactions, which are based on the two-component exciton model. In this model, it is assumed that when the incident particle enters the nucleus, it creates more and more complex states of excited particles and holes (divided in proton and neutron particles and holes) in the system consisting of the incident particle and the target nucleus step by step. Therefore, the memory of the incident particle's initial energy and direction is gradually lost [101]. Transitions between these exciton states are assumed to occur due to intranuclear two-body interactions. Therefore, the cross sections mainly depend on a general matrix element determining the damping of more and more complex exciton states, as well as the particle-hole density of both neutrons and protons. This model is further explained in Ref. [101]. Furthermore, nucleon transfer, break-up, and knock-out reactions are considered separately based on phenomenological models by Kalbach [102], because reactions in which the particle number of the projectile and ejectile differ are not included in the exciton model.

### Multiple Emissions

For incident energies above the neutron separation energy, a secondary particle can be emitted by the residual nucleus remaining after a first binary reaction in a so-called multiple emission [51]. For multiple Hauser-Feshbach decays, which are relevant in the energy range considered in this work, the only differences between binary and multiple emissions are that width fluctuations are not included in the latter and that the compound nucleus energy  $E^{\text{tot}}$  is replaced by the excitation energy bin  $E$  of the mother nucleus for multiple emissions.

### Resonance Data for the Neutron Sublibrary

In TALYS, single resonances are not calculated as for most calculations, statistical and optical models are used that, due to their averaging nature, are not suitable for calculating cross sections in the resolved energy range [56]. Still, resonance data for this range is included for all nuclides in the neutron sub-library, which comes either from existing experimental libraries, the Atlas of Neutron Resonances [103] or, if no experimental resonance parameters are given there, calculations of the TARES code are performed using the so-called High Fidelity Resonance approach, in which the optical model calculations performed with TALYS are extended to virtually 0 eV to compute average parameters that are used to compute statistical resonances.

### **Production of the TENDL library**

The TENDL library is produced for all nuclides and formatted in ENDF-6 in one process by using the so-called T6 codes, among which are TALYS and TARES, in a way that makes the library reproducible and the data traceable [51]. For many nuclides, the TALYS input parameters are adjusted to fit the experimental data, for very important or very light nuclides, experimental data is directly included in the library, and for nuclides with hardly any available data, the default TALYS calculations based on global models and parameters are executed. To estimate the uncertainties of the calculated values that don't come with an experimental covariance matrix, the input parameters are varied to generate statistical covariance matrices in this way.

The considerations about the two libraries of nuclear data, the NON-SMOKER data and the TENDL-2019 library, show how many models and approximations are necessary to calculate nuclear cross sections, and they illustrate how a plethora of (slightly) differing models for the same quantities exist, even though both codes only use well-established ones that show good agreement with experimental data. However, such experimental data is not available for many neutron-rich isotopes, so that for such nuclides, especially current phenomenological models are highly uncertain. New and better models for quantities crucial to nuclear reaction calculations are still subject of intensive research. This further emphasizes the necessity of cross section measurements for neutron-rich nuclides and, therefore, for experiments as proposed in this work. In chapter 7, comparisons of TENDL-2019 and NON-SMOKER data to ENDF/B-VIII.0 data will be carried out, respectively, to investigate the accuracy of cross sections from these datasets.

### 3 Neutron Capture Nucleosynthesis

Most light elements in the universe are produced by nuclear fusion reactions [17]. However, such reactions come to an end once atoms around iron are reached, as the binding energy per nuclide peaks for  $^{56}\text{Fe}$ , and the production of even heavier elements via fusion becomes energetically unfavourable. However, when regarding the abundance curve of isotopes in the solar system, one can see that there is a non-negligible amount of so-called "heavy elements" with  $A > 56$ , and that the distribution of these shows clear peaks at specific mass numbers (see Fig. 3.1). This structure is what led Burbidge, Burbidge, Fowler and Hoyle (often referred to in literature as B<sup>2</sup>FH) in their famous paper Ref. [17] to deduce that there must be different mechanisms of producing such heavy elements - processes they called the s-, r- and p-process. (The abundance curve shown in their original paper [17] can be seen in Fig. 3.1.)

This distinction in three processes has been made because in the solar abundance curve measured at this time (Fig. 3.1), a low fraction of proton-rich nuclides has been found, and the two-peak structure for the solar abundances of heavy, neutron-rich nuclides, has suggested two different processes producing such nuclides, with one of the processes occurring near the valley of stability, while in the other one, very neutron-rich nuclides far off stability are produced, which then  $\beta$ -decay back to stable nuclides, as it is illustrated in Fig. 3.2 [17]. The production process of proton-rich isotopes mainly through proton capture ( $p, \gamma$ ) has, consequently, been named the p-process. The two other processes both rely on neutron capture reactions ( $n, \gamma$ ) to produce heavy elements at different speeds, so that they have been called the slow and rapid neutron capture process (s-process and r-process), respectively. Both these processes are of great astrophysical relevance because approximately 50% of all produced heavy nuclides in the universe are assumed to be created in either of them [16]. However, despite extensive research on the r- and s-process, some problems remain unresolved, first and foremost the astrophysical site(s) of the r-process. Therefore, neutron capture studies on nuclides relevant to these processes with neutron fluxes similar to those present in the astrophysical environments could help understand the production of heavy nuclides in the universe better. In the following, the basic mechanisms and models describing the s- and r-process will be illustrated. Furthermore, the environments in which the processes occur will be described, and lastly, a few issues of current research will be addressed for which the present work might be relevant.

### 3 Neutron Capture Nucleosynthesis

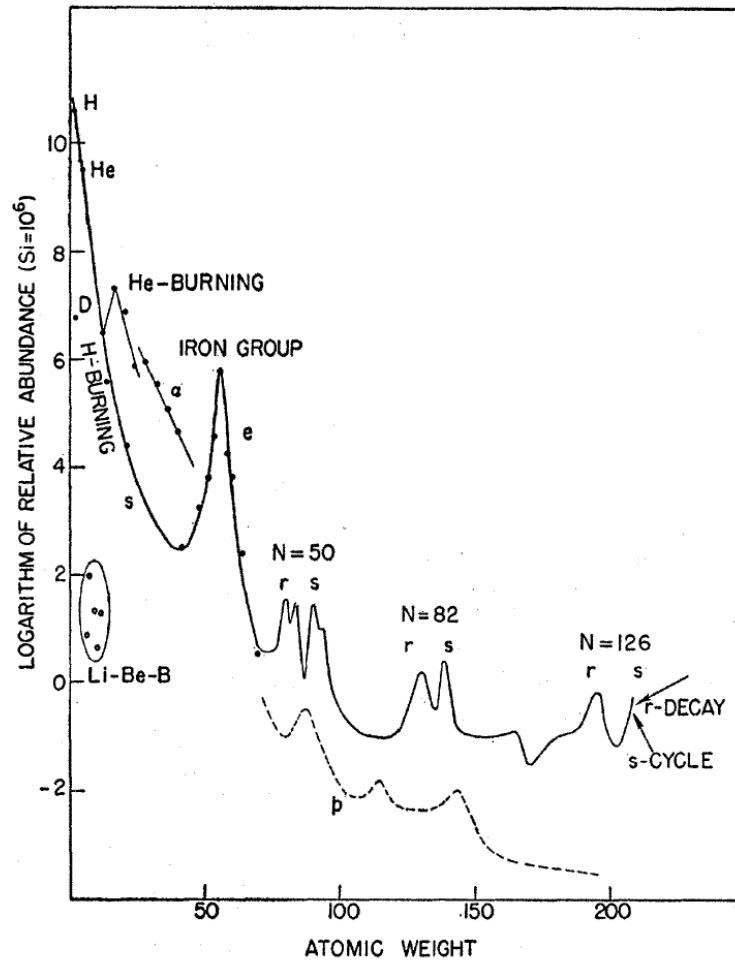


Figure 3.1: Schematic atomic abundance curve as a function of atomic weights according to the measurements of [104], with assignments of the abundances to specific processes made by B<sup>2</sup>FH in Ref. [17].

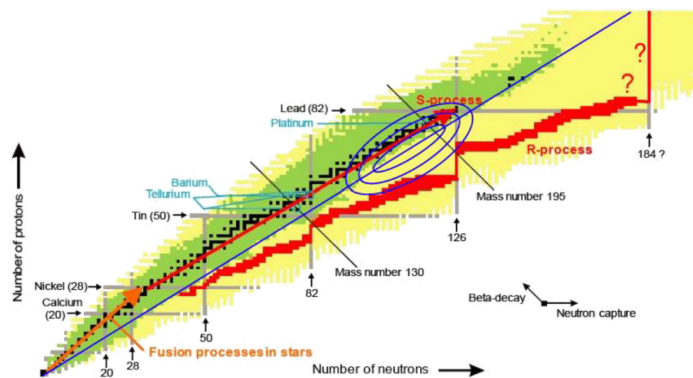
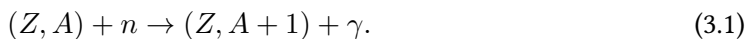


Figure 3.2: Chart of nuclides with the paths of the r- and s-process illustrated, taken from Ref. [47]. The nuclides marked in black are stable (valley of stability).

As mentioned above, both the r- and the s-process are based on neutron capture and successive  $\beta$ -decay [105]. They, therefore, rely on a sufficient amount of neutrons being present together with so-called seed nuclei that capture the neutrons. The conditions under which these processes occur and the ways of production of those neutrons and seed nuclei, which differ heavily for the two processes, will be discussed in the following sections. For now, we simply assume that seed nuclei and neutrons are both present to discuss the fundamentals of both processes.

When a seed nucleus is exposed to a neutron flux, it will capture a neutron with the capture rate  $R_{n\text{-cap}} = n_n n_A \sigma_{n\text{-cap}} v$  depending on the neutron density  $n_n$ , the relative thermal velocity  $v$  between neutrons and seed nuclides, the density of seed nuclides  $n_A$ , and the cross section  $\sigma_{n\text{-cap}}$  for the neutron capture process [105]:



If the nuclide with  $(Z, A + 1)$  is stable, a new stable isotope of the former element is produced that can then again capture another neutron to produce a new nuclide. If, however,  $(Z, A + 1)$  is a  $\beta$ -emitter, two different processes could happen: Firstly, the nuclide could experience a  $\beta$ -decay to  $(Z + 1, A + 1)$  first and then capture another neutron, or it could capture a second or even multiple neutrons before finally decaying. What process happens depends on the relative reaction rates of the neutron capture process and the  $\beta$ -decay, and it is also the ratio of reaction rates that distinguishes the s- from the r-process.

If the neutron flux, for example, and, therefore, the neutron capture rate is so low that the  $\beta$ -decays of elements happen before another neutron can be captured, the neutron capture process occurs uninterrupted as long as it produces stable isotopes [105]. However, if a radioactive nuclide is reached, it most certainly decays before it can capture another neutron. Because in this kind of process, neutrons are captured on a rather long timescale, this is called the slow neutron capture process, or s-process. Therefore, especially nuclides near the valley of stability are produced in this process (see Fig. 3.2) [105]. The s-process terminates in a cycle starting with  $^{209}\text{Bi}$  and ending with the same nuclide, so that no heavier stable nuclides are produced [106].

If the neutron flux and, therefore, the neutron capture rate is much higher than the  $\beta$ -decay rates of most isotopes, successive neutron capture cascades occur with no  $\beta$ -decays in between captures [105]. Thus, such a process is called rapid neutron capture process or r-process. The capture chains of this process can extend to the so-called neutron drip line, which is the line on the chart of nuclides beyond which no stable nuclides can exist as additional neutrons would have a negative separation energy [107]. Therefore, the r-process yields especially neutron-

rich isotopes [105], and it can produce elements with higher  $Z$  than the s-process.

### 3.1 The S-Process

Of the two processes, the s-process is quite well investigated. The astrophysical sites on which this process occurs, for example, are identified as low mass AGB stars, as well as massive stars that explode as supernovae type II, for which quite well-established stellar models exist [15]. In such stellar models, the astrophysical conditions for neutron capture processes are simulated as a function of time, with the variations based on the changing astrophysical conditions [24]. In this changing environment, a reaction network consisting of the processes in which neutrons are produced as well as neutron capture and  $\beta$ -decay reactions is employed to simulate the produced abundance of s-process isotopes. The astrophysical conditions under which the s-process occurs and current challenges of the s-process models are illustrated in the following.

#### 3.1.1 Models, Conditions and Sites of the S-Process

##### The Main S-Process in AGB Stars

It was found by Iben and Renzini [108] and Hollowell and Iben [109] that the production of most s-process nuclides in the so-called main process of slow neutron capture nucleosynthesis can be associated to the stellar site of low mass stars in the asymptotic red giant branch (AGB). Stars in this phase of stellar evolution consist of a degenerate core made of mainly  $^{12}\text{C}$  and  $^{16}\text{O}$  surrounded by a helium burning shell, a helium- and carbon-rich intershell, a hydrogen burning shell and a highly convective envelope [110]. This is illustrated in Fig. 3.3. The AGB phase stars undergo two processes that are crucial for the synthesis of s-process elements: thermal pulses (TP) and the so-called third dredge-ups (TDU).

In a thermal pulse (TP) in an AGB star, a large amount of energy is released due to He-burning in the He intershell, leading to convection in this intershell, in which a huge quantity of  $^{12}\text{C}$  is produced through the triple-alpha-process in partial He-burning [108]  $^4\text{He}(\alpha, \gamma)^8\text{Be}(\alpha, \gamma)^{12}\text{C}$ . Furthermore, the convective envelope expands and the H-burning is shut off. After a few of these pulses, in a phase where the convective zone in the He intershell is extinguished and He burning shuts off as well, a so-called third dredge-up (TDU) can occur [15]. In such a TDU, the convective envelope penetrates the He-intershell, so that the elements produced in this shell during several thermal pulses are brought to the surface of the star.

For the s-process to occur, free neutrons must be present that can be captured by already existing seed nuclei in this secondary neutron capture process [15]. In the main s-process, two

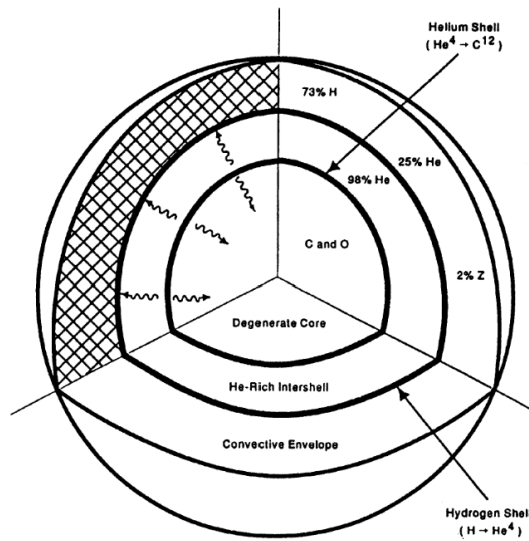


Figure 3.3: Schematic sketch of an AGB star prior to a thermal pulse, taken from Ref. [110].

sources for neutron-production are suggested by most stellar models of AGB stars. The first possible neutron source is the  $^{13}\text{C}(\alpha, n)^{16}\text{O}$  reaction [15]. Most models suggest that the  $^{13}\text{C}$  needed for this reaction are produced via  $^{12}\text{C}(p, \gamma)^{13}\text{N}(\beta^+ \nu)^{13}\text{C}$  during the TDU when protons from the H-rich envelope can enter the He intershell, which is rich in  $^{12}\text{C}$  [111]. The models, furthermore, propose that the  $^{13}\text{C}$  atoms then form a pocket in the intershell, in which neutron densities of about  $10^6 - 10^8 \text{ cm}^{-3}$  can be produced at temperatures of about  $0.9 \times 10^8 \text{ K}$ , corresponding to neutron energies of about 8 keV and a neutron flux of  $10^4 - 10^6 \text{ cm}^{-2}\text{s}^{-1}$  [15]. However, no hydrodynamical models have been developed for the formation of the  $^{13}\text{C}$  pocket. Furthermore, in lower mass stars, protons can also be ingested into the intershell during a TP [111]. When the temperature is higher than  $2.5 \times 10^8 \text{ K}$  at the bottom of the convective zone of the He intershell during a TP, neutron production via the  $^{22}\text{Ne}(\alpha, n)^{25}\text{Mg}$  reaction is possible as well, leading to a neutron density of up to  $10^{10} \text{ cm}^{-3}$  and neutron energies of about 23 keV [15] and, therefore, a neutron flux on the order of  $7 \times 10^7 \text{ cm}^{-2}\text{s}^{-1}$ . The  $^{22}\text{Ne}$  needed for this can be produced from the abundant  $^{12}\text{C}$  during the course of a TP [108]. As opposed to the about 10,000 years that the  $^{13}\text{C}(\alpha, n)^{16}\text{O}$  neutron source is active, the s-process via  $^{22}\text{Ne}(\alpha, n)^{25}\text{Mg}$  neutrons is only supposed to last for a few years [15].

The neutrons produced in these processes then interact with present seed nuclides, and the relatively high neutron fluences allow for an equilibrium between neutron captures and  $\beta$ -decays to establish [15]. The resulting s-nuclide abundance, which is highest for nuclides with low neutron capture cross sections, is transported to the surface of the star via the next TDU [15]. From there, they are carried away into the interstellar medium via wind during the

### 3 Neutron Capture Nucleosynthesis

AGB phase, due to ejection of planetary nebula or after explosions as a supernova [108].

Due to the thermal pulses, TDUs and the convections in the shells, the s-process is highly dynamic with varying temperature and neutron density. Therefore, correctly modeling the s-process relies heavily on advanced hydrodynamical models of the astrophysical conditions, some of which have not been developed yet [111]. To test such models against the measured s-process abundances, especially nuclides at so-called branching points are important. Despite that when classifying the s-process, we distinguished it from the r-process by postulating that  $\beta$ -decay happens at a faster rate than the slower neutron capture, the rates of  $\beta$ -decay  $R_\beta = n_{\text{seed}} \ln(2)/T_{1/2}$  and neutron capture  $R_{n\text{-cap}}$  are comparable for some s-nuclides [15]. For these nuclides, the two processes compete and so-called branching occurs [15], so that some nuclides might decay, while others might capture an additional neutron, creating different "branches" of the s-process on the chart of nuclides. Because the  $\beta$ -decay and neutron capture reaction rates depend heavily on the stellar temperature and the neutron density during the process, the abundances of nuclei at branching points are a sensitive test for the dynamics of the stellar environment of the s-process and, therefore, stellar models. Such an improvement to the stellar models could not only make the s-process predictions better, but also have a strong impact on studies on the Milky Way, as well as surrounding galaxies [15]. However, for reliable information to be deduced about the s-process conditions from branching point abundancies, the unstable nuclides involved in s-process branchings and, especially, their cross sections must be examined experimentally with a high precision. These isotopes, however, are largely unexplored in experiments because of their relatively low half-lives [15]. Therefore, observing neutron capture processes for such nuclides and producing more neutron-rich nuclides near the branching points of the s-process, as it is simulated in the present work, for further investigation of the quantities relevant to the s-process, like  $\beta$ -decay properties or different cross sections, could highly improve our understanding of the s-process of nucleosynthesis.

#### The Weak S-Process in Massive Stars

In the main s-process, too little s-isotopes with  $A > 90$  are produced. Therefore, another process must exist that contributes to the production of those nuclides. According to the stellar models for this process, which is called the weak s-process, it occurs in massive stars with  $M > 8M_\odot$  and high metallicity that explode as supernovae type II.

In the case of the weak s-process, the neutrons to be captured are all produced by the  $^{22}\text{Ne}(\alpha, n)^{25}\text{Mg}$  reaction, both in the phase of He-burning in the convective core of the star and in the consecutive phase of convective shell C-burning [15]. According to current stellar models, the weak s-process during core He-burning occurs at temperatures of  $T \propto 3 \times 10^8$  K, corresponding to neutron energies of 26 keV and the temperature during shell C-burning amounts

to approximately  $T \propto 1 \times 10^9$  K and, therefore, a thermal energy of 90 keV [15, 24]. Thus, the weak s-process happens at significantly higher temperatures than the main process. The neutron densities are assumed to amount to about  $10^6 \text{ cm}^{-3}$  for core He-burning, and for shell C-burning, an initial neutron density of approximately  $10^{11} - 10^{12} \text{ cm}^{-3}$  is predicted, which then quickly decreases exponentially [24]. Therefore, the neutron fluxes have values around  $10^5 \text{ cm}^{-2}\text{s}^{-1}$  and up to  $10^{10} \text{ cm}^{-2}\text{s}^{-1}$  in the two scenarios of the weak s-process.

Because of the quite low timescales on which the weak s-process occurs, especially in the convective shell, the neutron fluence for the weak s-process is not high enough to achieve reaction flow equilibrium as opposed to the main process, and only nuclides of relatively low mass are produced [24]. Furthermore, this means that instead of a neutron capture cross section for one nuclide only influencing the abundance of said nuclide itself, as it is the case for the main s-process, the cross section has an effect on the abundances of the heavier isotopes on this branch.

It is, hence, hard to correctly calculate the contribution of the s-process, especially the weak s-process, to the solar system abundances of heavy elements with stellar models and nuclear reaction network, as there are still high uncertainties on neutron capture cross sections, especially for nuclides with low half-lives between Fe and Se. Therefore, experimental access to cross section measurements for relevant s-process nuclei is essential to the predictive power of the s-process stellar models [15, 24].

## 3.2 The R-Process

### 3.2.1 Models and Conditions for the R-Process

As already described in the introduction to this chapter, the r-process produces highly unstable nuclei far from the valley of stability. Therefore, this process allows the production of heavy nuclei up to U and Th and very neutron-rich isotopes [16]. However, the nuclear structure quantities and cross sections for such unstable heavy isotopes are poorly known and rely heavily on theoretical models, models which, as illustrated in chapter 2, differ for diverse nuclear datasets. Furthermore, the solar r-abundance curve which a possible r-process site should reproduce is object to uncertainties of the s-process and p-process models, which are used to calculate the solar r-process abundances by subtracting them from the total abundance curve. (The resulting curve is shown in Fig. 3.4 for nuclides up until the termination point of the s-process,  $^{209}\text{Bi}$ ). These are just some of many reasons that make the determination of the r-process site difficult, and why this site is heavily under debate [16, 81, 112, 113], even though the process itself has been introduced more than 60 years ago [81]. Despite the astrophysical site of the r-process still not being fully known, some conditions that characterize the r-process site can still be identified based on the observed r-process abundances. The most important is

### 3 Neutron Capture Nucleosynthesis

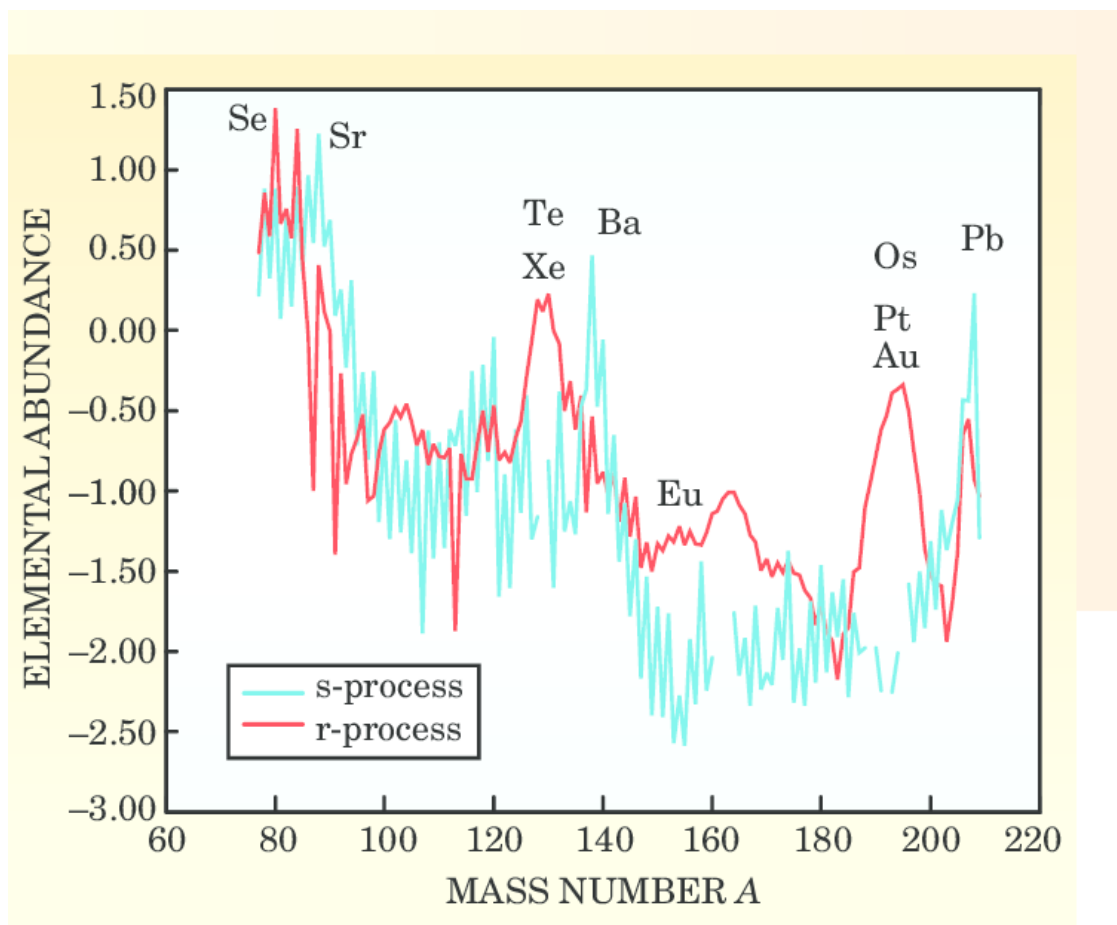


Figure 3.4: Solar r-process and s-process abundances, taken from Ref. [114].

a high neutron density of more than  $10^{20} \text{ cm}^{-3}$  [115], without which the neutron capture rate could not be significantly higher than the  $\beta$ -decay rate. For the production of the heaviest elements, neutron-to-seed ratios exceeding 100 are needed [113]. Furthermore, the abundances suggest an explosive environment as the site of the r-process [19], with the process occurring at a timescale on the order of seconds [81]. With these assumptions and the goal of reproducing the r-abundance curve, several site-independent models have been developed with which the r-processes in the different environments can be calculated. The basic underlying concepts of these will be briefly introduced in the following.

### Hot R-Process

Generally, sites for the r-process can be divided into hot and cold sites [81]. For a hot r-process to occur, the temperatures have to be high enough for photodisintegration, i.e.  $(\gamma, n)$  reactions, to become efficient, which corresponds to temperatures of  $T \gtrsim 10^9 \text{ K}$  or neutron energies of more than 86 keV. In this case, the amount of nuclides that can be captured by each seed nucleus is mainly dependent on the competition between  $(n, \gamma)$  and  $(\gamma, n)$  reactions as well as  $\beta$ -decay half-lives of the nuclei, and it was proposed already by B<sup>2</sup>FH[17] that a so-called  $(n, \gamma) \leftrightarrow (\gamma, n)$  equilibrium is established, if only the temperature and density are high enough [116, 117]. Further studies have found that this is even the case in dynamical environments [117], so that such equilibria are assumed to establish in most hot r-process environments. For a  $(n, \gamma) \leftrightarrow (\gamma, n)$  equilibrium, it is assumed that seed nuclides rapidly capture neutrons up to so-called waiting point nuclides, which are determined by a specific  $Q$ -value of the capture reaction depending on the neutron density and temperature of the environment for the equilibrium, where they await  $\beta$ -decay and the iso- $Z$  neutron capture chains are connected. In this model, these waiting point nuclides define the r-process path, and the abundances that are reached are only determined by the temperature, the neutron density, the masses of the nuclides, which are needed to calculate the separation energies, and the  $\beta$ -decay half-lives, which determine how many nuclides accumulate at the waiting points before decaying.

However, the system, even in initially hot environments, eventually falls out of equilibrium, for example because the highly temperature dependent  $(\gamma, n)$  reactions decrease as the r-process site, usually consisting of some kind of ejecta, cools down and expands [112]. Directly after such a freeze-out, current models assume that the neutron density is still high enough that competition of neutron capture,  $\beta$ -decay, and even  $(\gamma, n)$  reactions occurs, so that even in the hot r-process case, neutron capture reactions play a role for determining the final abundances [118].

#### Cold R-Process

A cold r-process occurs when the temperatures in the environment are not high enough for  $(\gamma, n)$  reactions to be efficient, so that the evolution of the abundances during the r-process is a result of the competition between neutron capture cross sections and  $\beta$ -decay [16, 81, 118]. Therefore, while for the hot process, especially nuclear masses for the calculation of separation energies, as well as  $\beta$ -half-lives of the nuclides are important, modelling of the cold process is dominated by  $\beta$ -half-lives and neutron capture cross sections.

#### High Density Environment and Fission Cycling

For very high neutron densities or very high neutron-to-seed ratios of about 150 [19], nuclides as heavy as the actinides can be produced in the r-process from seed nuclei with  $A$  between 50 and 100. In these cases, neutron-induced as well as spontaneous fission of heavy, neutron-rich isotopes influences the r-process abundances of nuclei heavier than  $A \approx 130$  (which corresponds to the second peak of the abundance curve) [119] in a process called fission cycling, in which fissioning nuclides from the trans-uranium region decay into fragments around  $A = 130$  [119]. Once produced, these nuclides can function as seed nuclides for the r-process [119]. However, because especially for the heavy neutron-rich nuclides involved in the r-process not many fission properties have been measured, the exact dynamics of fission cycling are still a subject of current research [119].

From the considerations above, it can be seen that for different environments, different nuclear quantities determine the abundances of r-process nuclides and the dynamics of the r-process. Because of the dynamical nature of the r-process and in order to account for all effects, even if they only contribute minutely, all current models for r-processes at different sites base on reaction networks. In these, neutron capture reactions  $(n, \gamma)$ , photodisintegrations  $(\gamma, n)$ ,  $\beta$ -decays like  $(\beta, \gamma)$  reactions and  $\beta$ -delayed neutron emissions  $(\beta, n)$  are included. Furthermore, for high densities and neutrino-rich environments, fission processes and interactions with neutrino fluxes have to be taken into account as well. One example for such a network can be found in [120].

#### 3.2.2 Astrophysical Sites of the R-Process

When it comes to the astrophysical sites of the r-process, the comparison of the r-abundances in the most metal-poor stars in the galaxy [19, 121] with solar abundances suggest a unique process for heavy elements with  $56 < Z < 70$  throughout the galactic evolution. R-process elements with lower  $Z$ , however, might be produced at (several) different sites. Though the general concepts and reactions underlying the r-process are known, the sites of the r-process are still not unambiguously identified. The most promising of sites that have been investigated

thoroughly during the last years are neutrino winds emitted by core collapse supernovae, as well as different kinds of ejecta of neutron star mergers. These scenarios and whether the production of r-process elements is probable there will be briefly discussed in the following.

### The R-Process in Neutrino-Driven Winds Emitted by Core Collapse Supernovae

Since the 1960s, the site of neutrino-driven winds emitted after core collapse supernovae has been thought to be the most promising for the r-process [19]. Such core collapse supernovae occur at the end of the lifetime of stars with  $M > 8M_{\odot}$  [22]. Though the details of such supernovae are still under investigation, it is known that after the explosion, the proto-neutron star left after the supernova cools down by emitting neutrinos, which can then drive a wind of protons and neutrons consisting of ablated matter from the proto-neutron star surface [16]. The material in the neutrino-driven wind is usually assumed to be very hot (with temperatures higher than  $10^{10}$  K) and have a low density and, therefore, a high entropy. Shortly after the ejection, the matter of the ejecta is then in nuclear statistical equilibrium, so that primarily nuclides up to the iron group are produced [122]. However, with the expansion and cooling of the material, the wind freezes out of equilibrium at about  $T = 3 \times 10^9$  K in an  $\alpha$ -rich freeze-out [19] due to which elements heavier than He are less abundant than for NSE, but shifted to higher  $A$  values, therefore providing heavy seed nuclides, which can then capture free nuclides available in the wind.

The exact conditions for the proposed r-process like the seed nuclide distribution, the temperature and the neutron density present during the neutron capture process are highly dependent on the entropy, the expansion time and the initial electron fraction of the ejecta [16]. The temperature and neutron density are then simulated over time by calculating the time evolution of these quantities along different trajectories of different ejecta [22]. However, due to the uncertainties about the supernovae themselves, also the models for these trajectories and, therefore, the conditions for the r-process are subject to uncertainties. Generally, the temperatures during the r-process are assumed to range between values at or slightly above the charged-particle freeze-out to temperatures as low as  $T \propto 10^8$  K, depending on the exact conditions assumed for the environment and if the process is mainly hot or cold [16, 20, 113, 123]. This corresponds to neutron energies between 8 keV and 300 keV. For the neutron densities, values between  $10^{20}$  and  $10^{27}$   $\text{cm}^{-3}$  are assumed in most models [20, 123], so that the neutron flux ranges between  $10^{19}$   $\text{cm}^{-2}\text{s}^{-1}$  and  $10^{27}$   $\text{cm}^{-2}\text{s}^{-1}$ . Early simulations like in Ref. [124] have predicted extremely high entropies in the wind, resulting in relatively low seed abundances and high neutron densities, so that these early models predicted the production of even the heaviest r-nuclides of the 3rd abundance peak. However, with newer hydrodynamical models lower entropies are predicted, so that the neutron-to-seed ratio calculated in these simulations is too low to produce high- $A$  nuclides beyond the second peak at  $A \propto 130$  [16, 19, 118, 123, 125]. Furthermore, it

### 3 Neutron Capture Nucleosynthesis

has been found recently with simulations including a detailed description of time-dependent neutrino physics that too many neutrons are converted into protons by  $\nu_e + n \rightarrow p + e^-$ , so that due to the hence lower neutron density only r-process nuclides up to silver ( $A=109$ ) can be produced [22].

If a high magnetic field, however, accompanies the supernova, it has been shown that the entropy is increased [126], and if the magnetic field is paired with rotational movements, jet-like supernovae can occur, in which, due to the high emission velocities, only few neutrons are converted into protons [22]. Therefore, in such modified supernovae environments, the production of third-peak nuclides could indeed be possible, but doubt has been casted recently on this site producing enough third-peak nuclides as well in Ref. [127]. To ultimately confirm or rule out neutrino-driven winds in supernovae as an astrophysical site of the r-process, maybe even for the production of high- $A$  nuclei, the predictions of the models for such scenarios would have to be more precise and, therefore, nuclear quantities for the neutron-rich nuclides involved in the process would have to be known well.

#### **The R-Process in Mergers**

The astrophysical site that is currently seen as the most promising for producing also heavy r-process elements are mergers of either two neutron stars, one neutron star and one black hole, or two black holes. Such merger events have been considered as a possible source for some time with the first calculations performed in Ref. [128], but the scenario in supernovae had been favoured because the neutron merger abundances did not seem to fit the abundance patterns in metal-poor stars [129]. However, more recent investigations have shown that the only infrequently occurring but high-yield neutron merger events could, in fact, be the dominant r-process source in the universe [130, 131]. The relevance of merger processes as an r-process environment has, furthermore, rapidly increased since the observation of the neutron star merger event GW170817 in 2017 [132], for which gravitational waves have been observed. Observations of this event with several telescopes (e.g. [133]) have confirmed the emission of a kilonova afterglow powered by the radioactive decay of heavy nuclides produced in an r-process, which has been predicted in Ref. [134], which confirmed the production of a wide spectrum of heavy r-isotopes [22].

The light and heavy elements produced in neutron star mergers are believed to be created in different phases of the merging process, the hydrodynamical evolution of which can be simulated using GR codes [19, 135]. After the merging process of the neutron stars, an extremely massive, compact neutron star is created surrounded by an accretion disc [22]. The neutron star can then, if it does not immediately turn into a black hole, emit neutrinos, which can drive

a wind of the material in the accretion disk similar to the neutrino-driven winds ejected after core collapse supernovae. However, because of the high neutrino density, again not enough neutrons per seed nucleus are present in these winds to produce elements beyond the second peak [22]. Heavier nuclides are produced in so-called dynamical ejecta emitted from the neutron star during the merging either from the interaction region of the two neutron stars (hot ejecta) or colder matter, which could be ejected by tidal torques [134] and is assumed to be shock-heated to energies above 1 MeV [136]. Because dynamical ejecta are extremely neutron-rich [134] with initial neutron densities between  $10^{33}$  and  $10^{35} \text{ cm}^{-3}$  [136] and neutron-to-seed ratios of up to 1000 [21], especially nuclides from the second peak to the third peak of the r-process abundances are produced in these ejecta according to current models [130]. Furthermore, the expansion time is assumed as long enough for all neutrons to be captured [21], so that for the r-process in these ejecta, regardless if it starts out hot or cold, the nuclear reactions during the freeze-out highly determine the resultant abundances. Similar conditions can also be found in black hole accretion disk winds powered by viscous heating [21] after the compact neutron star has eventually turned into a black hole [19]. Generally, all ejecta of binary mergers are, assumed to be either sufficiently hot when ejected or heat up sufficiently for NSE with subsequent freeze-out of charged particle reactions to occur, and the r-process is supposed to occur both in hot and cold processes, depending on the initial conditions and the evolution of the ejecta [21]. The temperature range in which the r-process occurs is, therefore, the same as for supernovae. However, especially for dynamical ejecta, the neutron densities are higher [16], so that the neutron flux can exceed the values for the r-process in supernovae.

A quite astonishing fact about the r-process in dynamical ejecta and black hole accretion disk winds is that in different simulations and with different astrophysical parameters used, the resultant abundances for heavy isotopes with  $A > 130$  do not change significantly [22, 134], therefore making these sites, in fact, a good candidate for the production of the unique r-process abundances. This is due to the fact that because of the high neutron densities, the r-processes in these ejecta proceeds very closely to the neutron drip line and fission cycling plays a great role as well [19, 130, 134], so that the abundances are almost entirely determined by the nuclear properties. High uncertainties about the properties of neutron-rich nuclides might also very likely be the reason why the abundances calculated in the different simulations are not in complete agreement with the observed values [22].

In conclusion, several uncertainties still surround the r-process, and especially the site is not unambiguously identified. These are partly due to uncertainties in the hydrodynamical models describing the different ejecta that are possible candidates for sites, but the main reason for the uncertainties is that the neutron-rich nuclides involved in the r-process are experimentally highly uninvestigated, so that the nuclear reaction networks for the r-process are subject to

### 3 Neutron Capture Nucleosynthesis

high uncertainties [112]. The influence of these uncertainties is especially high for cold processes or the part of the r-process occurring when the system is frozen out of equilibrium, as well as for nuclides so heavy that the highly uninvestigated fission cycling plays a role. Especially for the r-process producing heavy nuclides up until the trans-uranium region, moreover, the nuclides around the  $N = 126$  waiting point are interesting. This waiting point is the last point at which the r-process path approaches the valley of stability before the production of the heaviest nuclides because of the low binding energy and the high half-life at the shell closure. Therefore, nuclides around this point are both important for producing third abundance peak and for producing elements higher than that. Therefore, measurements on quantities like  $\beta$ -decay rates or neutron capture cross sections on very neutron-rich nuclides that are either relevant to fission cycling or that lie around the  $N = 126$  waiting point, and which could be produced in the investigated scenario of laser-driven neutron sources, could heavily improve the predictions of the r-process models and, therefore, help identifying the site of the r-process, for example by confirming or ruling out neutrino-driven winds with high magnetic fields or neutron star mergers as the unique source for the production of heavy nuclides. Moreover, if it is possible to observe neutron capture cascades similar to those in the r-process at similar neutron fluxes as in r-process environments in experiments with laser-driven neutron sources, the process itself could be studied in the laboratory and, therefore, understood better.

To conclude our discussions of nucleosynthesis processes for heavy nuclides, we want to note that in recent years, several more processes other than the r-, s- and p-process, for example the i-process [25, 26], the Lighter Element Primary Process [15, 27], the  $\nu p$  process [28], and the rp-process [29] have been suggested to account for differences of observations of nuclear abundances at different astrophysical sites. However, such processes hardly influence the solar abundances. Still, especially the understanding of the i-process, which is thought to occur in CEMP stars via the  $^{13}\text{C}(\alpha, n)^{16}\text{O}$  at neutron densities slightly higher than for the s-process could be improved with neutron capture experiments with laser-driven neutron sources. Furthermore, because slightly different parameters for the main s-process could also make a LEPP redundant [27], the investigations of the s-process branching nuclides could also confirm or rule out the need for such a source.

## 4 Laser-based Neutron Sources

In the present work, simulations of neutron capture processes in targets irradiated with laser-driven neutron sources. Therefore, different methods of neutron production with such sources that are either currently possible or will be in the near future are addressed in the following to illustrate the neutron pulse parameters possible with such sources and compare them to conventional neutron sources as well as those at the astrophysical sites of the r- and s-process. To be able to conduct such comparisons, the conventional methods for neutron production will be briefly introduced first.

### 4.1 Conventional Neutron Sources

Until recently, the experimental production of high neutron fluxes relied mostly on large reactor and accelerator based facilities. Reactor facilities base on nuclear fission chain reactions, in which thermal neutrons are absorbed by a fissile nuclide like  $^{235}\text{U}$ , which then splits in two lower-mass nuclides, emitting 2-3 neutrons in the process [33]. Of these, one neutron is needed to maintain the chain reaction, whereas the other neutrons can be used for experiments that are usually carried out by placing the sample to be studied in the reactor. Because of the continuous nature of the chain reaction, the neutrons produced in such a reactor are not pulsed but there is a continuous flux and the spectra of the neutrons are polychromatic. The number of neutrons produced in a fission reactor scales with its thermal energy production and amounts to about  $7.5 \times 10^{16}$  neutrons per second and megawatt of energy produced, which, for leading reactor facilities, means that a total neutron flux of over  $3 \times 10^{15} \text{ cm}^{-2}\text{s}^{-1}$  and thermal neutron fluxes of above  $2 \times 10^{15} \text{ cm}^{-2}\text{s}^{-1}$  can be achieved with reactors like the HFIR [137] at Oak Ridge, Tennessee, as can be seen in Fig. 4.1. For fast neutrons, for instance the peak neutron flux of the FRM-II reactor in Munich, amounts to about  $5 \times 10^9 \text{ cm}^{-2}\text{s}^{-1}$  [37]. However, the energy output and, therefore, the flux of such reactor facilities is limited by reactor safety considerations.

The second important class of conventional neutron sources are accelerator based facilities that produce neutrons in single pulses in contrast to the continuous production in reactors [33].

Firstly, there are small accelerator sources, in which accelerated ions, often protons, produce

#### 4 Laser-based Neutron Sources

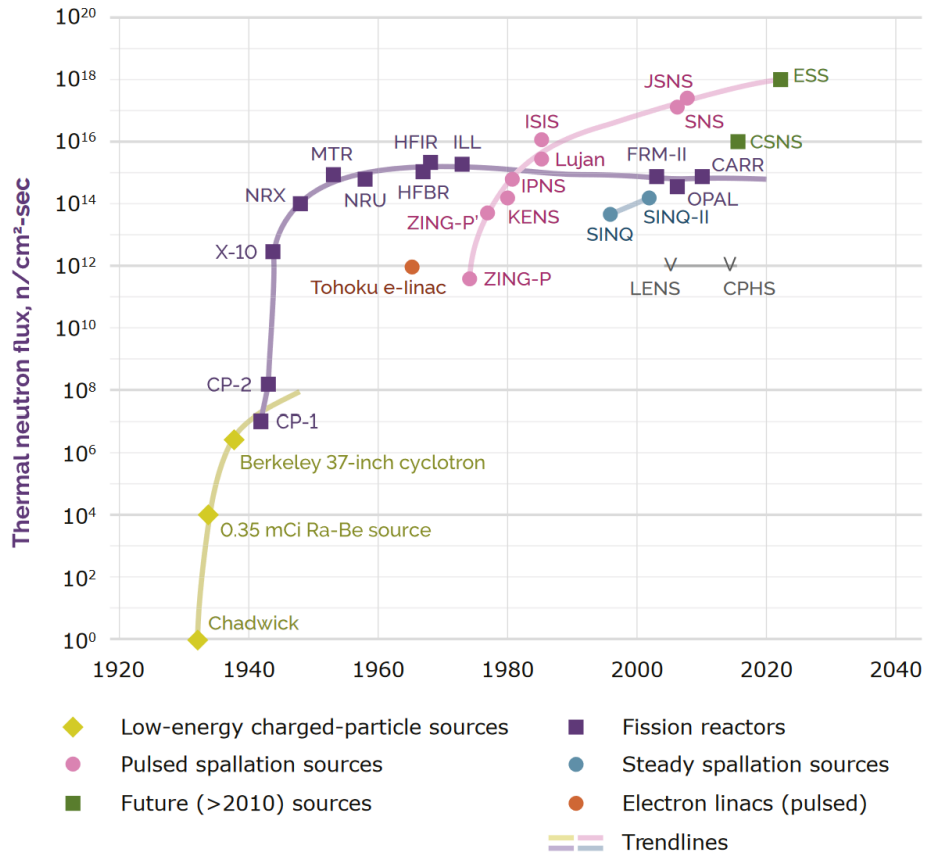


Figure 4.1: Thermal neutron flux achieved by conventional neutron sources, taken from Ref. [32].

neutrons in reactions like  ${}^7\text{Li}(p, n){}^7\text{Be}$  or  ${}^{18}\text{O}(p, n){}^{18}\text{F}$  [15]. The advantage of such sources is that in these reactions, neutron spectra similar to those present in the s-process can be simulated and there is only a very low background. However, the neutron beam is not very intense for such sources. Small accelerator sources are primarily used to conduct activation measurements.

Higher neutron fluxes are possible with neutron sources based on electron linear accelerators like e\_LIBANS in Italy, ORELA at Oak Ridge, Tennessee [15] or Tohoku e-linac in Japan, with which a thermal neutron flux of  $10^{12} \text{ cm}^{-2}\text{s}^{-1}$  is possible as can be seen in Fig. 4.1. For fast neutrons, e\_LIBANS, for instance, produces a peak neutron flux of about  $5 \times 10^5 \text{ cm}^{-2}\text{s}^{-1}$ . The number of neutrons per pulse totals about  $10^{11}$  for ORELA. In such facilities, electrons are accelerated with a LINAC and subsequently shot at a high-Z target, causing the emission of high-energy bremsstrahlung. These photons then produce neutrons of a continuous energy spectrum via  $(\gamma, n)$  reactions in a further target, with the neutron energy ranging between

thermal energies to some tens of MeV. Because there is a strong  $\gamma$ -flash where the electron beam hits the target, measurements with such a neutron source have to be carried out at large distance to the source. Such a large neutron flight path allows a very high energy resolution of measurements with this source with time-of-flight filtering techniques. Furthermore, electron accelerator based facilities have the shortest pulse widths of all conventional sources of only a few nanoseconds [138].

Finally, the accelerator sources with the highest intensities are spallation sources. In such sources, either positive or negative hydrogen ions are accelerated in vacuum up to energies on the order of 1 GeV and thereafter injected into a proton storage ring, where they are converted to proton bunches, which are directed towards a high- $Z$  spallation target [33]. When bombarded by the protons, the nuclides in the target undergo spallation, i.e. they break up into several fragments, among them a number of neutrons. This number varies for different spallation sources with about 20 neutrons per proton for the LANCSE facility at the Los Alamos National Laboratory in the USA and up to 300  $n/p$  in the case of the n\_TOF facility at CERN [15]. In the case of LANCSE, this leads to about  $6 \times 10^{14}$  neutrons per pulse [34] and in the case of n\_TOF to  $1.1 \times 10^7$  with about  $10^5$  per energy decade [139]. The emission in such sources is isotropic, however, so that in cases in which a small target should be irradiated with neutrons or the neutrons are supposed to be moderated to lower energies, which is almost always the case, only a fraction of these neutrons are available [138]. For LANCSE, for example, only about  $10^{13}$  of the initially produced neutrons are available for moderation [33]. n\_TOF is the only spallation source with a pulse duration, which, with 7 ns, is comparable to those for electron acceleration facilities [138]. For LANSCE or the SNS source in the US, for instance, the pulse duration are on the order of several hundred nanoseconds instead. With the latter spallation source, a thermal neutron peak flux of over  $10^{17} \text{ cm}^{-2} \text{ s}^{-1}$  is possible, while for the thermal neutron source of LANCSE, Lujan, it is slightly larger than  $10^{15} \text{ cm}^{-2} \text{ s}^{-1}$ . For fast neutrons, LANCSE produces a peak neutron flux of about  $5 \times 10^6 \text{ cm}^{-2} \text{ s}^{-1}$  [37]. There are plans for spallation sources with even higher peak neutron fluxes like the ESS facility [32] with thermal neutron fluxes of up to  $10^{18} \text{ cm}^{-2} \text{ s}^{-1}$ , but they are planned to be delivered in relatively long neutron pulses, as already the proton pulses will be 3 ms long, therefore making such a source unsuitable for processes for which a high temporal resolution is required. A problem for building even better or even more spallation sources is that for ultra-short neutron pulses with a high number of neutrons to be achievable, large storage rings and pulse compressors are required [33] which not only are extremely big but also very expensive - the cost of ESS exceed 1 billion dollars [34]. Therefore, especially for smaller institutions like universities or hospitals, such sources are not feasible.

Instead, in the last few years, laser-driven neutron sources have been developed that provide

ultra-short neutron pulses with high numbers of neutrons per pulse. These sources are far more compact than comparable conventional neutron sources and have many other advantages that shall be addressed in the following.

## 4.2 Neutron Production with Light Ion Beams

One method of laser-driven neutron production is achieved using laser-generated light ion-beams. This method has been studied and tested by several authors at different laser facilities like Roth et al. [35] at the TRIDENT laser at Los Alamos National Laboratory in the USA, Kleinschmidt et al. [37] with the PHELIX laser at GSI in Darmstadt, Germany, and Kar et al. [46] with the Vulcan laser at the Central Laser Facility of STFC in the UK.

For such a laser-driven neutron source, a pitcher-catcher setup is used like it is shown in Fig. 4.2, where the first target (pitcher) is used to produce light ions, usually protons and deuterons, which then react with the second target (catcher) to produce neutrons in nuclear reactions. For the production and acceleration of the protons and deuterons in the target, several different mechanisms can be employed, all basing on the acceleration of these ions in electron-generated electric fields. Conventionally, a mechanism called TNSA (target normal sheath acceleration) is used, in which the ultra-intense laser pulse deposits energy into the electrons in the pitcher target, causing fast electrons to travel through the target and creating a "sheath" on the rear surface, where a large electric field of  $\propto 10 \text{ TV m}^{-1}$  accelerates the ions on the surface of the target [140]. This acceleration mechanism, which has been used in [37] and [46], for example, favours protons and only utilizes ions at the surface. The neutron yield can be improved using other acceleration mechanisms available at laser intensities higher than  $10^{21} \text{ Wcm}^{-2}$ , the so-called break-out afterburner (BOA) and the radiation pressure acceleration (RPA) mechanisms. For BOA, on the one hand, which has been used by Roth et al. [35], if the pitcher target thickness is comparable to the laser skin depth, the laser pulse creates a concomitant electron beam in the target and, due to instabilities in the plasma, electromagnetic waves are produced that resonate with the ions and accelerate ions from the whole target volume to higher energies than possible with TNSA. For RPA, on the other hand, the radiation pressure of the laser is directly transformed to the objects to be accelerated, which increases the intensity scaling of the ion beam energy compared to TNSA significantly [141]. The ions that are accelerated with TNSA and BOA typically have energies up to 94 MeV for protons and a few MeV/u for heavier ions, while for RPA, proton energies above this value have been reported [142].

The light ions accelerated like this are then shot at the catcher target, which is typically made out of a low- $Z$  material like Li or Be, similar to the small conventional accelerator sources introduced above. There, several nuclear reactions take place. First of all, compound nuclear

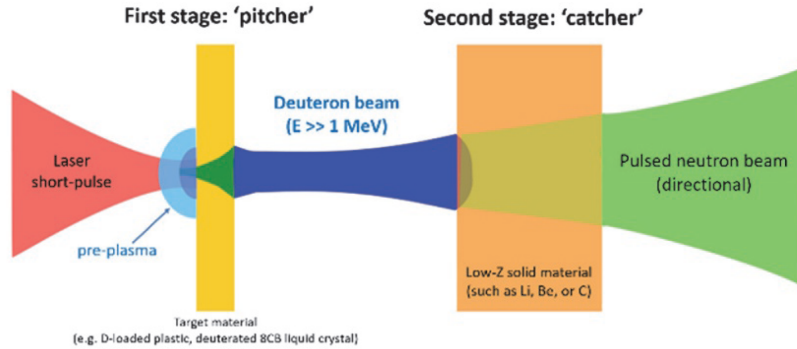


Figure 4.2: Schematic drawing of the experimental setup for neutron generation with laser-accelerated light ion beams, taken from Ref. [34].

processes occur, which lead to a isotropic neutron emission, but as the energy of the incoming protons is tens of MeV high, a significant part of the neutron yield is also due to pre-equilibrium reactions and - in case of  $d$  - direct stripping and break-up reactions for high energy ions. Because for these reaction mechanisms, the incoming ions do not lose their identity, as it is the case for compound nuclear reactions, the neutrons produced in these processes are characterized by their forward-directionality. In fact, when comparing the TNSA and BOA mechanism, Roth et al. [35] found that for the former, the isotropical emission dominates the emitted neutron pulse, while the neutrons emitted for BOA-produced ions were mainly directed forward. Using the BOA setup at the 0.1 PW laser at the TRIDENT laser facility operated with 600 fs pulses, a power of 200 TW and an energy of 70 kJ per pulse,  $10^{10}$  neutrons per pulse and steradian and a total of up to  $10^{11}$  neutron per pulse could be produced in the forward direction with sub-nanosecond neutron-pulse widths and energies mainly from 0.1 - 10 MeV before moderation [35], [143]. Therefore, the duration of neutron pulses generated by such laser-driven neutron sources is significantly lower than for conventional neutron sources, and the energies of the neutrons are generally higher than, for instance, at spallation sources. Thus, also the peak neutron flux produced with laser-driven light ion neutron sources is higher than possible with currently available conventional spallation sources, amounting to  $6 \times 10^{17} \text{ cm}^{-2} \text{ s}^{-1}$  for the peak flux achieved by Roth et al. [35]. Still, the pulse duration, as well as the width of the energy spectrum can be further improved by focusing the proton beam with techniques like laser-triggered plasma-based microlenses [39].

For the LANCSE and TRIDENT facilities in Los Alamos National Laboratory, the latter of which achieves one the highest neutron fluxes for a light ion laser-driven neutron source, a quantitative comparison carried out in Ref. [34] shows that while the peak neutron flux is higher and the pulse duration is lower at TRIDENT, the number of neutrons shot through the beamline

and at the moderators is about several orders of magnitude higher at LANCSE. According to [34], however, this difference could be decreased to only one order of magnitude only by using higher energy lasers that are already available and a different pitcher target than it was used for TRIDENT, leading to neutron yields of up to  $10^{12}$  neutrons per pulse in the forward direction.

Because the neutron yield scales with the laser intensity and energy of the laser beam [34], these quantities are seaked to be improved in future laser facilities. One laser facility promising to be a high-yield neutron source is the High Power Laser System (HPLS) at ELI-NP in Romania [47], for which the construction has just been finished in March 2019 [144]. The HPLS consists of two simultaneously operating arms that each have three outputs that can be used one at a time:

- a 100 TW beam with a pulse frequency of 10 Hz
- a 1 PW beam with a pulse frequency of 1 Hz
- and a 1 PW beam with a pulse frequency of at least 1/minute.

With these lasers, it will be possible for the first time to reach focal beam intensities of  $10^{22} - 10^{23} \text{ Wcm}^{-2}$  [47]. Therefore, the boundaries of laser power and intensities will be expanded with the HPLS by orders of magnitude compared to the currently running laser sources.

But not only the laser beam intensity is increased: because the ELI laser-driven neutron sources based on light ions are supposed to use the BOA and RPA mechanisms to produce the light ions, the maximal proton energy is expected to increase to up to 200 MeV [48]. Therefore, much higher neutron yields and also higher possible neutron energies as well as greater forward-directionality are to be expected with the HPLS. In the present work, simulations for the laser-driven neutron sources based on the ELI-NP laser system are carried out.

### 4.3 Neutron Production via Photonuclear Reactions

With the High Power Laser System, neutrons are not only supposed to be produced with laser-driven light ion beams but, especially for the 10 PW beam, also via photonuclear reactions in a setup that even allows the simultaneous operation of the two mechanisms [47].

The production of neutrons via photonuclear reactions has been studied intensively by Pomerantz et al. in Ref. [38] with the Texas Petawatt Facility in Austin, Texas, using a 90 J, 700 TW laser with ultrashort laser pulses of 150 fs FWHM. The experimental setup used in these studies can be seen in Fig. 4.3. To produce the electron beam required for the production of photons

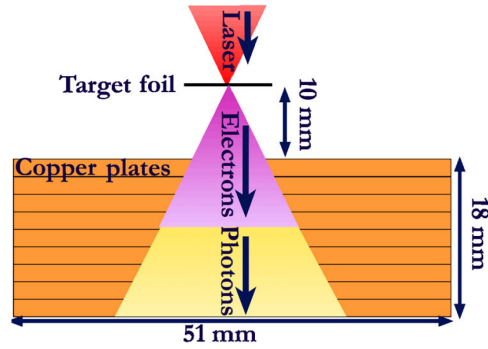


Figure 4.3: Schematic drawing of the experimental setup for laser-driven neutron generation via photonuclear reactions as used by Pomerantz et al. [38], taken from Ref. [38].

for the  $(\gamma, n)$  reactions, a thin plastic target is irradiated with the laser beam. Furthermore, already  $\propto 100$  ns before the main beam reaches the target, low level laser light deposits energy into the target, therefore turning it into an expanding "plasma plume" [38]. When the main laser beam reacts with this plume, relativistic electrons are generated with a mean energy of around 10 MeV in case of the studies by Pomerantz et al. [38], which thereafter propagate along the laser beam direction. These electrons then interact with a high- $Z$  - in case of Ref. [38] copper - converter target, where bremsstrahlung and, therefore, high energy photons are produced, which, when they are stopped in the converter, produce up to  $4 \times 10^9$  isotropically distributed neutrons with energies up to several MeV in  $(\gamma, n)$ , with the energy spectrum centered at 0.5 MeV in reactions with the converter nuclides.

Because the electron emission and the target-to-converter temporal dispersion both happen in less than 1 ps in [38], neutron pulses with a duration of less than 50 ps could be produced with the used laser, which has a pulse duration of 150 fs. This neutron pulse duration is significantly lower than for both the conventional sources and the laser-driven light ion neutron production sources introduced in the sections above. With that low pulse duration, a peak neutron flux of  $1.1 \times 10^{18} \text{ cm}^{-2} \text{ s}^{-1}$  has been reached in the studies in Ref. [38], which, again, exceeds the fluxes available for all neutron sources presented above.

If higher- $Z$  converters and higher power laser facilities than the laser used in [38] are used, as it will be the case for ELI-NP, the peak neutron flux is expected to exceed  $10^{20} \text{ cm}^{-2} \text{ s}^{-1}$  [38, 47].

## 4.4 Neutron Production in Thermonuclear Fusion Reactions

Other than through the two aforementioned laser-driven production mechanisms that will be employed at ELI-NP in the near future, it has been proposed by Wu in Ref. [40] that an intense neutron beam could also be achieved via thermonuclear reactions, i.e. the reaction  ${}^2\text{H}(d, n){}^3\text{He}$ , in plasmas generated by the interaction of Petawatt lasers with either  $\text{D}_2$  gas jets or solid  $\text{CD}_2$  targets. When using such Petawatt lasers with low intensities  $\leq 10^{18} \text{ Wcm}^{-2}$ , the plasma is expected to exist long enough to be able to equilibrate so that thermonuclear reactions can occur [40]. In [40], simulations for the experimental setup of a  $10^{18} \text{ Wcm}^{-2}$  laser beam with a pulse duration of 100 fs have been carried out, predicting a neutron yield of up to  $10^9$  neutrons being emitted isotropically per laser pulse with a laser energy of 500 J. Therefore, compared to the well established sources based on laser-driven light ion beams studied in [35], the yield is two orders of magnitudes lower. However, also the spectral width of the beam simulated in this work is smaller by two orders of magnitudes than that in Ref. [35], with a FWHM on the order of 100 keV instead of 10 MeV, making such a source also suitable for studying the energy dependence of the neutron capture experiments studied in this work as it provides neutron beams with gaussian-shaped spectra with significantly less energy uncertainty than the neutron beams produced in the mechanisms described above.

Finally, neutrons can be produced in laser-induced thermonuclear deuterium-tritium fusion reactions by inertial confinement fusion (ICF). This method is carried out, for instance, at the National Ignition Facility (NIF) at Lawrence Livermore National Laboratory in the USA [41, 43–45]. For ICF to occur, a spherical target capsule made out of a CH shell, part of which is doped with Si, surrounding a deuterium-tritium (DT) ice shell and a DT fuel core, is placed in the center of a cylindric hohlraum made out of gold or uranium [41, 44]. With laser pulses, energy is delivered to the hohlraum shell, which then emits x-rays that are absorbed by the capsule, resulting in the ablation and expansion of the CH-shell material [45]. Therefore, a reaction force occurs, accelerating the rest of the capsule including the enclosed DT fuel core inward [43], compressing and heating the fuel in the process. Consequently, a "hot-spot" forms in the center of the capsule surrounded by a colder layer of DT-fuel. If the temperature and density are high enough, thermonuclear deuterium-tritium fusion reactions  $d(t, n)\alpha$  occur, yielding neutrons as well as  $\alpha$ -particles, which, as they quickly thermalize, continue to contribute to heating the core. The neutrons in the  $d(t, n)\alpha$  reaction are emitted with an energy of 14 MeV, so that most neutrons produced by this source have energies near 14 MeV, with a few neutrons with different energies due to thermalization or secondary reactions.

Using the ICF technique, a neutron yield of  $1.9 \times 10^{16}$  has been produced in one pulse with a duration on the order of 100 ps by Le Pape et al. [41] at NIF, therefore leading to a peak

#### 4.4 Neutron Production in Thermonuclear Fusion Reactions

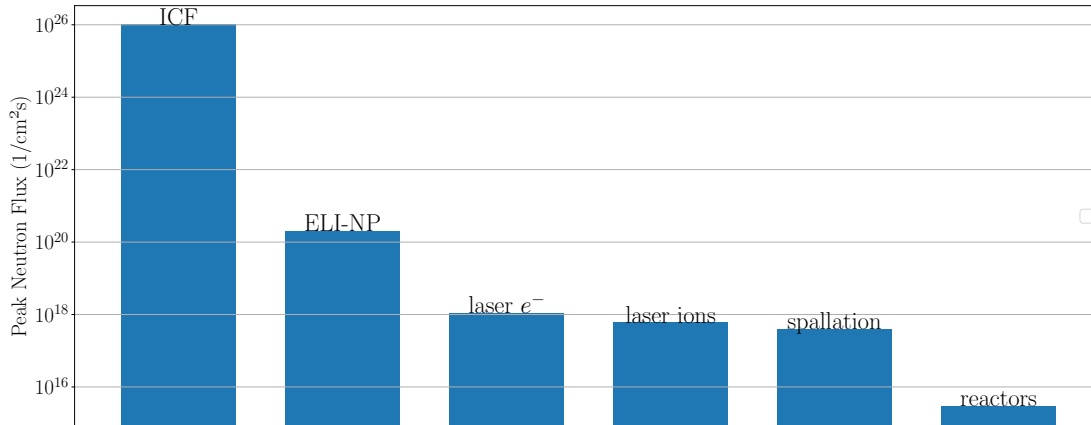


Figure 4.4: Comparison of the peak neutron fluxes achieved in different neutron sources [32, 35, 38, 48, 137].

neutron flux on the order of  $10^{26} \text{ cm}^{-2}\text{s}^{-1}$ . Thus, this neutron source overtrumps all of the regarded neutron sources - conventional and laser-driven - in terms of flux and neutron yield and is therefore especially suitable for the simulations of neutron capture reactions astrophysically relevant to the r- and s-process.

In Fig. 4.4, the total (and in case of the spallation source, thermal) peak neutron fluxes achievable at neutron production facilities of different types that have been introduced in this chapter are shown, with the peak fluxes taken from Ref. [137] for the HFIR reactor, Ref. [32] for the JSNS spallation source, Ref. [35] for neutrons generated with laser-driven ion beams at Los Alamos National Laboratory, from Ref. [38] for laser-driven photonuclear reaction sources at the Texas Petawatt Beam Facility, and from Ref. [41] for the ICF. Furthermore, the prediction of the possible neutron fluxes of over  $10^{20}$  at ELI-NP is shown in the figure as well.

This comparison also shows that with all of these neutron sources, even with reactors, neutron fluxes higher than those for the s-process can be produced. However, only with the proposed laser-driven source at ELI-NP and the currently operating ICF facility at the NIF is it possible to produce neutron fluxes sufficiently high to simulate the fluxes higher  $10^{19} \text{ cm}^{-2}\text{s}^{-1}$ . Thus, with these laser-driven neutron sources it is possible for the first time to simulate neutron fluxes similar to those in r-process scenarios like the neutrino-driven winds that are ejected by core collapse supernovae or ejecta of neutron mergers, both possible r-process sites. Such neutron fluxes could, therefore, enable the opportunity to study neutron capture cascades similar to those in the r-process in the laboratory for the first time, and such experiments could immensely contribute to the further understanding of the r-process and the identification of the sites for this process.

# 5 Theoretical Approach of the Present Work

## 5.1 Neutron Capture in Beam-Target Interaction

The purpose of this thesis is to calculate neutron capture cascades and, therefore, the production of neutron-rich isotopes in a setup where a target of seed nuclides is irradiated by a laser-driven neutron source. In order to calculate the neutron-enrichment of the target nuclides, we follow the theoretical approach developed in Ref. [49]. In this section, we give an overview of this framework.

For our calculations, we regard a single-component target of thickness  $L$  and area  $A$  that is irradiated by neutron pulses with  $N_p$  neutrons per pulse at different incident neutron energies. When carrying out such an experiment, the energy spectrum of the incident neutrons is not necessarily given by a Maxwell-Boltzmann distribution as it is the case for processes in stellar environments, but it is determined by the energy spectrum delivered by the neutron beam, which, in our case, we assume as gaussian shaped like the spectrum for neutrons produced by thermonuclear reactions [40, 41]. The raw cross sections from the nuclear data libraries have to be averaged over this gaussian spectrum with relative standard deviation  $\sigma_{rel} = \sigma_{\text{gaussian}}/E_{\text{inc}}$  to compute the cross section values with which the calculations are performed:

$$\langle \sigma \rangle(E_{\text{inc}}) = \int \sigma \frac{1}{\sqrt{2\pi}\sigma_{rel}E_{\text{inc}}} \exp\left(-\frac{1}{2}\left(\frac{E - E_{\text{inc}}}{\sigma_{rel}E_{\text{inc}}}\right)^2\right) dE. \quad (5.1)$$

For simplicity, however, the brackets  $\langle \rangle$  indicating the integration over the neutron spectrum will be left out in the following equations and it is implicitly assumed that all appearing cross sections have been averaged over energy according to Eq. (5.1). Furthermore, it should be noted that we do not assume any spatial variations of the beam intensity, but it is assumed that all neutron-target interactions occur in the target volume  $a \cdot L$ , and that the number of these interactions is the same at every point of the area  $A$ .

Because in our calculations, we are interested in the production of neutron-enriched isotopes of the seed nuclides, we will only be calculating the abundances of those. To make a realistic estimate of the yield of these neutron-enriched nuclides, several different processes have to be taken into account: neutron capture, loss of nuclides via transmutation, the damping of the

neutron beam inside the target and radioactive decay.

Neutron capture ( $n, \gamma$ ) is the process during which the enriched isotopes the abundances of which we calculate are created. Because during this process, the nuclide is changed as it gains mass in form of neutrons, radiative capture is a nuclear transmutation process. However, as discussed in chapter 2, it is not the only one that can occur, with processes like neutron-induced particle emission or fission also possible, and whatever transmutation happens, the nucleus of a specific species undergoing such a process changes its species in the process. To distinguish these species, an isotope of the seed nuclide enriched by a specific number  $i$  of neutrons will be called the  $i$ -species isotope of the seed in the following. Furthermore, we regard the damping that the neutron beam experiences due to all kinds of interactions possible with the seed nuclides. This damping reduces the interaction rate for nuclides further away from the surface of the target that is hit with the beam. Finally, radioactive decay is regarded as another way of losing nuclei of a regarded species.

By only including these processes and only calculating the populations of neutron-enriched isotopes of the seed nuclides, we make a few approximations. Firstly, we disregard "looped" transmutation processes like  $^{177}\text{Lu}(n, p)^{177}\text{Yb}(\beta^-)^{177}\text{Lu}$  in which transmutation processes other than neutron capture can lead the original nuclide to be restored again. This effect, however, can be assumed as small, because for such a process to happen, a particle emission reaction must occur, and cross sections for such processes are small below incident energies corresponding to the particle separation energies and, therefore, a few MeV. Consequently, such looped transmutation processes could only affect our results for the higher energies regarded. Other than this, we make the approximation to disregard that any secondary particles emitted in the nuclear reactions of the neutrons with the target nuclei could react with the nuclei in the target again. However, because, again, reactions producing secondary particles only begin to become significant for energies above a few MeV, the number of emitted secondary particles is several orders of magnitude smaller than the number of neutrons in the pulse, and the cross sections for charged particle reactions are lower than those for reactions with neutrons as projectiles due to the Coulomb barrier of the nuclei, these effects are negligible for our purposes. It should be noted that, for example in Refs. [145, 146], more sophisticated approaches to modeling neutron capture processes, including loops, have been developed.

### 5.1.1 Neutron Captures During One Neutron Pulse in a Thin Target

Firstly, a framework will be developed describing what happens to the populations of seed and neutron-enriched nuclei during one single pulse. To be able to neglect damping for now, we regard a thin target that has a thickness  $L$  much smaller than the minimal penetration depth of the neutron beam in the target material. Another approximation we make is that we as-

## 5 Theoretical Approach of the Present Work

sume the interaction time of  $T_p$  of the neutron pulse with the target to be much smaller than all lifetimes of the regarded seed nuclides, as well as the neutron-enriched isotopes, so that we can safely assume that no radioactive decays occur during the interaction. Considering the extremely low pulse durations of laser-driven neutron pulses for the sources introduced in chapter 4 of less than a nanosecond, this approximation applies for many nuclides.

Therefore, with the assumptions made above, the only two effects that have to be regarded for the description of the number of seed nuclides and neutron-enriched isotopes during one neutron pulse are nuclear transmutation and neutron capture. Let now  $N_0$  be the number of seed nuclei and  $N_i, i > 0$  the numbers of nuclei of the  $i$ -species. Only these populations are accounted for in our calculations, so that because  $N_0$  has the lowest neutron number, it cannot grow due to neutron capture but just lose nuclides in nuclear transmutation. Therefore, the development of  $N_0$  during one neutron pulse can be described with the following differential equation:

$$\dot{N}_0(t) = - \frac{\sigma_{\text{tr},0}}{A} N_0(t) R_{\text{inc}} \quad (5.2)$$

Here,  $R_{\text{inc}}$  is the rate at which neutrons from the neutron source irradiate the target. This rate can be calculated from the neutron current density  $j_{\text{inc}}$  via

$$R_{\text{inc}} = j_{\text{inc}} \cdot A, \quad (5.3)$$

which is generally time dependent. Furthermore,  $\sigma_{\text{n-cap},i}$  are the (energy-averaged) neutron capture cross sections and  $\sigma_{\text{tr},i}$  the nuclear transmutation species-loss cross sections for nuclides with  $i$  more neutrons than the seed. A big part of the nuclear transmutation reactions of the seed nuclei will usually occur due to neutron capture, so that when regarding the abundance of  $N_1$  nuclides during one pulse, the number grows due to neutron capture of the seed nuclides and decreases, just like  $N_0$ , due to transmutation processes, making the differential equation of  $N_1$

$$\dot{N}_1(t) = \frac{\sigma_{\text{n-cap},0}}{A} N_0(t) R_{\text{inc}} - \frac{\sigma_{\text{tr},1}}{A} N_1(t) R_{\text{inc}}. \quad (5.4)$$

For all other neutron-enriched species, the differential equations follow the same scheme as Eq. (5.4). However, in our calculations, the abundance of the species with  $i$  neutrons more than the seed will be smaller than species  $i - 1$ , so that we can make the approximation that for a certain number  $k$  of captured neutrons, the abundance  $N_k$  is so small that  $N_j, j > k$ , as well as the transmutational loss of  $N_k$  are negligible. For these species, we then assume the

differential equations:

$$\dot{N}_k(t) \approx \frac{\sigma_{\text{n-cap},k-1}}{A} N_{k-1}(t) R_{\text{inc}} \quad (5.5)$$

$$\dot{N}_j(t) \approx 0 \quad \forall j > k. \quad (5.6)$$

Therefore, we have a complete set of coupled differential equations describing the species gain and loss due to neutron capture and nuclear transmutation processes during one neutron pulse:

$$\dot{N}_0(t) = -\frac{\sigma_{\text{tr},0}}{A} N_0(t) R_{\text{inc}} \quad (5.7)$$

...

$$\dot{N}_i(t) = \frac{\sigma_{\text{n-cap},i-1}}{A} N_{i-1}(t) R_{\text{inc}} - \frac{\sigma_{\text{tr},i}}{A} N_i(t) R_{\text{inc}} \quad \forall i < k \quad (5.8)$$

...

$$\dot{N}_k(t) \approx \frac{\sigma_{\text{n-cap},k-1}}{A} N_{k-1}(t) R_{\text{inc}} \quad (5.9)$$

$$\dot{N}_j(t) \approx 0 \quad \forall j > k. \quad (5.10)$$

To eliminate the time dependence of  $R_{\text{inc}}$ , a new variable can be introduced:

$$\tau(t) = \frac{1}{N_p} \int_0^t R_{\text{inc}}(t') dt' \quad (5.11)$$

$$\Leftrightarrow dt = \frac{N_p}{R_{\text{inc}}(t)} d\tau, \quad (5.12)$$

which is essentially equivalent with replacing  $R_{\text{inc}}(t)$  with  $N_p$  and  $t$  with  $\tau$  in the equations above. Because in our calculations, we are only interested in the evaluation of the populations at the end of one pulse, i.e. after  $T_p$  with  $\tau(T_p) = 1$ , we might as well rename  $\tau \rightarrow t$  and evaluate the populations at  $t = 1$ . Moreover, the quantities

$$\mu_i = \frac{\sigma_{\text{n-cap},i}}{A} N_p; \quad \eta_i = \frac{\sigma_{\text{tr},i}}{A} N_p \quad (5.13)$$

can be introduced for further simplification of Eqs. (5.10).

With these simplifications, the system of differential equations can be written as

$$\dot{N} = BN_0 \quad (5.14)$$

## 5 Theoretical Approach of the Present Work

with the matrix

$$B = \begin{pmatrix} -\eta_0 & 0 & 0 & \dots & 0 & 0 & 0 \\ \mu_0 & -\eta_1 & 0 & \dots & 0 & 0 & 0 \\ 0 & \mu_1 & -\eta_2 & \dots & 0 & 0 & 0 \\ \vdots & \vdots & \vdots & \ddots & \vdots & \vdots & \vdots \\ 0 & 0 & 0 & \dots & \mu_{k-2} & -\eta_{k-1} & 0 \\ 0 & 0 & 0 & \dots & 0 & \mu_{k-1} & 0 \end{pmatrix} \quad (5.15)$$

and the vectors of populations during  $\mathbf{N} = (N_0, N_1, \dots, N_k)^\top$  and before the pulse  $\mathbf{N}_0 = (N_0^0, N_1^0, \dots, N_k^0)^\top$ . The solution of this set of differential equations can then easily be identified as  $\mathbf{N}(t) = e^{Bt} \mathbf{N}_0$ , so that at the end of one pulse, i.e. at  $t = 1$ , we get

$$\mathbf{N}(1 \text{ pl}) = \left( \sum_{j=0}^{\infty} \frac{B^j}{j!} \right) \mathbf{N}_0. \quad (5.16)$$

### 5.1.2 Neutron Captures During One Neutron Pulse in a Thick Target

The next step is to include the damping of the neutron beam into the calculation. It is assumed that every kind of neutron interaction makes this neutron unable to interact with any more target nuclei, so that the rate at which the incoming neutrons hit target nuclides can be described by the following differential equation when neglecting spatial variations of the target nuclide density  $n_T$ :

$$dR_{\text{inc}}(x) = -n_T \sigma_{\text{tot},0} dx, \quad (5.17)$$

where it is assumed that most of the nuclides present in the target are the seed nuclides, and therefore, the cross section for those nuclides is used in Eq. 5.17, along with the total number of target nuclides  $N_T$ . With the initial condition  $R_{\text{inc}}(0) \equiv R_{\text{inc}}^0$ , the solution is given by

$$R_{\text{inc}}(x) = R_{\text{inc}}^0 e^{-x/\lambda} \quad (5.18)$$

with the approximate penetration depth

$$\lambda = \frac{1}{n_T \cdot \sigma_{\text{tot},0}}. \quad (5.19)$$

Because the rates of incoming neutrons are different at different depths  $x$  of the target, the production of new nuclides with  $i$  neutrons more than the seed also varies, as does the total number of neutrons  $N_p(x)$  that reach different depths and that can be described by  $N_p(x) = N_p e^{-x/\lambda}$ . Therefore, it makes sense to regard only the infinitesimal number of nuclides  $dN_i$  in

an infinitesimal interval  $dx$ . If we assume that the distributions of  $i$ -species isotopes present in the target before the pulse,  $N_i^0$ , are all homogeneous in the target of length  $L$ , namely  $dN_i^0 = \frac{N_i^0}{L} dx$ , and substitute the new expression for the neutron number in the values of  $\mu_i$  and  $\eta_i$ , Eq. (5.16) transforms into the following differential equation in  $x$ :

$$d\mathbf{N}(1 \text{ pl}) = \left( \sum_{j=0}^{\infty} \frac{(e^{-x/\lambda} B)^j}{j!} \right) \mathbf{N}_0 \frac{dx}{L} \quad (5.20)$$

where  $e^{-x/\lambda}$  has been factored out of the matrix. When integrating over the length of the target  $L$ , one gets for the abundances  $\mathbf{N}$  after one pulse

$$\mathbf{N}(1 \text{ pl}) = \left( \sum_{j=0}^{\infty} \frac{\gamma_j B^j}{j!} \right) \mathbf{N}_0 \equiv M \mathbf{N}_0 \quad (5.21)$$

with factors  $\gamma_j = \frac{\lambda}{jL} (1 - e^{-jL/\lambda})$  and  $\gamma_0 = 1$ .

### 5.1.3 Neutron Captures for Multiple Neutron Pulses in a Thick Target

The considerations so far have only been for one pulse. However, we will regard up to several billion neutron pulses for a single target in this work. In pulsed neutron sources as considered in the calculations in the present work, these pulses are delivered with a certain repetition rate  $f_{\text{rep}}$ , so that there is a delay time  $T_{\text{del}} = 1/f_{\text{rep}}$  in between pulses. Let us now assume that  $s - 1, s \in \mathbb{N}$  pulses have already been delivered, and consider the  $s$ th pulse. Because it is assumed that the duration of the pulse is much smaller than the half-lives of all nuclides, the decay during the pulse can be neglected when calculating the population  $\mathbf{N}(s)$  right after the  $s$ th pulse, so that the formula for the population directly after the pulse is almost exactly the same as Eq. (5.21) for calculating the population directly after one pulse.

$$\mathbf{N}(s) = M \mathbf{N}_d(s - 1) \quad (5.22)$$

The subscript  $d$  for the abundance vector  $\mathbf{N}_d(s - 1)$  is supposed to indicate the fact that at the time when the  $s$ th neutron pulse is shot at the target, and with the assumption  $T_p \ll T_{\text{del}}$  also approximately the time directly after the pulse, the population  $\mathbf{N}(s - 1)$  has undergone decay. To include this decay, each population has to be multiplied by a factor  $e^{-T_{\text{del}}/\tau_i}$

$$N_{i,d} = e^{-T_{\text{del}}/\tau_i} N_i \quad (5.23)$$

where  $\tau_i$  is the half-live of the  $i$ -species isotope, if it exists. In this equation, it is again assumed that  $T_p \ll T_{\text{del}}$ , so that  $T_{\text{del}} - T_p \approx T_{\text{del}}$  and the duration of the time window from after the  $s - 1$ th pulse to the  $s$ th pulse, in which the decay is assumed to occur, is approximated as  $T_{\text{del}}$ .

## 5 Theoretical Approach of the Present Work

In vector notation, the decay can be interpreted as a matrix multiplication of a "decay matrix"  $D$  with the vector  $N(s)$  to obtain  $N_d(s)$ :

$$N_d(s) = \underbrace{\begin{pmatrix} e^{-T_{\text{del}}/\tau_0} & 0 & \dots & 0 \\ 0 & e^{-T_{\text{del}}/\tau_1} & \dots & 0 \\ \vdots & \vdots & \ddots & \vdots \\ 0 & 0 & \dots & e^{-T_{\text{del}}/\tau_k} \end{pmatrix}}_{\equiv D} N(s). \quad (5.24)$$

In case a nuclide is stable,  $e^{-T_{\text{del}}/\tau_i}$  would have to be substituted with 1, whereas for instantly decaying nuclides, 0 would have to be written on the corresponding diagonal element of  $D$ .

Eqs. (5.22), (5.23), and (5.24) then allow to directly calculate the abundances of the seed nuclei as well as all  $i$ -species isotopes with  $i > 0$  after an arbitrary number of pulses with the neutron beam via

$$N(s) = (MD)^{s-1} M N_0 \quad (5.25)$$

$$\Leftrightarrow N(s) = D^{-1} (DM)^s N_0. \quad (5.26)$$

### Approximations

For some more qualitative insight into the theoretical approach for multiple pulses, one can disregard the decay between the pulses ( $\tau_i = \infty$ ) and neglect the damping ( $\gamma_k = 1 \forall k$ ) [49], so that Eq. (5.26) becomes

$$N(s) = M^s N_0 = e^{sB} N_0 = \left( \sum_j \frac{s^j B^j}{j!} \right) N_0. \quad (5.27)$$

On this formula, a Taylor expansion can be made if  $s\eta_i \ll 1$  and  $s\nu_i \ll 1$ . If, furthermore,  $N_0 = (N_t, 0, \dots, 0)^T$  is assumed, the leading order terms for  $N_i$  appear in  $B^i$ , so that the populations approximately scale with

$$N_i(s) = \frac{s^i}{i!} \left( \prod_{j=0}^{i-1} \mu_j \right) N_t, \quad i > 0. \quad (5.28)$$

Therefore, if decay and damping are neglected, the abundances  $N_i$  scale polynomially with the pulse number according to  $s^i$ . This scaling, as investigated in Ref. [49], is caused by the accumulation of neutron-rich nuclides during multiple pulses if the decay is neglected.

If decay and damping are taken into account, no such direct approximative formula as the

one in Eq. (5.28), which has been developed by [49], can be found anymore. However, for qualitative insight, one can still evaluate the recursive Eq. (5.22) up to a few orders. For this to work, it is only required that  $\mu_i, \eta_i \ll 1$ . If the same initial condition  $\mathbf{N}_0 = (N_t, 0, \dots, 0)^T$  is considered, the leading order expansion of Eq. (5.22) in  $\mu$  and  $\eta$  including terms from all populations  $N_j$ ,  $j \leq i$  and, therefore, from  $B^0 - B^i$  is given by

$$N_i(s+1) = N_i(s)e^{-T_{\text{del}}/\tau_i} + \sum_{l=0}^{i-1} e^{-T_{\text{del}}/\tau_l} N_l(s) \left( \prod_{j=l}^{i-1} \mu_j \right) \frac{\gamma_{i-l}}{(i-l)!}. \quad (5.29)$$

It should be noted that if several pulses are applied, because of the  $s^j$ -scaling deduced in Eq. (5.28), the  $N_j(s)$  terms in Eq. (5.29) have a higher influence on  $N_i(s+1)$  the higher  $j$  is if  $\eta_j$  and  $\mu_j$  are comparable. Therefore, this approximative equation shows that most enrichments occur via the capture of exactly one neutron during one pulse.

Finally, when including one more order for each population  $N_j$ ,  $j < i$ , the effect of the nuclear transmutation can be seen as well in the expansion:

$$\begin{aligned} N_i(s+1) = & N_i(s)e^{-T_{\text{del}}/\tau_i} + \sum_{l=0}^{i-1} e^{-T_{\text{del}}/\tau_l} N_l(s) \frac{\gamma_{i-l}}{(i-l)!} \left( \prod_{j=l}^{i-1} \mu_j \right) \\ & - \sum_{l=0}^i N_l(s) e^{-T_{\text{del}}/\tau_l} \frac{\gamma_{i-l+1}}{(i-l+1)!} \left( \sum_{j=l}^i \eta_j \right) \left( \prod_{j=l}^{i-1} \mu_j \right) \end{aligned} \quad (5.30)$$

where for  $i = k$ ,  $\eta_i = 0$  has to be assumed.

### 5.1.4 Total Number of Produced Nuclides

Finally, a further quantity relevant to our calculations is not only the number of nuclei of a specific species  $N_{i+1}$  after a certain number of pulses, but also the number of pulses that are produced in total with all pulses during the experiment. The differential equation for this quantity during the interaction with the neutron pulse reads

$$\dot{N}_{i+1}^{\text{tot}} = \mu_i N_i(t) \quad (5.31)$$

where  $N_i(t)$  is the number of  $i$ -species isotopes during the interaction with the pulse (i.e.  $t < 1$ ) calculated via Eq. (5.21), in which  $t$  is inserted for the time instead of 1:

$$N_i(t) = \left[ \left( \sum_{j=0}^{\infty} \frac{\gamma_j B^j t^j}{j!} \right) \mathbf{N}_0 \right]_i. \quad (5.32)$$

## 5 Theoretical Approach of the Present Work

After integrating Eq. (5.31) from  $t = 0$  until the end of the pulse, i.e  $t = 1$ , one gets for the total number of nuclides after one pulse

$$N_{i+1}^{tot}(1 \text{ pl}) = \mu_i \left[ \left( \sum_{j=0}^{\infty} \frac{\gamma_j B^j}{(j+1)!} \right) \mathbf{N}_0 \right]_i \equiv \mu_i [M' \mathbf{N}_0]_i \quad (5.33)$$

When generalizing for multiple pulses, the operator in front of  $\mathbf{N}_0$  has to be applied on the decayed populations after all pulse numbers  $l$  leading up to the  $s$ th pulse,  $\mathbf{N}_d(l)$ , and the resultant abundances have to be added, so that the total number of produced nuclei of the  $i + 1$ -species isotope yields:

$$N_{i+1}^{tot}(s) = \mu_i \sum_{l=0}^{s-1} [M' \mathbf{N}_d(l)]_i. \quad (5.34)$$

with  $\mathbf{N}_d(0) = \mathbf{N}_0$ , as we assume the first pulse to be applied directly at the start of the experiment.

## 5.2 Neutron Sources and Targets

In the current work, the framework introduced in the last section is employed to calculate the populations of nuclides enriched by up to 4 neutrons (Expressed in the conventions of the former section, this corresponds to  $k = 4$ ). For the neutron beams causing the neutron enrichment, two laser-driven neutron sources are considered:

1. One neutron source that yields  $10^{12}$  neutrons per pulse with three different repetition rates of
  - a) 10 Hz
  - b) 1 Hz
  - c) 1 pulse per minute
2. and a second neutron source that yields  $10^{16}$  neutrons per pulse with a repetition rate of 3 pulses per day.

Therefore, we do not only employ the first neutron source at a repetition rate of 1 Hz, as done in Ref. [49], but the investigation of the influence of different repetition rates is possible in this work, and a second neutron source is studied as well. The first neutron source (called neutron source 1 in the following) represents a laser-driven neutron source at Petawatt-class laser systems like ELI-NP [47]. The number of neutrons per pulse,  $10^{12}$ , is expected to be produced at this facility in sub-nanosecond pulses with laser-accelerated high-ion beams and with laser-driven electron based photonuclear reactions. For the second neutron source, an ICF-driven source at NIF is considered, which has been shown to produce even slightly more than the  $10^{16}$  neutrons per pulse considered here.

Neutron beam energies  $E_{\text{inc}}$  between 50 keV and 10 MeV with the gaussian energy spectrum in Eq. (5.1) are considered. Therefore, a great range of the available neutron energies in current and planned laser-driven neutron sources is covered (see chapter 4), and we limit us to energies for which our assumptions that secondary particle emissions do not play too big of a role apply. Especially the low energies of up to a few hundred keV are of great importance because these are the energies at which the weak s-process (90 keV) and the r-process are considered to operate. The gaussian energy spectrum is selected because it is the spectrum that neutrons produced in thermal reactions exhibit [40]. For the relative standard deviation of the gaussian profile,  $\sigma_{\text{rel}} = \sigma_{\text{gaussian}}/E_{\text{inc}} = 10\%$  is assumed, and the averaging calculation is executed on an energy grid in the interval  $[-4E_{\text{inc}}\sigma_{\text{rel}}, 4E_{\text{inc}}\sigma_{\text{rel}}]$  with 1000 grid points. We note that with these parameters, it is not our goal to exactly reproduce the conditions at the laser facilities at ELI-NP and NIF, but rather to employ the total numbers of neutrons per pulse and the repetition frequencies of these sources in calculations in which a broad range of energies available at any laser driven neutron source is investigated for a quite high energy resolution. To achieve

## 5 Theoretical Approach of the Present Work

energy spectra comparable to those used in our calculations, the neutrons of the ELI-NP and the NIF source would have to be filtered and/or moderated, so that the number of neutrons per pulse would most possibly be reduced compared to that used in the calculations.

For the considered neutron sources and the incident neutron energies, the irradiation of a target with a target area of  $A = 10^4 \mu\text{m}^2$  and a length of  $L = 100 \mu\text{m}$  is considered. Therefore, the target area is significantly larger and more realistic than for the target assumed in Ref. [49]. For this target, it is assumed that only consists of one type of seed nuclides at the beginning. The following two sets of seeds are considered in the present work:

- Nuclides I:  $^{75}_{33}\text{As}$ ,  $^{126}_{51}\text{Sb}$ ,  $^{176}_{71}\text{Lu}$ ,  $^{187}_{75}\text{Re}$ ,  $^{192}_{76}\text{Os}$ ,  $^{226}_{88}\text{Ra}$ ,  $^{233}_{91}\text{Pa}$  and  $^{244}_{95}\text{Am}$
- Nuclides II:  $^{171}_{69}\text{Tm}$ ,  $^{193}_{77}\text{Ir}$ ,  $^{197}_{79}\text{Au}$ ,  $^{227}_{89}\text{Ac}$  and  $^{255}_{99}\text{Es}$

These nuclides have been chosen for the following reasons. Firstly, these isotopes are the heaviest available for each element in the ENDF/B library and they each are characterized by the fact that at least one of the neutron-enriched nuclides has a lifetime longer than one hour. Such long-lived neutron-enriched nuclei are both promising to produce a high number of nuclei enriched by even more neutrons, and a long half-life makes it possible to conduct further experiments with the neutron-enriched nuclides. Furthermore, the selected seed nuclides have been found to perform well in the production of neutron-rich isotopes with neutron capture cascades in Ref. [49] in the interaction of a laser-driven neutron beam with a single-component target. Lastly, most of the nuclides considered in this work are relevant to the astrophysical r- and s-process.

$^{176}\text{Lu}$ , for instance, is an s-only nuclide and, in fact, a highly temperature-sensitive branching point nuclide of the s-process [147] because of the fact that in stellar environments,  $^{176}\text{Lu}$  and  $^{176m}\text{Lu}$  with lifetimes  $4 \times 10^{10}$  years and 3.68 hours are both present with the distribution depending highly on the temperature of the environment. Moreover,  $^{171}\text{Tm}$  is an s-process branching nuclide as well [23], and  $^{126}\text{Sb}$  lies near both the s-process branchings of  $^{122}\text{Sb}$  and  $^{121}\text{Sn}$ . Furthermore,  $^{187}\text{Re}$ , which is predominantly produced in the r-process, is an important chronometer for the r-process as its decay contributes to the abundance of the otherwise s-only nuclide  $^{187}\text{Os}$  [148], and  $^{187}\text{Re}$  is also right next to the  $^{186}\text{Re}$  s-process branching point. Moreover,  $^{75}\text{As}$  and its enriched nuclides are all produced in the weak s-process, and  $^{75}\text{As}$  is near the branching point of  $^{75}\text{Ge}$  [24]. As explained in chapter 3, a precise knowledge of the quantities for such nuclides in the region of branching points and the simulation of the behaviour of these nuclides in environments of high neutron flux could help improve s-process models and provide information on the dynamical environments for the s-process. Because especially in the weak s-process, the neutron capture cross sections of the individual nuclei are relevant for the final abundances of all nuclides on a branch, the investigation of the neutron-enriched

nuclides of  $^{75}\text{As}$  and the simulation of neutron capture cascades on these nuclides are of great importance.

$^{126}\text{Sb}$  and more neutron-rich isotopes of this nuclide can be produced by fission of actinides, so that a better understanding of the cross sections of the nuclides for Sb, but also the investigation of the fission probabilities of the regarded actinide nuclides is crucial for the understanding of fission cycling in the r-process [149–151]. Moreover, the neutron-enriched nuclides and seed nuclides of Tm, Lu, Re, Os, Ir, and Au are close to the  $N = 126$  waiting point of the r-process, which is the last point at which the r-process path comes close to the valley of stability before producing the heaviest elements. Therefore, as explained in chapter 3, investigating neutron capture cascades with laser-driven neutron sources delivering neutron fluxes similar to those in the r-process in this region and producing neutron-rich nuclides for these seeds with which further experiments can then be conducted is crucial in understanding the production of very heavy nuclides in the r-process. This is especially true regarding the fact that with the laser sources under investigation, neutron fluxes comparable to those in the r-process can be produced. Some neutron-rich nuclides relevant to the r-process that are considered in the present work ( $^{195}\text{Os}$ ,  $^{196}\text{Os}$ ,  $^{172}\text{Tm}$ ,  $^{191}\text{Re}$ ,  $^{128}\text{Sb}$ , and  $^{129}\text{Sb}$ ) have also been investigated in a sensitivity study by Mumpower et al. [112], which has shown that the neutron capture cross sections of these nuclides, especially that of  $^{195}\text{Os}$ , have great influence on the r-process abundances produced in several current models of both supernovae and binary mergers. Therefore, exploring the reaction cross sections of these seed nuclides in experiments with laser-driven neutron sources could help identify the r-process site.

Moreover, three of the nuclides that can be produced from the seed nuclides by capturing 3 or 4 neutrons, i.e.  $^{258}\text{Es}$ ,  $^{259}\text{Es}$ , and  $^{248}\text{Am}$  have never been produced in the laboratory before [1–3]. Furthermore,  $^{129}\text{Sb}$  has been recently shown to be a good nuclide for studying nuclear collectivity [152]. Finally, some of the neutron-rich nuclides that we aim to calculate the production of, like  $^{177}\text{Lu}$  [12],  $^{198}\text{Au}$  [9],  $^{199}\text{Au}$  [11] and  $^{188}\text{Re}$  [10], have medical applications. Thus, if our calculations show a significant production of these nuclides, laser-driven neutron sources could provide a space-saving and relatively cheap alternative for reactor- and accelerator-based facilities currently used to produce such nuclides for hospitals [33]. Therefore, nuclear medicine could become more broadly available.

The half-lives, mass densities and minimal penetration depths of these seed nuclides and the isotopes that can be created by neutron capture of up to 4 more nuclides are shown in Table 5.1. The half lives in this table are taken from the ENDF/B-VIII.0 decay sublibrary[50] and half-lives of neutron-enriched nuclides greater than 1 h are printed in bold letters. If only a bound is known to the lifetime, this bound is used for the calculations, and in case that the half-life is

## 5 Theoretical Approach of the Present Work

Seed	$\rho$ (g/cm <sup>3</sup> )	$\lambda$ (mm)	$T_{1/2}$	$T_{1/2}^{+1n}$	$T_{1/2}^{+2n}$	$T_{1/2}^{+3n}$	$T_{1/2}^{+4n}$
<sup>75</sup> <sub>33</sub> As	5.75	23	stable	1 d	2 d	2 h	9 min
<sup>126</sup> <sub>51</sub> Sb	6.68	48	12 d	4 d	9 h	4 h	40 min
<sup>171</sup> <sub>69</sub> Tm	9.32	30	2 y	3 d	8 h	5 min	15 min
<sup>176</sup> <sub>71</sub> Lu	9.84	28	4E10 y	7 d	28 min	5 h	6 min
<sup>187</sup> <sub>75</sub> Re	20.80	9	4E10 y	17 h	1 d	3 min	10 min
<sup>192</sup> <sub>76</sub> Os	22.59	9	stable	1 d	6 y	9 min	35 min
<sup>193</sup> <sub>77</sub> Ir	22.56	11	stable	19 h	2 h	52 s	6 min
<sup>197</sup> <sub>79</sub> Au	19.30	14	stable	3 d	3 d	48 min	26 min
<sup>226</sup> <sub>88</sub> Ra	5.00	54	2E03 y	42 min	6 y	4 min	2 h
<sup>227</sup> <sub>89</sub> Ac	10.00	27	22 y	6 h	1 h	2 min	8 min
<sup>233</sup> <sub>91</sub> Pa	15.40	19	27 d	7 h	24 min	9 min	9 min
<sup>244</sup> <sub>95</sub> Am	12.00	25	10 h	2 h	39 min	23 min	10 min
<sup>255</sup> <sub>99</sub> Es	8.84	37	40 d	25 min	8 d	2 min	-

Table 5.1: Half-lives and minimal penetration depths of the selected seed nuclides and their neutron-enriched isotopes

not known at all, it is assumed as zero. One case of such an isotope with zero half-life is <sup>259</sup>Es, for which it is hence assumed in the calculations that any produced nucleus of this isotope instantly decays, so that the abundances  $N_i$  are assumed as 0. For the other nuclides, however, the half-lives are so high that the approximation that the pulse duration, which amounts to less than a nanosecond for the considered laser-driven neutron sources, as illustrated in chapter 4, is negligible compared to the half-lives of the nuclei is applicable for all of the regarded nuclides.

The mass densities of the elements are taken from the 97th edition of the CRC Handbook of Chemistry and Physics [153] and the data provided by the Royal Society of Chemistry [154]. For Es, the value is predicted in [155]. With these values of the mass densities, the masses of the nuclides, and the total cross sections  $\sigma_{\text{tot},0}$  for neutron interactions with the seed nuclei taken from the ENDF-B library [50] in the considered energy range of 50 keV to 10MeV, the penetration depths, furthermore, have been approximately calculated according to Eq. (5.19). The minimal penetration depths listed in Table 5.1 are the smallest values of  $\lambda$  for energies in the considered energy range. From the  $\lambda$  values it becomes apparent that because even the smallest one with 9mm is still 90 times as great as the length of the probe, the influence of neutron damping in the target as regarded in section 5.2 is small. At most, the average neutron number "seen" by a nucleus decreases from the original one by 1.2% at the rear of the target.

Apart from the neutron enrichment of the seed nuclides after 1 and several pulses, as done in Ref. [49], we also analyze the saturation of neutron enrichment in the present work. For this, the following two conditions are considered for each of the populations  $N_i$ :

- **Saturation Condition 1:**

The population  $N_i$  is maximal.

- **Saturation Condition 2:**

The difference of the population  $N_i$  after  $s$  pulses and  $s - 1$  pulses is smaller than the enrichment after one pulse.

$$N_i(s) - N_i(s - 1) < N_i(1pl) \quad (5.35)$$

The first saturation condition, therefore, is important to investigate as it indicates how many nuclei of a specific species can be present at once and, therefore, are simultaneously available for further experiments. The second saturation condition is of importance as it indicates when, for example, the target should be changed to uphold the production speed of new nuclei.

### 5.3 Cross Section Data

As explained in section 5.1, the required cross sections for our calculations are the neutron capture cross section  $\sigma_{n\text{-cap}}$ , the cross section for nuclear transmutations,  $\sigma_{tr}$ , and the total cross section  $\sigma_{tot}$  for all neutron-nucleus interactions. While the neutron capture cross section is readily available in all of the regarded libraries and the total cross section can be obtained from ENDF/B-VIII.0 and TENDL-2019, this is not the case for the transmutation cross section. In order to calculate it according to Eq. 2.5, we need the elastic neutron scattering cross section  $\sigma_{el}$ , the inelastic neutron scattering cross section  $\sigma_{inel}$  and the non-elastic neutron interaction cross section  $\sigma_{non-el}$ .

All cross sections for the seed nuclides are obtained from the ENDF/B-VIII.0 data that has been preprocessed using the PREPRO 18 codes. However, for most of the nuclides, and in fact for all nuclides on which we focus in the present work (see Table 5.1), the non-elastic cross section is not provided in the ENDF/B-VIII.0 data. Therefore, this cross section has to be estimated by Eq. (2.3). Comparisons of this estimate with the value directly taken from ENDF-B for the cases that this data exists show that the mean relative error of  $\sigma_{non-el}$  calculated by Eq. (2.3) is on the level of less than 1% for most of the heaviest nuclides for which a file exists in the ENDF/B-VIII.0 library [49]. Just  $^{41}\text{Ar}$  exhibits a relatively large relative deviation of 16%. These deviations are most probably caused by misalignments on the energy grids of the elastic and the inelastic cross sections of the nuclides. With the non-elastic cross section calculated like this, the cross section for any kind of species-loss of the seed nuclides  $\sigma_{tr}$  can be calculated according to Eq. (2.5).

## 5 Theoretical Approach of the Present Work

As explained above, the seed nuclides used in this simulation are each the highest- $A$  isotopes available for the corresponding nuclide, so that no cross section data is available for the neutron-enriched isotopes in the ENDF/B-VIII.0 library. Thus, for the isotopes enriched by neutrons, we use the cross sections from the TENDL-2019 library preprocessed with PREPRO 18. This library is used because, as explained in chapter 2, it includes models for most important processes and as much experimental data as possible. Therefore, the cross section data used for the calculations of the numerical results presented below differs from those used in Ref. [49]. Like for the seed nuclides, the neutron capture cross sections can be taken directly from the preprocessed TENDL library. Furthermore, because of the ambition of TENDL-2019 to be a complete nuclear data library, non-elastic cross sections exist in the corresponding TENDL datafile for all of the nuclides considered in the present work, i.e. the isotopes in the two sets of nuclides as well as their neutron-enriched isotopes, so that estimates via Eq. (2.3) do not have to be made here. From these non-elastic cross sections, the species-loss cross sections for the neutron-enriched nuclides are then calculated according to Eq. (2.5). Because there has been misalignment on the energy grid when calculating the non-elastic cross section from the ENDF-B data, we have checked for any kind of energy grid misalignment between the non-elastic and the inelastic cross sections in the TENDL data as well and came to the conclusion that for the preprocessed TENDL data, there are none.

In general, less approximations have to be made when using TENDL cross section data than NON-SMOKER data, as is done in [49], for neutron-rich nuclides in our calculations. To check the precision of the TENDL data and, therefore, the validity of our results, the TENDL-2019 data is compared to the ENDF data in chapter 7.

# 6 Numerical Results

## 6.1 Numerical Results for Neutron Source 1

### 6.1.1 Results after 1 Pulse

Now, we turn to analyzing the numerical results of our calculations. We first consider the case of one pulse of the first neutron source. This case has already been studied in Ref. [49], however, a target of different area and different cross section data has been used in that work. The framework established in section 5.1 is used to calculate the abundances of the neutron-enriched isotopes in a thick target. Moreover, 300 energies from 50 keV up until 10 MeV are included in the calculations. The resulting populations of the neutron-enriched isotopes with up to 4 neutrons more than the seed directly after this one pulse and, therefore, without any decay included, are shown in Fig. 6.1 for the nuclides from the first set and in Fig. 6.2 for the second set of nuclides.

It can be seen in Figs. 6.1 and 6.2 that the populations  $N_i$  decrease with higher incident neutron energies, therefore making the production of neutron-rich isotopes most efficient with low incident neutron energies. The highest abundances of neutron-enriched isotopes after one pulse can generally be found for the Am, Pa, Lu and Re isotopes for the first nuclide set. Furthermore, the Ra and Os isotope abundances have distinct maxima for a few MeV. For the second set of nuclides, the populations are generally the highest for the Ir isotopes and lowest for the Es isotopes. Because of the low deviations between the populations of the second set nuclides, all of the second set abundances lie in between the highest and lowest of the first set.

More careful analysis shows that the features of the abundance  $N_1$  depends mainly on the neutron capture cross section of the seed nuclide. For larger  $i$ , however, the abundance  $N_i$  depends on a combination effect of all neutron-capture cross sections  $\sigma_{n\text{-cap},j}$ ,  $j < i$ . Such feature is expected because with our theoretical approach, the abundance after one pulse is calculated via

$$N_i(1\text{pl}) = \frac{1}{i!} \left( \prod_{k=0}^{i-1} \mu_k \right) N_t \quad (6.1)$$

## 6 Numerical Results

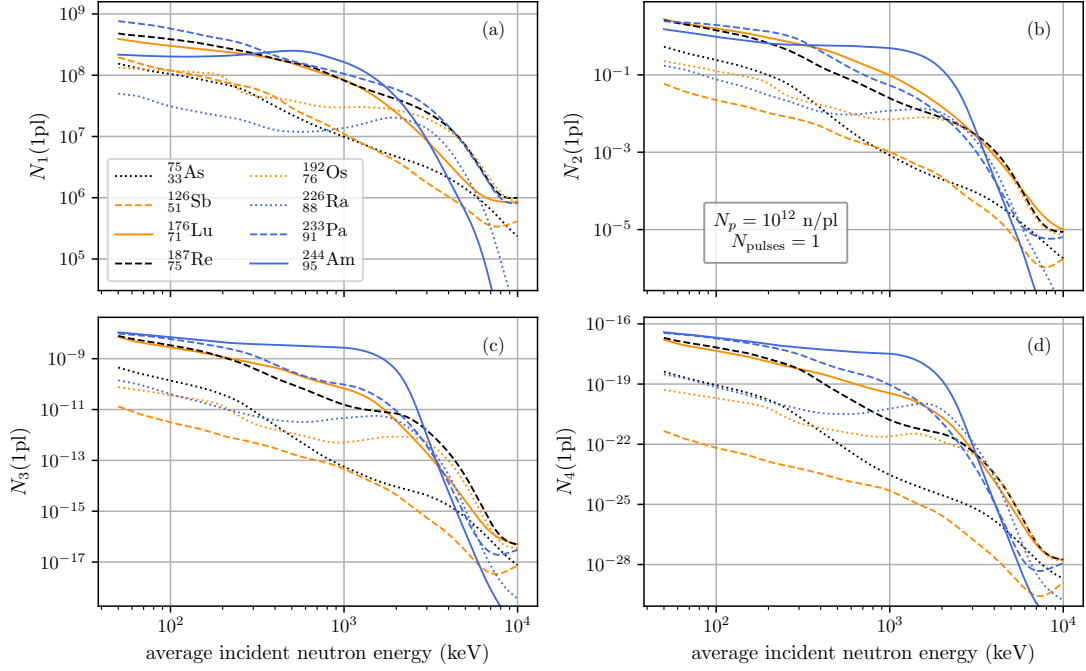


Figure 6.1: Populations  $N_i$ ,  $i \in \{1, 2, 3, 4\}$  of neutron-enriched isotopes directly after 1 pulse of  $10^{12}$  neutrons for the first set of nuclides.

in leading order and neglecting damping, with  $\mu_i$  being directly proportional to  $\sigma_{n\text{-cap},i}$ . This also explains the observation that the abundances  $N_i$  get lower by a factor of at least  $10^8 - 10^{11}$  for each added neutron, depending on the energy, as  $\mu_i \propto \frac{N_p}{A_t} \cdot \sigma_{n\text{-cap},i} = 10^{16} \text{cm}^2 \cdot \sigma_{n\text{-cap},i} = 10^{-11} \dots 10^{-8}$ .

That the populations mainly depend on the neutron capture cross sections and that they get lower by a factor corresponding to  $\mu_i$  has also been found in Ref. [49]. However, when comparing the one pulse results from Ref [49] to ours, it can be seen that the relative position of the abundance curves, as well as the course of these curves themselves differ. This can be explained by Eq. (6.1), as different cross section data is used in Ref. [49]. Moreover, it can be seen that our results for the  $N_i$  populations are significantly lower than those in Ref. [49] for  $i > 1$ . This can be explained by the lower neutron-to-seed ratio in the larger target employed in this work and, therefore, by the scaling of  $N_i$  with  $N_p^i/A^{i-1}$ , which results from the theoretical approach and which has been investigated in Ref. [49].

Even though the populations resulting from our calculations are significantly lower than those for the same number of neutrons per pulse in Ref. [49], as shown in Figs. 6.1 and 6.2, our results still suggest that with only one pulse of  $10^{12}$  neutrons, a large number of nuclides of the 1-species can be produced for all seed nuclides and at all considered energies, with over

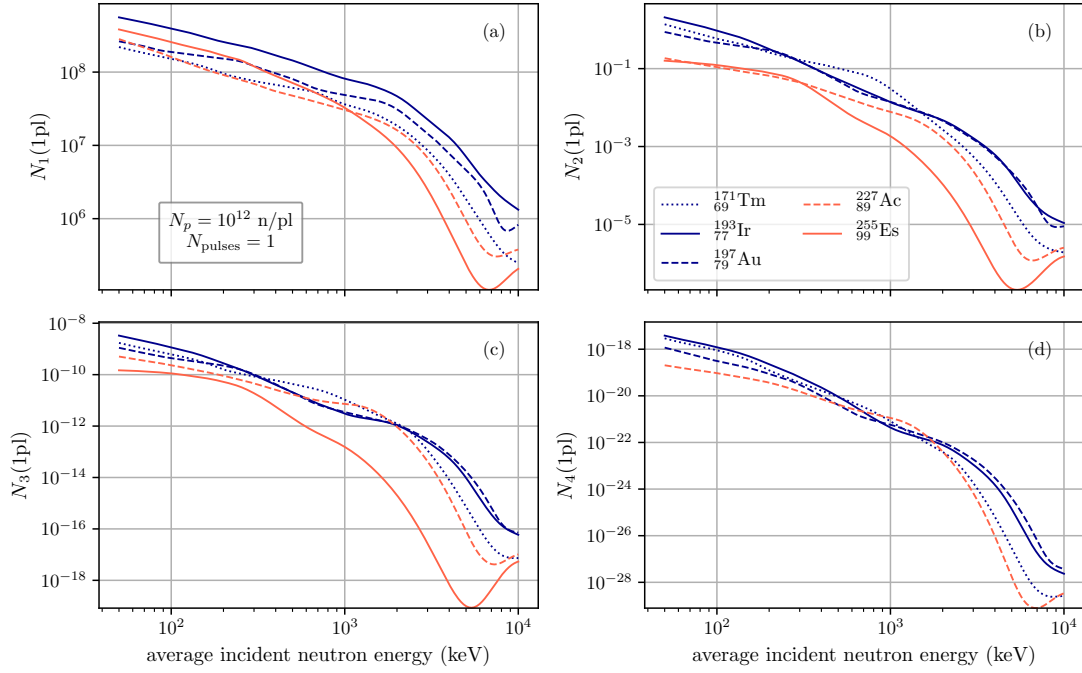


Figure 6.2: Populations  $N_i$ ,  $i \in \{1, 2, 3, 4\}$  of neutron-enriched isotopes directly after 1 pulse of  $10^{12}$  neutrons for the second set of nuclides. Because  ${}^{259}_{99}\text{Es}$  has no half-life,  $N_4$  for this nuclide is not shown in subplot d).

$10^8$  nuclei at low energies for all seed nuclides except  ${}^{226}\text{Ra}$ , for which the population only reaches slightly above  $5 \times 10^7$  though the neutron capture cross sections for this nuclide being comparable to those for the others, as this seed nuclide has the lowest number density and, thus, the lowest number of seed nuclei  $N_i$  in the target.

Furthermore, for some nuclides, i.e. Lu, Re, Pa, Am, Tm, and Ir, the abundances  $N_2$  are greater than 1 at low mean neutron energies around 50 keV. Therefore, even for the larger, more realistic target considered, one pulse of neutron source 1 with  $10^{12}$  neutrons is sufficient to make the capture of multiple neutrons on unstable nuclides, as they occur in the r-process, possible. However,  $N_2$  is only slightly greater than 1 for the mentioned nuclides, and for the others, it is improbable that a nuclide enriched by more than 1 neutron is even produced. Isotopes enriched by more than 2 neutrons are even more unlikely to be created with only one pulse, with the abundances all below  $10^{-8}$ . Thus, multiple pulses seem to be needed to observe the production of even more neutron-rich isotopes with this neutron source.

### 6.1.2 Results after $10^4$ Pulses

We now turn to the case of  $10^4$  pulses of the first neutron source. For this pulse number, we will only be regarding the seed nuclides for the first set of nuclides. Furthermore, 100 energies between 50 keV and 10 MeV are considered as mean incident neutron energies for the calculations of the results for  $10^4$  pulses. In the case of multiple pulses, not only the cross sections and number densities of the nuclides are of importance, but also the repetition rates  $f_{\text{rep}}$ , with which the pulses are delivered, as after each pulse (for which the duration  $T_p$  is assumed to be much smaller than the delay time  $T_{\text{del}}$  between the pulses), the populations of unstable nuclides decay. In case of the first neutron source, three repetition rates are examined: 1 Hz, 10 Hz and 1 pulse per minute. Because of the possibility of the produced nuclei decaying and transmutation to occur, the total number of produced nuclei are shown as well as the enriched nuclei left directly after the  $10^4$  pulses, for the last of which the decay therefore is not included.

The totally produced numbers of neutron-enriched nuclei, as well as the ones present after  $10^4$  pulses delivered with a repetition rate  $f_{\text{rep}} = 1$  Hz are shown in Fig. 6.3 for the first set of nuclides. Therefore, the results shown in this figure correspond to those investigated for multiple pulses in Ref. [49], just with a more realistic target and different cross section data used in the calculations. According to Eq. (5.28), the populations should, in leading order, scale approximately with  $10^{4i}$  compared to the enrichment after one pulse if the decay and damping are neglected. And in fact, the populations of nuclides present after  $10^4$  pulses are much higher than those after just one pulse, while still following the same course of the abundance curves. With a repetition rate of 1 Hz, up to  $6.6 \times 10^{12}$  nuclei of the 1-species are present at the end of the  $10^4$  pulses for Pa, and apart from Ra, all other nuclides reach  $N_1$  values of over  $10^{12}$  as well. Furthermore, while for one pulse hardly above one nucleus of the 2-species is produced for any of the seeds, over  $10^8$  nuclei of the 2-species are present for Re after the  $10^4$ th pulse at low energies, and the other nuclides all also reach abundances above  $10^6$ . Thus, the calculated abundances  $N_1$  and  $N_2$  are both significantly above 1, which suggests that in the setup under consideration, nuclides enriched by both 1 and 2 neutrons can be produced in large quantities with the laser-driven neutron source 1.

The biggest difference to the 1 pulse case is, however, that with  $10^4$  pulses, 3-species isotopes can be produced for all of the seed nuclides, and for all of the seeds, such neutron-enriched isotopes are still present at the end of the  $10^4$  pulses. At low energies, even more than  $10^3$  nuclei of the 3-species isotopes  ${}_{71}^{179}\text{Lu}$ ,  ${}_{75}^{190}\text{Re}$ ,  ${}_{91}^{236}\text{Pa}$  and  ${}_{95}^{247}\text{Am}$  are produced, with more than  $10^3$  still remaining at the end for  ${}_{95}^{247}\text{Am}$  and  ${}_{71}^{179}\text{Lu}$ . Nevertheless, the production of 4-species isotopes is still negligible, even though  $N_4^{\text{tot}}$  has increased from up to  $1.6 \times 10^{-17}$  for one pulse to up to  $8.1 \times 10^{-2}$  for  $10^4$  pulses, both for Am at 50 keV.

### 6.1 Numerical Results for Neutron Source 1

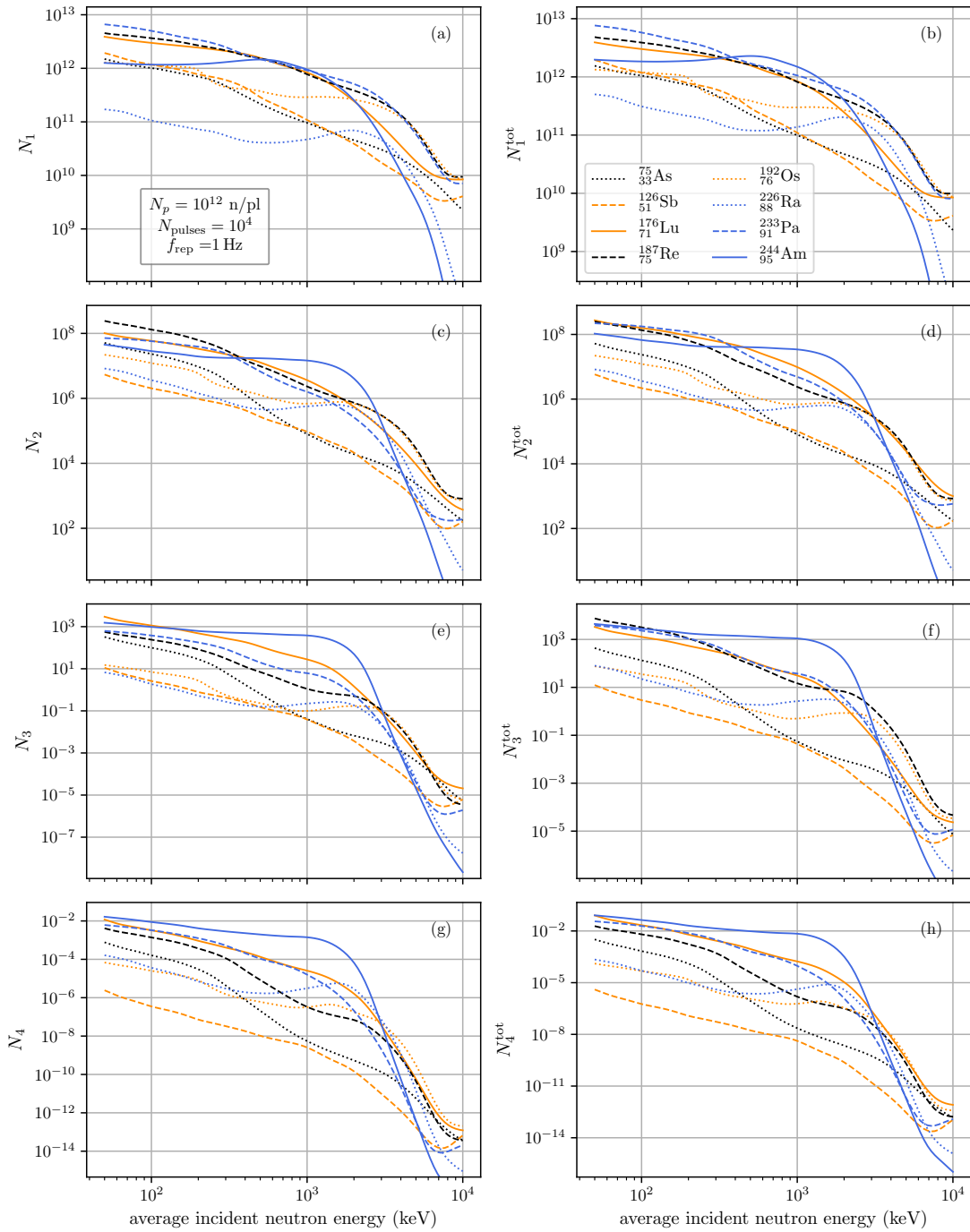


Figure 6.3: Populations  $N_i, i \in \{1, 2, 3, 4\}$  as well as total produced abundances  $N_i^{tot}, i \in \{1, 2, 3, 4\}$  of neutron-enriched isotopes directly after  $10^4$  pulses of  $10^{12}$  neutrons each delivered with a repetition rate of 1 Hz for the first set of nuclides.

Therefore, while the results in Ref. [49] suggest the capture of up to 4 neutrons for all seed nuclides, this is not the case when using the target area employed in our work. However,

## 6 Numerical Results

when analyzing the abundances as a function of the pulse number, it becomes clear that all populations have reached their maximum at the last,  $10^4$ th pulse. Therefore, the populations of neutron-enriched isotopes produced with the first neutron source operating at a repetition rate of 1 Hz are likely to be improved by simply applying more pulses.

Comparison of abundance curves in Fig. 6.3 with the populations after one pulse of the same neutron source in Fig. 6.1 shows that the relative location of the abundance curves  $N_i$  for different seed nuclides is different for 1 and  $10^4$  pulses. In order to investigate this effect, we analyze the ratios of  $N_i$  after  $10^4$  pulses to the corresponding abundances after 1 pulse. The analysis shows that the energy dependence of this ratio is very weak for all the considered nuclides. Furthermore, the approximate scaling with  $N_{\text{pulses}}^i$  is quite accurate for some nuclides, especially for those of population  $N_1$  and  $N_2$ , while for  $N_3$  and  $N_4$ , the scaling becomes weaker than  $N_{\text{pulses}}^i$ . The approximation yielding the  $N_{\text{pulses}}^i$  scaling does not take into account higher order terms including nuclear transmutation, damping of the beam in the target as well as the decay that occurs between beams. Because the target thickness is at least about two orders of magnitude smaller than any of the minimal  $\lambda$  values from Table 5.1, the damping effect is quite low. Furthermore, species-loss due to nuclear transmutation is decreased compared to the leading order by a factor of up to  $(10^8 - 10^{11}) \times 10^4$  (the order of magnitude of  $\mu_i \times N_{\text{pulses}}$ ), as according to Eq. (5.30),  $\eta_i$  operates on  $N_i$  and  $\mu_i$  operates on  $N_{i-1}$  in leading order. Therefore, the main reason for the weaker scaling in our theoretical approach is the decay, and indeed, the abundances increase least for nuclides for which the half-lives are low. The duration of the interactions, which amounts to 2 h, 48 min and 39 s, is longer than the half-lives of several of the neutron enriched isotopes and especially higher than all half-lives of the 3- and 4-species isotopes of the considered seed nuclei (see Table 5.1). Consequently, many nuclei decay and, thus, do not remain at the end of the  $10^4$  pulses anymore, and cannot contribute to the production of isotopes with more neutrons. This leads to a dependence of the abundances  $N_i$  firstly on the half-life of the  $i$ -species,  $T_{1/2}^{+in}$ , but also on all half-lives  $T_{1/2}^{+jn}$  for  $j < i$ , as it can be quantitatively seen in the approximate formula Eq. (5.29). The dependence on  $T_{1/2}^{+in}$  can be seen, for example, for the Ra and Am  $N_1$  abundances, which, of all set-1 nuclides, have increased the least compared to the 1 pulse populations because they have the lowest  $T_{1/2}^{+1n}$ . Furthermore, even though the 2-species Radium isotope has the longest lifetime, the factor is still one of the lowest. There, the effect comes into play that when  $N_j$ ,  $j < i$  decreases due to decay, this also means a lower  $N_i$ .

However, not only the abundances  $N_i$  at the end of the  $10^4$  pulses are object to decay, but also the totally produced abundances  $N_i^{\text{tot}}$ . For these abundances, the decay of the  $i$ -species itself is not included (see Eq. (5.34)). Still, a lower number of nuclei of  $i$ -species isotopes can be produced in total if nuclei of the  $j$ -species with  $j < i$  decay during the interaction. Therefore,

we find the scaling of  $N_i^{\text{tot}}$ , which has also been investigated in Ref. [49], to be more than 1 order of magnitude lower than  $10^{16}$  for the  $N_4^{\text{tot}}$  populations of Ra and Re, the nuclides with the lowest  $T_{1/2}^{+3n}$  of the first set, and we observe that generally, the scaling is lowest if all nuclides contributing to the capture cascade leading to the  $i$ -species have low half-lives. Therefore, we can confirm the observation in Ref. [49] that the scaling for  $N_4^{\text{tot}}$  is noticeably lower than expected if  $T_{1/2}^{+3n}$  is short and generalize this observation.

We now turn to the case of the first neutron source with a repetition rate of 10 Hz and, therefore, the first case that has not been investigated in Ref. [49]. The numbers of totally produced nuclei and those still present at the end of the  $10^4$  applied neutron pulses for this repetition rate are shown in Fig. 6.4 for the first nuclide set. Because of the lower delay time  $T_{\text{del}} = 0.1$  s between the pulses compared to  $T_{\text{del}} = 1$  s for the 1 Hz repetition rate, the total duration of the interaction amounts to only 16 min 39.9 s. Therefore, the decay of the nuclei has less influence on the populations than for  $f_{\text{rep}} = 1$  Hz. Thus, especially for species enriched by multiple neutrons and short lifetimes,  $N_i^{\text{tot}}$  as well as  $N_i$  are higher than for 10 Hz.

To compare the isotope abundances for the different repetition rates, we analyze the ratios of the populations at 10 Hz and 1 Hz. The totally produced abundances  $N_i^{\text{tot}}$  for  $f_{\text{rep}} = 10$  Hz are hardly higher than twice the abundances for  $f_{\text{rep}} = 1$  Hz for  $i < 4$ . For the 1-species isotopes of stable seed nuclides, the totally produced abundances are in fact the same, as no decay influences the produced nuclides of the 1-species for these seeds. However, because of the low half-lives for the 3-species, the abundances  $N_4^{\text{tot}}$  are up to 8 times higher for 10 Hz than for 1 Hz in case of Radium, and up to 6.9 times as high for Palladium. These two nuclides also have the lowest half-lives for the 3-species with 3 min and 4 min, respectively. Generally, the totally produced abundances  $N_i^{\text{tot}}$  become significantly higher for higher repetition rates in cases in which the  $j$ -species isotopes with  $j < i$  have low half-lives, as for 10 Hz, the populations of these species then do not decrease as much due to decay as with 1 Hz because of the lower delay time. Consequently, the more abundant  $j$ -species also produce more  $+in$ -nuclides in neutron capture cascades.

In the case of the populations remaining at the end of the  $10^4$  pulses,  $N_i$ , the enhancement factors for 10 Hz compared to 1 Hz are even higher than for  $N_i^{\text{tot}}$  because in these cases, the decay of the  $i$ -species also comes into play. For 10 Hz, up to 3 times as many low-half-life 2-species nuclei are left after the  $10^4$  pulses as for 1 Hz, and  $N_3$  increases by a factor up to over 10. For the 4-species, 32 times as many Palladium nuclides are left than for 1 Hz. Nevertheless, for seed nuclides with generally long lifetimes like  $^{126}\text{Sb}$  or also  $^{75}\text{As}$ , the improvement for the increased repetition rate is not too high.

## 6 Numerical Results

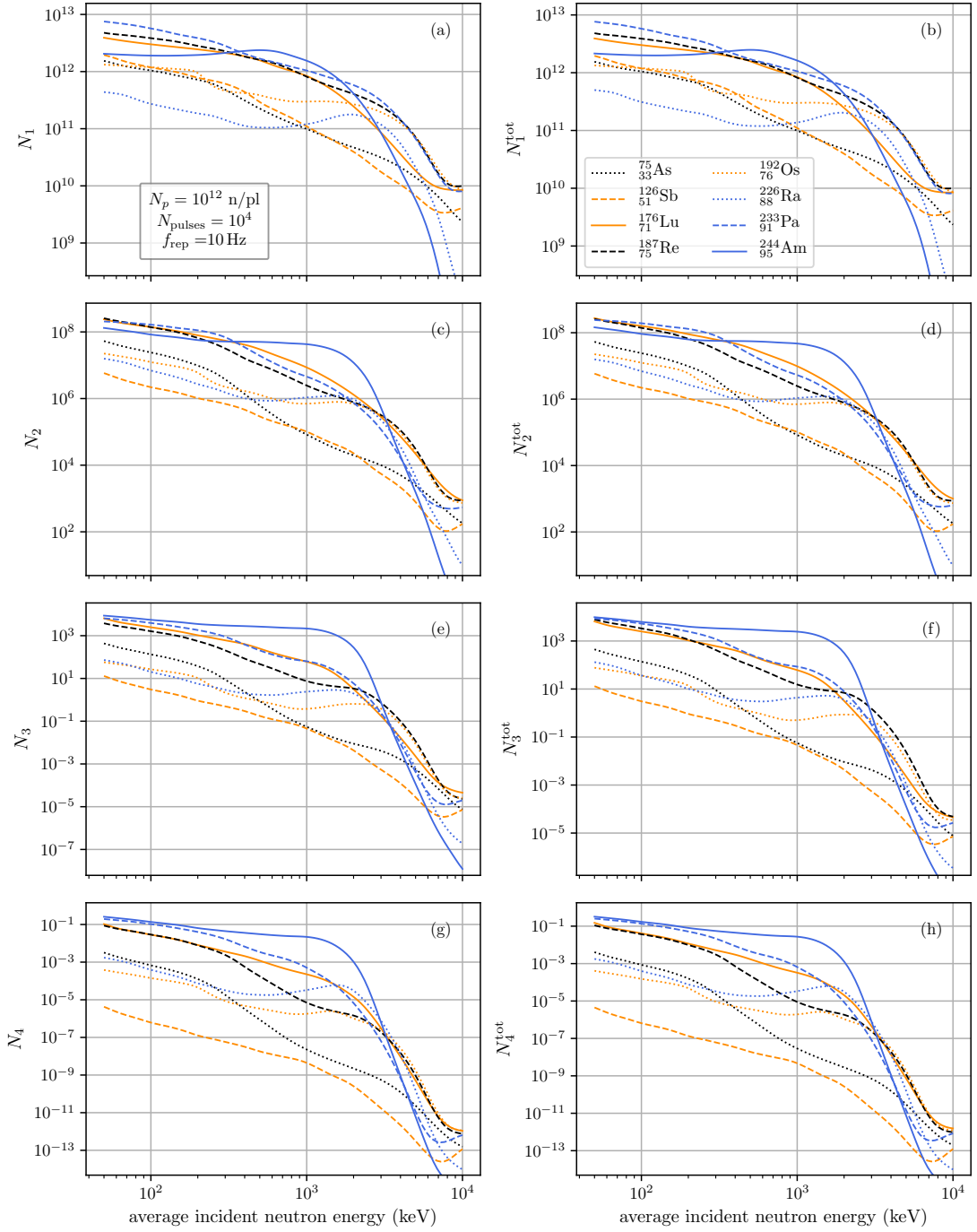


Figure 6.4: Populations  $N_i, i \in \{1, 2, 3, 4\}$  as well as total produced abundances  $N_i^{\text{tot}}, i \in \{1, 2, 3, 4\}$  of neutron-enriched isotopes directly after  $10^4$  pulses of  $10^{12}$  neutrons each delivered with a repetition rate of 10 Hz for the first set of nuclides.

In conclusion, a higher repetition rate enhances the abundances for nuclides with low half-lives significantly, both the totally produced populations and the populations remaining after the

last pulse. As an example, for the 4-species isotope of Re, the neutron cross section of which has been shown to influence the predicted r-process abundances, the abundance  $N_i$  could be improved by over a factor of 21 by employing a repetition rate of 10 Hz instead of 1 Hz. In contrast, for relatively long-living nuclides like Sb, which is relevant to both the branching points of the s-process and the r-process, the improvement of a higher repetition rate is not too high and the 10 Hz populations  $N_i$  and  $N_i^{\text{tot}}$  are never higher than 1.2 times the 1 Hz populations. Nevertheless, even though the abundances  $N_i$  and  $N_i^{\text{tot}}$  are higher than for the lower repetition rate, the production of 4-species isotopes is unlikely as shown in Fig. 6.4, as the total abundances of 4-species isotopes are not higher than 1. However, just like for 1 Hz, all abundances  $N_i$  reach their maximum at the last pulse, thus the abundances promise to increase by applying more pulses.

Lastly, we turn to the case of the first neutron source with the repetition rate of one pulse per minute. The total duration of the interaction, thus, amounts to 6 d, 22 h and 39 minute. The number of nuclei of the isotopes enriched by one to four neutrons produced in total,  $N_i^{\text{tot}}$ , as well as their populations  $N_i$  remaining after the  $10^4$  pulses are shown in Fig. 6.5. As expected, the populations of neutron-enriched isotopes produced in  $10^4$  pulses delivered with a repetition rate of one pulse per minute are much smaller than those produced with the other investigated repetition rates. Not only is it very improbable for nuclei of the 4-species to be produced in this experimental setup, but the  $N_3$  and  $N_3^{\text{tot}}$  abundances drastically decrease as well compared to higher repetition rates. Only for very low energies and the long-living 3-species isotopes of Lu and As is  $N_3$  above 1 after the last pulse, and for Am, not even 2-species nuclides remain at the end of the interaction. This drastical decrease is due to the exponential nature of the decay.

The most striking feature of Fig. 6.5 is how low the abundances  $N_i$  and  $N_i^{\text{tot}}$  of the nuclide Am are compared to the other nuclides, especially because the Am nuclide abundances are among the highest for the other two repetition rates because of its high cross sections for neutron capture. The reason for the low abundances are the generally low half-lives of the Am isotopes, including the seed nuclide  $^{244}\text{Am}$ , which only has a half-life of 10 h, which is 16 times shorter than the time it takes for the considered neutron source to deliver all neutron pulses. Consequently, after already about 2015 pulses, less than 10% of the initial seed nuclei left so that the production of neutron-enriched nuclides decreases rapidly<sup>1</sup>.  $N_1$  of Am is actually so low that for a mean neutron energy of 10 MeV, less than one nuclide enriched by one neutron is left after all pulses.

---

<sup>1</sup>and therefore, the approximation that the seed nuclides are the most abundant species in the target, which is needed if the penetration depth is calculated according to (5.19), is no longer valid. However, the damping of the neutron beam has quite a low effect on the final abundance, so that the error made should not be too high.

## 6 Numerical Results

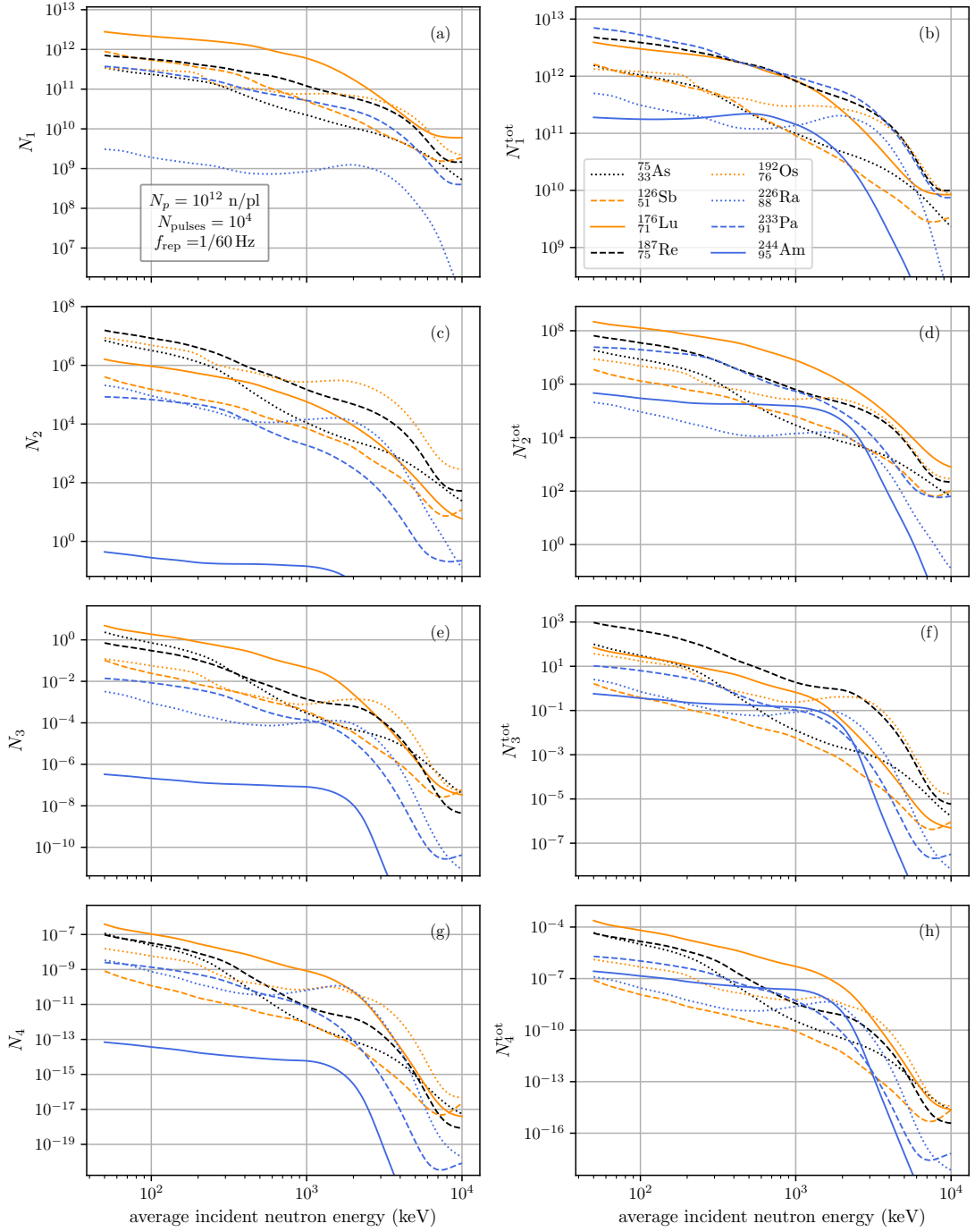


Figure 6.5: Populations  $N_i, i \in \{1, 2, 3, 4\}$  as well as total produced abundances  $N_i^{\text{tot}}, i \in \{1, 2, 3, 4\}$  of neutron-enriched isotopes directly after  $10^4$  pulses of  $10^{12}$  neutrons each delivered with a repetition rate of 1 pulse per minute for the first set of nuclides.

Moreover, all populations  $N_i$  for Am are even smaller after  $10^4$  pulses than they are after only one pulse.

Following the considerations above, it is not surprising that the  $N_i$  populations of the Am nuclides are already beyond their maximum after  $10^4$  pulses. That the abundances reach their maximum during the  $10^4$  applied pulses is also the case for all Pa isotopes because of the short half-life of 27 days for the seed nuclide, and for the  $N_1$  population of Radium, with a half-life of 42 minutes for the 1-species isotope. For Sb, even though the seed nuclide has a half-life of 12 days, however, the maximum is not reached for any  $N_i$  because of its relatively high half-lives for neutron-enriched isotopes. Therefore, for Sb and all other nuclides of the first set of nuclides except Am and Pa, higher abundances of nuclides  $N_i$  are probable to be reached by using more pulses.

### 6.1.3 Saturation Condition 1

Now, we turn to the investigation of the saturation conditions for the first neutron source. While a population reaching its maximum before the end of all pulses has been observed with the 2-species isotope of Es in Ref. [49], the saturation has not been systematically investigated. This will be done in the following. First, we study how high the maximally possible abundances are for each nuclide and repetition rate and after how many pulses they are reached. In other words, the first saturation condition is analyzed for the first neutron source. For this, the bombarding of a seed nuclide target is calculated for 80 mean incident neutron energies from 50 keV to 10 MeV, 40 of which are logarithmically distributed over the entire range, and another 40 are distributed in the range between 1 MeV and 10 MeV.

Before analyzing the numerical results, some general considerations for saturation condition 1 shall be made. Generally, the maximal population of  $N_i$ ,  $N_i^{\text{C1}}$ , is reached when, with more pulses applied than the number  $N_{\text{pulses},i}^{\text{C1}}$  required for the maximum, the growth of the population due to neutron capture of the  $j$ -species with  $j < i$  is smaller than the loss of nuclei of the  $i$ -species through nuclear transmutation and decay. For an approximate quantitative formula describing the main dependencies of the populations  $N_i$ ,  $i > 0$ , Eq. (5.30) can be applied, in which, as explained in section 5.1.3, the terms including  $N_j$  generally become more influential with increasing  $j$  for many pulses. Therefore, the loss of  $N_i$  is mainly determined by  $\eta_i$  and the decay probability  $1 - e^{-T_{\text{del}}/\tau_i}$ , both operating on the population produced with one pulse less than the regarded population and, consequently, the absolute loss increases with increasing  $N_i$ .

For most neutron-enriched isotopes, the decay during the delay time between the pulses has a greater influence on the species-loss than nuclear transmutation reactions because of the low half-lives, as has been seen when investigating the results after  $10^4$  pulses for different repetition rates, where the abundances of short-lived nuclides have been shown to drastically decreased for lower  $f_{\text{rep}}$ . For the 4-species, it is even assumed in our calculations that the

## 6 Numerical Results

transmutation is negligible, which, regarding the low half-lives of 2 hours or less, is a good approximation. However, for the 2-species isotopes of Ra and Os, which both have half-lives of more than 6 years, the decay is dominated by the neutron-induced transmutations for low delay times. The transmutational loss of Ra is higher than the loss through radioactive decay during the delay time of 0.1 s at a repetition rate of 10 Hz at all energies, as well as at energies between 1.5 and 4 MeV and those above 7 MeV for 1 Hz. For Os, the loss induced by  $\eta_i$  is greater than that of the decay as well for most energies for a repetition rate of 10 Hz, and at energies greater than about 7 MeV for a repetition rate of 1 Hz. For  $f_{\text{rep}} = 1/60$  Hz, however, the decay dominates for these nuclides as well. When it comes to the seed nuclides, it is the other way around: in most cases, more nuclei of the 0-species are lost due to the neutron-induced transmutation than through decay, especially for the stable seed nuclides. However, this is not the case for Am, Sb, Ac, Pa and Es, where the loss through decay dominates that through transmutation for all repetition rates in the cases of Am, Sb, Pa and Es, for 1/60 Hz, 1 Hz and some energies for 10 Hz in the case of Tm, and for 1/60 Hz and some energies for 1 Hz in the case of Ac. Even for Ra, the decay dominates in case of  $f_{\text{rep}} = 1/60$  Hz for a few energies of several MeV.

The number of nuclei of the  $i$ -species isotope gained per pulse depends in leading order on neutron capture of less neutron-rich isotopes of the  $j$ -species with  $j < i$ . For the 1-species, therefore, the gain of nuclei depends mainly on the population  $N_0$ , which constantly decreases with every pulse in our theoretical model. The gain of nuclei enriched by more than 1 neutron, however, does not decrease instantly because even though  $N_0$  decreases, the populations  $N_j$  increase at first. Therefore, given that especially for multiple applied pulses, the nuclide gain from neutron capture of isotopes of the  $j$ -species increases with higher  $j$ , i.e. the neutron capture of one neutron is more probable than a capture cascade involving multiple neutrons in one pulse, as the considerations in section 5.1.3 show, the gain of  $i$ -species nuclei should increase at first as well. More precisely, the gain should be mainly dependent on the magnitude of the population  $N_{i-1}$  and the corresponding neutron capture cross section.

However, we note that because differences between gain and loss have to be considered when determining the maximum, even lower orders can play a decisive role when it comes to the exact pulse number at which the maximum is reached.

We consider at first the saturation condition 1 for a repetition rate of 1 Hz. To reach the maximum, we make calculations up to  $3 \times 10^9$  pulses. Furthermore, we note that we only save the pulse numbers and populations for every 100 pulses due to the limit of computational power, hence the number of pulses needed to reach the population maximum are determined with an uncertainty of 100 pulses. The maximal populations, therefore, have an uncertainty as well.

This error is negligible, however, because for all considered nuclides, the relative deviation of the abundances within 100 pulses near the saturation condition is less than a few times of  $10^{-5}$ .

Figs. 6.6 and 6.7 show the maximal abundances  $N_i^{C1}$ , as well as the numbers of pulses  $N_{\text{pulses},i}^{C1}$  at which the maximal populations and, thus, the first saturation condition is reached. It is shown that the lowest number of pulses required for reaching the first saturation condition for the first set of nuclides is  $2.13 \times 10^4$  for the 1-species isotope of Am, which has been expected from the analysis of the  $10^4$ -pulses results for the repetition rate of 1 pulse per minute. For the second set of nuclides, the maximal  $N_1$  abundance of Es is already reached after  $1.68 \times 10^4$  pulses for some energies, because Es has not only a relatively short lifetime of the seed nuclide with  $T_{1/2} = 40$  d but also the shortest half-life for  $N_1$  of only 25 minutes. Therefore, the numbers of pulses required to reach saturation condition 1 is lowest if both the seed nuclides decrease fast and the loss of the 1-species is high as well (low half-life of the 1-species isotopes). The highest number of pulses required to reach the maximal abundance of  $N_1$  is the one for Lu, due to its extremely long-lived seed nuclides and the 1-species half-life of over 7 days, which is the highest for all considered 1-species isotopes.

In addition, it is shown that there is an energy dependence in  $N_{\text{pulses},1}^{C1}$ . This energy dependence is mainly due to the transmutational loss of seed nuclides. For most seed nuclides, loss due to transmutation dominates over that through radioactive decay, and the transmutation cross sections  $\sigma_{\text{tr},0}$  decrease up to a few MeV, from which on they increase again because particle emission reactions become dominant. At the energies where the seed nuclide transmutation cross sections are low, the seed nuclides available to capture neutrons, consequently, decrease slowly, and so does the nuclide gain per pulse of  $N_1$ . Therefore, the saturation condition is reached after more pulses of neutrons with incident energies for which the seed nuclide transmutation cross sections are low than for those with high values of  $\sigma_{\text{tr},0}$ . This also explains why for nuclides for which the seed nuclides are extremely long-lived and for which the transmutation cross sections vary most with energy, the pulse numbers show the greatest energy dependence. For rather short-lived, fissile seed nuclides, for which loss through radioactive decay plays a role or the cross sections do not show much variation with energy, the energy dependence of the pulse numbers is hardly visible. The effect of seed nuclide decay on the energy dependence of the pulse number can be seen, for example, when comparing the pulse numbers of Au and Tm, the latter of which, despite having comparable  $\sigma_{\text{tr},0}$  to Au, shows hardly any energy dependence in the pulse numbers because of the relatively short half-life of the seed nuclide of 2 years. Furthermore, Am, for which  $T_{1/2}$  is lowest with 10 hours and for which  $\sigma_{\text{tr},0}$  is nearly constant as a function of energy, is the only nuclide which shows no energy dependence in the pulse numbers. For Lu, the variation of the pulse number with energy is highest.

## 6 Numerical Results

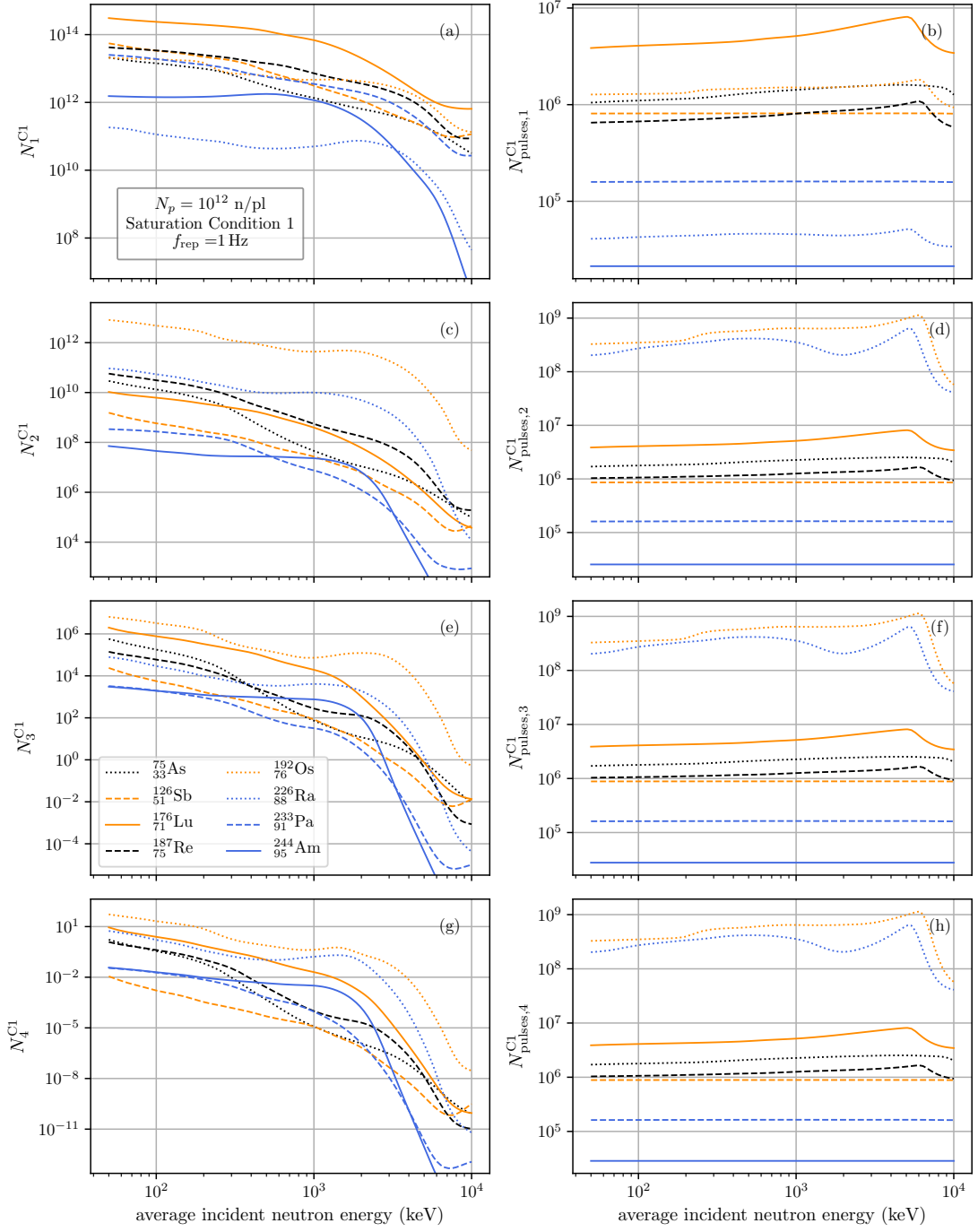


Figure 6.6: Maximally reached abundances  $N_i^{\text{Cl}}$ ,  $i \in \{1, 2, 3, 4\}$  of neutron-enriched isotopes for the first set of nuclides as well as the numbers of pulses  $N_{\text{pulses},i}^{\text{Cl}}$ ,  $i \in \{1, 2, 3, 4\}$  it takes to reach them with a neutron source with  $10^{12}$  neutrons per pulse that delivers pulses with a repetition rate of 1 Hz.

## 6.1 Numerical Results for Neutron Source 1

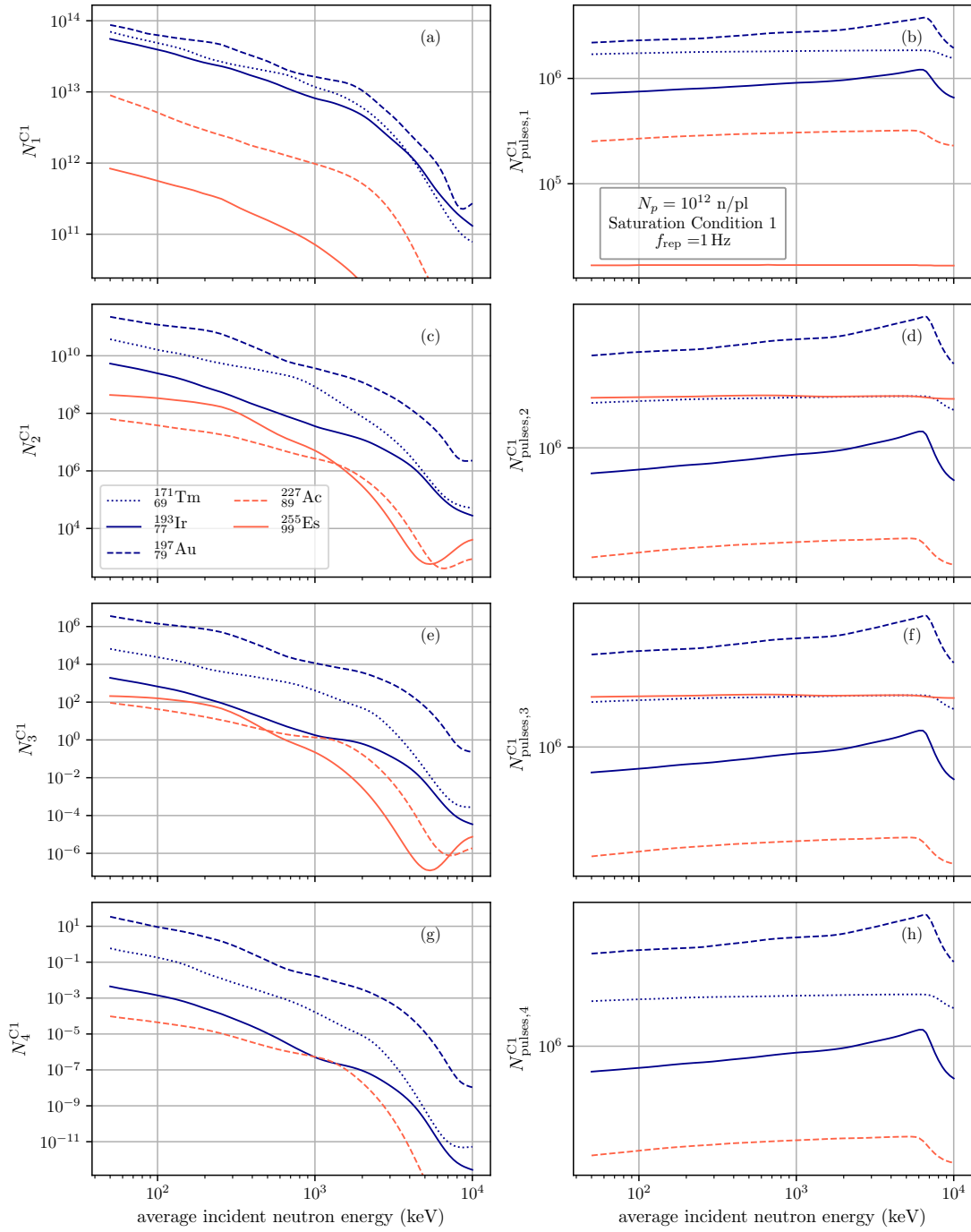


Figure 6.7: Maximally reached abundances  $N_i^{C1}$ ,  $i \in \{1, 2, 3, 4\}$  of neutron-enriched isotopes for the second set of nuclides as well as the numbers of pulses  $N_{pulses,i}^{C1}$ ,  $i \in \{1, 2, 3, 4\}$  it takes to reach them with a neutron source with  $10^{12}$  neutrons per pulse that delivers pulses with a repetition rate of 1 Hz. Because  $^{259}_{99}\text{Es}$  has no half-life,  $N_4^{C1}$  and  $N_{pulses,4}^{C1}$  for this nuclide are not shown in subplots g) and h), respectively.

## 6 Numerical Results

This is also due to the long half-life of the 1-species, such that the transmutional loss of the  $N_1$  nuclides is up to only one order of magnitude lower than that of the decay. Therefore, not only does the nuclei gain decrease slower for low  $\sigma_{\text{tr},0}$ , but the loss of the 1-species is also lower for a few MeV, so that it takes even longer to reach the maximal population for these energies than with a solely constant loss rate due to decay.

This can also be seen when analyzing the pulse numbers of Ra and Os. For the 2-species isotopes of these seed nuclides, the species-losses due to neutron-induced transmutation and radioactive decay are around the same order of magnitude for a delay time of 1 s. Therefore, the loss is not only very low, leading to generally very high pulse numbers to reach saturation, it is also highly dependent on the transmutation cross section  $\sigma_{\text{tr},2}$ . Another observation to be made for  $N_{\text{pulses},2}^{\text{C1}} - N_{\text{pulses},4}^{\text{C1}}$  is that for almost all nuclides, the number of pulses  $N_{\text{pulses},i}^{\text{C1}}$  increases with increasing  $i$ . This increase is especially high if the half-life of the  $i$ -species is far longer than that of the  $i - 1$ -species, as it is the case e.g. for Ra from  $N_1$  to  $N_2$ . The only nuclide for which there is no increase of pulse number is the 3-species of Ir, for which  $N_{\text{pulses},2}^{\text{C1}}$  is the same as  $N_{\text{pulses},3}^{\text{C1}}$  for some energies because of the low half-life  $T_{1/2}^{+3n} = 52\text{s}$ . This, however, is at least partly due to the pulse number resolution of only 100 pulses. Thus, the numerical results confirm the theoretical considerations that for the gain of new neutron-rich nuclei of the  $i$ -species after several pulses, the neutron capture contributions from the  $(i - 1)$ -species are most relevant, so that the maximal population of  $N_i$  can only be reached simultaneously or after that of  $N_{i-1}$ . Therefore, even though the half-life of the  $i$ -species of a nuclide might be low, as it is the case for the 3-species of Ra and Os, the pulse number required to reach the maximum, as well as the energy-dependence of the pulse numbers are still high if the  $(i - 1)$ -species is very long-lived.

As explained above, it takes a very long time to reach the maximal abundances  $N_2^{\text{C1}} - N_4^{\text{C1}}$  for Ra and Os. The pulse numbers for Os even exceed  $10^9$  pulses because the 2-species of Os has both the highest half-life and a relatively small transmutation cross section, so that more than 30 years would be necessary to reach the maximal populations of these nuclides with the considered neutron source, operating at  $f_{\text{rep}} = 1\text{ Hz}$ , at all energies, and for Ra more than 20 years would be necessary as well. This, therefore, is highly unrealistic experimentally. For the rest of the nuclides from set 1, the maximal abundances can be reached in under 95 days for all energies, and if one disregards Lu, which, because of its long  $T_{1/2}^{+1n}$ , also requires relatively high pulse number of almost up to  $9 \times 10^6$ , the abundances can even be reached in under a month. In case of Am, all maximal abundances can even be produced in under 8 hours. For the nuclides from set 2, the highest number of pulses is needed to reach the first saturation condition for Au, but the condition is still fulfilled in under two months. Finally, the other maximal abundances for the second set can be reached in less than 22 days.

Now that the pulse numbers needed to reach the maximal abundances have been discussed, we focus on the abundances  $N_i^{C1}$  themselves. These are significantly increased compared to the populations after both 1 pulse and  $10^4$  pulses. However, the scaling with  $N_{\text{pulses}}^i$  no longer applies once the first saturation condition is reached because of the large influence of the decay and the fact that, for example for Ra and Os, the approximation  $s\mu_i, s\eta_i \ll 1$  is no longer correct. Furthermore, some scaling factors compared to the one pulse results show a similar energy dependence as the pulse numbers, especially for  $N_2 - N_4$  for Os and Ra and for all populations of Lu, implying that the maximal abundances depend to a high degree on the nuclear transmutation cross sections of the longest-lived neutron-rich nuclides. This energy dependence is due to the energy dependence of the loss through nuclear transmutation, as well as the effect of the nuclear transmutation on the saturation condition.

In general, the nuclides for which the pulse numbers required to reach the saturation condition are high oftentimes have high maximal populations as well, especially for the 1-species isotopes. However, this is not always the case, especially for abundances of short-lived nuclides, for which the reason why many pulses are needed to reach the saturation condition is that a  $j$ -species with  $j < 1$  has a low half-life, or for nuclides for which the abundances for 1 pulse are low already due to low neutron capture cross sections. For Lu, for example, the  $N_3$  and  $N_4$  populations are higher than those for Ra for low energies even though requiring several orders of magnitude less pulses because of the extremely high  $T_{1/2}^{+2n}$  and the relatively low  $T_{1/2}^{+3n}$  and  $T_{1/2}^{+4n}$  for Ra, as well as the low number of seed nuclides for this nuclide. Furthermore, the Re nuclides perform quite good despite their relatively low pulse number needed for achieving the maximal population, with abundances greater than those for As in case of  $N_2^{C1}$  for all energies,  $N_3^{C1}$  for some energies between a few hundred keV and a few MeV and  $N_4^{C1}$  for most energies except very high and very low ones. In case of  $N_2^{C1}$ , the abundance of Re is even higher than that of Lu for all energies. Therefore, the Re-isotopes, which are important for both the r- and the s-process, could be studied well with this neutron source. Moreover, the abundance of Au is always among the highest. Es, however, has one of the lowest abundances for all neutron-enriched species even though requiring one of the highest numbers of pulses of the second set of nuclides for  $N_2^{C1}$  and  $N_3^{C1}$ , which is due to its low neutron capture cross sections and its low lifetimes.

The maximal abundances  $N_1^{C1}$  of the considered nuclides can, in the case of Lu, exceed  $10^{14}$ , making improvements of the abundances of up to 2 orders of magnitude possible compared to those after  $10^4$  pulses. The improvements compared to  $10^4$  nuclides are even larger for isotopes enriched by more than one neutron. If one were to wait more than 30 years for the production of the maximal Os population  $N_2^{C1}$ , it would be possible to have more than  $10^{12}$  nuclides

## 6 Numerical Results

at once available for experiments. Furthermore, the maximal Ra population, with Ra having one of the lowest populations of those for the first nuclide set after 1 pulse, also exceeds  $10^{11}$  2-species nuclei for the saturation condition of  $N_2$ . Moreover, Re, Lu, As, Au and Tm all also have  $N_2^{C1}$  values greater than  $10^{10}$ . When it comes to the 3-species, all seed nuclides from set 1 have maximal abundances greater than  $10^3$  nuclides, and those from set 2 all reach maximal abundances of at least 92. Au, Lu and Os can even reach  $N_3^{C1}$  values greater than  $10^6$ , and for all nuclides but Es, Ac, Ir, and Am, abundances higher than  $10^4$  can be achieved. Furthermore, the abundance of  $^{258}\text{Es}$  is supposed to be over 100 nuclei high, so that this nuclide, which has never before been discovered in the laboratory [1–3], could be produced in quite a large number, therefore making it available for studying.

The probably most important observation is, however, that when simulating the neutron enrichment up to the maximal  $N_i$  values, it is very probable to observe nuclides enriched by more than 4 neutrons. For Au, Os, Lu, Ra, As and Re, abundances  $N_4^{C1}$  are possible. For Au and Os, even more than 10 nuclides of this species are present in our simulation for low energies of up to about 100 keV. For Ra, these nuclides even have a half-time of more than 2 hours, for Os  $T_{1/2}^{+4n} = 35$  min, and for Au one of 26 minutes, therefore making experiments with these nuclides possible. The half-lives of the other produced 4-species with observable maximal abundances lie between 6 and 10 minutes. Though the maximal abundances of the other nuclides do not exceed 1 according to our calculations, the total abundance of those is still higher than 1 after all pulses applied for this simulation except for  $^{259}\text{Es}$ , so that for these nuclides, the observation of neutron capture cascades with up to 4 neutrons could still be observed.

We now turn to the case of the first neutron source with the repetition rate of  $f_{\text{rep}} = 10$  Hz. Up to  $6 \times 10^9$  pulses are calculated to reach the saturation for all isotopes. Furthermore, we only save the abundances after every 1000 pulses, so that there is an uncertainty of 1000 pulses for the saturation condition 1 and its maximal abundances. For the latter, this only leads to relative deviations on the order of up to  $10^{-5}$  from the determined maximal population, however. The results for the maximally reached abundances and the pulse numbers required to reach them are shown in Fig. 6.8 for the first set of nuclides and in Fig. 6.9 for the second set.

When analyzing the pulse numbers, one can see that they show even more variation with energy than for 1 Hz because the loss of nuclei due to the decay of a population is lower as the delay time amounts to only 0.1 s, so that more pulses are needed to reach the saturation and the transmutation cross sections have a higher influence on both the maximal abundances and the pulse numbers when they are reached. Consequently, even the Am pulse numbers show quite strong energy dependence for 10 Hz.

## 6.1 Numerical Results for Neutron Source 1

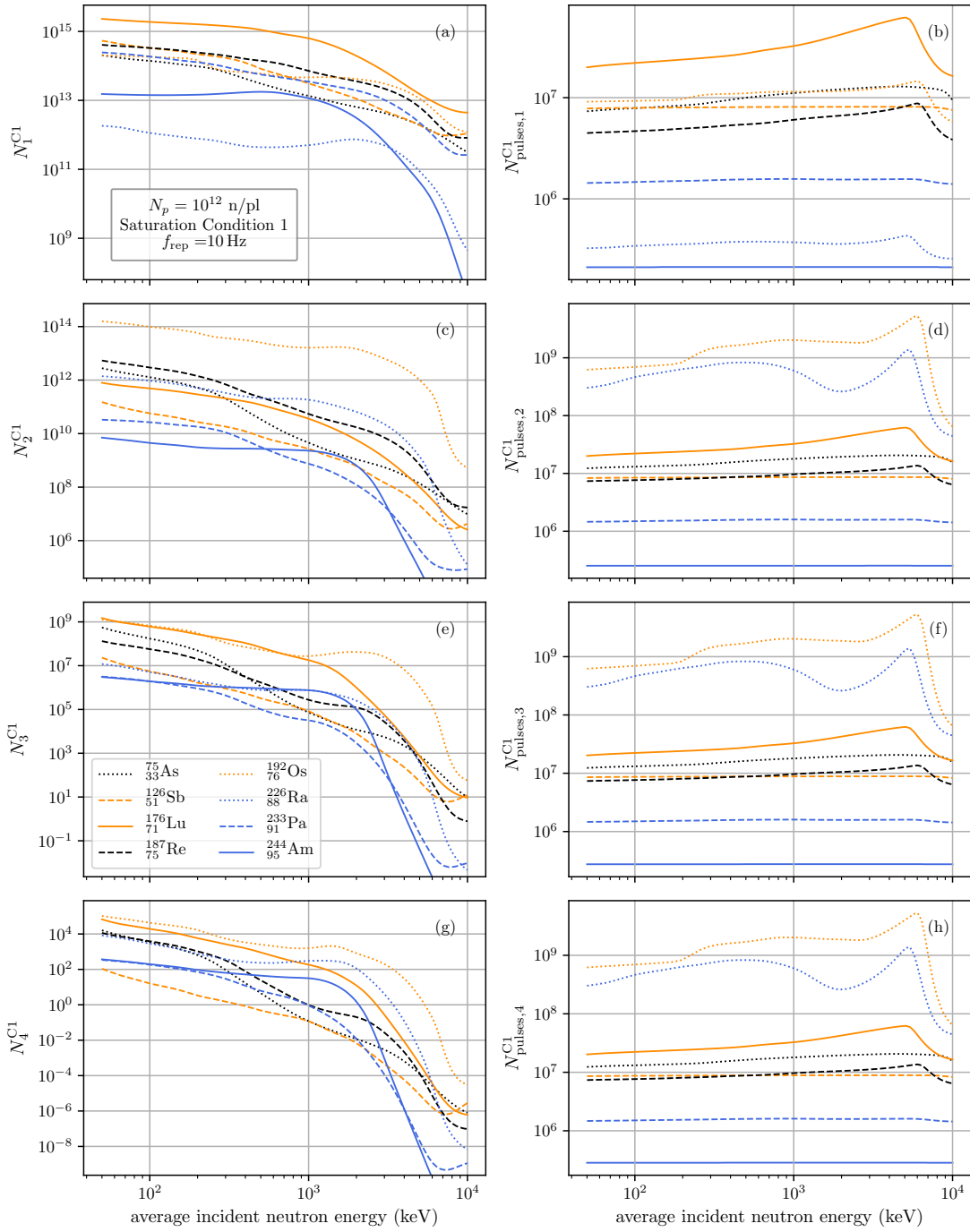


Figure 6.8: Maximally reached abundances  $N_i^{C1}$ ,  $i \in \{1, 2, 3, 4\}$  of neutron-enriched isotopes for the first set of nuclides as well as the numbers of pulses  $N_{pulses,i}^{C1}$ ,  $i \in \{1, 2, 3, 4\}$  it takes to reach them with a neutron source with  $10^{12}$  neutrons per pulse that delivers pulses with a repetition rate of 10 Hz.

## 6 Numerical Results

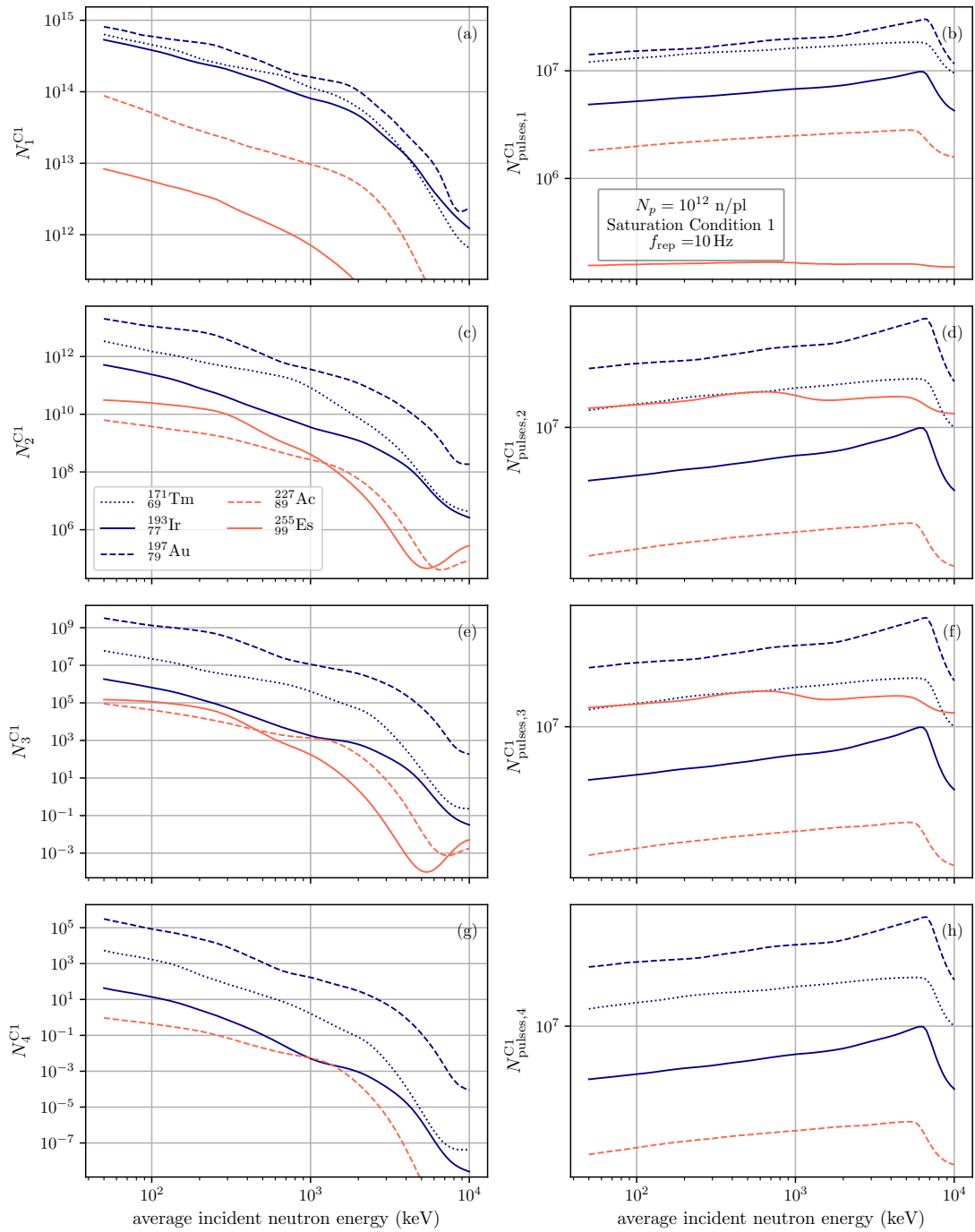


Figure 6.9: Maximally reached abundances  $N_i^{C1}$ ,  $i \in \{1, 2, 3, 4\}$  of neutron-enriched isotopes for the second set of nuclides as well as pulse numbers  $N_{\text{pulses},i}^{C1}$ ,  $i \in \{1, 2, 3, 4\}$  it takes to reach them with a neutron source with  $10^{12}$  neutrons per pulse that delivers pulses with a repetition rate of 10 Hz. Because  ${}^{259}_{99}\text{Es}$  has no half-life,  $N_4^{C1}$  and  $N_{\text{pulses},4}^{C1}$  for this nuclide are not shown in subplots g) and h), respectively.

For the 2-species isotopes of Ra and Os, the transmutation even dominates over the radioactive decay. Therefore, the pulse numbers required for reaching the saturation condition for the 2- to 4-species isotopes of these nuclides even vary with the energy by up to almost 2 orders of magnitude in the case of Os. Furthermore, our results show that the numbers of pulses needed to fulfill the first saturation condition are up to 10 times as high than those for 1 Hz for the considered nuclides, indicating a scaling of the pulse numbers of up to  $f_{\text{rep}}$ . This increase in the pulse number  $N_{\text{pulses},i}^{\text{C1}}$  compared to that for 1 Hz is especially high for nuclei for which the seed nuclides have low half-lives, such as Am and Pa, and for which the transmutation cross sections are additionally especially low, like for Sb. For these three nuclides, the enhancement factor for 10 Hz is greater than 9 for all energies, while for all populations of Lu as well as for  $N_{\text{pulses},2}^{\text{C1}}$ - $N_{\text{pulses},4}^{\text{C1}}$  of Ra and Os, the scaling factor is as low as 4.82, 1.08 and 1.13, respectively. These lowest values are reached for very high energies, because the scaling factor is energy-dependent and generally increases with lower transmutation cross section and, therefore, more influence of decay on  $N_{\text{pulses},i}^{\text{C1}}$ . This can be seen, for example when regarding the pulse numbers  $N_{\text{pulses},2}^{\text{C1}}$  for Ra, which are almost identical for 10 MeV to  $N_{\text{pulses},2}^{\text{C1}}$  for a repetition rate of 1 Hz, with a scaling factor of only 1.08 as the contribution of neutron-induced nuclear transmutation to the loss of nuclides dominates for these energies for both 1 Hz and 10 Hz, while for a few MeV, where  $\sigma_{\text{tr}}$  is lowest and decay dominates species-loss for 1 Hz, the pulse number is over 4.6 times as high for 10 Hz than for 1 Hz. Therefore, the pulse numbers vary most for different repetition rates for nuclides with low seed nuclide half-lives and least for isotopes for which the pulse number is highly influenced by the transmutation of a long-lived neutron-rich isotope. However, for nuclides for which neither of these conditions applies, the values of the scaling factors cannot be so simply determined from considerations of single half-lives, suggesting that the saturation condition for these nuclides is influenced by multiple effects and also higher-order terms. Therefore, future investigations of the saturation conditions for such nuclides with more elaborate theoretical approaches are of great interest.

That the pulse numbers of most nuclides are not exactly 10 times higher than for 1 Hz and, therefore, the scaling of the pulse numbers is generally weaker than  $f_{\text{rep}}$ , especially for isotopes which either have very long half-lives or are produced by neutron capture cascades in which a neutron-rich isotope with long half-life is encountered, means that it takes less time for the maximal abundances to be reached with neutron source 1 operating at 10 Hz than at 1 Hz. To reach the maximal abundances of Lu, for example, it does not take longer than 72 days for all energies, and the longest times to reach the maximal abundances of Ra and Os decrease to under 4.4 and under 16.7 years, respectively. The other nuclides from set 1 reach the maximal abundances even in under 24 days. For Au,  $N_i^{\text{C1}}$  is reached in under 48 days, and for the rest of the nuclides of set 1, even hardly more than 3 weeks are required.

## 6 Numerical Results

In case of the abundances  $N_i^{C1}$ , it is shown that the maximal populations reached with  $f_{\text{rep}} = 10$  Hz increase compared to  $f_{\text{rep}} = 1$  Hz by a factor of up to  $10^i$ , indicating a scaling with up to  $f_{\text{rep}}^i$ . Just like in case of the pulses, the scaling factors are lowest for nuclides for which the saturation condition is heavily influenced by the transmutational loss of a neutron-rich nuclide instead of radioactive decay. There is an energy dependence for this scaling as well, making the factors higher for lower values of the transmutation cross sections. For all nuclides except Es, Lu, Ra and Os,  $N_i^{C1}$  increases by more than a factor of  $9 \times 10^{i-1}$  for all populations, while for Es, Lu, Ra and Os, which have neutron-rich nuclides with the four lowest half-lives of all regarded neutron-enriched nuclei, the factor goes down to  $6.87 \times 10^{i-1}$ ,  $6.79 \times 10^{i-1}$ ,  $1.08 \times 10^{i-1}$  and  $1.08 \times 10^{i-1}$ , respectively, after the neutron capture cascades for these isotopes encounter nuclides with relatively long half-lives and, thus, high influence of nuclear transmutation compared to decay on the saturation condition. Still, the scaling of the populations with  $f_{\text{rep}}^i$  applies generally better than that of the pulse numbers with  $f_{\text{rep}}$ .

Because of the increase in the abundances, over  $10^{15}$   $N_1$ -nuclides can be reached with  $f_{\text{rep}} = 10$  Hz for Lu, and apart from Am, Ra, Ac and Es, all other  $N_1$ -populations exceed  $10^{14}$  as well for low energies, which is only possible with Lu for  $f_{\text{rep}} = 1$  Hz. Because of the approximate scaling being non-linear in  $i$ , the populations increase more the more neutron-rich the nuclides are. In case of the 2-species, Os reaches a population greater than  $10^{14}$ , therefore exceeding the maximal  $N_1^{C1}$  abundances of Am, Ra, Ac and Es. Furthermore, apart from those for Ac and Am, all populations  $N_2^{C1}$  exceed  $10^{10}$  nuclides, with the populations of Ac and Am still over  $10^9$  for energies up to about 1 MeV. Moreover, it is notable that because of the relatively low increase that both Ra and Os experience for populations of the  $i$ -species with  $i > 1$  compared to 1 Hz due to their long  $T_{1/2}^{+2n}$  and, therefore, low influence of decay, the abundances of these nuclides are relatively low compared to those of the other seed nuclides for  $f_{\text{rep}} = 10$  Hz when comparing the curves to those for 1 Hz. For example,  $N_2^{C1}$  of both Re and As exceed the corresponding Ra population, and while Os has the largest population for all  $i$  in case of  $f_{\text{rep}} = 1$  Hz,  $N_3^{C1}$  of Lu and Au are higher than that of Os for some energies for  $f_{\text{rep}} = 10$  Hz. The maximal populations  $N_3^{C1}$  for these three nuclides exceed  $10^9$ , and  $f_{\text{rep}} = 10$  Hz allows to produce more than  $10^6$  nuclides for all seeds of the first set, as well as Au, Ir and Tm. For Es and Ac, the maximal abundances are higher than  $10^5$  and  $9 \times 10^4$  nuclides of the 3-species, respectively, for low energies. Furthermore, with this repetition rate, it is possible for the first time for the population  $N_3^{C1}$  to exceed 1 nucleus of the 3-species at all considered energies, as the simulation indicates this to happen for Os, As, Sb, Lu, Re and Au.

Lastly, the results suggest that with a repetition rate of  $f_{\text{rep}} = 10$  Hz, it is possible to achieve maximal populations of more than one nucleus of the 4-species isotope for all of the regarded nuclides except Es, for which the 4-species has a negligible lifetime anyway, and Ac. With this

repetition rate, it is even possible for over  $10^5$  such nuclides to exist at one time for Au and Os. For all nuclides of the first set as well as Au and Tm,  $N_4^{C1}$  moreover exceeds 100 nuclides, and with Ir, at least up to 42 nuclides are present when saturation condition 1 occurs. Therefore, over 100 nuclei of the 4-species isotope of Am,  $^{248}\text{Am}$ , which has never been produced in a laboratory before [1–3], show the possibility to be present at once with the this neutron source operating at 10 Hz.

Though the populations  $N_4^{C1}$  are smaller than 1 for Es and Ac, the total number of produced nuclei after  $6 \times 10^9$  applied pulses do show values higher than 1 for both of these nuclides. Therefore, the observation of neutron capture cascades of up to 4 neutrons is possible for all regarded seed nuclides, even for  $^{259}\text{Es}$ , though we assume this nuclide to decay instantly after production, so that it does not remain after the interaction with the neutron pulse. Therefore, another nuclide that has never been produced in the laboratory before [1–3] could be accessible through neutron capture experiments with laser-driven neutron sources.

In conclusion, reaching the maximal abundances does not only generally take less time with a higher repetition rate because of the relatively great deviations from the scaling of the pulse numbers with  $f_{\text{rep}}$ , but because of the scaling with  $f_{\text{rep}}^i$ , which applies quite well, the populations produced with the higher repetition rate are also far higher, especially for very neutron-rich nuclides. Therefore, the production of the maximal abundances of neutron-rich nuclides is more efficient for higher repetition rates than for lower ones.

Finally, we turn to the analysis of the first saturation condition for the first neutron source operating at the repetition rate  $f_{\text{rep}} = 1/60$  Hz, i.e. 1 pulse per minute. For this source,  $3 \times 10^8$  pulses are calculated to reach the maximal populations of all nuclides. Moreover, we save the populations for every pulse in this case. The maximal abundances  $N_i^{C1}$  and the pulse numbers  $N_{\text{pulses},i}^{C1}$  needed to reach them are shown in Figs. 6.10 and 6.11 for the first and second set of nuclides, respectively. Because, only Tm, Os, Lu, As, and Ra show potential of producing nuclides only enriched by 3 neutrons and the maximal 4-species abundances are smaller than 1 for all nuclides, the populations  $N_4^{C1}$  and the corresponding pulse numbers are not shown in this case.

As shown in the figures, the pulse numbers required to reach the saturation condition decrease compared to the pulse numbers needed for the repetition rates of 1 Hz and 10 Hz. They are up to 60 times lower than for 1 Hz, with especially high decreases for the nuclides Am, Pa, Sb and Es, for which the pulse number are at least 59 times smaller than for 1 Hz at all energies. For all populations of Lu and  $N_{\text{pulses},2}^{C1}$ - $N_{\text{pulses},4}^{C1}$  of Os and Ra and, therefore, the nuclides with both long-living seed nuclides and the longest half-lives of neutron enriched nuclides, however, the pulse numbers are a factor of down to only 30, 4.7 and 4 times smaller

## 6 Numerical Results

than for 1 Hz, with the lowest scaling factors, again, for very high energies. Furthermore, generally, the pulse numbers scaling factors are energy dependent with them decreasing more at energies for which the transmutation cross section is low.

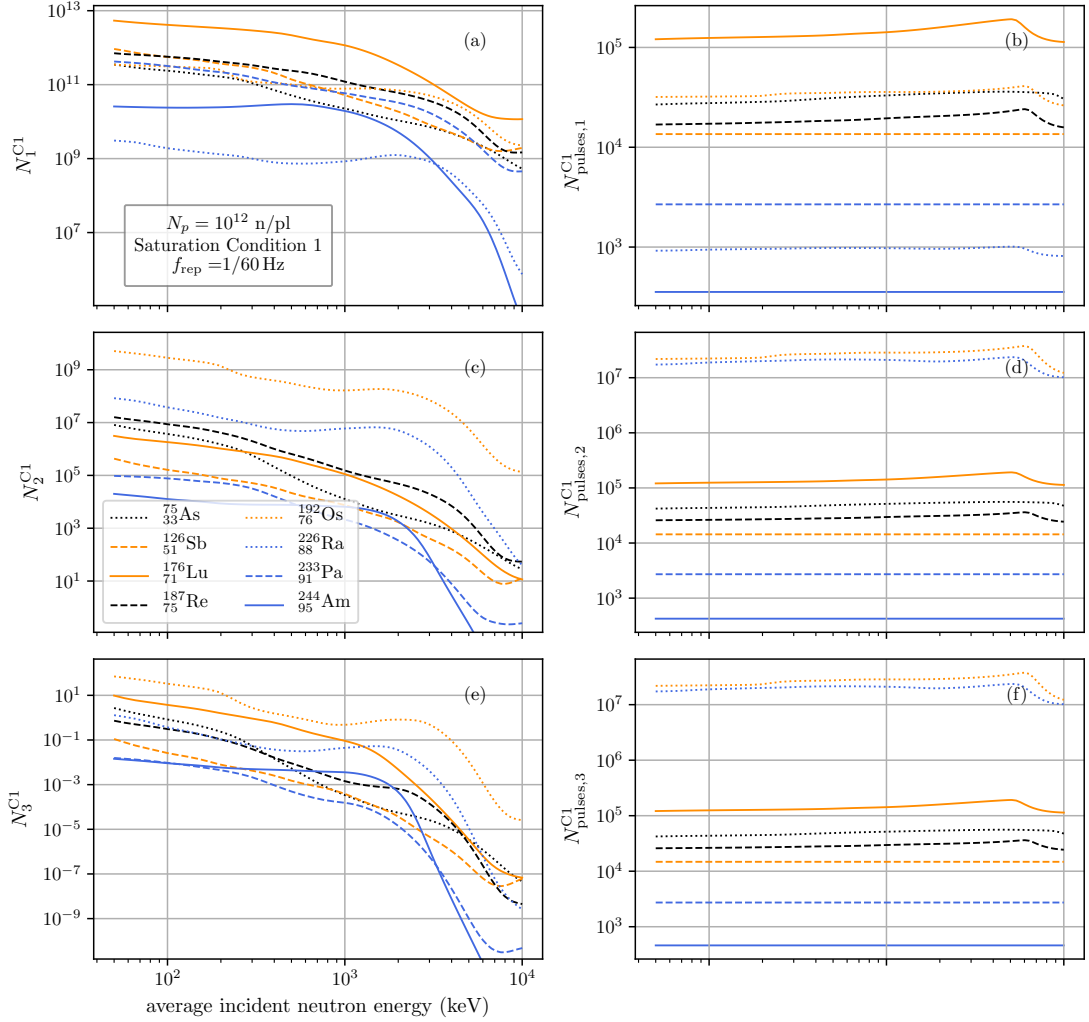


Figure 6.10: Maximally reached abundances  $N_i^{C1}$ ,  $i \in \{1, 2, 3\}$  of neutron-enriched isotopes for the first set of nuclides as well as pulse numbers  $N_{\text{pulses},i}^{C1}$ ,  $i \in \{1, 2, 3\}$  it takes to reach them with a neutron source with  $10^{12}$  neutrons per pulse that delivers pulses with a repetition rate of 1 pulse per minute. Contrary to the other repetition rates,  $N_4^{C1}$  is not shown here because the maximal population of the 3-species is already hardly above  $10^0$ .

Therefore, reaching the maximal abundances takes generally more time with this lower repetition rates than with 1 Hz or 1/60 Hz, with the times only comparable for Am, Pa, Sb and Es as their seed nuclides have low half-lives. The maximal times it takes to reach the saturation condition 1 are shown in Fig. 6.12 for all repetition rates.

## 6.1 Numerical Results for Neutron Source 1

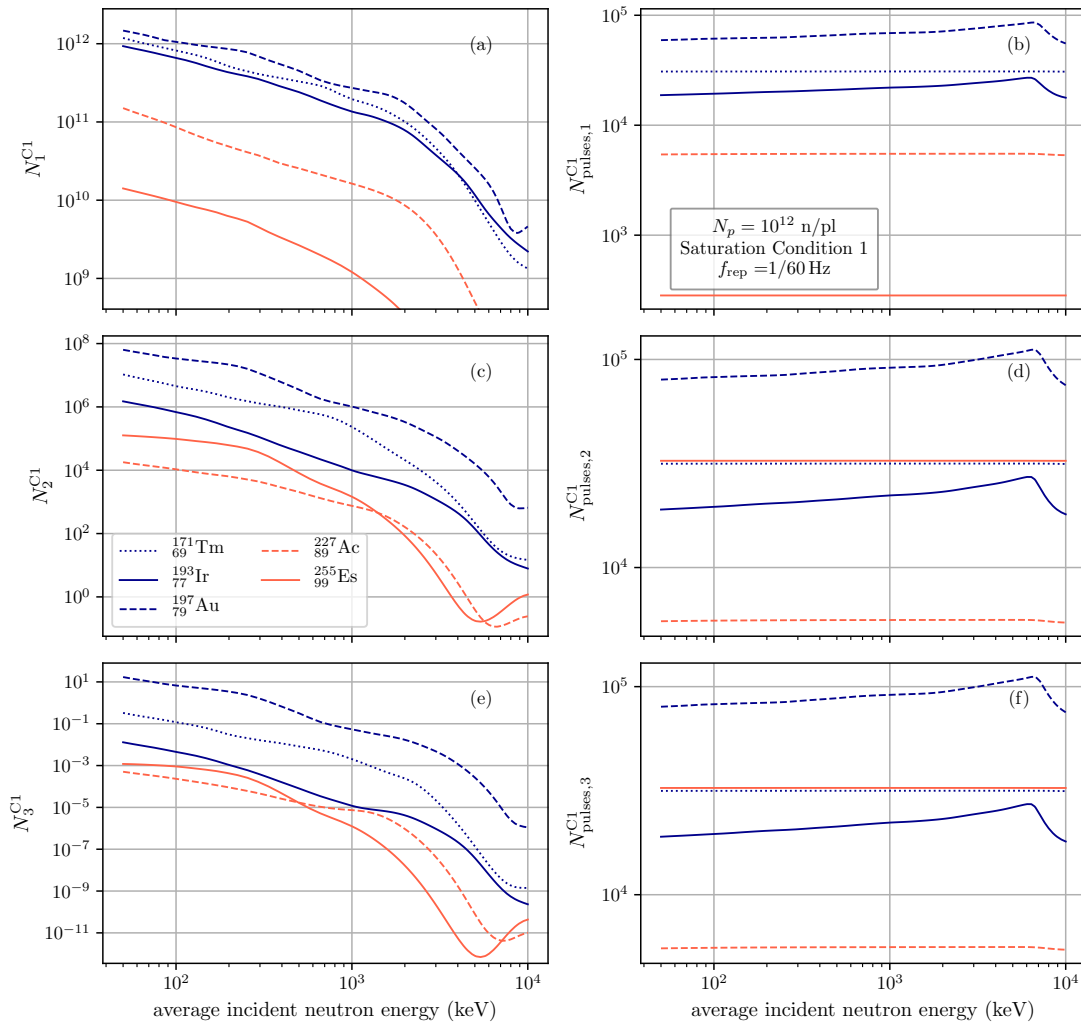


Figure 6.11: Maximally reached abundances  $N_i^{C1}$ ,  $i \in \{1, 2, 3, 4\}$  of neutron-enriched isotopes for the second set of nuclides as well as pulse numbers  $N_{pulses,i}^{C1}$ ,  $i \in \{1, 2, 3, 4\}$  it takes to reach them with a neutron source with  $10^{12}$  neutrons per pulse that delivers pulses with a repetition rate of 1 pulse per minute. Contrary to the other repetition rates,  $N_4^{C1}$  is not shown here because the maximal population of the 3-species is already hardly above  $10^0$ .

Furthermore, the energy dependence of the pulse numbers is weaker for  $f_{rep} = 1/60$  Hz due to the lower influence of nuclear transmutation. This is especially visible for the pulse numbers  $N_{pulses,2}^{C1} - N_{pulses,4}^{C1}$  of Ra, which hardly show the distinct peak for a few keV that is the signature of the influence of  $\sigma_{tr,2}$  because, in case of the delay time of 60 s, the species-loss of the 2-species isotope of Ra is dominated by radioactive decay, the loss due to which is greater by more than one order of magnitude for this repetition rate.

## 6 Numerical Results

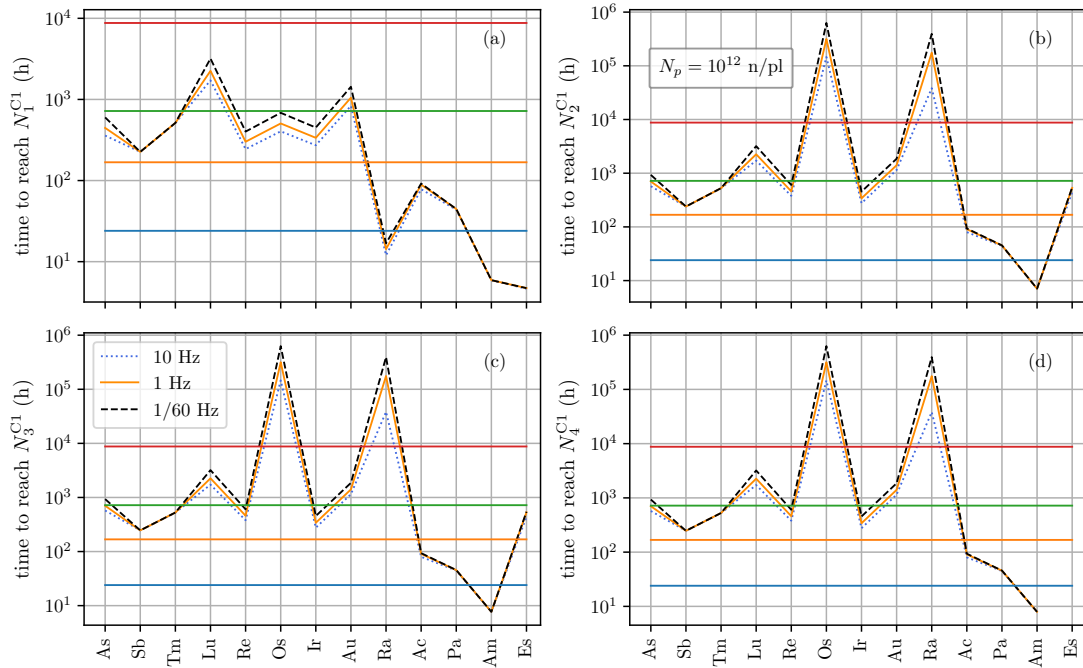


Figure 6.12: Maximal time in hours it takes to reach the first saturation condition for each nuclide with the first neutron source and the three different repetition rates. For comparison, lines are shown indicating one day (blue), one week (orange), 1 month (red) and one year (green).

In the case of the abundances, it can be seen that they decrease compared to 1 Hz by a factor of up to  $60^i$ . Again, the decrease of the abundances for the lower repetition rates is generally lowest for Ra, Os, Es, and Lu because of their low half-lives and, therefore, high influence of the transmutation cross section on the species-loss for 1 Hz. However, the  $N_3^{C1}$  abundances also show low scaling factors  $N_3^{C1}(1 \text{ Hz})/N_3^{C1}(1/60 \text{ Hz})$  for Re, Ac and Ir, where Re even shows a lower scaling factor than Lu for the 3-species, and that for Ir is lower than that for Es, while for the comparison between 1 Hz and 10 Hz, all of these nuclides and nuclides with relatively low half-lives in general have rather shown high scaling factors. The comparably low scaling factors might be partly due to the fact that the abundances of every 100th pulse are saved for a repetition rate of 1 Hz compared to every pulse being saved for 1/60 Hz, so that, especially for Ir, the time for the 100 pulses equals almost twice the decay time, so that the populations could significantly vary after reaching the maximum for these nuclides. However, as comparisons of the maximal abundances of these isotopes for a repetition rate of 1 Hz with the populations with 100 pulses less and more applied show, which exhibit low relative deviations of not more than  $10^{-4}$ , this is most probably not the only reason. As already investigated for the scaling of the pulses between 1 Hz and 10 Hz, one reason for this might be that the saturation condition of these nuclides might be subject to influences of multiple effects and higher-order terms.

Therefore, further studies should be performed on the saturation condition. For this, firstly, the abundances should be saved after every pulse, and calculations using more elaborate models as in Refs. [145] and [146] including non-dominant processes, which could still influence the sensitive saturation conditions, could paint a more realistic picture on the saturation.

The maximal numbers of nuclei of the 1-species isotopes are higher than  $10^{11}$  at low energies for all seed nuclides but Ra, Es, and Am, for which only abundances greater than  $10^{10}$ ,  $10^{10}$ , and  $10^9$  can be reached, respectively, due to the low half-lives  $T_{1/2}$  and  $T_{1/2}^{+1n}$  and the low abundance of seed nuclei, in case of Ra. Thus, the  $N_1^{C1}$  values are even lower than the  $N_2^{C1}$  populations reached with 1 Hz in most cases. When it comes to the population  $N_2^{C1}$ , over  $10^4$  nuclei of the 2-species isotopes can be reached for all seed nuclides, with abundances over  $10^9$  for Os. However, the simulated maximal abundance of  $N_2$  nuclides with a repetition rate of 1/60 Hz is not higher than 1 for Es, Ac, Pa and Am for high energies, so that with highly energetic neutrons, only nuclides enriched by at most 1 neutron can be studied for these seeds with this source. Lastly, it is only possible for Os, Au, Lu, As and Ra to produce nuclei of the 3-species isotope for low energies, and the population  $N_4^{C1}$  is lower than 1 for all nuclides and energies.

### 6.1.4 Saturation Condition 2

In this next section, the second saturation condition Eq. (5.35), is investigated, which determines the pulse number  $s$  from which on the difference of the abundances of neutron-enriched nuclides after pulse  $s$  and  $s - 1$  is lower than the abundance gained for one pulse.

At first, the condition is analyzed for  $f_{\text{rep}} = 1$  Hz. For the analysis of the second saturation condition, the same data is used as for the first saturation condition, so that the populations are only available for every 100 pulses. Therefore, the saturation condition cannot be simply determined using Eq. (5.35), but this formula has to be adapted according to

$$(N_i(s) - N_i(s - 100))/100 < N_i(1 \text{ pl}) \quad (6.2)$$

This, however, brings some uncertainties with it, because it could be that, even though condition (5.35) is fulfilled in the regarded interval  $[s - 100, s]$ , the average difference  $(N_i(s) - N_i(s - 100))/100$  is still lower than  $N_i(1 \text{ pl})$ , so that there is an error in the pulse number  $N_{\text{pulses},i}^{C2}$  larger than 100 pulses. The only case in which the saturation is calculated explicitly

## 6 Numerical Results

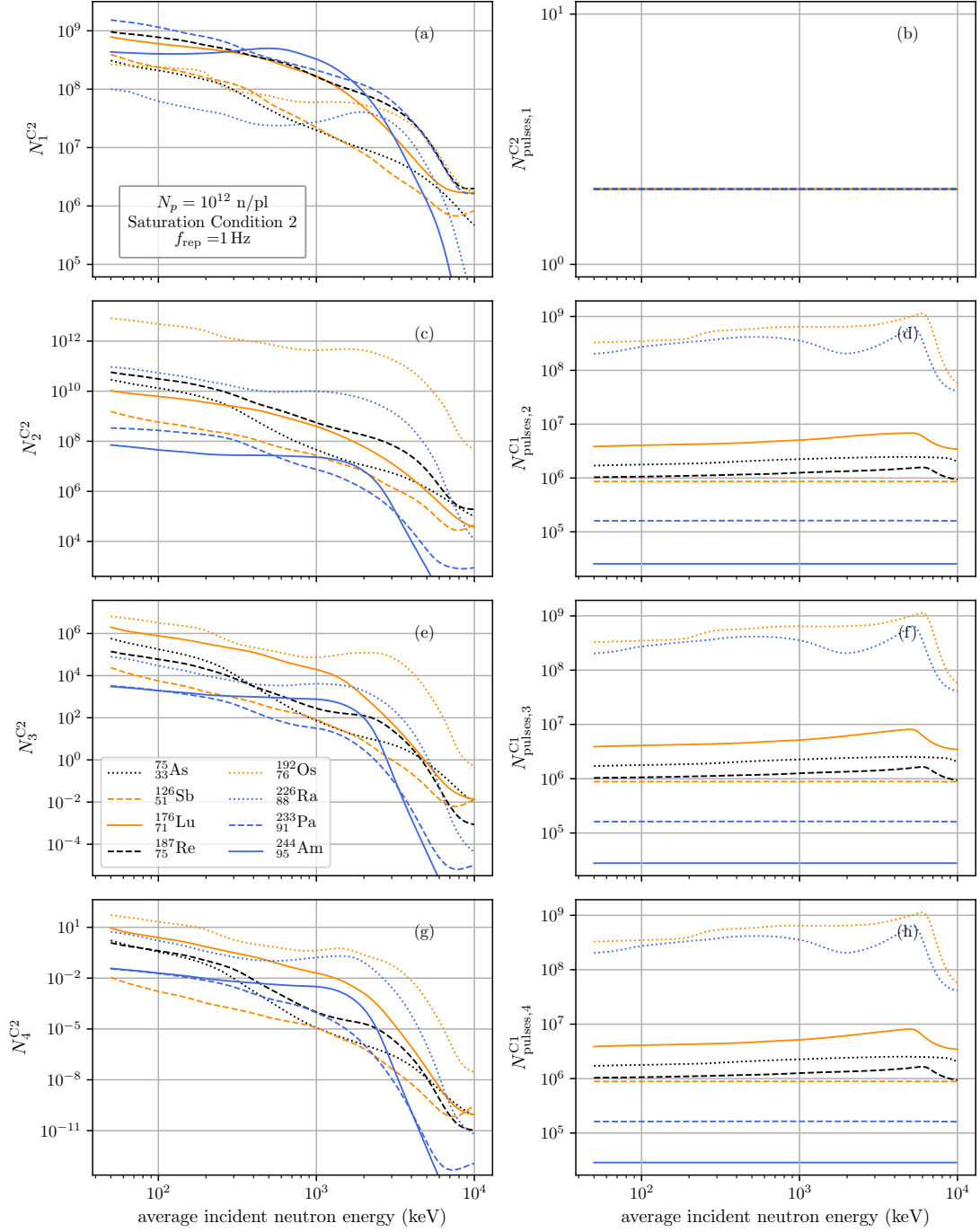


Figure 6.13: Numbers of pulses  $N_{pulses,i}^{C2}$ ,  $i \in \{1, 2, 3, 4\}$  needed to fulfill the second saturation condition for the abundances of populations  $N_i$ ,  $i \in \{1, 2, 3, 4\}$  of neutron-enriched isotopes for the first set of nuclides with a neutron source with  $10^{12}$  neutrons per pulse that delivers pulses with a repetition rate of 1 Hz as well as the abundances  $N_i^{C2}$ ,  $i \in \{1, 2, 3, 4\}$  at these pulse numbers.

## 6.1 Numerical Results for Neutron Source 1

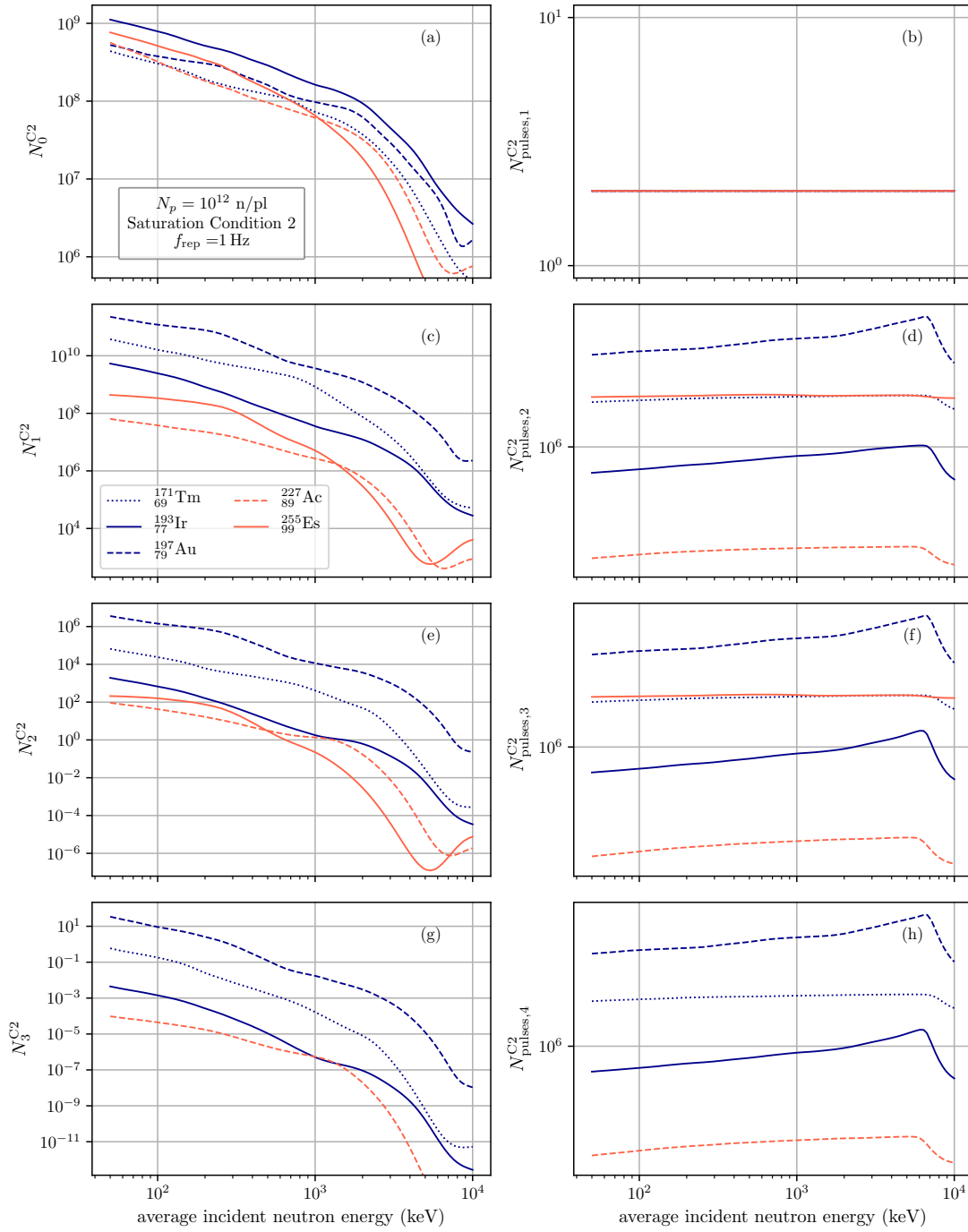


Figure 6.14: Numbers of pulses  $N_{\text{pulses},i}^{\text{C2}}$ ,  $i \in \{1, 2, 3, 4\}$  needed to fulfill the second saturation condition for the abundances of populations  $N_i$ ,  $i \in \{1, 2, 3, 4\}$  of neutron-enriched isotopes for the second set of nuclides with a neutron source with  $10^{12}$  neutrons per pulse that delivers pulses with a repetition rate of 1 Hz as well as the abundances  $N_i^{\text{C2}}$ ,  $i \in \{1, 2, 3, 4\}$  at these pulse numbers. Because  ${}_{99}^{259}\text{Es}$  has no half-life,  $N_4^{\text{C2}}$  and  $N_{\text{pulses},4}^{\text{C2}}$  for this nuclide are not shown in subplots g) and h), respectively.

## 6 Numerical Results

via Eq.(5.35) is for  $N_1$ , for which the abundances are saved for every pulse of the first 100 pulses.

This is done because, as it is shown in Figs. 6.13 and 6.14, where the pulse numbers  $N_{\text{pulses},i}^{C2}$  to reach saturation condition 2 as well as the corresponding abundances  $N_i^{C2}$  are plotted,  $N_{\text{pulses},1}^{C2} = 2$  for all energies and nuclides. This makes sense because the abundance of seed nuclei decreases with every pulse due to either neutron-induced transmutation during the pulse or radioactive decay in the delay time between the pulses. Furthermore, the abundance  $N_1$  itself decreases during the time between the first and second pulse due to decay, so that in each case, the difference between  $N_1(2 \text{ pl})$  and  $N_1(1 \text{ pl})$  is lower than  $N_1(1 \text{ pl})$ .

For the populations  $N_i^{C2}$ ,  $i > 1$ , of isotopes enriched by more than one neutron, the argument is not that easy because, as can be seen, for example, in Eq. 5.30, nuclei of the  $i$ -species isotopes can be gained from neutron-enrichment of any  $j$ -species isotopes with  $j < i$ , not only the seed nuclei, with the neutron capture of exactly one neutron by a  $i - 1$ -species nuclide generally the most probable phenomenon. Therefore, the gain of  $i$ -species nuclei does not constantly decrease as it is the case for  $N_1$ , but it experiences a rise at first due to the growing populations  $N_j$ ,  $j < i$ , with the gain decreasing again at the latest once all populations  $N_j$ ,  $j < i$  have reached their maximum. For neutron source 1 operating at a repetition rate of  $f_{\text{rep}} = 1 \text{ Hz}$ , the number of nuclei of the  $i$ -species isotopes with  $i > 1$  gained in the second pulse are, therefore, higher than the number of nuclei lost of this species due to decay and transmutation and the population  $N_i(1 \text{ pl})$  added together. Thus, the second saturation condition is not already reached after the second pulse for all  $i$ -species isotopes with  $i > 1$ . Instead, the pulse numbers  $N_i^{C2}$ ,  $i > 1$ , needed to reach saturation condition 2 are all in the same order of magnitude as the pulse numbers required for saturation condition 1,  $N_i^{C1}$ ,  $i > 1$ , and when analyzing the gain and loss of nuclei of the  $i$ -species isotopes in leading order around the saturation conditions, it becomes apparent that  $N_i(1 \text{ pl})$  is several orders of magnitude smaller around these pulse numbers than both the gain and loss. Therefore, just like for the maximal abundance, the number of pulses it takes to reach the saturation condition 2 depends mostly on the difference of the gain and loss of neutron-rich nuclei of the  $i$ -species.

It is shown in Figs. 6.13 and 6.14 that the pulse numbers  $N_{\text{pulses},i}^{C2}$ ,  $i > 1$  have values around the same order of magnitude as  $N_i^{C1}$ ,  $i > 1$ . A thorough comparison with Figs. 6.6 and 6.7 shows, however, that, especially for  $N_{\text{pulses},2}^{C2}$ , the pulse numbers of some nuclides, especially Lu, Ir, Ac, Re and As, are lower than  $N_{\text{pulses},2}^{C1}$ , by factors of up to 1.18 in case of Lu, especially at energies where  $N_{\text{pulses},2}^{C1}$  is maximal. Consequently, the pulse numbers for the second saturation condition also show less energy dependence for these nuclides than for the first condition. For Lu, Ir and Ac, the saturation condition 2 for  $N_2$  is even reached before the maximal abundance of the 1-species isotopes. What these nuclides have in common is that they all have neither very

short-living 0- and 1-species isotopes nor too long half-lives of the 2-species isotopes  $T_{1/2}^{+2n}$ . If a nuclide has long half-lives  $T_{1/2}$  and  $T_{1/2}^{+1n}$ , the gain of new nuclei of the 2-species reaches its maximum only relatively late, with the gain only slowly changing around the maximum. If a nuclide has a low half-life of the 2-species, moreover, loss of nuclei of the 2-species isotope increases quickly, so that loss and gain are around the same order of magnitude long before the abundance has reached its maximum and often even before the nuclide gain is maximal. Therefore, both these features combined contribute to the difference  $N_2(s) - N_2(s - 1)$  being small quite early on and to it only decreasing slowly, so that for nuclides for which both of these conditions apply,  $N_2(s) - N_2(s - 1)$  can be lower than  $N_2(1 \text{ pl})$  several pulses before eventually decreasing to values lower than  $0^2$ . With the same logic, it can also be explained why the difference between the pulse numbers  $N_{\text{pulses},2}^{\text{C1}}$  and  $N_{\text{pulses},2}^{\text{C2}}$  is especially high for energies for which  $\sigma_{\text{tr}}$  is low, because for these energies, the gain of  $i$ -species nuclei reaches its maximum later and varies slower around this maximum, leading to even lower values of  $N_2(s) - N_2(s - 1)$ . Lastly, a factor influencing the pulse number difference between the two conditions, is the magnitude of  $N_2(1 \text{ pl})$ , which is among the highest for Lu, Ir and Re.

While for most nuclides, the pulse numbers for the first condition are greater than those for the second one, the 2-species isotopes of Sb and Am, which have the lowest lifetimes for the seed nuclides, require even 100 pulses more to reach the second saturation condition compared to the first one. This is due to the fact that saturation condition 1 can be formulated as

$$N_i(s + 100) - N_i(s) < 0 \quad (6.3)$$

so that if one were to assume  $N_2(1 \text{ pl})$  as 0, the second saturation condition would be reached 100 pulses after the maximum. Because of their low seed nuclide lifetimes, the gain of new nuclei of the 2-species isotopes decreases extremely quickly once the maximal gain is reached for these nuclides, so that the differences  $(N_i(s + 100) - N_i(s))/100$  never have a positive value below  $N_2(1 \text{ pl})$  and, therefore, Eq. (6.2) corresponds to the same condition as Eq. (6.3) with  $s \rightarrow s + 100$ .

For nuclides enriched by even more neutrons, the pulse numbers  $N_{\text{pulses},i}^{\text{C2}}$  amount to  $N_{\text{pulses},2}^{\text{C1}} + 100$  for most nuclides. For the 3-species isotopes, the only nuclide for which more than just a few hundred pulse numbers less are needed to reach the second saturation condition than the first one is Ir. Lastly, in case of the 4-species isotopes,  $N_{\text{pulses},4}^{\text{C2}} = N_{\text{pulses},4}^{\text{C1}} + 100$  applies even for all considered nuclides. Therefore, the energy dependence of the pulse numbers also gets more distinct with higher  $i$ . This could be explained by the fact that the populations of neutron-enriched isotopes are several orders of magnitude higher around the saturation

---

<sup>2</sup>This consideration also shows in general that especially for nuclides with low half-lives following such with long ones, the saturation conditions could be subject to the influence of higher-order terms.

## 6 Numerical Results

condition than the population after only one pulse. The difference between  $N_i(1 \text{ pl})$  and  $N_i^{\text{C2}}$  increases for populations of  $i$ -species isotopes with higher  $i$  because of the scaling of the populations in leading order with  $N_{\text{pulses}}^i$ , which, even though it is not fully applicable due to the high influence of decay, still applies in so far that the populations of isotopes enriched by  $i$  neutrons increase significantly more with the pulse number for higher  $i$  than for lower ones. For example, the saturation abundance  $N_4^{\text{C2}}$  is over 20 orders of magnitude higher than  $N_4(1 \text{ pl})$ . This, consequently could be the reason why also the difference  $N_4(s) - N_4(s - 1)$  decreases faster than for  $N_4(1 \text{ pl})$  to make a difference in the saturation condition.

We now turn to the analysis of the second saturation condition for a repetition rate of 10 Hz. The pulse numbers  $N_{\text{pulses},i}^{\text{C2}}$  and the abundances  $N_i^{\text{C2}}$  at which the saturation condition 2 is reached are shown in Figs. 6.15 and 6.16 for the two sets of nuclides. Because the abundances are only stored for every 1000 pulses in the data used for the determination of the second saturation condition, the condition has to be reformulated to

$$(N_i(s) - N_i(s - 1000))/1000 < N_i(1 \text{ pl}) \quad (6.4)$$

for a repetition rate of 10 Hz.

Like for  $f_{\text{rep}} = 1 \text{ Hz}$ , however, the  $N_1$  populations are saved after every pulse for the first 100 pulses, so that Figs. 6.15 and 6.16 show that for 10 Hz the second saturation for all 1-species isotopes is also reached already at the second pulse. For the pulse numbers  $N_{\text{pulses},i}^{\text{C2}}$ ,  $i > 1$  of the isotopes enriched by more than 1 neutron, the figures show that the pulse numbers are very close to the values  $N_{\text{pulses},i}^{\text{C1}}$  for the first saturation condition. In the case of the 2-species isotopes,  $N_{\text{pulses},i}^{\text{C1}}$  is only up to 1.007 times higher than  $N_{\text{pulses},i}^{\text{C2}}$  for Ir and Ac, and only up to 1.005 times higher for Lu. For even more neutron-rich isotopes of both the 3- and 4-species, the pulse numbers  $N_{\text{pulses},i}^{\text{C2}}$  for all nuclides are exactly 1000 pulses higher than  $N_{\text{pulses},i}^{\text{C1}}$ . Therefore, for this higher repetition rate,  $N_i(1 \text{ pl})$  has even less influence on the second saturation condition than for 1 Hz. This is due to the fact that because of the higher gain and the lower loss of nuclei of the  $i$ -species due to the lower delay time and, therefore the lower influence of decay, the populations after  $s$  and  $s - 1$  pulses vary highly, especially at the beginning, and, thus, the second saturation condition is only reached after a significantly higher pulse number and at significantly higher abundances than for 1 Hz. Because the abundances around the saturation condition are then up to  $10^i$  times as high as for 1 Hz, both the absolute loss and the gain of  $i$ -species nuclei, as well as the variations of these quantities with the pulse number are higher than for 1 Hz, even despite the relative loss of nuclides being smaller due to the shorter delay time. This is especially true for nuclei enriched by many neutrons. Thus,  $(N_i(s) - N_i(s - 1000))/1000$  does not reach positive values smaller than  $N_i(1 \text{ pl})$ , so that

### 6.1 Numerical Results for Neutron Source 1

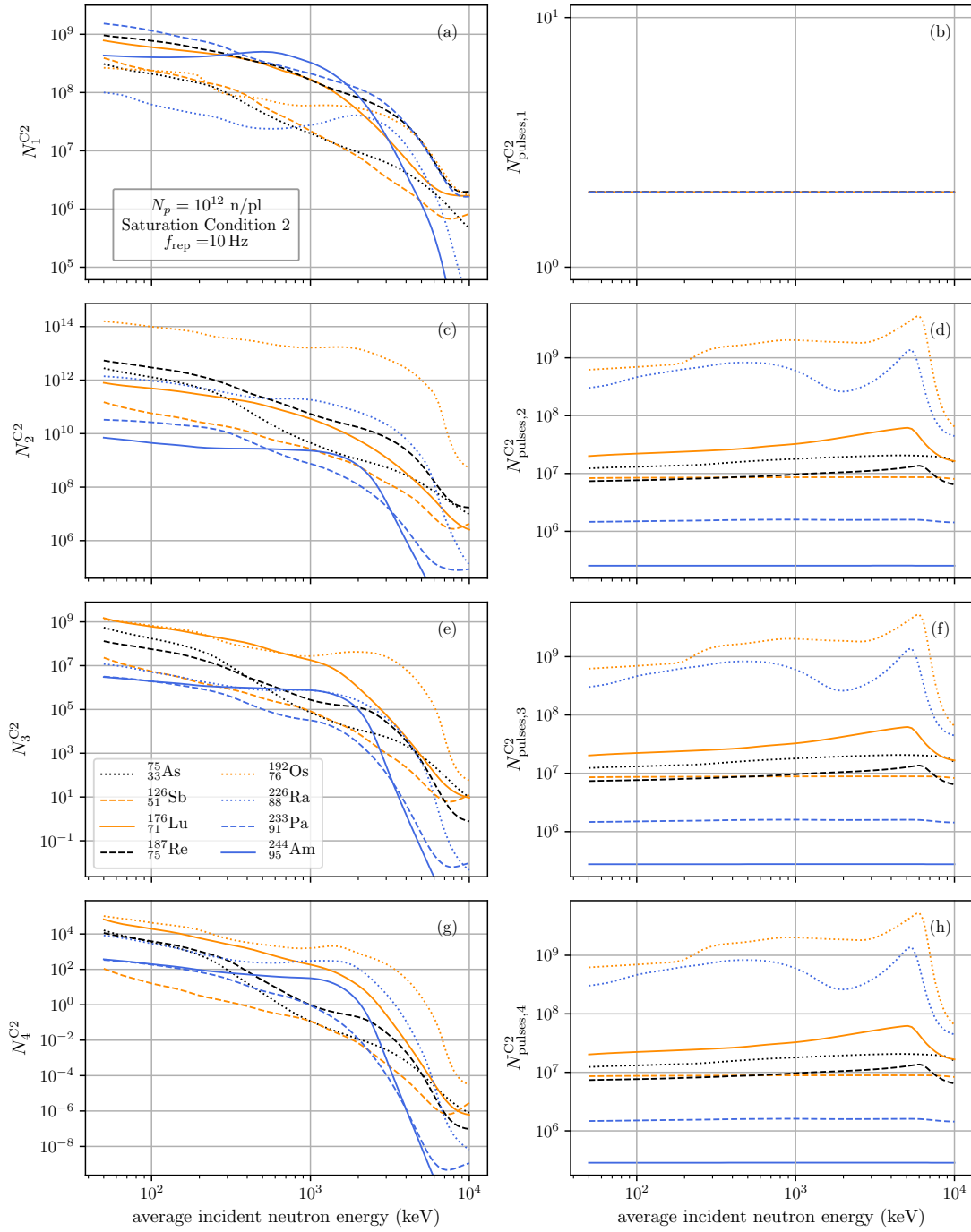


Figure 6.15: Numbers of pulses  $N_{pulses,i}^{C2}$ ,  $i \in \{1, 2, 3, 4\}$  needed to fulfill the second saturation condition for the abundances of populations  $N_i$ ,  $i \in \{1, 2, 3, 4\}$  of neutron-enriched isotopes for the first set of nuclides with a neutron source with  $10^{12}$  neutrons per pulse that delivers pulses with a repetition rate of 10 Hz as well as the abundances  $N_i^{C2}$ ,  $i \in \{1, 2, 3, 4\}$  at these pulse numbers.

## 6 Numerical Results

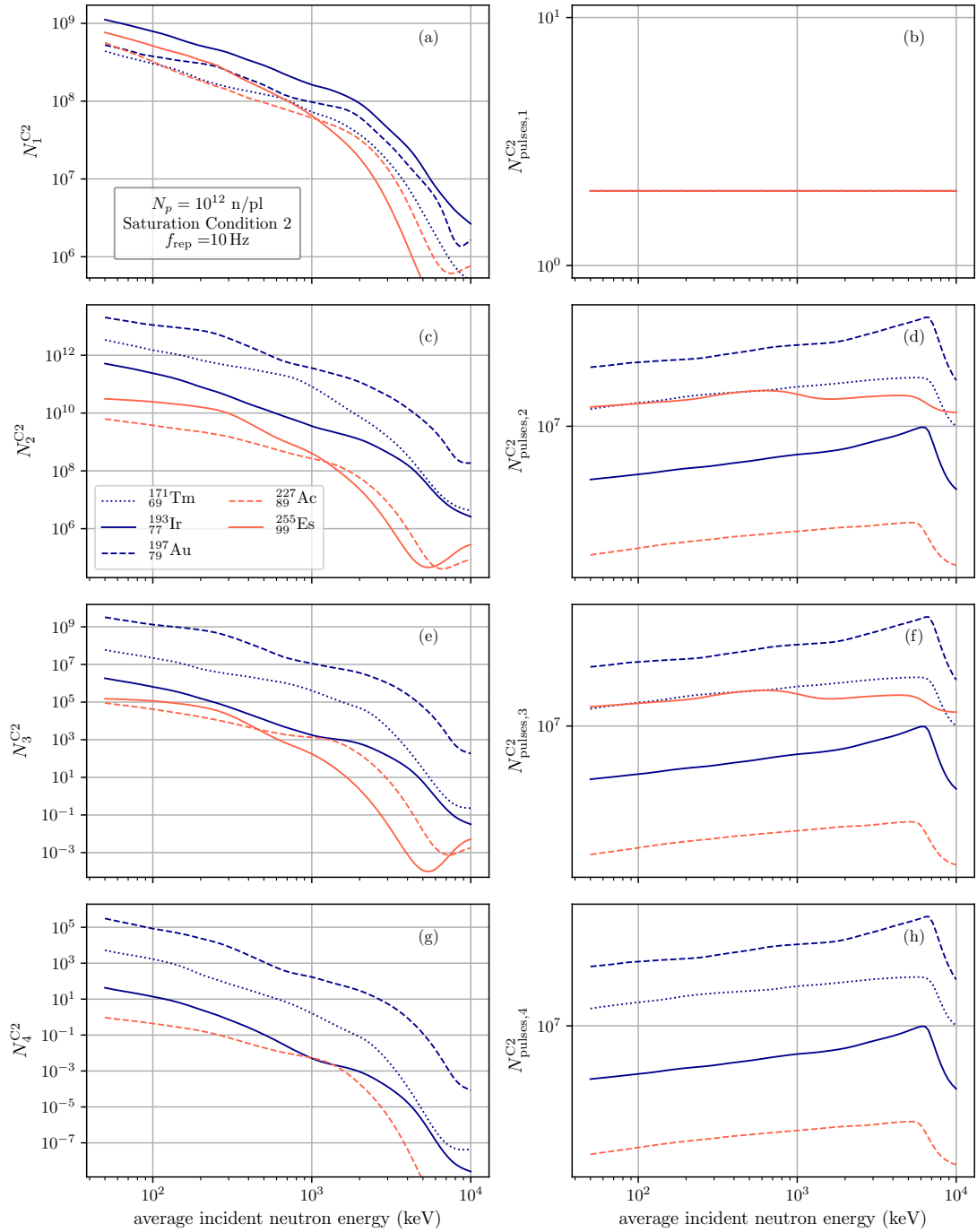


Figure 6.16: Numbers of pulses  $N_{\text{pulses},i}^{\text{C2}}$ ,  $i \in \{1, 2, 3, 4\}$  needed to fulfill the second saturation condition for the abundances of populations  $N_i$ ,  $i \in \{1, 2, 3, 4\}$  of neutron-enriched isotopes for the second set of nuclides with a neutron source with  $10^{12}$  neutrons per pulse that delivers pulses with a repetition rate of 10 Hz as well as the abundances  $N_i^{\text{C2}}$ ,  $i \in \{1, 2, 3, 4\}$  at these pulse numbers. Because  ${}^{259}_{99}\text{Es}$  has no half-life,  $N_4^{\text{C2}}$  and  $N_{\text{pulses},4}^{\text{C2}}$  for this nuclide are not shown in subplots g) and h), respectively.

the second saturation condition is reached directly after reaching the maximal population  $N_i^{C1}$  for the 3- and 4-species. For 10 Hz, the second saturation condition for the  $i$ -species is also only reached after the first saturation condition of the  $i - 1$ -species.

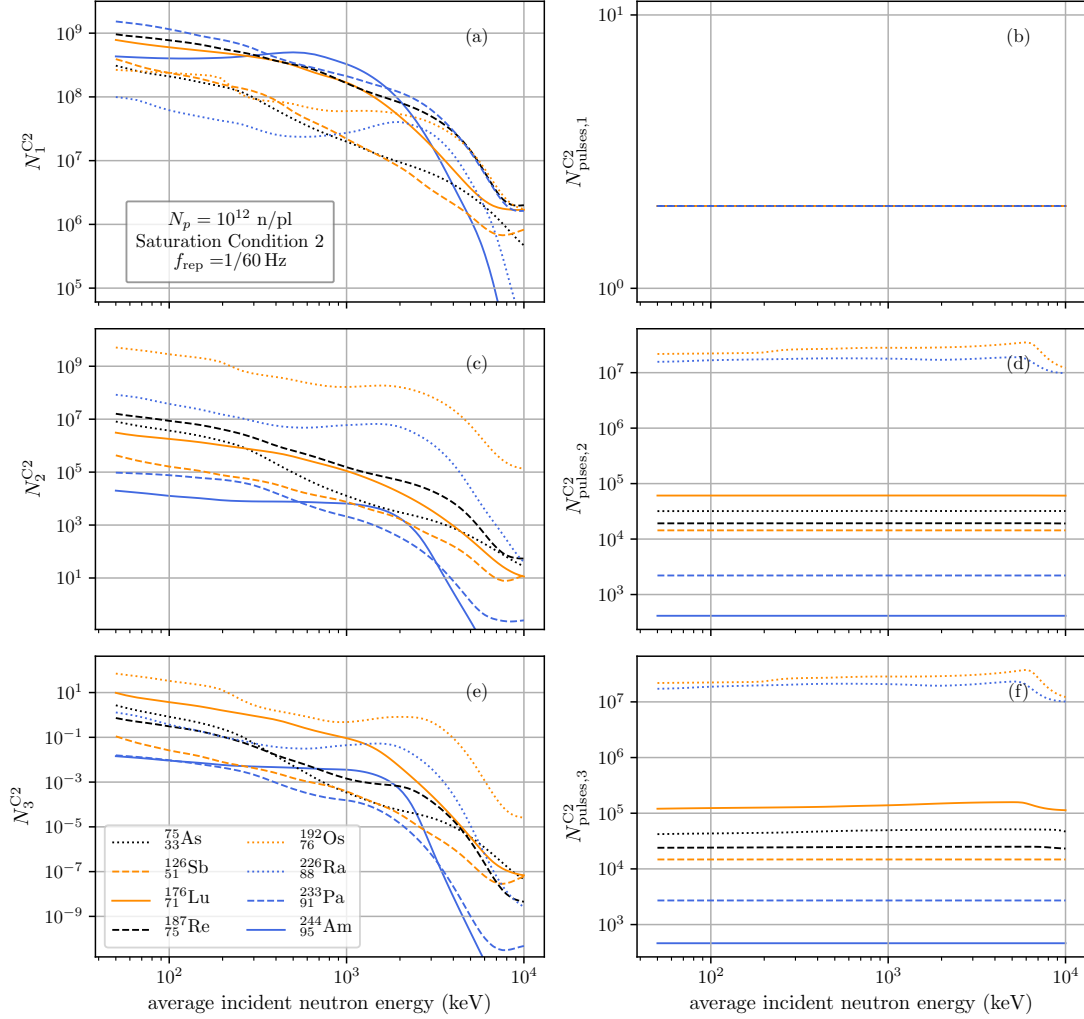


Figure 6.17: Numbers of pulses  $N_{\text{pulses},i}^{C2}$ ,  $i \in \{1, 2, 3\}$  needed to fulfill the second saturation condition for the abundances of populations  $N_i$ ,  $i \in \{1, 2, 3\}$  of neutron-enriched isotopes for the first set of nuclides with a neutron source with  $10^{12}$  neutrons per pulse that delivers pulses with a repetition rate of 1 pulse per minute as well as the abundances  $N_i^{C2}$ ,  $i \in \{1, 2, 3\}$  at these pulse numbers. Contrary to the other repetition rates,  $N_4^{C2}$  is not shown here because the population of the 3-species for the second saturation condition is already hardly above  $10^0$ .

Lastly, we investigate the second saturation condition for the repetition rate of 1 pulse per minute,  $f_{\text{rep}} = 1/60$  Hz. Because for this repetition rate, the populations are saved after every pulse in the performed calculations, the second saturation condition can be determined with

## 6 Numerical Results

the original Eq. (5.35). The results for the pulse numbers  $N_{\text{pulses},i}^{C2}$  and the abundances  $N_i^{C2}$  at the second saturation condition are shown in Figs. 6.17 and 6.18 for the two sets of nuclides.

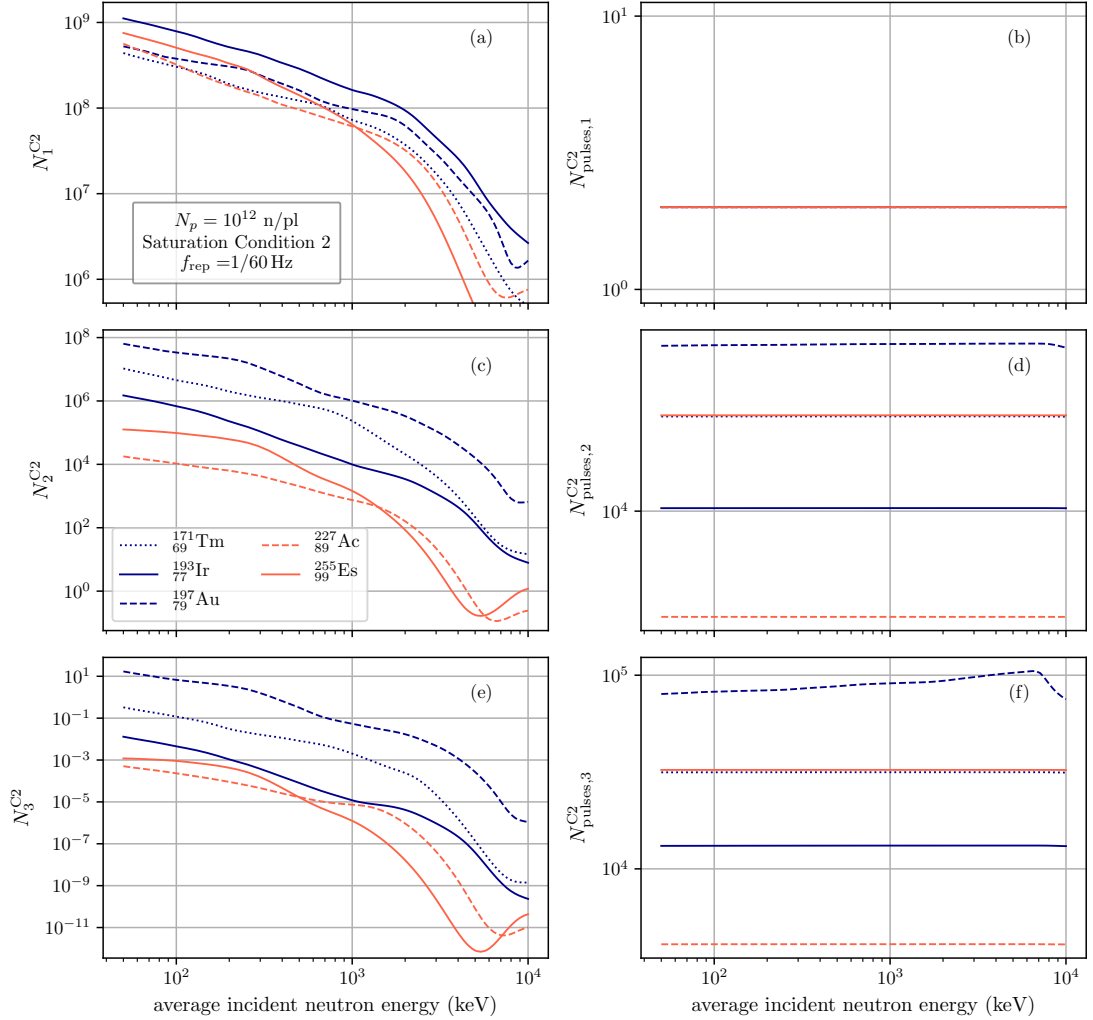


Figure 6.18: Numbers of pulses  $N_{\text{pulses},i}^{C2}$ ,  $i \in \{1, 2, 3\}$  needed to fulfill the second saturation condition for the abundances of populations  $N_i$ ,  $i \in \{1, 2, 3\}$  of neutron-enriched isotopes for the first set of nuclides with a neutron source with  $10^{12}$  neutrons per pulse that delivers pulses with a repetition rate of 1 pulse per minute as well as the abundances  $N_i^{C2}$ ,  $i \in \{1, 2, 3\}$  at these pulse numbers. Contrary to the other repetition rates,  $N_4^{C2}$  is not shown here because the population of the 3-species for the second saturation condition is already hardly above  $10^0$ .

Just like for the other repetition rates, the second saturation condition is reached at the second pulse for the 1-species isotopes of all seed nuclides. Furthermore, Figs. 6.17 and 6.18 show that for 1/60 Hz the pulse numbers are even more reduced compared to those for the first saturation condition, which is due to the same reasons why the deviation for 1 Hz are higher than for 1 Hz.

Thus,  $N_{\text{pulses},2}^{\text{C1}}$  of Lu is up to 3.2 times higher than  $N_{\text{pulses},2}^{\text{C2}}$ , and for Ir the factor increases up to 2.6. Therefore, there is hardly any energy dependence of  $N_{\text{pulses},2}^{\text{C2}}$  for these nuclides anymore. Furthermore, also other nuclides for which virtually no deviations in the pulse number occur for the other repetition rate have pulse numbers  $N_{\text{pulses},2}^{\text{C2}}$  lower than  $N_{\text{pulses},2}^{\text{C1}}$ , most notably Au with ratios  $N_{\text{pulses},2}^{\text{C1}}/N_{\text{pulses},2}^{\text{C2}}$  of up to 1.5, and Pa and Ra with ratios up to 1.23, as for Ra the loss of nuclei of the 2-species isotope is around the same order of magnitude around the saturation condition as  $N_2(1 \text{ pl})$ .

Because of the high loss of nuclei of the  $i$ -species due to decay, while the gain of nuclei through neutron capture per pulse stays approximately the same or is even lower due than for the other repetition rates due to decay of the  $j$ -species isotopes with  $j < i$ , the second saturation condition for this repetition rate is reached for  $N_2$  before the maximal population of  $N_1$  for all nuclides but Ra, Os, Sb, Am and Es and, therefore, the nuclide with among the lowest seed nuclide half-lives or the highest  $T_{1/2}^{+2n}$ . For the 3-species isotopes, the condition is actually reached before the maximum of  $N_2$  for all nuclides but Am and Sb. These are also the only nuclides for which  $N_{\text{pulses},3}^{\text{C2}} = N_{\text{pulses},3}^{\text{C1}} + 1$ , while for the 2-species this is the case for none of the considered seed nuclides. This, however, is most probably not only due to the lower repetition rate but also due to the better pulse resolution.

## 6.2 Numerical Results for Neutron Source 2

After having discussed the populations that can be reached with the first neutron source, the results of the second neutron source and, therefore, an ICF-based source are illustrated in the following.

### 6.2.1 Results after 1 Pulse

We start with the case of 1 pulse. In Figs. 6.19 and 6.20, the abundances directly after one pulse are illustrated for the two sets of seed nuclides, so that no decay is included. The calculations are performed for the same 300 mean incident neutron energy values between 50 keV and 10 MeV as for the first neutron source.

The populations  $N_i$  of neutron-enriched isotopes achieved with one pulse of this neutron source are almost exactly  $10^{4i}$  times higher than those for the first neutron source. The relative deviations of the populations produced with one pulse of neutron source 2 from the results from the first source multiplied by  $10^{4i}$  for the different energies are in fact only on the order of up to  $10^{-4}$ . This is due to the fact that in leading order, the populations  $N_i$  after one pulse scale exactly with  $N_p^i$  in our theoretical approach (as also investigated in Ref. [49]). Because no de-

## 6 Numerical Results

cay is taken into account for this one pulse, which is fair regarding the sub-nanosecond pulse duration of the NIF ICF neutron source that is considered here, the second neutron source, therefore, achieves populations slightly higher than those possible with  $10^4$  pulses with the first neutron source. The abundances  $N_3$  and  $N_4$  of Re, for example, are up to 2 times as high as those for the first neutron source operating at 10 Hz, as the 3-species isotope of Re has a lifetime of only 3 minutes. The abundances after one pulse of the second neutron source are even higher than the maximally possible populations  $N_i^{C1}$  with neutron source 1 operating at 1/60 Hz for all nuclides but the 2-species isotopes of Ra and Os.

With only one pulse of the second neutron source, neutron cascades leading to nuclides enriched by up to 3 more neutrons can be observed for all seed nuclides from both sets. Up to almost  $10^{13}$  nuclides enriched by one neutron can be produced with this source for low energies. For  $N_2$ , the populations of Lu, Pa, Re and Am even exceed  $10^9$  nuclei, which was not possible with  $10^4$  pulses of the first neutron source, even with the highest repetition rate of 10 Hz. Furthermore, the populations for the 3-species isotope of Am even exceed  $10^4$ . However, more pulses than just one are required for the second source to be able to produce nuclides of the 4-species.

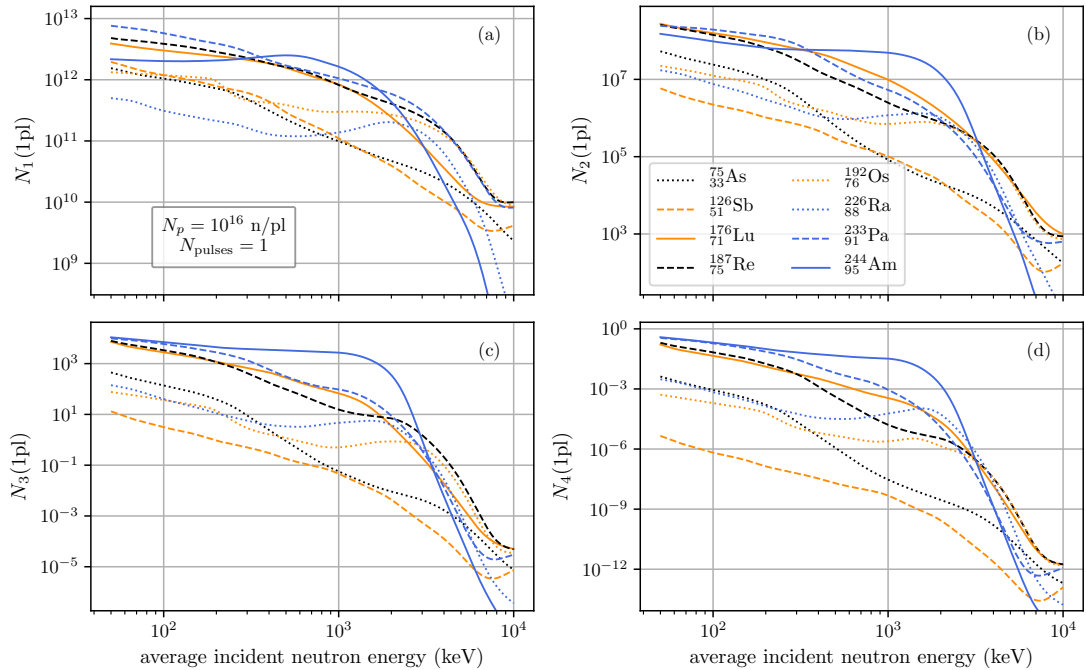


Figure 6.19: Populations  $N_i$ ,  $i \in \{1, 2, 3, 4\}$  of neutron-enriched isotopes directly after 1 pulse of  $10^{16}$  neutrons for the first set of nuclides.

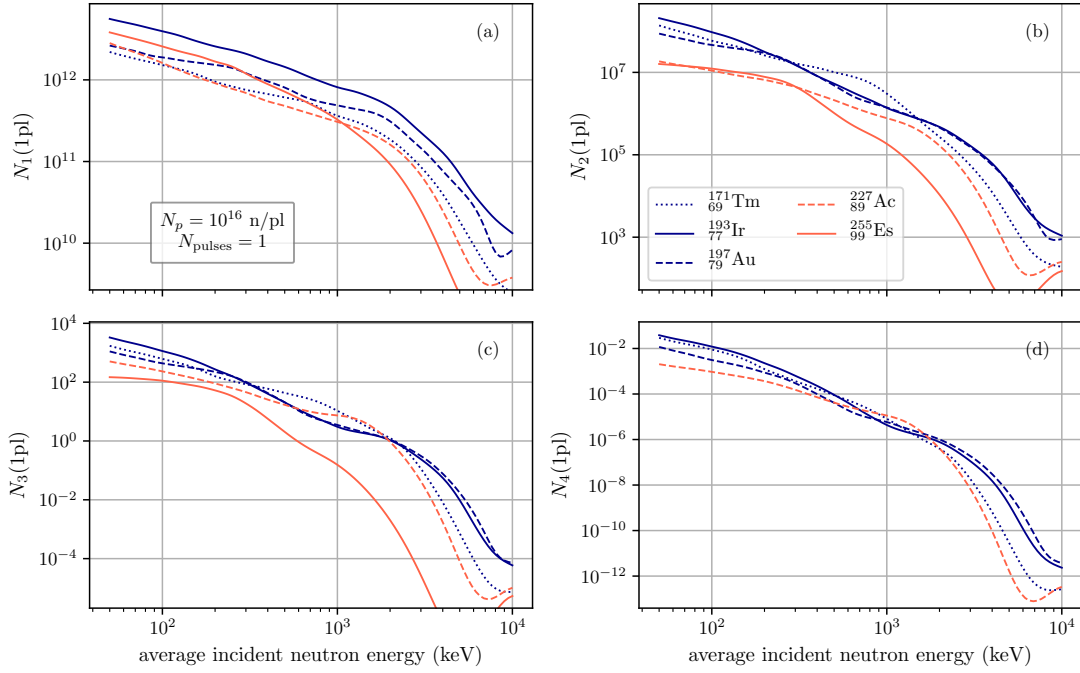


Figure 6.20: Populations  $N_i$ ,  $i \in \{1, 2, 3, 4\}$  of neutron-enriched isotopes directly after 1 pulse of  $10^{16}$  neutrons for the second set of nuclides. Because  $^{259}_{99}\text{Es}$  has no half-life,  $N_4$  and  $N_4^{\text{tot}}$  for this nuclide are not shown in subplots d).

### 6.2.2 Results after 100 Pulses

Because of the low repetition rate assumed for this source of only 3 pulses per day, corresponding to a delay time of 8 hours, only 100 pulses are calculated for this source, which, still, corresponds to a total duration of the interaction of 33 days. The populations  $N_i$  and  $N_i^{\text{tot}}$  are shown in Figs. 6.21 and 6.22 for the two sets of nuclides. For this calculation, the same 300 energies as for one pulse are employed.

When considering  $N_i^{\text{tot}}$ , it can be seen in these plots that for all seeds, far more nuclides enriched by 1-4 neutrons are produced in 100 pulses than in only one. Therefore,  $N_4^{\text{tot}}$  is higher than 1 for most nuclides except Sb, Ac and Es, at least for low energies, so that the observation of neutron capture cascades with up to 4 captured neutrons seems possible for this neutron source. For Lu and Re, even more than  $10^3$  isotopes of the 4-species are produced. However, only for Lu, Re, Os, Ra, Au and Tm are there any nuclei of the 4-species left after the 100th pulse.

## 6 Numerical Results

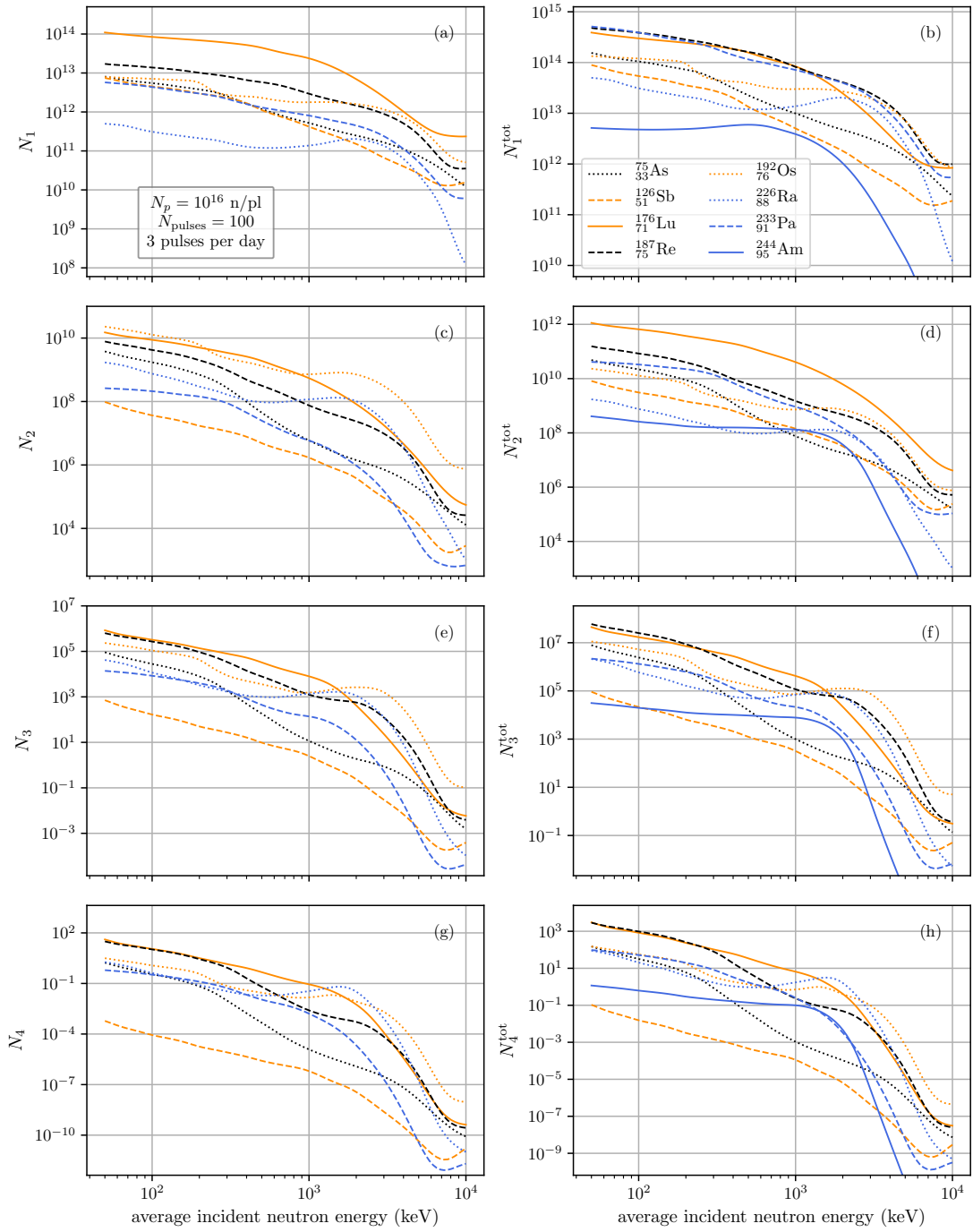


Figure 6.21: Populations  $N_i, i \in \{1, 2, 3, 4\}$  as well as total produced abundances  $N_i^{\text{tot}}, i \in \{1, 2, 3, 4\}$  of neutron-enriched isotopes directly after 100 pulses of  $10^{16}$  neutrons each delivered with a repetition rate of 3 pulses per day for the first set of nuclides.

## 6.2 Numerical Results for Neutron Source 2

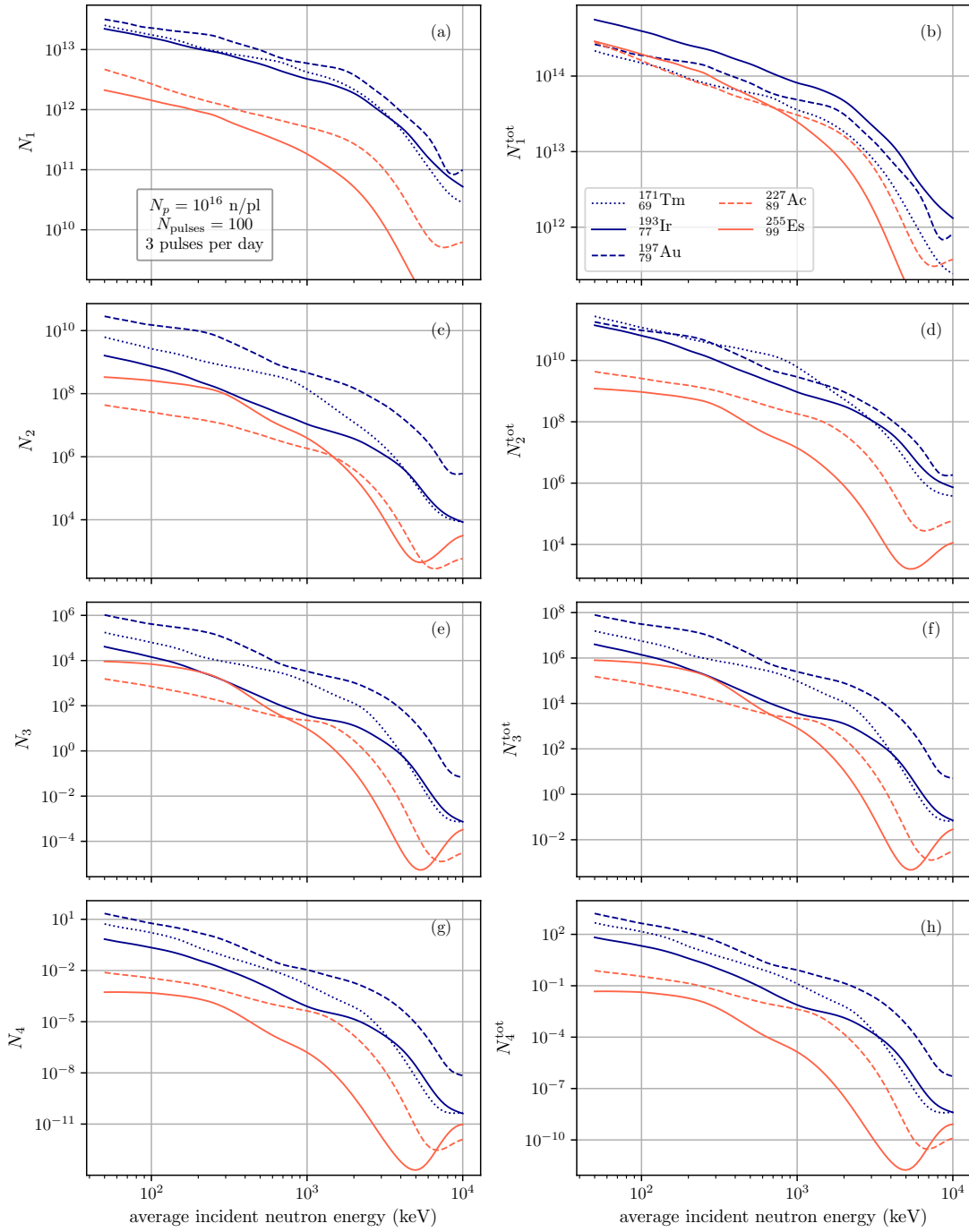


Figure 6.22: Populations  $N_i, i \in \{1, 2, 3, 4\}$  as well as total produced abundances  $N_i^{\text{tot}}, i \in \{1, 2, 3, 4\}$  of neutron-enriched isotopes directly after 100 pulses of  $10^{16}$  neutrons each delivered with a repetition rate of 3 pulses per day for the second set of nuclides.

Because of the higher delay time in between pulses for the repetition rate of 3 pulses a day at which the second neutron source operates in this simulation, the differences between  $N_i^{\text{tot}}$  and

## 6 Numerical Results

$N_i$  are even higher than for all repetition rates of the first neutron source, with ratios  $N_i/N_i^{tot}$  never greater than 0.2 for  $i > 2$ . For Am, these ratios are even lower because no population of this nuclide is higher than  $10^{-11}$ . This is, again, due to the low half-life of the Am seed nuclide, which, with 10 h, is only slightly longer than the delay time, so that while during the first few pulses quite many nuclides are produced due to the high neutron capture cross section of this nuclide, the seed nuclide abundance is lower than 1 from 71 pulses on.

Thus, no new nuclides can be produced from there on and the remaining enriched species decay quickly as well, as their half-lives are significantly lower than the delay time. Therefore, not even nuclides of the 1-species of Am are left after the 100 pulses. But Am is not the only nuclide of which the population has already surpassed its maximum in the span of 100 pulses. This is the case for all nuclides but for all nuclides but Lu and the  $N_2 - N_4$  populations of Ra and Os. Still, the abundances after 100 pulses are higher than after one pulse for most nuclides except the  $N_1$  populations of Ra, Pa and Es and all Am abundance.

### 6.2.3 Saturation Condition 1

Now, we turn to the analysis of the saturation condition 1. The maximal abundances of the regarded nuclides as well as the required pulse numbers can be seen in Fig. 6.23 for the first set and in Fig. 6.24 for the second set of nuclides. For the calculation of this data, 500 energies logarithmically distributed between 50 keV and 10 MeV are used, and the populations and pulse numbers are saved for every pulse.

The second neutron source has both a higher pulse number and higher delay times than the first one, so that both the nuclide loss rate through radioactive decay in between pulses and through nuclear transmutation are higher. For the seed nuclides, transmutation dominates for all nuclei but Es, Am, Pa, Tm, Sb and a few intermediate energies of Ac, and for the neutron-enriched nuclides, only  $\eta_2$  of Ra is higher than the decay probability for high energies. Still, when analyzing the pulse numbers needed to reach the maximal populations  $N_{pulses,i}^{C1}$ , it can be seen that the pulse numbers of most nuclides show an energy dependence just like for the first neutron source. The only isotopes for which this is not the case are those of all species for Sb, Pa and Am and the 1-species isotopes of Es and Ra. The lack of energy dependence is most probably due to their low half-lives of the seed or neutron-rich nuclides, so that there is virtually no dependence of the saturation condition on the transmutation cross sections of the nuclides. Because of the high half-lives  $T_{1/2}^{+2n} = 8$  d of Es and  $T_{1/2}^{+2n} = 6$  h of Ra, however,  $N_{pulses,2}^{C1} - N_{pulses,3}^{C1}$  of Es vary slightly with energy, though, and the pulse numbers  $N_{pulses,2}^{C1} - N_{pulses,4}^{C1}$  of Ra are the second highest, showing high variations with energy as well.

Just like for the first neutron source, the pulse numbers needed to reach the maximal popula-

tions do not decrease with higher  $i$ . However, for most nuclides of the 3- and 4-species, the increase of  $N_{\text{pulses},i}^{\text{C1}}$  compared to  $N_{\text{pulses},i-1}^{\text{C1}}$  amounts to only one pulse, and for several short-lived nuclides, the maximal abundances  $N_i^{\text{C1}}$  are even reached at the same time as  $N_{i-1}^{\text{C1}}$ .

Furthermore, it is worth mentioning that, because of the low half-lives of both the seed and the 1-species of Es and Am, these nuclides have already reached their maximum of  $N_1$  at the first pulse, and for the same species of Ra, only two pulses are needed. In fact, most nuclides reach their maxima within 100 pulses and, therefore, 33 days. The only seeds for which this is not the case are, Au, Lu, Ra and Os. To reach the maximal populations of all neutron-enriched Au nuclides for all energies, 63 days and 8 hours are needed, 104 days for Lu, and for Os and Ra, over 45 and 29 years are required, respectively. Therefore, more time than for the first neutron source operating at a repetition rate of 1 Hz or 10 Hz is required to reach the maximal abundances of these nuclides, but less time than for  $f_{\text{rep}} = 1/60$  Hz. For the high- $Z$  nuclides Am, Pa, Ac and the  $N_1$  abundances of Ra and Es for which only a few pulses are required to reach the maximum, however, the times are lower than for all repetition rates of the first neutron source.

When it comes to the maximal abundances  $N_i^{\text{C1}}$  that can be reached with the second neutron source, it is apparent that the abundances are all higher than those reached with the first neutron source operating at  $f_{\text{rep}} = 1/60$  Hz (which is also the case for only one pulse of this source for most nuclides), but lower than all abundances for  $f_{\text{rep}} = 10$  Hz. Furthermore, the populations are even higher than the maximal ones to be reached with neutron source 1 at 1 Hz for nuclides with low half-lives. For instance, the maximal abundances  $N_1^{\text{C1}}$  of Ra, Am and Es, which are all reached within 1-2 pulses, are significantly higher than for neutron source 1 operating at 1 Hz, and  $N_4^{\text{C1}}$  for the second neutron source is even higher than the abundances produced with neutron source 1 at 1 Hz for all nuclides but Au and Sb. The reason for this is that to produce the same abundance as with one pulse of neutron source 1 with neutron source 2, more  $10^4$  pulses are needed, during which the produced nuclides decay, however. Therefore, especially for the nuclides like Ra, Es and Am with  $N_{\text{pulses},1}^{\text{C1}}$  only slightly higher than  $10^4$  for neutron source 1 and  $f_{\text{rep}} = 1$  Hz, as well as for those nuclides for which  $N_{\text{pulses},i}^{\text{C1}}$  is only a few pulses higher than  $N_{\text{pulses},i-1}^{\text{C1}}$  like it is the case for the 3- and 4-species of most nuclides, the maximal abundances for neutron source 2 are higher. Therefore, when comparing the relative magnitude of the abundance curves of the different nuclides, it is apparent that especially the Am and Pa abundances are relatively high, while the abundances of rather long-lived nuclides like the neutron-enriched isotopes of As, Au or Sb have relatively low abundances.

## 6 Numerical Results

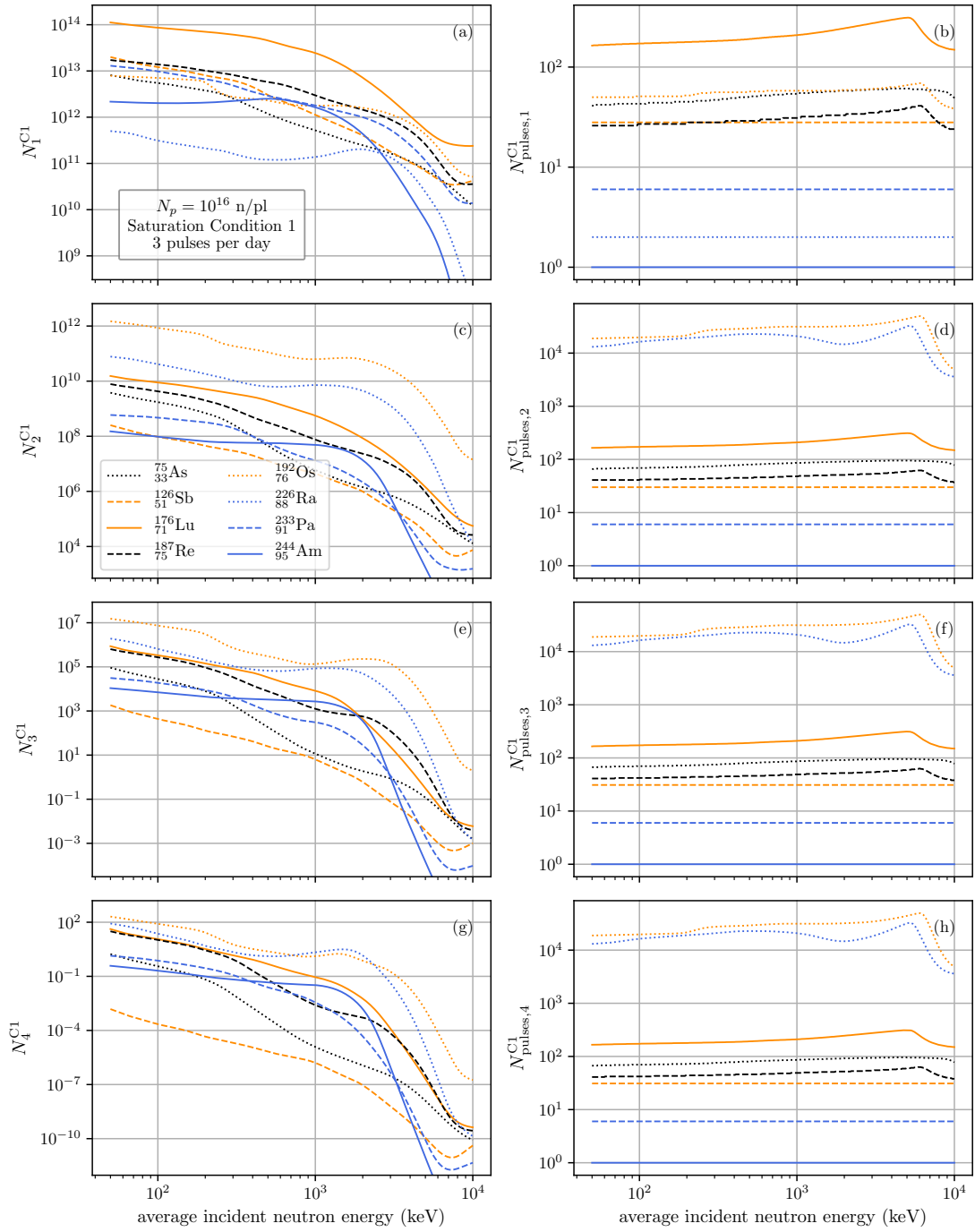


Figure 6.23: Maximally reached abundances  $N_i^{C1}$ ,  $i \in \{1, 2, 3, 4\}$  of neutron-enriched isotopes for the first set of nuclides as well as the numbers of pulses  $N_{pulses,i}^{C1}$ ,  $i \in \{1, 2, 3, 4\}$  it takes to reach them with a neutron source with  $10^{16}$  neutrons per pulse that delivers pulses with a repetition rate of 3 pulses per day.

6.2 Numerical Results for Neutron Source 2

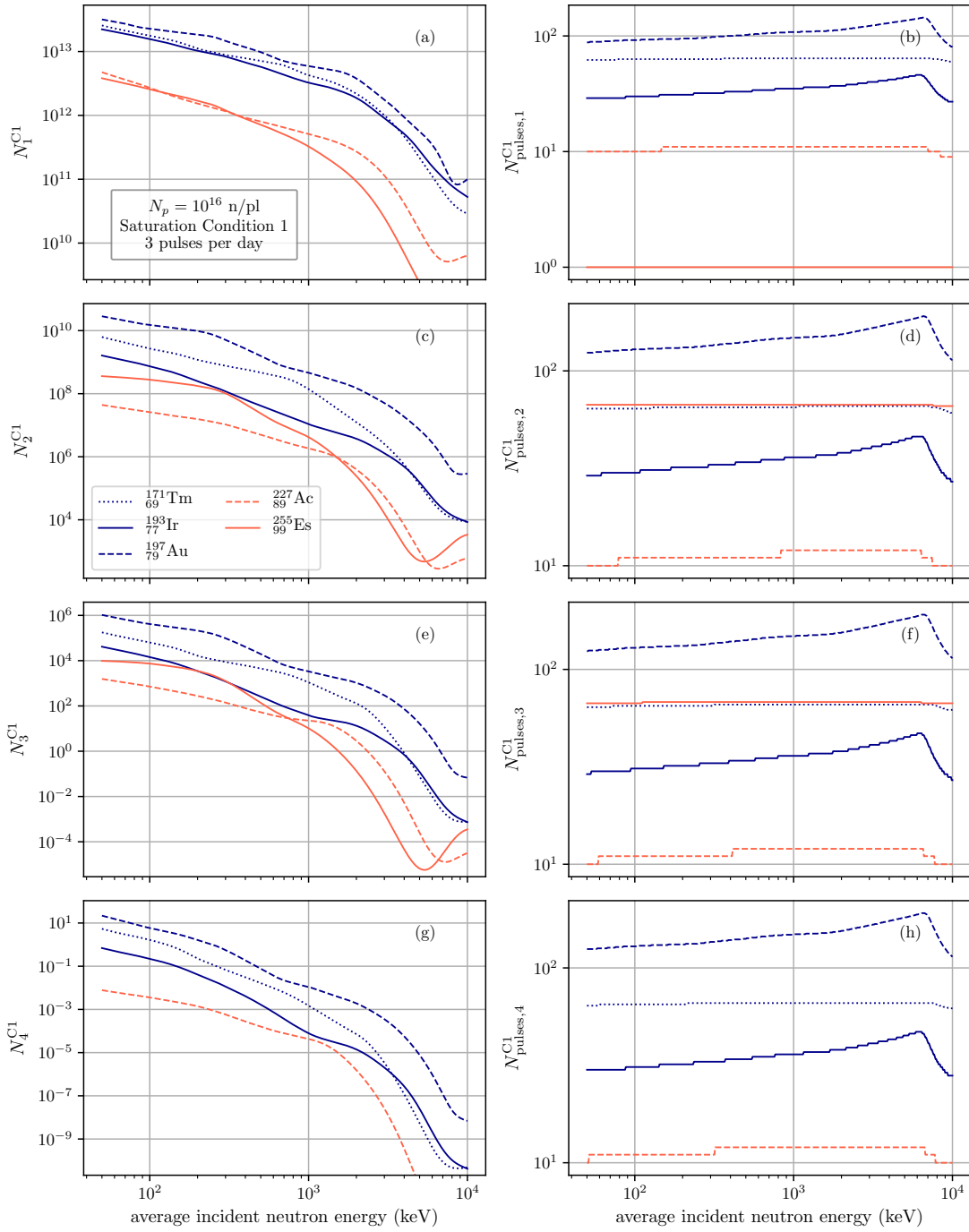


Figure 6.24: Maximally reached abundances  $N_i^{C1}$ ,  $i \in \{1, 2, 3, 4\}$  of neutron-enriched isotopes for the second set of nuclides as well as the numbers of pulses  $N_{pulses,i}^{C1}$ ,  $i \in \{1, 2, 3, 4\}$  it takes to reach them with a neutron source with  $10^{16}$  neutrons per pulse that delivers pulses with a repetition rate of 3 pulses per day. Because  $^{259}_{99}\text{Es}$  has no half-life,  $N_4^{C1}$  and  $N_{pulses,4}^{C1}$  for this nuclide are not shown in subplots d).

The maximal abundances for the 1-species produced with neutron source 2 reach up to over  $10^{14}$  in case of Lu, and all nuclides but Ra also reach populations higher than  $10^{12}$ . Nuclides enriched by one or two neutrons can be produced for all energies for all seed nuclides, and the abundances  $N_2^{C1}$  reach up to over  $10^{12}$  for Os and over  $10^{10}$  for Ra, Lu, and Au. Furthermore, all nuclides but Ac reach  $N_2$ -abundances higher than  $10^8$ . Also, nuclides enriched by 3 neutrons can be produced for all seeds up to energies of a few MeV, and  $N_3^{C1}$  higher than  $10^3$  can be achieved with this neutron source for all nuclides at low energies. For Os, the maximal abundance even exceeds  $10^7$  nuclides. When it comes to the 4-species isotopes, the maximal abundance reaches over  $10^2$  nuclei for Os. Furthermore,  $N_4^{C1}$  is greater than 1 for Tm and Pa, which is not the case for neutron source 1 operating at 1 Hz. However, not for all seed nuclides can abundances greater than 1 be observed for the 4-species isotopes: for Am, Sb, Ac, Es, and Ir, this is not the case. At least for all nuclides but Es, however, the number of totally produced nuclei of the 4-species over the course of  $10^4$  pulses of the second neutron source is greater than 1, so that for almost all nuclides, neutron capture cascades with up to 4 neutrons could still be observed.

#### 6.2.4 Saturation Condition 2

Lastly, we analyze the second saturation condition for the second neutron source. The data for this condition is the same as for the first saturation condition, with the same 500 energies used and the populations saved after every pulse. Therefore, the pulse numbers  $N_{\text{pulses},i}^{C2}$  to reach the condition are calculated directly with Eq. (5.35). The results for the pulse numbers  $N_{\text{pulses},i}^{C2}$  and abundances  $N_i^{C2}$  are shown in Figs. 6.25 and 6.26 for the two sets of nuclides.

These figures show that for neutron source 2, the saturation condition for  $N_1$  is reached at the second pulse as well. However, the isotopes of the 1-species are not the only ones for which the saturation condition is reached so early. For the 2-species isotopes of Ac, Pa and Es, as well as all considered neutron-enriched isotopes of Am this is also the case, and the pulse numbers for the 3- and 4-isotopes of Ac and Pa only have values as low as 3. The reason for this is that all these nuclides have relatively short half-lives of the seed nuclides and half-lives of the 1-species isotopes that are smaller than the delay time. Therefore, for Ac, Es and Am, the gain of new nuclei of the 2-species via neutron capture is already lower at the second pulse than for one pulse. For Pa, this is not quite the case, but the loss of nuclei of the 2-species isotope between the first and second pulse is so high due to the short half-life  $T_{1/2}^{+2n} = 24$  min that the saturation condition is still reached at the second pulse. For Am, Ac and Pa the low half-lives of the 3- and 4-species are then responsible that only few pulses are needed for reaching the saturation conditions for these species as well. For Es, on the other hand,  $T_{1/2}^{+2n}$  is quite long with 8 d, so that  $N_{\text{pulses},3}^{C2}$  and  $N_{\text{pulses},4}^{C2}$  are significantly higher than 2.

That  $N_{\text{pulses},2}^{\text{C2}}$  is very low for a nuclide despite a high  $T_{1/2}^{+2n}$  is also true for Ra. While, just like for Es, the pulse numbers  $N_{\text{pulses},2}^{\text{C2}}$  for this nuclide only slightly deviate from those for the first saturation condition for the first neutron source, this is not the case here. In fact, the pulse numbers  $N_{\text{pulses},2}^{\text{C2}}$  for this nuclide do not exceed 8 pulses and, therefore, are over 3 orders of magnitude lower than  $N_{\text{pulses},2}^{\text{C1}}$ . The reason for this is, again, the low half-life of the 1-species, which amounts to only 42 minutes, so that there is virtually no neutron capture contribution from the 1-species isotope to the population  $N_2$ . However, because of the long half-life of the seed nuclide, the gain decreases more slowly than, for example, for Am or Es, and the loss of nuclides is quite low due to the long  $T_{1/2}^{+2n}$ , the condition is not already fulfilled at the second pulse. Another striking detail about the Ra pulse number is that it depends heavily on energy, while some significantly higher pulse numbers of other nuclides do not. This could be explained by the loss of nuclei, which depends highly on transmutation and, therefore, energy for Ra, so that the relative loss is over twice as high for 10 MeV than for 7 MeV, for example. Because of the high  $T_{1/2}^{+2n}$ , however, the pulse numbers for the 3- and 4-species isotopes to reach the second saturation condition are only up to 3.8 and 2.3 times lower compared to  $N_{\text{pulses},3}^{\text{C1}}$  and  $N_{\text{pulses},4}^{\text{C1}}$ , respectively.

But not only for isotopes for which the seed or 1-species isotopes have extremely short half-lives are the ratios  $N_{\text{pulses},i}^{\text{C1}}/N_{\text{pulses},i}^{\text{C2}}$  high due to the extremely low repetition rate. This is also the case for nuclides with quite high half-lives of the 1-species isotope, as the high influence of decay leads to both a low increase of the gain of nuclei of the  $i$ -species isotope and a high loss of those. Therefore, the populations for different pulse numbers do not deviate much and the second saturation condition is reached quickly. In fact, saturation condition 2 is reached at such low pulse numbers and relatively low abundances due to the high influence of decay that  $N_i(1 \text{ pl})$  is only 1-2 orders of magnitude lower than  $N_i$  itself and several orders of magnitude higher than the influence of the transmutation cross sections on the abundances. Thus, the saturation condition 2 is reached long before the maximal abundance, and the only nuclides for which the pulse numbers show a significant energy dependence are the long-lived Ra and Os due to the high influence of transmutation on the loss.

For higher  $i$ , the deviations of the pulse numbers  $N_{\text{pulses},i}^{\text{C2}}$  from  $N_{\text{pulses},i}^{\text{C1}}$  generally decrease just like it is the case for the first neutron source. Because of the low number of pulses applied and the high influence of decay, however, the pulse numbers for the second saturation condition are still significantly lower than the pulse numbers for the first saturation condition for the 3- and 4-species isotopes, and an energy dependence of  $N_{\text{pulses},i}^{\text{C1}}$  only develops for Tm, Au and Lu for the 3- and 4-species isotopes.

## 6 Numerical Results

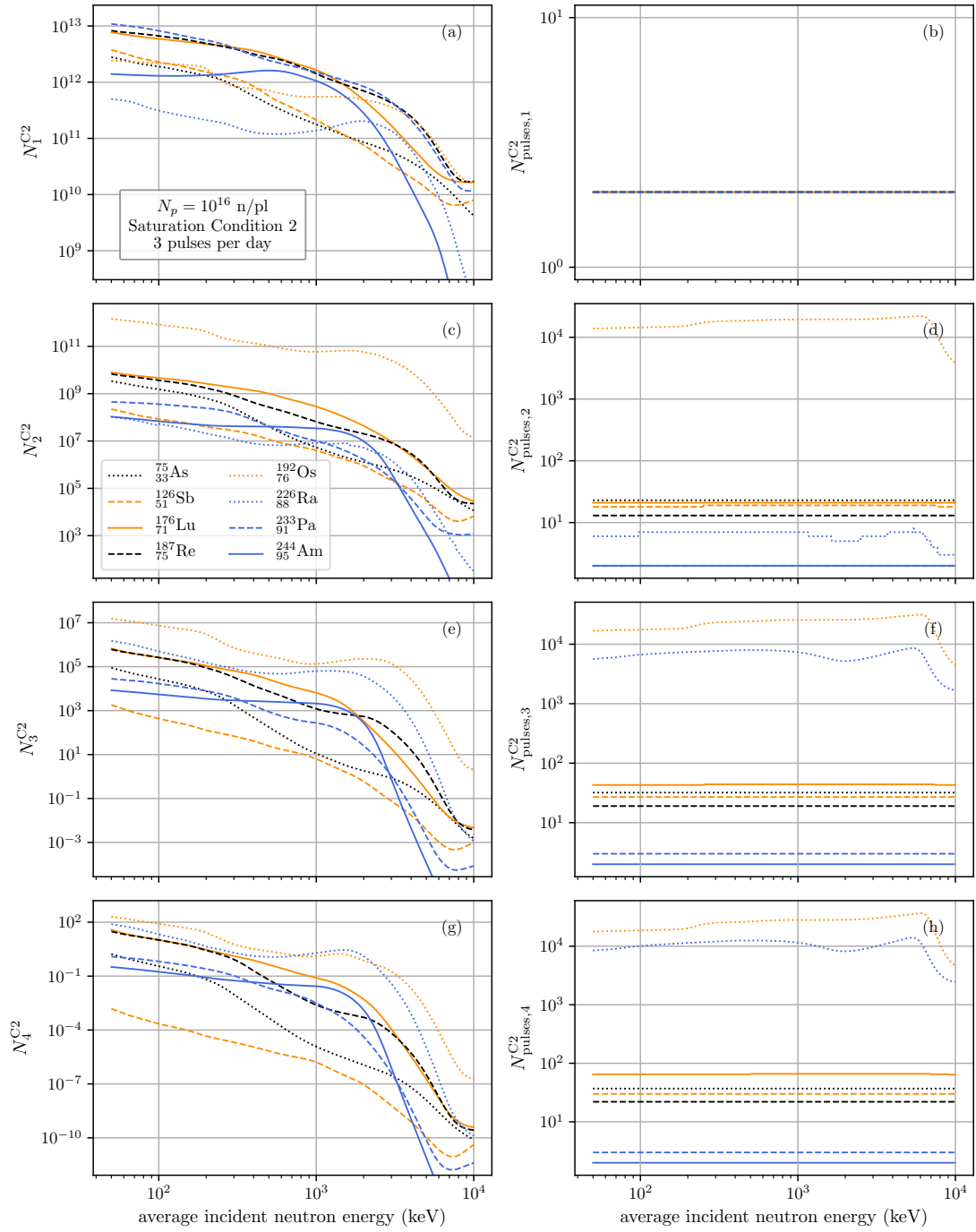


Figure 6.25: Numbers of pulses  $N_{pulses,i}^{C2}$  needed to fulfill the second saturation condition for the abundances of populations  $N_i, i \in \{1, 2, 3, 4\}$  of neutron-enriched isotopes for the first set of nuclides with a neutron source with  $10^{16}$  neutrons per pulse that delivers pulses with a repetition rate of 3 pulses per day as well as the abundances  $N_i^{C1}, i \in \{1, 2, 3, 4\}$  at these pulse numbers.

## 6.2 Numerical Results for Neutron Source 2

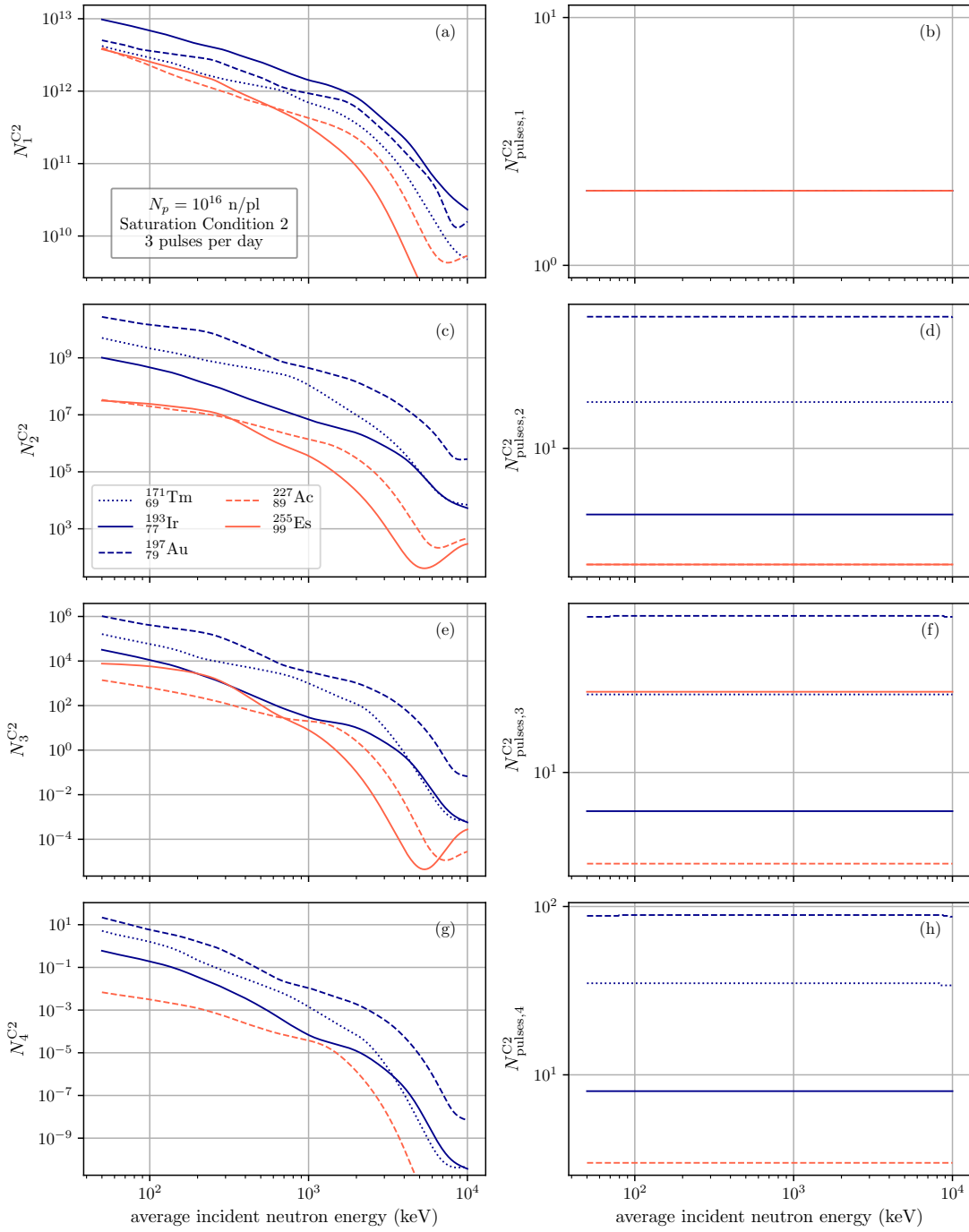


Figure 6.26: Numbers of pulses  $N_{pulses,i}^{C2}$ ,  $i \in \{1, 2, 3, 4\}$  needed to fulfill the second saturation condition for the abundances of populations  $N_i$ ,  $i \in \{1, 2, 3, 4\}$  of neutron-enriched isotopes for the first set of nuclides with a neutron source with  $10^{16}$  neutrons per pulse that delivers pulses with a repetition rate of 3 pulses per day as well as the abundances  $N_i^{C1}$ ,  $i \in \{1, 2, 3, 4\}$  at these pulse numbers. Because  $^{259}_{99}\text{Es}$  has no half-life,  $N_4^{C2}$  and  $N_{pulses,4}^{C2}$  for this nuclide are not shown in subplots d).

## 6 Numerical Results

Because, as explained above, the abundances  $N_i$  for different pulse numbers produced with the second neutron source are quite similar, the abundances  $N_i^{C2}$  differ from  $N_i^{C1}$  by less than one order of magnitude, except for the populations for the 2-species isotope of Ra. Furthermore, Figs. 6.25 and 6.26 show that, contrary to the first neutron source, for which  $N_2^{C2}$  is higher than  $N_1^{C2}$  for all repetition rates, the abundances  $N_1^{C2}$  for the 1-species isotopes are higher than  $N_2^{C2}$  for the second neutron source due to the high loss of 2-species nuclei due to decay.

## 7 Comparisons

### 7.1 Comparing the 1 Pulse $N_1$ for TENDL and ENDFB Data

To analyze quantitatively how well the calculated cross sections in the TENDL-2019 data, which are used for the calculations of the results shown above, live up to the experimentally determined cross sections in the ENDF/B-VIII.0 data, we study the effect that the use of cross sections from the ENDF-B or the TENDL data has on the resulting populations of nuclides that have captured one neutron after one neutron pulse. This comparison is carried out in the following way: The population  $N_1$  after one neutron pulse with  $N_p = 10^{12}$  neutrons is calculated in leading order according to

$$N_1(1 \text{ pl}) \approx \mu_0 N_T \mu_0 = N_T N_p \sigma_{n\text{-cap}} / A \quad (7.1)$$

for the heaviest isotopes of all nuclei between  $Z = 3$  and  $Z = 100$  that are available in the ENDF/B-VIII.0 library, once using the neutron capture cross-section from the ENDF/B-VIII.0 data and once using the TENDL-2019 cross. This calculation is executed for 300 logarithmically spaced energies from 50 keV to 10 MeV. Then, for each nuclide and each energy, we compute the relative deviation between the  $N_1(1 \text{ pl})$  values for the different datasets via:

$$\text{relative deviation} = \frac{N_1(1 \text{ pl})_{\text{TENDL}} - N_1(1 \text{ pl})_{\text{ENDF}}}{N_1(1 \text{ pl})_{\text{ENDF}}} \quad (7.2)$$

This leading order estimation is a good approximation to the complete calculation, as comparisons with TENDL cross sections of this approximation to a complete calculation with the full matrix exponential show relative deviations of the populations  $N_1$  after one pulse on the order of only  $10^{-3}$ .

For the populations  $N_1$  obtained by this calculation, the maximal, minimal and mean relative deviation are calculated for each nuclide by considering all 300 different energies. The resulting values for the nuclides for which a TENDL file exists can be seen in Fig. 7.1, where we use the same parameters as above for our calculations: a target area of  $10^4 \mu\text{m}^2$ , a length of  $100 \mu\text{m}$ , and a neutron beam with a gaussian energy distribution with a width-maximum ratio of 10%. As shown in Fig. 7.1, there are no deviations between the TENDL and ENDFB-B data for the nuclides Li, Be, B, C, N, O and F because as already explained in chapter 2, the evaluated files

## 7 Comparisons

for these nuclides in the TENDL-2019 library have been taken from the ENDF/B-VIII.0 data. For higher  $Z$  nuclides, there is, however, a deviation, so that the mean relative deviation for the heaviest nuclides in the ENDF data from  $Z = 3$  to  $Z = 84$  and from  $Z = 88$  to  $Z = 100$  amounts to 299% on average, with an average relative standard deviation of 765%. If only the nuclides are regarded for which the TENDL data is not taken from ENDF/B-VIII.0, the deviation is higher with a mean relative deviation of 323% on average and an average mean standard deviation of 826%. These significant deviations indicate that even though the TENDL library includes models for the most important processes, these still do not fully describe reality, as these models are only approximations to reality, so that not every single physical process is accounted for and the models are subject to uncertainties. It can be seen that the highest relative deviations occur especially for nuclides with either very high or very low  $Z$ . For high- $Z$  nuclides, this might be due to the uncertainties of fission transmission coefficients in the TENDL library, and for nuclides with low  $Z$ , the reason could be that the Hauser-Feshbach model with transmission coefficients calculated from the optical potential is not fully applicable for such light nuclei, as the level density cannot be assumed to be high enough to be treated statistically and the resonances are not quite overlapping. Therefore, if only the nuclides in the range between  $Z = 10$  and  $Z = 83$  (which is the range for the FRDM NON-SMOKER data) are considered, the average mean relative deviation is slightly lower with only 307% and the mean relative standard deviation 708%.

For the nuclides considered in the present work, the mean relative deviation amounts to 236% on average, and the average relative standard deviation is as high as 1144%. Most of the considered nuclides actually only show a mean relative deviation significantly smaller than one, as can be seen in Fig. 7.1, with the only nuclides for which the mean relative deviation is higher being  $^{244}\text{Am}$  and  $^{255}\text{Es}$ . For  $^{244}\text{Am}$ , the mean relative deviation of the  $N_1$  populations is even greater than 10 due to very high deviations of both the neutron capture cross section for high energies by up to 3 orders of magnitude and high deviations of the transmutation cross section of up to over one order of magnitude in the complete considered energy range. Therefore, this high deviation accounts for the relatively high average. If only the nuclides are considered which are also present in NON-SMOKER data, i.e. nuclides with  $Z < 84$ , the mean relative deviation even is as low as 38% on average. We can, therefore, conclude that for our seed nuclides, the TENDL and ENDF data produce comparable results for the population of nuclides enriched by one neutron, with only the deviation of  $^{244}\text{Am}$  being high.

When it comes to the cross sections of the nuclides, an analysis shows that most TENDL cross sections, both for neutron capture and transmutation, deviate from those of the ENDF data by no more than one order of magnitude in the considered energy range, with larger deviations only for high- $Z$  nuclides like Ra or Am at high energies.

## 7.2 Comparing the 1 Pulse $N_1$ for NON-SMOKER and ENDFB Data

It should be noted, however, that for the nuclides for which these comparisons are conducted, experimental data is available to adjust the input parameters of TENDL to. Therefore, for more neutron-rich isotopes under investigation in the present work, the deviations are likely to be higher.

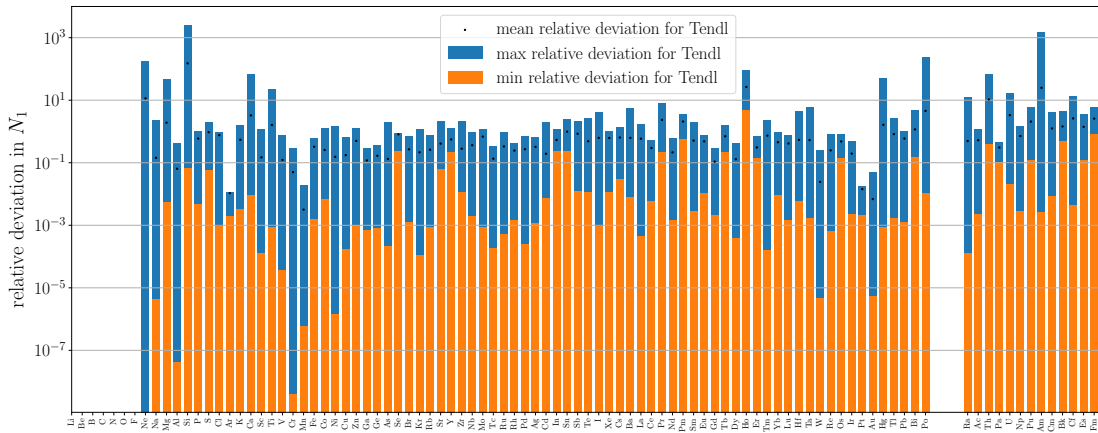


Figure 7.1: Comparison of the populations  $N_1$  of the seed nuclides that are enriched by 1 neutron after one applied pulse with  $10^{12}$  neutrons when either ENDFB-data or TENDL-data are used for the neutron-capture cross sections.

## 7.2 Comparing the 1 Pulse $N_1$ for NON-SMOKER and ENDFB Data

Apart from the results analyzed above in which TENDL-2019 data is used, the same calculations are also carried out for different datasets in which NON-SMOKER FRDM cross section data is employed. Therefore, we make further comparisons of  $N_1$  after one pulse calculated with the cross section data from the ENDF/B-VIII.0 library and the FRDM NON-SMOKER data. The results can be seen in Fig. 7.2 for the complete  $Z$ -range available in this dataset,  $Z = 10 - 83$ . For the nuclides in this range, the mean relative deviation of the populations amounts to 723% on average, with a mean standard deviation of 973%. It is obvious that especially the light nuclei suffer from a large deviation, which could, again, be explained by the fact that for light nuclei, the Hauser-Feshbach model with which the NON-SMOKER cross sections are calculated, is not well applicable. In fact, if one leaves out the mean relative deviation of Ne, which amounts to over  $4 \times 10^2$ , the average mean relative deviation of the nuclides is only 92%. Comparison with Fig. 7.1 shows that for such low- $Z$  nuclides, the mean relative deviations for the TENDL cross sections are generally lower than for the NON-SMOKER data, which is due to the fact that in TENDL, more models and experimental data is included, which is especially

## 7 Comparisons

relevant for such low- $Z$  nuclides for which the sole use of the Hauser-Feshbach model is not justified. Finally, for those nuclides considered in the present work that also are included in the NON-SMOKER data, the mean relative deviation amounts to only 35% on average, with a mean relative standard deviation of 19%. Therefore, the mean relative deviations for those nuclides are comparable to those for the TENDL data, with the deviations for the NON-SMOKER data even slightly lower than for TENDL.

In Ref. [49], Hill and Wu have carried out comparisons of the NON-SMOKER data with ENDF-B data not only for the FRDM but also the ETFSI-Q dataset for  $Z = 23 - 83$ . They have found that the deviation of the neutron capture cross sections for the same nuclides are never larger than one order of magnitude. Furthermore, they have investigated the relative deviation of the  $N_1$  populations similarly to how it is done in this work, only with slightly different parameters, i.e  $A = 25\mu\text{m}^2$  and a neutron pulse number of  $N_p = 10^{11}$ . With these parameters, they have found that the relative deviation between the populations calculated in leading order with the neutron capture cross sections of the ENDF and the NON-SMOKER data are on the level of 50% on average for both the FRDM and the ETFSI-Q NON-SMOKER data in the range  $Z = 23 - 83$ , so that both of these codes can be considered equally good, which makes it legitimate for us to use the FRDM data because of the greater range of nuclides it covers.

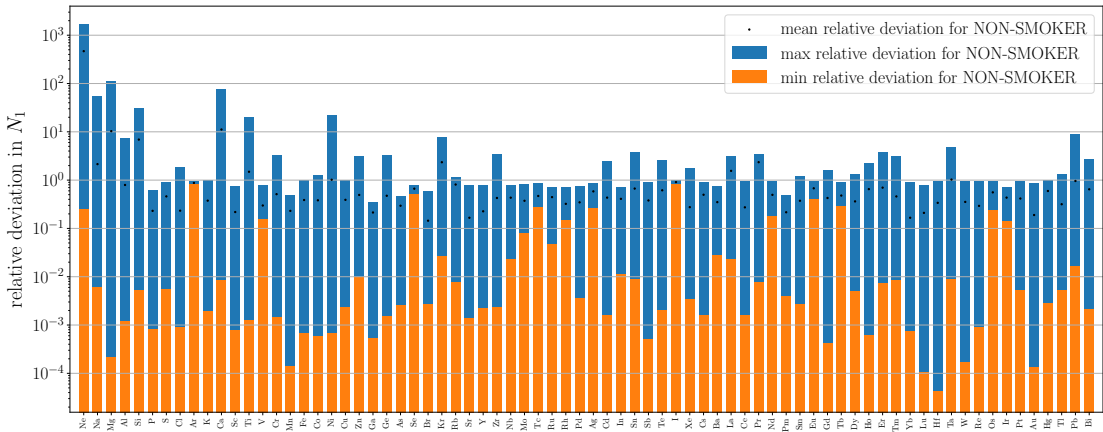


Figure 7.2: Comparison of the populations  $N_1$  of the seed nuclides that are enriched by 1 neutron after one applied pulse with  $10^{12}$  neutrons when either ENDFB-data or NON-SMOKER-data are used for the neutron-capture cross sections.

### 7.3 Comparison of the Results for Different Cross Section Datasets

#### Datasets

In the calculations the results of which have been explained in detail above, solely TENDL-2019 cross section data has been used for the neutron-enriched isotopes. However, there are also other data available for cross sections, as discussed in section 2.2. In Ref. [49], for instance, a combination of ENDF-B data and NON-SMOKER data has been employed. To investigate the precision of our results, the original results will be compared to those for two other datasets (denoted as dataset A and dataset B) in the following, to determine how much and in which way the potential differences of the cross sections calculated using different models and parameters influence our results, and the differences of which nuclear quantities have the highest influence on which pulse numbers or populations. For datasets A and B, the cross section data for seed nuclides is taken from the ENDF/B-VIII.0 library as well, as this is the most reliable library of the three considered due to its focus on experimental data. However, the cross section values for neutron-enriched nuclides differ from the ones used in the original dataset, as both datasets include NON-SMOKER neutron capture cross section values so far they are available.

For dataset A, the cross sections for neutron-enriched isotopes are calculated in the same way as in Ref. [49]. For  $10 < Z < 84$ , the neutron capture cross section are taken from FRDM NON-SMOKER data. For the nuclides where the cross section is not available from the NON-SMOKER data, the neutron capture cross sections are approximated by the cross section of the seed nuclide from the ENDFB data. Concerning the species loss cross of the neutron-enriched isotopes, the  $\eta_i$  values are estimated from the NON-SMOKER  $\mu_i$  values with the following formula:

$$\eta_i = \mu_i + \eta_0 - \mu_0 \quad (7.3)$$

where  $\eta_0$  and  $\mu_0$  can be exactly calculated with the ENDF cross sections of the seed nuclides. This approximation is best if the species-loss cross section is dominated by the neutron capture cross section. However, this condition is not valid anymore for larger energies, as can be seen when regarding the TENDL  $\sigma_{tr}$  values, due to the fact that particle emission reactions begin to dominate at about 7 MeV. Furthermore, for fissile isotopes of, for example, Es, Am, Pa, and Ac, the condition is truly applicable at non of the considered energies. However, NON-SMOKER data does not exist for these isotopes anyway.

In dataset B, data from both the NON-SMOKER FRDM data and the TENDL-2019 data are employed to determine the neutron capture and species-loss cross sections for neutron-enriched isotopes. For this, the neutron capture cross sections are, just like for dataset A, taken from

## 7 Comparisons

the FRDM NON-SMOKER data as long as they are available, i.e. as long as the atomic number of the nuclide lies between 10 and 83. For the rest of the nuclides, the neutron capture cross section is taken from the TENDL library. To calculate the species-loss cross sections for computing the  $\eta_i$  values, we proceeded as follows. If there is NON-SMOKER data available for the nuclide, the species-loss cross section is calculated according to

$$\sigma_{\text{tr},i} = \sigma_{\text{tr},i}^{\text{TENDL}} - \sigma_{\text{n-cap}}^{\text{TENDL}} + \sigma_{\text{n-cap}}^{\text{NON-SMOKER}} \quad (7.4)$$

$$= \sigma_{\text{non-el},i}^{\text{TENDL}} - \sigma_{\text{inel},i}^{\text{TENDL}} - \sigma_{\text{n-cap}}^{\text{TENDL}} + \sigma_{\text{n-cap}}^{\text{NON-SMOKER}} \quad (7.5)$$

where in the second equation, Eq. (2.5) is used. For these calculations, it had to be checked if there is any misalignment on the energy grid for the neutron capture cross section, the non-elastic and the inelastic cross section of the TENDL data. And even though there are some energy misalignments on the energy grid between the inelastic cross section and the neutron capture cross section, this does not lead to any unphysical species-loss cross sections. The cross sections calculated according to Eq. (7.5) largely follow the course of the NON-SMOKER neutron capture cross sections for lower energies, while for higher energies, they are almost the same as the TENDL species-loss cross sections. In the cases for which no NON-SMOKER data is available, the species-loss cross sections from TENDL-2019 are used.

In the following, the numerical results for the first neutron source calculated with dataset A and B will be compared to the original results shown in chapter 6. For this, the relative deviations of the abundances  $N_i$  and, for the saturation conditions, the pulse numbers  $N_{\text{pulses},i}$  are calculated according to

$$\text{relative deviation} = \frac{|N_i(\text{Dataset A/B}, f_{\text{rep}}) - N_i(f_{\text{rep}})|}{N_i(f_{\text{rep}})} \quad (7.6)$$

$$\text{relative deviation} = \frac{|N_{\text{pulses},i}(\text{Dataset A/B}, f_{\text{rep}}) - N_{\text{pulses},i}(f_{\text{rep}})|}{N_{\text{pulses},i}(f_{\text{rep}})}, \quad (7.7)$$

respectively, for dataset A/B. These deviations are calculated on the same energy grids as used for the calculation of the results in chapter 6. Therefore, energy ranges between 50 keV and 10 MeV are considered, with 300 and 100 logarithmically spaced energies for 1 and  $10^4$  pulses of the first neutron source, respectively. For the saturation conditions, the energy grid consists of 80 grid points. Of these, 40 are distributed logarithmically spaced over the whole energy range, and 40 more energy grid points are found in the interval between 1 and 10 MeV, because the pulse numbers required to reach the saturation vary most there. Therefore, when considering the mean relative deviations for the saturation condition results, it should be noted that the deviations for high energies are given more weight than those for low ones.

### 7.3.1 Comparison of the Original Results with the Results Calculated From Dataset A

At first, a comparison of the original results shown in chapter 6 with the results calculated with dataset A is performed. The minimal, maximal, and mean relative deviations are shown in Fig. 7.3 for the two sets of nuclides. It is illustrated in this figure that for isotopes enriched by only one neutron, the deviations are much smaller than those of the other populations, with the mean relative deviations between  $7.1 \times 10^{-11}$  for Sb and  $8.6 \times 10^{-9}$  for Es. The reason for this is that the populations, in leading order in  $\mu_i$  and  $\eta_i$  (see Eq. (5.28)), depend on the  $\mu_i$  values and, therefore, the neutron capture cross sections for the nuclides with less neutrons, which, in the case of the 1-species, are only the seed nuclides. Because for those, ENDF/B-VIII.0 data is used in both of the datasets, the  $\mu_0$  values are the same. The deviations come from higher order terms. For  $N_1$ , they are especially due to the different  $\eta_i$  values, which amount to  $10^{-12}$  and  $10^{-8}$ , depending on the mean neutron energy, just like the mean relative deviations of  $N_1$ . Therefore, the  $N_1$  relative deviations are greatest where the  $\sigma_{tr}$  values differ most for the different datasets, like the fissile, heavy nuclides Es and Am, as for these nuclides the transmutation cross section for dataset A is approximated with that of ENDF, and the TENDL library's greatest uncertainty is the determination of fission transmission coefficients, as discussed in chapter 2.

For the populations  $N_2 - N_4$  of isotopes enriched by more than 1 neutron after one pulse, the mean relative deviations are significantly higher than for  $N_1$  with mean deviations greater than  $2.5 \times 10^{-1}$  for all of the nuclides and populations. Therefore, it is plausible to say that these deviations mainly depend on the deviations of the neutron capture cross sections used in the different datasets on which the populations depend in leading order. It becomes clear from the significant relative deviations that occur for the nuclides with  $Z < 84$ , for which NON-SMOKER neutron capture cross sections are used for the calculations of  $\mu_i$ ,  $i > 0$ , that the cross sections calculated from these two codes differ. As explained in chapter 2, the TALYS code, on which TENDL-2019 is mainly based, includes pre-equilibrium and direct effects, which is not the case for NON-SMOKER, and even in the calculations of compound reaction cross sections with the Hauser-Feshbach model, which should mainly dominate for these nuclides and the considered energy range, that are implemented in both TALYS and NON-SMOKER, the two codes differ in the parameters of the nuclear level densities, the calculation of the width fluctuation correction factors, the way the transmission coefficients are calculated and which transmission coefficients are regarded at all.

For those nuclides (As, Sb, Tm, Lu, Re, Os, Ir and Au), the mean relative deviations for  $N_2 - N_4$  are always in the range between  $2.5 \times 10^{-1}$  and  $9 \times 10^{-1}$  except Sb, for which the mean relative deviation for  $N_4$  reaches over  $2 \times 10^0$ . Generally, the deviations increase with larger  $i$  because

## 7 Comparisons

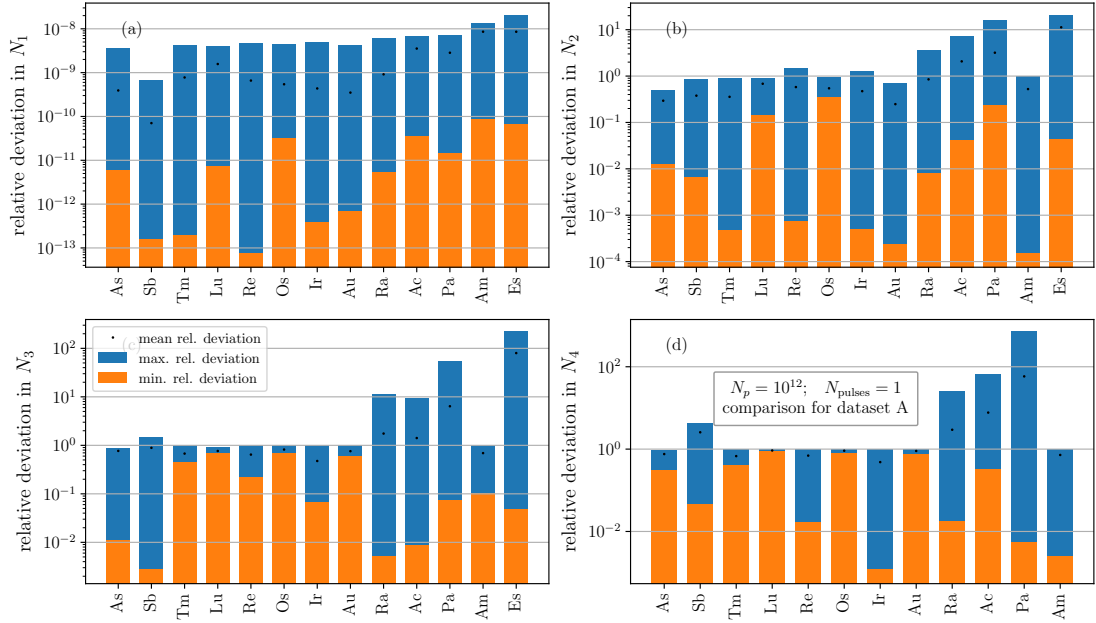


Figure 7.3: Relative deviations of the populations  $N_i$  directly after one pulse of neutron source 1 calculated with dataset A from the population calculated with the original dataset for both sets of nuclides. The deviations for the  $+4n$  nuclide of Es are not shown in subplot d) because it has no half-life.

for growing  $i$ , more neutron capture cross sections influence the population of the  $i$ -species, cross sections that deviate from one dataset to the other. However, this is not the case for Ac, for which the deviation of  $N_3$  is smaller than that for  $N_2$ . This is due to the fact that  $\sigma_{n-cap,1}$  for TENDL is lower than the ENDF cross section for most energies, while  $\sigma_{n-cap,2}$  is higher, so that the deviations cancel each other out to some degree.

Among the two sets of nuclides are also several seeds with  $Z > 84$  for which no NON-SMOKER data is available. For these nuclides - Ra, Ac, Pa, Am and Es - the mean relative deviations for all  $N_i$  are significantly higher than for those for which NON-SMOKER data is used for the  $\mu_i$  and  $\eta_i$  values for  $i > 0$  in dataset A. For  $N_3$  and  $N_4$ , all mean relative deviations for these nuclides exceed  $10^0$  apart from Am. For the population of the 3-species, the mean relative deviation for Es even reaches 80. The highest relative deviations - at least for the populations for which their half-time is not zero - are those for the neutron-enriched isotopes for  $^{255}\text{Es}$ . This is due to the fact that for Es, the TENDL neutron capture cross sections for the neutron-enriched nuclides are at least about one order of magnitude smaller than the ENDF cross section for the seed for all energies.

Apart from the relative deviations, we have investigated the ratios between the populations

### 7.3 Comparison of the Results for Different Cross Section Datasets

calculated with the original dataset and those for dataset A. The analysis of these ratios confirms that the deviations of  $N_1$  are due to variations in  $\sigma_{\text{tr},1}$ , and the deviations of  $N_2 - N_4$  are mainly caused by the different neutron capture cross sections. For  $N_1$ , the ratios all show extrema around the energy where the rapid rise of  $\sigma_{\text{tr}}$  due to particle emission reactions sets in, as this point is different for the ENDF and TENDL transmutation cross sections. Moreover, the ratios indicate that the populations  $N_1$  for dataset A are slightly higher than those for the TENDL data in the original dataset. Like the deviations, the ratios between the populations deviate more from one for  $N_2 - N_4$ , with typical values of the ratios between  $10^{-1}$  and  $10^1$  for energies up to a few MeV. For high energies, the ratios are mostly lower for the nuclides with  $Z < 84$ , for which the neutron capture cross sections in the TENDL data experience a rise, while this is not the case for most NON-SMOKER cross sections. Especially, however, the ENDF cross section for Am, which is used in dataset A, shows a steep decrease for high energies, while the TENDL cross section does not, leading to ratios as low as  $10^{-4}$  for this nuclide. Generally, the populations produced with dataset A are lower than the original results for most energies, except for Sb, Am, Pa and Es, for which the opposite is the case. One of the reasons that the original abundances are higher than for dataset A is most probably the fact that in the TENDL data, more models and processes are incorporated than in NON-SMOKER, making the neutron capture cross sections generally higher.

Knowing that the abundances of most nuclides for dataset A are lower than the original ones, the mean relative deviations of up to  $9 \times 10^{-1}$  for the nuclides for which NON-SMOKER data is available can be interpreted as the abundances for dataset A being one order of magnitude lower than the original results.

We now turn to analyze the deviations between the abundances after  $10^4$  pulses with the first neutron source. The mean relative deviations of the abundances  $N_i$  are shown in Fig. 7.4. For  $N_1$ , the first thing that is noticeable is that the mean relative deviations for the regarded nuclides are up to four orders of magnitude higher than those for 1 pulse as the deviations are up to  $10^4$  times as high as for one pulse. This is due to the fact that in every pulse, nuclides are lost due to transmutation, so that the influence of this effect becomes greater with increasing pulse number. Furthermore, it can be observed that the mean relative deviations of the abundances of nuclides get higher with increasing repetition rate. Especially from  $f_{\text{rep}} = 1/60$  Hz to  $f_{\text{rep}} = 1$  Hz, there is a significant increase for all considered seed nuclei, which is biggest for the nuclides with the lowest half-lives of the 1-species isotope, i.e. Es and Ra with half-lives of 25 min and 42 min, respectively. Specifically for Es it is striking that, while the mean relative deviation for this nuclide is highest for 1 pulse, it is the second lowest for  $f_{\text{rep}} = 1/60$  Hz after that of Ra. Furthermore, for Lu, for which the deviations of the transmutation cross sections are lower than those for Ac, Pa, Am and Es, the relative deviations are the highest of all nuclides for

## 7 Comparisons

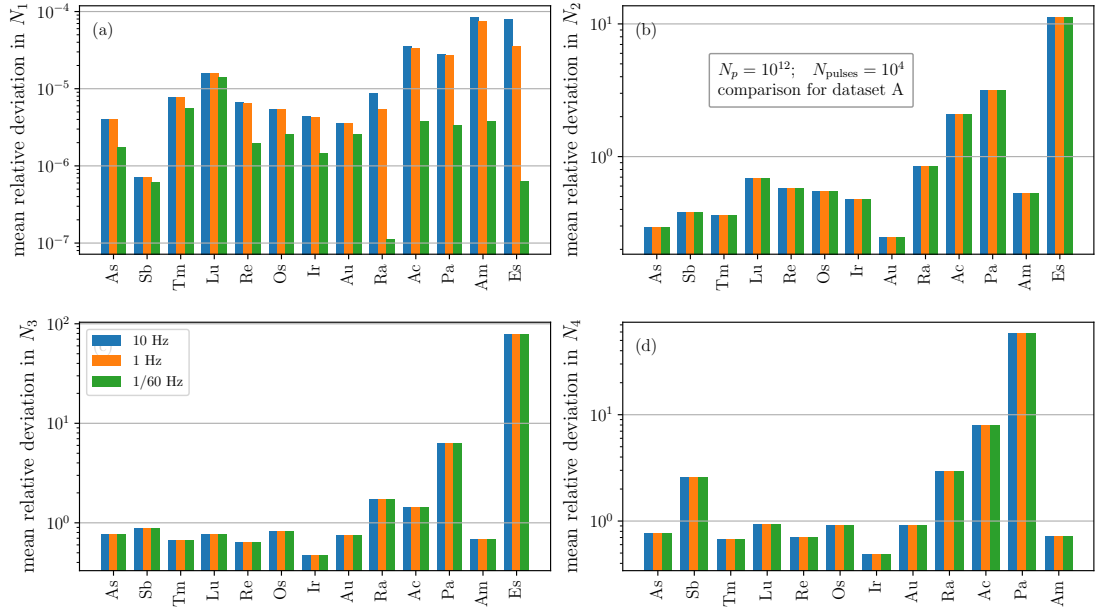


Figure 7.4: Mean relative deviations of the populations  $N_i$  directly after  $10^4$  of neutron source 1 calculated with dataset A from the population calculated with the original dataset for both sets of nuclides. The deviations for the  $+4n$  nuclide of Es are not shown in subplot d) because it has no half-life.

$f_{\text{rep}} = 1/60$  Hz because the 1-species of Lu has the lowest half-life, so that the transmutation has the greatest influence on Lu for this low repetition rate. Generally, the relative deviations are, hence, lower the higher the repetition rate and the shorter the half-lives of the nuclides of the 1-species are, and, thus, the more radioactive decay influences the populations, as for a high influence of radioactive decay the differing cross sections play a comparably smaller role.

For  $N_2 - N_4$ , the deviations seem to be the same for the different repetition rates. When comparing them directly, one can see that the ratios between the 10 Hz and the 1/60 Hz deviations only differ from one by up to  $10^{-4}$ . Therefore, the effect of the different repetition rates is negligible when regarding the mean standard deviations for  $N_2 - N_4$ . In fact, the deviations for  $10^4$  pulses are not even significantly different than for only one pulse with the ratios between the relative deviations differing from one by not more than  $10^{-4}$  as well. Therefore, the deviations of the neutron capture cross sections of the two datasets are the main reason for the deviations of the populations  $N_2 - N_4$ , and the abundances for nuclides for which NON-SMOKER data exists being about one order of magnitude smaller on average for the first dataset is applicable here as well.

We now turn to compare the saturation condition 1. In Figs. 7.6 and 7.5, the mean relative

### 7.3 Comparison of the Results for Different Cross Section Datasets

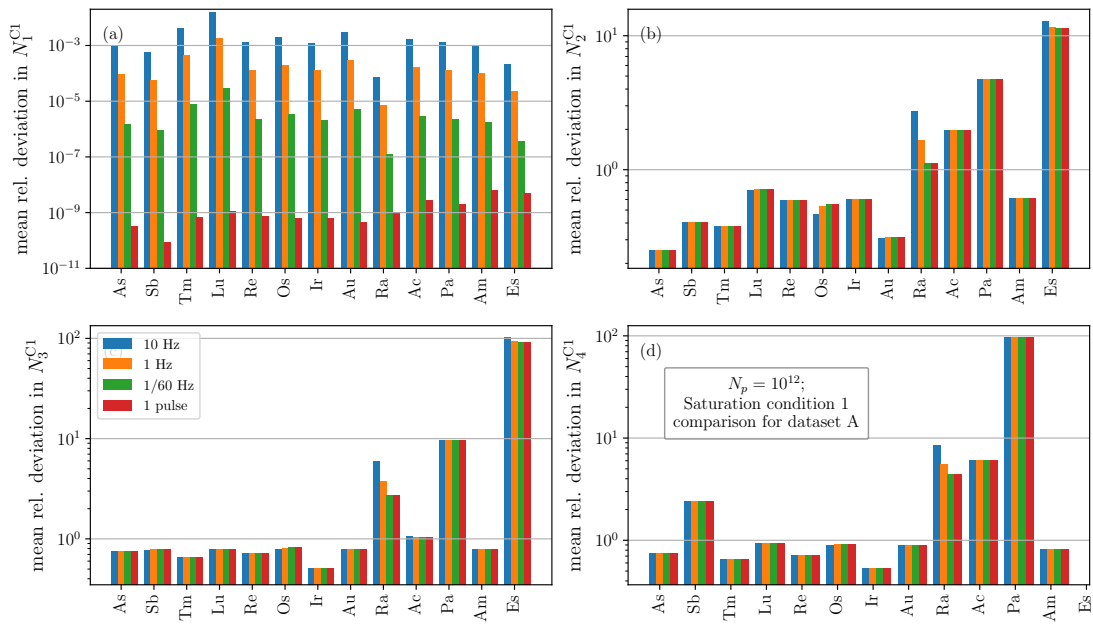


Figure 7.5: Mean relative deviations of the maximal populations  $N_i^{C1}$  calculated with dataset A from the population calculated with the original dataset for both sets of nuclides and for the three different repetition rates compared to the mean relative deviations after 1 pulse, all calculated on the same energy grid. The deviations for the  $+4n$  nuclide of Es are not shown in subplot d) because it has no half-life.

## 7 Comparisons

deviations of the pulse numbers  $N_{\text{pulses},i}^{\text{C1}}$  to reach the first saturation condition as well as the maximal abundances possible to reach with the first neutron source,  $N_i^{\text{C1}}$ , are shown, respectively. The deviations of  $N_1^{\text{C1}}$ , as the deviations of the populations  $N_1$  after 1 and  $10^4$  pulses, vary in leading order only due to the different nuclear transmutation cross sections  $\sigma_{\text{tr},1}$  of the 1-species. The mean relative deviations shown in Fig. 7.5 (a) vary from  $10^{-9}$  for Ra at  $f_{\text{rep}} = 1/60$  Hz to over  $10^{-2}$  in case of Lu. For all nuclides, the mean relative deviations of the maximal population  $N_1^{\text{C1}}$  exceed those for 1 pulse, and the deviations are also higher than those for  $10^4$  pulses for all nuclides and repetition rates except for Ra, Ac, Pa, Am and Es in case of  $f_{\text{rep}} = 1/60$  Hz. That the deviations are higher for the maximal abundances is, firstly, due to the fact that more pulses are applied than only  $10^4$  except for Ra, Ac, Pa, Am and Es in case of  $f_{\text{rep}} = 1/60$  Hz. Furthermore, especially for 1 Hz and 10 Hz, the pulse numbers of long-lived nuclides like Lu are also influenced by  $\sigma_{\text{tr},1}$ , so that not only the loss of nuclei smaller for lower transmutation cross sections, but also more pulses are applied at these energies, therefore making the abundance greater. For Ra, Ac, Pa, Am and Es however, the maximal populations at a repetition rate of 1 pulse per minute are all reached before  $10^4$  pulses and, as can be seen in Fig. 7.6, the pulse numbers for  $f_{\text{rep}} = 1/60$  Hz do not even vary for Ra, Am, and Es for the two datasets because of the low half-lives  $T_{1/2}^{+1n}$ .

For all 1-species isotopes, the loss due to decay is higher than due to transmutation. However, the higher the repetition rate and the longer the half-lives of the isotopes, the more influential neutron-induced transmutation reactions become. Therefore, and because for higher repetition rates, more pulses are applied, the deviations of  $N_1^{\text{C1}}$  increase with increasing repetition rate. For  $10^4$  pulses, it has, moreover, already been seen for a repetition rate of  $f_{\text{rep}} = 1/60$  Hz that instead of the magnitude of the deviations only depending on how much the cross sections themselves deviate, it is heavily influenced by the half-lives of the  $N_1$  nuclides with the deviations being higher for higher half-lives. This is also the case for  $N_1^{\text{C1}}$  for all repetition rates, so that, for example, Lu with the longest  $T_{1/2}^{+1n}$  has the highest deviation, but the Es isotopes, which has the lowest half-live, still has a higher deviation than Ra because of its generally large differences between the transmutation cross sections for the two datasets.

When analyzing the mean relative deviations of  $N_2^{\text{C1}} - N_4^{\text{C1}}$ , one notices that for most nuclides, they cannot be visibly distinguished for the different repetition rates. For most repetition rates, they are even virtually the same as for one pulse and, therefore, dominated primarily by the differences of the neutron capture cross sections. However, this is not the case for isotopes of Es, Ra and Os with 2 or more additional neutrons and, therefore, the three nuclides for which  $T_{1/2}^{+2n}$  is highest and the transmutation loss has the greatest influence. Furthermore, for all of these nuclides, analysis on the nuclear transmutation cross sections shows that they vary for the two datasets 1 and 2 by up to 1 order of magnitude. Therefore, as detailed a detailed analysis

### 7.3 Comparison of the Results for Different Cross Section Datasets

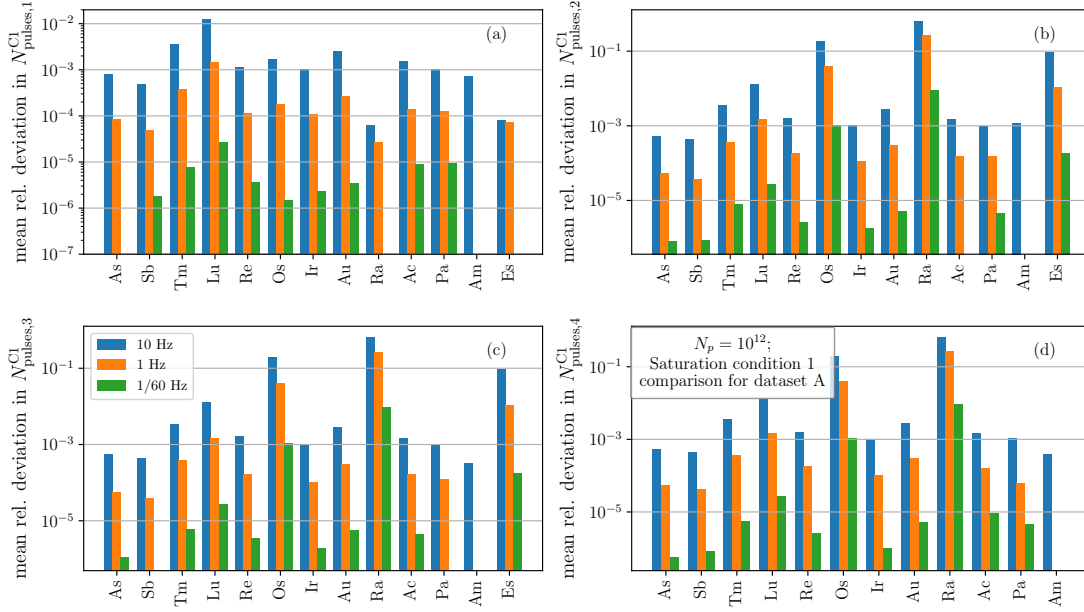


Figure 7.6: Mean relative deviations of the numbers of pulses  $N_{\text{pulses},i}^{\text{C1}}$  it takes to reach the maximal populations  $N_i^{\text{C1}}$  for dataset A from those calculated with the original dataset for both sets of nuclides and for the three different repetition rates. The deviations for the  $+4n$  nuclide of Es are not shown in subplot d) because it has no half-life.

of the ratios between the populations shows, the differing deviations are due to the differing  $\sigma_{\text{tr},2}$  values in the different datasets. Depending on whether the different neutron capture and transmutation cross sections in dataset A cause the resulting abundances  $N_2^{\text{C1}} - N_4^{\text{C1}}$  to change in the same or in an opposite way, the deviations increase or decrease with higher repetition rate and, therefore, a higher influence of nuclear transmutation.

For the relative deviations of the pulse numbers  $N_{\text{pulses},i}^{\text{C1}}$ , Fig. 7.6 shows that the deviations increase with higher repetition rate, like the deviations of  $N_1^{\text{C1}}$ . There are even several nuclides for which relative deviations of the pulse numbers for  $f_{\text{rep}} = 1/60 \text{ Hz}$  are 0. This is due to the fact that for  $f_{\text{rep}} = 1/60 \text{ Hz}$ , the energy dependence of the pulse numbers comes mostly from the seed nuclide transmutation cross section for most of the considered nuclides, which is the same in both datasets. The influence of the (differing) transmutation cross section of the neutron-enriched nuclides on the pulse numbers is so small for all nuclides except all Lu-isotopes and the 2- to 4-species isotopes of Ra, Os, and Es that the pulse numbers for the different datasets vary by at most 1-3 pulses. Lu, Ra, Os, and Es, however, have neutron-rich isotopes with sufficiently high transmutation cross sections and half-lives for the deviations to reach values over  $10^{-3}$  in case of Ra.

## 7 Comparisons

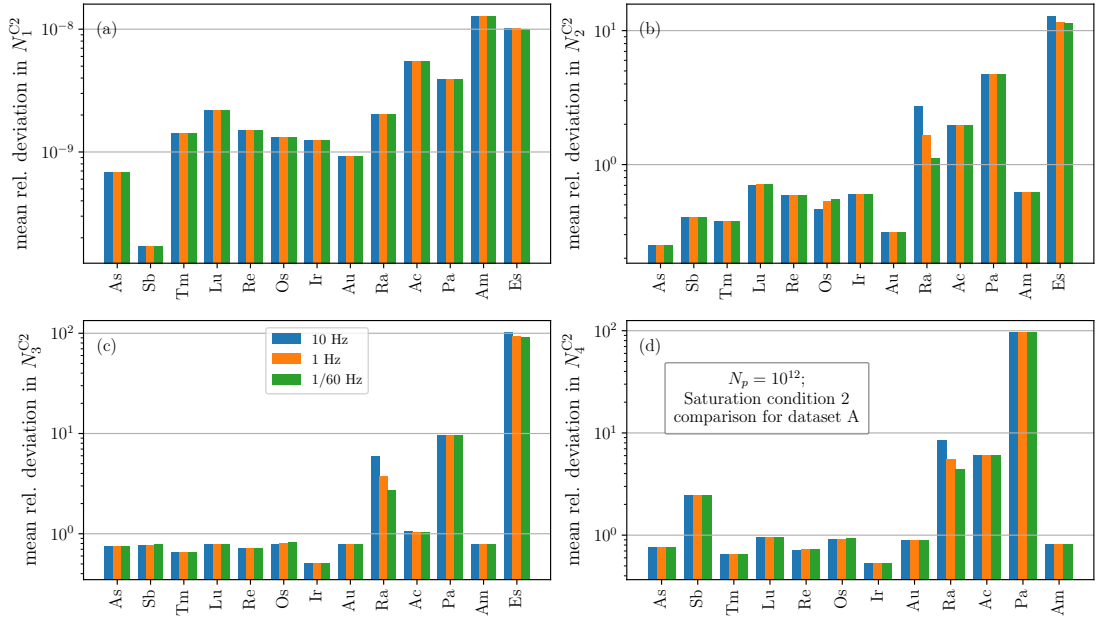


Figure 7.7: Mean relative deviations of the populations  $N_i^{C2}$  at the second saturation condition for dataset A from the population calculated with the original dataset for both sets of nuclides and for the three different repetition rates. The deviations for the  $+4n$  nuclide of Es are not shown in subplot d) because it has no half-life.

For all repetition rates, the deviations are highest for nuclides with a high half-life and a high deviation of nuclear transmutation on the species-loss. For  $f_{\text{rep}} = 1$  Hz and  $f_{\text{rep}} = 10$  Hz, the influence of nuclear transmutation is also high enough for most nuclides for the pulse numbers to differ by significantly more than only 100 or 1000 pulses for  $f_{\text{rep}} = 1$  Hz and  $f_{\text{rep}} = 10$  Hz, respectively. Therefore, the longest-lived nuclide  $^{177}\text{Lu}$  for  $N_1$  shows deviations of  $N_{\text{pulses},i}^{C1}$  of over  $10^{-2}$  for  $f_{\text{rep}} = 10$  Hz, while for  $N_2 - N_4$  the relative deviations for Ra and Os even exceed  $10^{-1}$  for  $f_{\text{rep}} = 10$  Hz. The only nuclide for which there are not even deviations for  $f_{\text{rep}} = 1$  Hz is Am, due to its generally low half-lives of both the seed nuclide and the neutron-enriched isotopes.

Lastly, we compare the pulse numbers and abundances of the nuclides at the second saturation condition. For this purpose, the mean relative deviations of the abundances  $N_i^{C2}$  and the pulse numbers to reach saturation condition 2 are shown in Figs. 7.7 and 7.8. The analysis of the relative deviations of the abundances shows that because for  $N_1$ , the second saturation condition is already reached after 2 pulses, the deviations of  $N_1^{C2}$  are up to two times higher than for the  $N_1$  abundances after one pulse. Furthermore, the figure shows that for the short-lived Ra, the mean relative deviations for a repetition rate of 1/60 Hz are smaller than for the other two rates.

### 7.3 Comparison of the Results for Different Cross Section Datasets

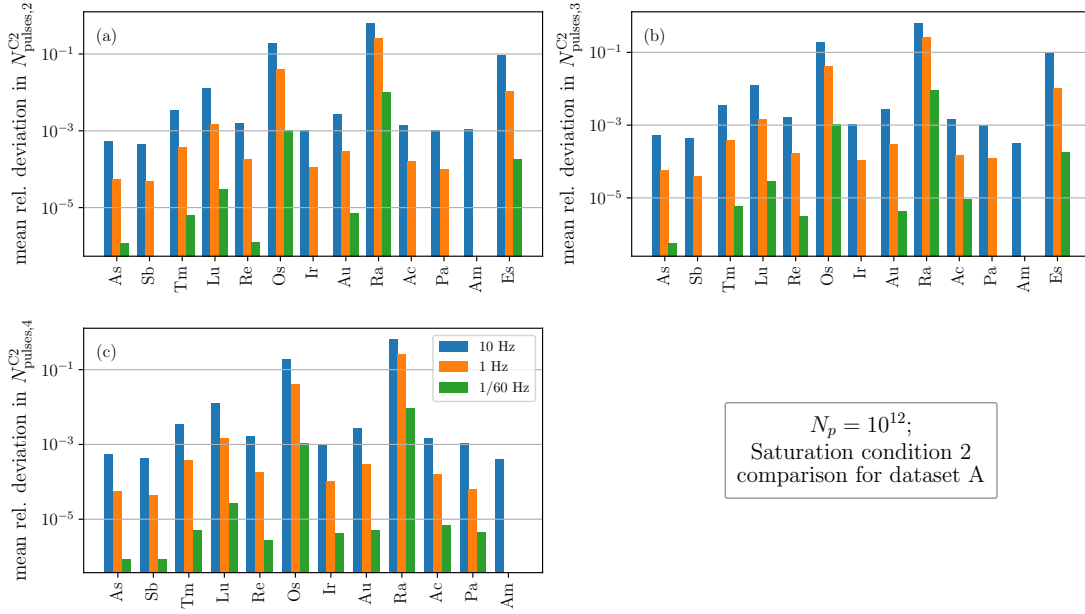


Figure 7.8: Mean relative deviation of the numbers of pulses  $N_{\text{pulses},i}^{\text{C2}}$  it takes to reach the second saturation condition for dataset A from the population calculated with the original dataset for both sets of nuclides and for the three different repetition rates. The deviations for the  $+4n$  nuclide of Es are not shown in subplot d) because it has no half-life.

For  $N_i^{\text{C2}}$  with  $i > 1$ , a comparison of Fig. 7.7 with Fig. 7.5 shows that the mean relative deviations are very similar, especially for high repetition rates and high  $i$ . This is due to the fact that especially for high  $f_{\text{rep}}$  and high  $i$  the pulse numbers required for the two saturation conditions only differ by 100 for 1 Hz and 1000 for 10 Hz, so that the abundances are almost the same as well. The mean relative deviations, in fact, only differ from those for the first saturation condition by at most  $10^{-5}$  for all  $N_i^{\text{C2}}$  with  $i > 1$ , with the deviations for saturation condition 2 both slightly higher and lower than for the first condition, depending on the nuclide and the repetition rate.

In Fig. 7.6 the mean relative deviations of the pulse numbers are shown for  $N_{\text{pulses},2}^{\text{C2}} - N_{\text{pulses},4}^{\text{C2}}$ . For  $N_{\text{pulses},1}^{\text{C2}}$ , it does not make sense to show the deviations because for dataset A, the second saturation condition for the 1-species isotopes is reached after 2 pulses for all seed nuclides too. For the pulse numbers  $N_{\text{pulses},2}^{\text{C2}}$ , not only Am and Ac do not show any deviations for a repetition rate of 1/60 Hz as it is the case for  $N_{\text{pulses},2}^{\text{C1}}$  but also Pa, Sb, and Ir, as is the case for  $N_{\text{pulses},3}^{\text{C2}}$ . Moreover, the deviations of  $N_{\text{pulses},2}^{\text{C2}} - N_{\text{pulses},4}^{\text{C2}}$  can be both higher and lower compared to those for the pulse numbers for the first saturation condition, depending on the nuclide. This could be due to the fact that while the influence of the transmutation cross section is decreased, that of the population  $N_i(1 \text{ pl})$  is higher. Generally, the differences between the deviations for the two

## 7 Comparisons

saturation conditions are highest relative to the deviations themselves for the repetition rate of 1/60 Hz, because for this repetition rate, the mean relative deviations for  $N_{\text{pulses},i}^{\text{C1}}$  as well as  $N_{\text{pulses},i}^{\text{C2}}$  are only due to absolute deviations of a few pulses. For 1 Hz, the deviations of the pulse numbers for Sb and Pa are also only caused by variations of at most 100 pulses, so that the mean relative deviations for  $N_{\text{pulses},2}^{\text{C2}} - N_{\text{pulses},4}^{\text{C2}}$  for these nuclides also differ from those for  $N_{\text{pulses},2}^{\text{C1}} - N_{\text{pulses},4}^{\text{C1}}$  by values only one order of magnitude lower than the mean relative deviation itself. For the other nuclides for a repetition rate of 1 Hz and for all seeds for 10 Hz, the differences are at least two orders of magnitude lower than the mean relative deviations.

### 7.3.2 Comparison of the Original Results with the Results Calculated From Dataset B

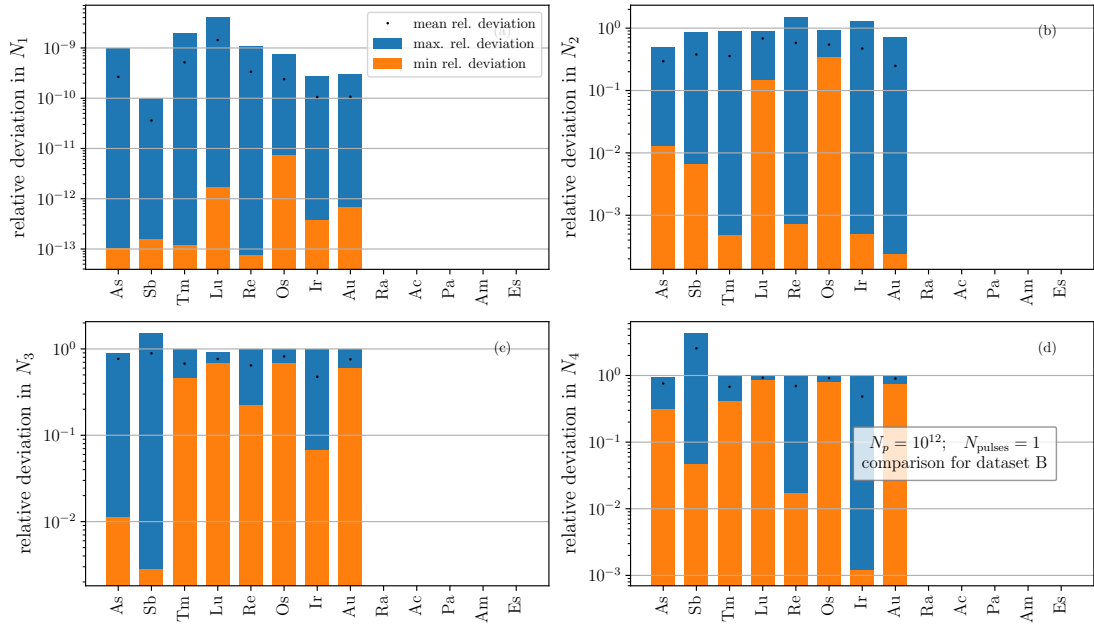


Figure 7.9: Relative deviations of the populations  $N_i$  directly after one pulse of neutron source 1 calculated with dataset B from the population calculated with the original dataset for both sets of nuclides.

Now, we turn to the analysis of the deviations between the original results and the results calculated from dataset B. We first compare the  $N_i$  after one pulse of the first neutron source. The mean relative deviations are shown in Fig. 7.9. We note that there is no deviation for all nuclides with  $Z > 83$ . This is due to the fact that for these nuclides, for which there is no NON-SMOKER data available, TENDL data is used. Hence, the cross sections are the same for the two datasets, and so are the populations  $N_i$ . Furthermore, the  $N_2 - N_4$  mean relative deviations are virtually the same as the ones from the comparison for dataset A. The reason for this is that for nuclides with NON-SMOKER data available, in both dataset A and B the neutron

### 7.3 Comparison of the Results for Different Cross Section Datasets

capture cross sections from the NON-SMOKER code are used, and the only difference lies in the way the nuclear transmutation cross sections are calculated. As the abundances depend on the neutron capture cross sections in leading order, which are the same for the datasets, the deviations hardly differ for dataset A and B.

For the relative deviations of  $N_1$ , the deviations mainly depend on  $\eta_1$ . As analyzed when introducing dataset B,  $\eta_1$  is dominated by the NON-SMOKER neutron capture cross section for low energies and by the nuclear transmutation cross section in TENDL for higher energies. Therefore, the relative deviations for  $N_1$  calculated with dataset B from the population of the original results are all about a factor of 1-2 lower than the relative deviations for dataset A because there are especially no high deviations of the transmutation cross sections at energies at which particle emission reactions set in, and, therefore, in the energy range which is given most weight due to the used energy grid.

We now turn to the comparison of the abundances after  $10^4$  pulses. The mean relative deviations are shown in Fig. 7.10. It is shown that, like for the comparison of the original results with those for dataset A, the mean relative deviations for  $N_2 - N_4$  are virtually the same for all repetition rates, and they do not even visibly differ from the deviations for one pulse. For  $N_1$ , the same phenomena as for the comparison with dataset A can be observed, i.e. that the relative deviations have increased by up to  $10^4$  compared to 1 pulse and that they increase with higher repetition rate, higher deviations of  $\sigma_{tr,1}$  and higher  $T_{1/2}^{+1n}$ . Furthermore, just like for 1 pulse, the mean relative deviations for  $N_1$  are lower than for the comparisons for dataset A.

Now, the comparisons for the first saturation condition are carried out. The mean relative deviations of the pulse number  $N_{pulses,i}^{C1}$  required to reach the first saturation condition, as well as the deviations of the maximal abundances  $N_i^{C1}$  are shown in Figs. 7.12 and 7.11, respectively. Because for the nuclides Ra, Ac, Pa, Am, and Es, the data used in the two datasets does not differ, only the mean relative deviations of As, Sb, Tm, Lu, Re, Os, Ir and Au are shown in Figs. 7.11 and 7.12. The deviations of  $N_1$ , as for the comparison for dataset A, grow with increasing repetition rate. Moreover, it is shown that, as in the comparison for dataset A, the deviations of the maximal populations do not only depend on how much the transmutation cross sections deviate, but also on the half-lives of the nuclides. Furthermore, it can be seen that the deviations are generally lower than in the comparison for dataset A because the transmutation cross sections do not differ as much as in the case of the comparison for dataset A, especially for energy above 5 MeV. For the populations of even more neutron-rich isotopes, the deviations are dominated by those of the neutron capture cross sections for the most part as well, so that most deviations are similar to those for 1 pulse. However, the populations  $N_2$  of Sb, Tm, Lu, Re, Os and Au,  $N_3$  of As, Tm, Lu, Re and Os, and  $N_4$  of Os show deviations that visibly differ from

## 7 Comparisons

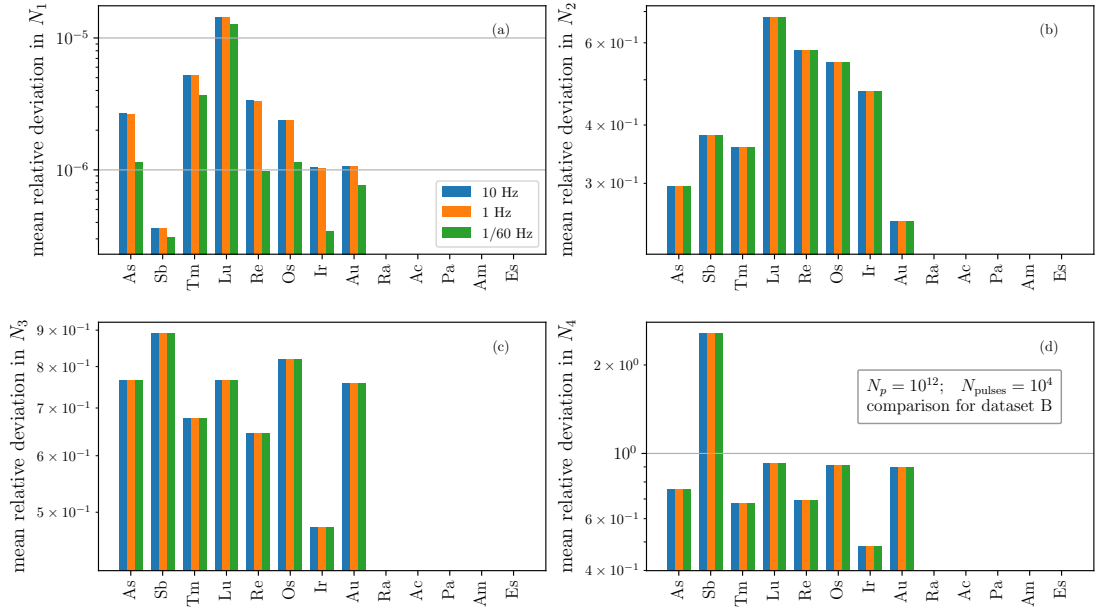


Figure 7.10: Mean relative deviations of the populations  $N_i$  directly after  $10^4$  of neutron source 1 calculated with dataset B from the population calculated with the original dataset for both sets of nuclides.

those for 1 pulse. This can, again, be explained with the influence of the transmutation cross sections on the maximal abundances, which grows larger for lower delay times and, therefore, higher repetition rates.

For the mean relative deviations of the pulse numbers, the same effect can be seen as in the comparison for dataset A: Again, the deviations increase with increasing repetition rate, and the pulse numbers for  $f_{\text{rep}} = 1/60$  Hz hardly deviate. However, the deviations are generally smaller than in the comparison for dataset A because of the lower deviations between the transmutation cross sections for high energies.

Lastly, we turn to the comparison of the results for the second saturation condition. In Figs. 7.13 and 7.14 the mean relative deviations of the pulse numbers and abundances at the second saturation condition are shown. As shown in Fig. 6.25, the mean relative deviations of the abundances  $N_1^{C2}$  at the second saturation condition and, therefore, after 2 pulses are up to 1.6 times as high as for 1 pulse. For the abundances of isotopes enriched by more nuclides, moreover, the mean relative deviations vary from the deviations for the first saturation condition at most by values on the order of  $10^{-9}$ . Therefore, the relative deviations of the abundances  $N_i^{C2}$  calculated from dataset B from those calculated with the original dataset differ less from from the deviations of  $N_i^{C1}$  than it is the case for the comparison for dataset A. Furthermore, like

### 7.3 Comparison of the Results for Different Cross Section Datasets

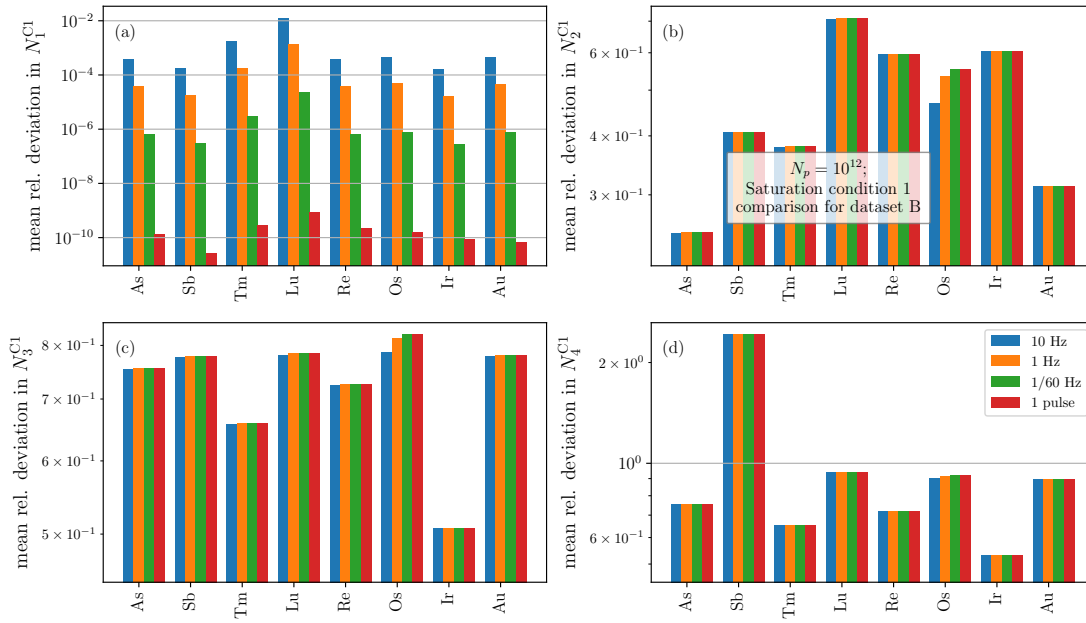


Figure 7.11: Mean relative deviations of the maximal populations  $N_i^{CI}$  calculated with dataset B from the population calculated with the original dataset for both sets of nuclides and for the three different repetition rates compared to the mean relative deviations after 1 pulse, all calculated on the same energy grid. Because there are no deviations for Ra, Ac, Pa, Am, and Es, the deviations for these nuclides are not shown.

## 7 Comparisons

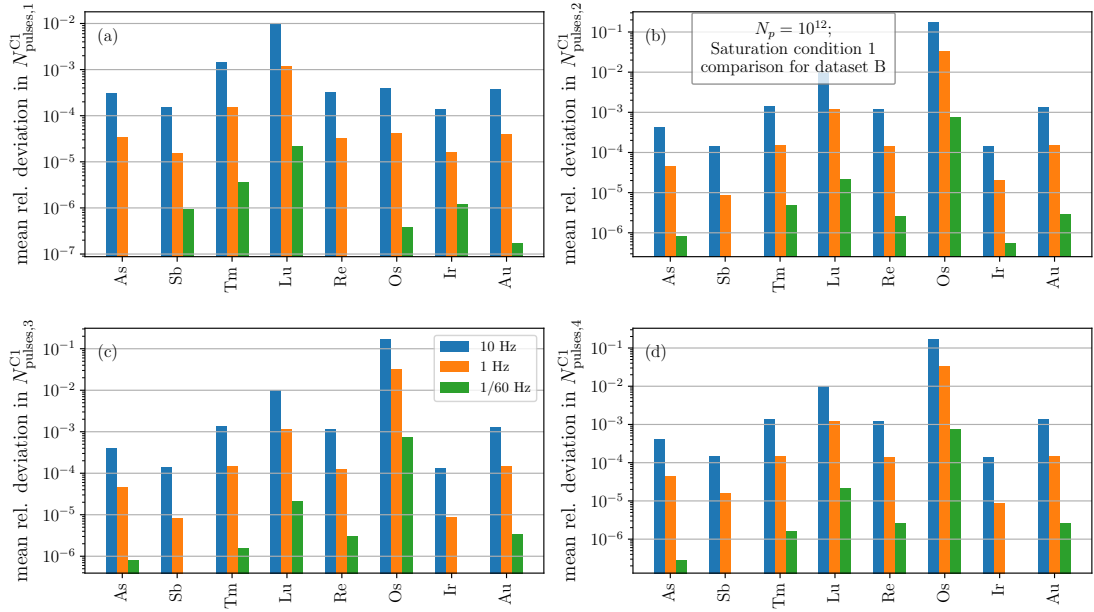


Figure 7.12: Mean relative deviations of the numbers of pulses  $N_{\text{pulses},i}^{\text{C1}}$  it takes to reach the maximal populations  $N_i^{\text{C1}}$  for dataset B from those calculated with the original dataset for both sets of nuclides and for the three different repetition rates. Because there are no deviations for Ra, Ac, Pa, Am, and Es, the deviations for these nuclides are not shown.

for the comparison of the  $N_i^{\text{C2}}$  abundances for dataset A, the deviations of  $N_i^{\text{C2}}$  can be either higher or lower than those of the maximal abundances, depending on the repetition rate and the nuclide.

In the case of the pulse numbers, those for the 1-species isotopes are not shown in Fig. 7.14 because for both datasets, the second saturation condition is reached at the second pulse. Thus, the deviations of  $N_{\text{pulses},i}^{\text{C2}}$  are zero. For  $N_{\text{pulses},2}^{\text{C2}}-N_{\text{pulses},4}^{\text{C2}}$ , the mean relative deviations are, again, very similar to those for  $N_{\text{pulses},2}^{\text{C1}}-N_{\text{pulses},4}^{\text{C1}}$ . A notable difference, however, is that there is no deviation of  $N_{\text{pulses},2}^{\text{C2}}$  between the datasets for Ir. Generally, the mean relative deviations of the pulse numbers can, again, be either higher or lower than those for  $N_{\text{pulses},2}^{\text{C1}}-N_{\text{pulses},4}^{\text{C1}}$ , and the differences relative to the mean relative deviations are greatest for  $f_{\text{rep}} = 1/60$  Hz.

To conclude the comparisons of the results for different datasets, it can be said that the relative deviations for the results calculated with datasets A and B from the original results are very similar for the NON-SMOKER nuclides in the cases that the neutron capture cross sections dominate, especially the populations of nuclei of the 2- to 4-species isotopes, while for quantities for which the differing transmutation cross sections of enriched seed nuclides are the main reason for the differences, the deviations for the comparison with dataset A are generally

### 7.3 Comparison of the Results for Different Cross Section Datasets

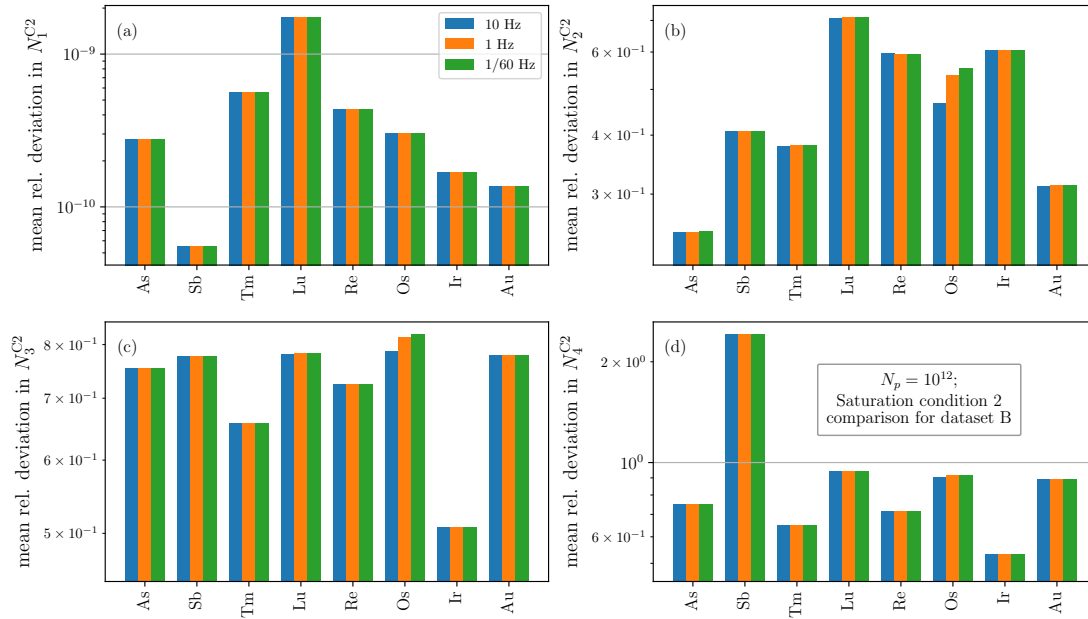


Figure 7.13: Mean relative deviations of the populations  $N_i^{C2}$  at the second saturation condition for dataset B from the population calculated with the original dataset for both sets of nuclides and for the three different repetition rates. Because there are no deviations for Ra, Ac, Pa, Am, and Es, the deviations for these nuclides are not shown.

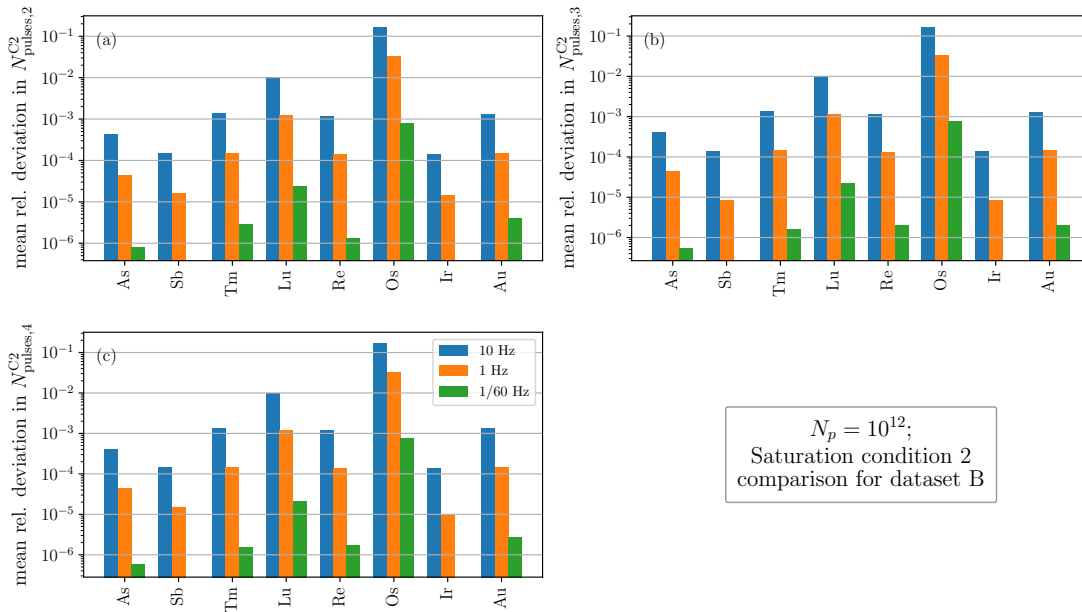


Figure 7.14: Mean relative deviation of the numbers of pulses  $N_{pulses,i}^{C2}$  it takes to reach the second saturation condition for dataset B from the population calculated with the original dataset for both sets of nuclides and for the three different repetition rates. Because there are no deviations for Ra, Ac, Pa, Am, and Es, the deviations for these nuclides are not shown.

## 7 Comparisons

slightly higher than for the comparison with dataset B. Such quantities, like the pulse numbers for the saturation conditions, also do not show too high relative deviations in general, so that for most nuclides, the predictions of the time it takes to reach the saturation illustrated in Fig. 6.12 applies quite well for all three datasets. However, for Ra and Os, the mean relative deviations of over  $10^{-1}$  correspond to quite large absolute differences, considering the theoretical experiment durations for saturation amount to several decades. Moreover, for the populations of  $N_1$ , for which there is experimental data for the seed neutron capture cross section available, which is used in all three datasets, the mean relative deviations are low as well.

For the populations of nuclei of the 2- to 4-species isotopes, however, for which for at least one neutron capture cross section no experimental data is available in the ENDF/B-VIII.0 library, all mean relative deviations are greater than 25%, and they are mainly dependent on the differing neutron capture cross sections, with contributions from the transmutation cross section deviations for the abundances at the saturation conditions. For dataset A, the deviations are especially high for fissile nuclides, for which the TENDL data has relatively high uncertainties, as shown in section 7.1, and for which the cross sections in dataset A are approximated by the seed nuclide data. For nuclides like Es and Pa, the mean relative deviations of the abundances even extend up to  $10^2$  for the deviations of  $N_3$  and  $N_4$ , respectively. For Es, this is especially relevant, because this nuclide has never been produced before in the laboratory before, and a population 2 orders of magnitude higher or lower could highly influence how well it could be studied in the proposed setup. Furthermore, our analysis has shown for both dataset A and B that even for nuclides for which there is NON-SMOKER data available, the  $N_4$  abundances of most nuclides are around 1 order of magnitude lower for the datasets A and B than for the original data. The relatively high deviations of the calculated populations for the different datasets, especially for populations of neutrons enriched with multiple neutrons, is most influential for the populations  $N_3$  and  $N_4$ , which are very low, depending on the setup, because a calculated abundance one or two orders of magnitude higher or lower could make or break if our calculations predict the production of this isotope or not. For example, neutron capture cascades with 4 neutrons cannot be observed for As and Re for the first neutron source operating at a repetition rate of 1 Hz according to the calculations with dataset A and B instead of the original dataset.

The TENDL data has mainly been selected for the original datasets because more models, reaction channels and experimental data are included, and cross section data is available for more nuclides as well. The observations from the comparisons now show how highly the models and input parameters on which the calculated cross sections are based can influence our results. This is especially astonishing because for the calculation of compound nuclear reactions, which, following the considerations from chapter 2, should dominate for neutron capture

### *7.3 Comparison of the Results for Different Cross Section Datasets*

reactions for most energies in the considered range, both libraries base on Hauser-Feshbach calculations, just with different transmission cross sections, width fluctuation corrections and nuclear densities entering the model. This shows that even though the models used in the codes are well established, they still are still subject to high uncertainties. Therefore, these comparisons with different datasets suggest that experimental measurements of cross sections are necessary to improve the current models for nuclear reactions. Furthermore, how highly our results of neutron capture cascades of only a few nuclides are influenced by different cross section data sets used for the neutron capture, but also the transmutation cross sections, also emphasizes the importance of experiments for determining the cross sections of these nuclides to provide better experimental data for the reaction networks in r- and s-process models and, therefore, improve their predictions and help resolve current questions, as for models of these processes even larger reaction networks with even more uncertainties are employed.

## 8 Summary and Conclusion

In this thesis, neutron capture cascades and, therefore, the production of neutron-rich isotopes occurring in single-component targets irradiated by laser-driven neutron sources operating at different repetition rates have been investigated for 13 different seed nuclides ( $^{75}_{33}\text{As}$ ,  $^{126}_{51}\text{Sb}$ ,  $^{176}_{71}\text{Lu}$ ,  $^{187}_{75}\text{Re}$ ,  $^{192}_{76}\text{Os}$ ,  $^{226}_{88}\text{Ra}$ ,  $^{233}_{91}\text{Pa}$ , and  $^{244}_{95}\text{Am}$  in the first set, and  $^{171}_{69}\text{Tm}$ ,  $^{193}_{77}\text{Ir}$ ,  $^{197}_{79}\text{Au}$ ,  $^{227}_{89}\text{Ac}$ , and  $^{255}_{99}\text{Es}$  in the second set). Two neutron sources have been considered in the present work. The first neutron source with the repetition rates of 1 Hz, 10 Hz, and 1/60 Hz and a neutron yield of  $10^{12}$  neutrons per pulse is expected to be achievable at ELI facilities. The second source represents the inertial confinement source at the NIF at LLNL in the USA that is currently under operation, with  $N_p = 10^{16}$  and a repetition rate of 3 pulses per day. It should, however, be noted once again that it is not the goal of this work to model these sources as realistically as possible, but rather the repetition frequencies and total neutron yields possible for these sources are taken to conduct neutron capture studies for a wide range of energies that are available at different laser-driven neutron sources and that are suitable for the theoretical model used. In this framework, we have studied the production of nuclei in one and multiple pulses, the influence of different repetition rates and pulse numbers on our results, and the saturation of the production of neutron-rich isotopes on the basis of two saturation conditions, which could be of great importance when conducting further experiments with the produced nuclei.

For our calculations, we follow the theoretical approach developed by Hill and Wu in Ref. [49], in which neutron capture, nuclear transmutation, damping effects and  $\beta$ -decay have been included. In Ref. [49], the production of neutron-rich nuclides in 1 and  $10^4$  pulses has already been studied for neutron source 1 operating at a repetition frequency of 1 Hz. However, our calculations differ from those in Ref. [49] in so far that cross section data from the ENDF/B-VIII.0 and TENDL-2019 libraries have been employed in our calculations instead of NON-SMOKER data, and we consider a larger area of the irradiated target of  $10^4 \mu\text{m}^2$  instead of  $25 \mu\text{m}^2$ , so that in the scenario of a realistic laser-driven neutron source, a significant amount of neutrons could actually hit the target.

Therefore, to study the the production of neutron-rich nuclides for a more realistic target, the neutron-enrichment of the seed nuclides after one pulse of neutron source 1 has been investigated in this work as well. Our numerical results show, as in Ref. [49], that the populations  $N_i$

of neutron-rich nuclides are generally higher for low energies than for high ones and decrease with increasing  $i$ . Further investigation of the abundance curves carried out by us illustrate that the populations after 1 pulse mainly depend on the employed neutron capture cross sections for the different nuclides involved in the capture cascades. Moreover, though the populations of neutron-rich nuclides are smaller than in Ref. [49] due to the more realistic target size, our results show that with one neutron pulse of the first neutron source, neutron capture cascades with up to 2 captured neutrons can be observed for some nuclides. In case of the second neutron source, which has not been investigated by Hill and Wu [49], even isotopes enriched by 3 neutrons can be observed after only one pulse according to our calculations. Therefore, our results show that it is, indeed, possible to simulate neutron capture cascades similar to those in nucleosynthesis in the laboratory with both investigated laser-driven neutron sources, even if a more realistic, larger target size is chosen than in Ref. [49].

For  $10^4$  pulses of the first neutron source, our results show that it is possible to produce isotopes of the 3-species for all nuclides of the first set for the repetition rates 1 Hz and 10 Hz. However, due to the large target area, our calculations of  $10^4$  pulses of the first neutron source do not show the possibility of observing successive captures of 4 neutrons for any seed nuclides, contrary to the results presented in Ref. [49]. Our results, however, have allowed us to study the influence of different repetition rates on the abundances of neutron-rich species. We have found that the abundances decrease with decreasing repetition rate due to the influence of  $\beta$ -decay, especially for the 3- and 4-species isotopes, which have relatively low half-lives. Therefore, analyses on our results show that the scaling of the populations  $N_i$  and  $N_i^{\text{tot}}$  with the pulse numbers via  $N_{\text{pulses}}^i$ , as proposed in [49], is only applicable for nuclides for which all isotopes involved in the neutron capture cascade leading to the  $i$ -species isotope (or the  $i - 1$ -species isotope in case of  $N_i^{\text{tot}}$ ) have high half-lives, and that this scaling improves with increasing repetition rate. That the half-lives of the nuclides influence the scaling of  $N_i^{\text{tot}}$  has already been proposed by [49], but only in this work is this dependence, as well as the influence of the repetition frequency on the scaling of  $N_i$ , thoroughly investigated. The scaling has, furthermore, been found to be especially weak for nuclides for which the maximal abundance has already been surpassed after the  $10^4$  pulses. In case of the 100 pulses of the second neutron source, the results show that the production of isotopes of seed nuclides enriched by even 4 neutrons is possible for most nuclides, at least for low energies, except for Sb, Ac, and Es. Therefore, neutron capture cascades with up to 4 neutrons can be observed within 100 pulses of the second neutron source for several of the regarded seed nuclides.

The saturation of the production of neutron-rich nuclei with laser-driven neutron sources has been studied in this work on the basis of two saturation conditions. By investigating the point at which the maximal populations are reached for each nuclide and, the saturation condition 1,

## 8 Summary and Conclusion

we have shown the limits of the production of neutron-rich isotopes, and investigated the time when most nuclei of one species are available for further experiments at once. We have found that, generally, the maximal population of an isotope of the  $i$ -species is reached no earlier than that of the  $i - 1$  species. Furthermore, the pulse numbers required for reaching the maximal populations of a nuclide for a fixed neutron source and repetition rate are, in general, higher the higher the half-lives of all isotopes contributing to the neutron capture cascade leading to this nuclide are. Moreover, the pulse numbers show a dependence on the transmutation cross sections, especially on those of the most long-lived isotopes in the neutron capture cascade, with the pulse numbers greatest where  $\sigma_{tr}$  is lowest. For the saturation conditions for the different repetition rates of the first neutron source, approximate scalings of the pulse number with up to  $f_{rep}$  and of the resulting maximal abundances of up to  $f_{rep}^i$  have been found. Because, furthermore, the scaling of the abundances applies better than that of the pulse numbers, which is often significantly weaker than  $f_{rep}$ , the neutron source operating at a higher repetition rate not only produces more neutron-rich nuclei, especially for isotopes of the 3- and 4-species, but it also, generally, takes less time to reach the maximal abundance. In general, however, the pulse numbers required to reach the maximal abundance do not take much longer than 1 month to deliver for most nuclides, except for neutron-rich isotopes of As, Au, Lu, Ra, and Os, for the latter two of which reaching the maximum can take up to several decades, which is experimentally unfeasible. With a repetition rate of 10 Hz, our results suggest it is possible to produce isotopes enriched by 4 neutrons and, therefore, to observe neutron capture cascades of 4 neutrons for all seed nuclides, with maximal abundances  $N_4^{C1}$  greater than 1 for all nuclides but the 4-species of Ac and Es. Therefore, the production of the isotopes  $^{248}\text{Am}$  and  $^{259}\text{Es}$ , which have never been accessed in the laboratory before, is possible for neutron source 1 according to our calculations with a more realistic target, though it takes a larger number of pulses and a higher repetition rate than according to Ref. [49]. However, as the nuclide  $^{259}\text{Es}$  is assumed to decay directly after the production, there are no nuclei of this species remaining after each neutron pulse interaction. Furthermore, the maximal abundances also show that for all repetition rates, the 3-species isotope  $^{258}\text{Es}$  can be produced, which has been experimentally unavailable as well so far. As the maximal abundances show for the second neutron source,  $^{258}\text{Es}$  can also be produced with this source, but the maximal abundances of the 4-species isotopes for several short-lived nuclides, including Am and Es, as well as Sb, Ac, and Ir, do not exceed 1. However, our results still show that the production of 4-species nuclides could be possible for all seed nuclides but Es over the course of  $10^4$  pulses, so that the production of  $^{248}\text{Am}$  is also possible with the second neutron source.

We have also analyzed another saturation condition, i.e. when  $N_i(s) - N_i(s - 1)$  is lower than the abundance  $N_i$  after one pulse. This condition is of experimental importance as it, for example, could indicate when to change the used target to uphold the production speed of

new nuclei. The second saturation condition is always reached at the second pulse for  $N_1$ . For higher  $i$ , the pulse numbers are generally lower than those for the first saturation condition, but the numbers are quite similar, with the pulse numbers for the two conditions growing closer for increasing  $i$  and increasing repetition rate. The greatest deviations between the two conditions can be seen, in case of the first neutron source, for nuclides for which neither the half-life of the 2-species isotope is extremely long nor the half-life of the seed nuclide is too short, and the differences are highest where the transmutation cross sections are lowest. For the second neutron source, the pulse numbers for the second saturation condition for isotopes enriched with more than 1 neutron are, moreover, comparably low if the 1-species decays quickly.

Lastly, the calculated results have been compared for different datasets including cross section data from different libraries, among which is a dataset that uses the exactly same cross section data as is used in Ref. [49]. The comparisons are carried out to check the precision of our results and to illustrate the dependence of the different abundances and pulse numbers investigated in this work on variations in different cross sections. These comparisons show that the differences of the pulse numbers for the saturation conditions and the  $N_1$  populations exhibit quite low relative deviations, which are mainly due to the differing transmutation cross sections. For these quantities, the deviations also increase with the repetition rate and the half-lives of the isotopes. For the populations  $N_2 - N_4$ , for which the mean relative deviations are mainly dominated by the differing neutron capture cross sections, the mean relative deviations are comparably higher and approximately the same for all pulse numbers, repetition rates and saturation conditions, with influences of the transmutation cross section only on the deviations for the saturated abundances. The quite high deviations, especially for  $N_3$  and  $N_4$  for some nuclides, illustrate the high influence of different cross section datasets on our results, and emphasize the need for cross section measurements for the investigated neutron-rich isotopes.

Among the considered seed nuclides are several that are relevant to the r- and s-process of nucleosynthesis, as the seed nuclides  $^{177}\text{Lu}$ ,  $^{198}\text{Au}$ ,  $^{199}\text{Au}$ , and  $^{188}\text{Re}$  lie at or near s-process branchings, especially neutron-rich isotopes of Tm, Lu, Re, Os, Ir, and Au come near the r-process  $N = 126$  waiting point, and the Sb nuclides, as well as the fissile, neutron-rich isotopes of the regarded actinides, could be important in the not very well investigated fission cycling of the r-process. As illustrated in chapter 3, there is an urgent need for the investigation of quantities like  $\beta$ -decay rates, neutron capture cross sections, masses, and fission properties of these nuclides to improve the models for the r- and s-process as well as their predictions. Such improvements could finally make it possible to identify the r-process site, and to improve the stellar models for the s-process as well, which could have a strong impact on studies on the galaxies around us. Therefore, our calculations suggest the production of nuclides experimental studies on which could have an enormous impact on our understanding of the universe.

## 8 Summary and Conclusion

Moreover, our considerations on laser-driven neutron sources have shown that it is possible with them to achieve neutron fluxes similar to those in the r-process. And in fact, our results confirm that neutron capture cascades similar to those in the r-process could be observed in experiments with laser-driven neutron sources, so that not only the production and subsequent study of nuclides important to the r-process seems possible, but also the observation of the r-process itself could be feasible in the laboratory for the first time with laser-driven neutron sources. Moreover, not only nuclides relevant to the r- and s-process are shown to be produced by these sources, but our results also suggest the production of  $^{248}\text{Am}$ ,  $^{258}\text{Es}$ , and  $^{259}\text{Es}$  for the very first time. While  $^{259}\text{Es}$  is assumed to decay instantly, the other two isotopes can be produced in quite large quantities according to our simulations and, therefore, could be experimentally investigated. Therefore, measurements on their nuclear quantities like the mass or their low-lying levels could improve our understanding of the nuclear forces in neutron-rich nuclei and help develop better microscopical models. Moreover, measurements on fission properties or cross sections could be relevant to improving current models for these processes as well. For studies on nuclear collectivity,  $^{129}\text{Sb}$ , which our simulations show to be produced with all considered neutron sources, has been proven recently to be of great interest. Lastly, several of the nuclides that can be produced with laser-driven neutron sources in great abundances, according to our calculations, have medical applications ( $^{177}\text{Lu}$ ,  $^{198}\text{Au}$ ,  $^{199}\text{Au}$ , and  $^{188}\text{Re}$ ), so that laser-driven neutron sources could provide a good alternative to nuclear reactors for producing such isotopes, which could make nuclear medicine more broadly available.

Finally, we note that our calculations could be improved by more elaborate codes, in which, for example, looped processes and the interactions of secondary particles are included, such as the VCINDER code [145] or the FISPACT-II simulation system [146]. Especially for the investigation of the saturation conditions, for which differences between abundances are of importance and for which, therefore, higher-order effects could play a significant role, such codes could give further insight in the mechanisms competing at saturation and allow us to investigate, for example, the scaling of the pulse numbers and abundances for the first saturation condition with the repetition frequency better. Furthermore, quantum mechanical effects like the Zeno effect, which is not accounted for in the present work, could play a role in prohibiting decays of neutron-rich nuclides for high repetition rates of the pulsed neutron sources, though the influence of such an effect is expected to be small as the decay occurs releasing energies of a few MeV, while the time between pulses is not lower than 100 ms.

## Acknowledgements

I would like to thank my supervisors Honorarprofessor Dr. Christoph H. Keitel and Dr. Yuanbin Wu for their suggestions, their comments and their great help.

## Selbstständigkeitserklärung

Ich versichere, dass ich diese Arbeit selbstständig verfasst und keine anderen als die angegebenen Quellen und Hilfsmittel benutzt habe.

Heidelberg, 10.06.

A handwritten signature in black ink, appearing to read "Anna-Maria Fick". The signature is written in a cursive style with a long, sweeping underline.

## Bibliography

- [1] M. Thoennessen. *The Discovery of Isotopes*. Springer International Publishing, 2016. DOI: 10.1007/978-3-319-31763-2.
- [2] M. Thoennessen. “Current status and future potential of nuclide discoveries”. In: *Reports on Progress in Physics* 76.5 (Apr. 2013), p. 056301. DOI: 10.1088/0034-4885/76/5/056301.
- [3] M. Thoennessen. “2018 update of the discoveries of nuclides”. In: *International Journal of Modern Physics E* 28.01n02 (Feb. 2019), p. 1930002. DOI: 10.1142/s0218301319300029.
- [4] A. Schwenk. “Mehr Neutronen gehen nicht”. In: *Physik Journal* 19 (3) (Mar. 2020), pp. 20–22. ISSN: 1617-9439.
- [5] F. Wienholtz et al. “Masses of exotic calcium isotopes pin down nuclear forces”. In: *Nature* 498.7454 (June 2013), pp. 346–349. DOI: 10.1038/nature12226.
- [6] O. B. Tarasov et al. “Discovery of Ca60 and Implications For the Stability of Ca70”. In: *Physical Review Letters* 121.2 (July 2018). DOI: 10.1103/physrevlett.121.022501.
- [7] Z. Y. Zhang et al. “New Isotope Np220 : Probing the Robustness of the N=126 Shell Closure in Neptunium”. In: *Physical Review Letters* 122.19 (May 2019). DOI: 10.1103/physrevlett.122.192503.
- [8] C. Gorges et al. “Laser Spectroscopy of Neutron-Rich Tin Isotopes: A Discontinuity in Charge Radii across the N=82 Shell Closure”. In: *Physical Review Letters* 122.19 (May 2019). DOI: 10.1103/physrevlett.122.192502.
- [9] A. G. James, U. K. Henschke, and W. G. Myers. “The clinical use of radioactive gold (Au198) seeds”. In: *Cancer* 6.5 (Sept. 1953), pp. 1034–1039. DOI: 10.1002/1097-0142(195309)6:5<1034::aid-cnrcr2820060524>3.0.co;2-y.
- [10] E. Allard et al. “188Re-loaded lipid nanocapsules as a promising radiopharmaceutical carrier for internal radiotherapy of malignant gliomas”. In: *European Journal of Nuclear Medicine and Molecular Imaging* 35.10 (May 2008), pp. 1838–1846. DOI: 10.1007/s00259-008-0735-z.
- [11] K. V. Vimalnath, Sudipta Chakraborty, and Ashutosh Dash. “Reactor production of no-carrier-added 199Au for biomedical applications”. In: *RSC Advances* 6.86 (2016), pp. 82832–82841. DOI: 10.1039/c6ra15407g.
- [12] A. Yordanova et al. “Outcome and safety of rechallenge [177Lu]Lu-PSMA-617 in patients with metastatic prostate cancer”. In: *European Journal of Nuclear Medicine and Molecular Imaging* 46.5 (Nov. 2018), pp. 1073–1080. DOI: 10.1007/s00259-018-4222-x.
- [13] M. Prelas et al. *Nuclear Batteries and Radioisotopes*. Springer International Publishing, 2016. DOI: 10.1007/978-3-319-41724-0.

- [14] J. S. Charlton, ed. *Radioisotope Techniques for Problem-Solving in Industrial Process Plants*. Springer Netherlands, 1986. DOI: 10.1007/978-94-009-4073-4.
- [15] F. Käppeler et al. “The s-process: Nuclear physics, stellar models, and observations”. In: *Reviews of Modern Physics* 83.1 (Apr. 2011), pp. 157–193. DOI: 10.1103/revmodphys.83.157.
- [16] M. Arnould, S. Goriely, and K. Takahashi. “The r-process of stellar nucleosynthesis: Astrophysics and nuclear physics achievements and mysteries”. In: *Physics Reports* 450.4-6 (Sept. 2007), pp. 97–213. DOI: 10.1016/j.physrep.2007.06.002.
- [17] E. M. Burbidge et al. “Synthesis of the Elements in Stars”. In: *Reviews of Modern Physics* 29.4 (Oct. 1957), pp. 547–650. DOI: 10.1103/revmodphys.29.547.
- [18] *Connecting Quarks with the Cosmos*. National Academies Press, Mar. 2003. DOI: 10.17226/10079.
- [19] F.-K. Thielemann et al. “Neutron star mergers and nucleosynthesis of heavy elements”. In: *Annual Review of Nuclear and Particle Science* 67 (2017), pp. 253–274.
- [20] T. Kajino et al. “Current status of r-process nucleosynthesis”. In: *Progress in Particle and Nuclear Physics* 107 (July 2019), pp. 109–166. DOI: 10.1016/j.pnpnp.2019.02.008.
- [21] J. J. Cowan et al. “Origin of the Heaviest Elements: the Rapid Neutron-Capture Process”. In: (Jan. 5, 2019). arXiv: 1901.01410v2 [astro-ph.HE].
- [22] A. Arcones. “Der Stern der Weisen”. In: *Physik Journal* 19 (3) (Mar. 2020), pp. 31–37. ISSN: 1617-9439.
- [23] C. Guerrero et al. “Prospects for direct neutron capture measurements on s-process branching point isotopes”. In: *The European Physical Journal A* 53.5 (May 2017). DOI: 10.1140/epja/i2017-12261-2.
- [24] M. Pignatari et al. “The Weak s-Process in Massive Stars and its Dependence on the Neutron Capture Cross Sections”. In: *The Astrophysical Journal* 710.2 (Feb. 2010), pp. 1557–1577. DOI: 10.1088/0004-637x/710/2/1557.
- [25] P. A. Denissenkov et al. “i-process nucleosynthesis and mass retention efficiency in He-shell flash evolution of rapidly accreting white dwarfs”. In: *The Astrophysical Journal Letters* 834.2 (2017), p. L10.
- [26] O. Clarkson, F. Herwig, and M. Pignatari. “Pop III i-process nucleosynthesis and the elemental abundances of SMSS J0313-6708 and the most iron-poor stars”. In: *Monthly Notices of the Royal Astronomical Society: Letters* 474.1 (2018), pp. L37–L41.
- [27] S. Cristallo et al. “On the need for the light elements primary process (LEPP)”. In: *The Astrophysical Journal* 801.1 (2015), p. 53.
- [28] C. Fröhlich et al. “Neutrino-induced nucleosynthesis of  $A > 64$  nuclei: the  $\nu$  p process”. In: *Physical Review Letters* 96.14 (2006), p. 142502.
- [29] H. Schatz et al. “rp-process nucleosynthesis at extreme temperature and density conditions”. In: *Physics Reports* 294.4 (Feb. 1998), pp. 167–263. DOI: 10.1016/S0370-1573(97)00048-3.
- [30] T. Kubo et al. “The RIKEN radioactive beam facility”. In: *Nuclear Instruments and Methods in Physics Research Section B: Beam Interactions with Materials and Atoms* 70.1-4 (Aug. 1992), pp. 309–319. DOI: 10.1016/0168-583x(92)95947-p.

## Bibliography

- [31] T. Suda. “Present status of the RIKEN Radioactive Ion Beam Factory, RIBF”. In: *Journal of Physics: Conference Series*. Vol. 267. 1. IOP Publishing. 2011, p. 012008.
- [32] C. Carlile and C. Petrillo. “Neutron scattering facilities in Europe-Present status and future perspectives”. In: *ESFRI Report, European Landscape of Research Infrastructures-ESFRI* (2016), p. 123.
- [33] S. C. Vogel and J. S. Carpenter. “Brief Introduction to Neutron Scattering and Global Neutron User Facilities”. In: *JOM* 64.1 (Jan. 2012), pp. 104–111. DOI: 10.1007/s11837-011-0220-1.
- [34] S. C. Vogel et al. “Short-Pulse Laser-Driven Moderated Neutron Source”. In: *EPJ Web of Conferences*. Vol. 231. EDP Sciences. 2020, p. 01008.
- [35] M. Roth et al. “Bright Laser-Driven Neutron Source Based on the Relativistic Transparency of Solids”. In: *Physical Review Letters* 110.4 (Jan. 2013). DOI: 10.1103/physrevlett.110.044802.
- [36] S. R. Mirfayzi et al. “Experimental demonstration of a compact epithermal neutron source based on a high power laser”. In: *Applied Physics Letters* 111.4 (July 2017), p. 044101. DOI: 10.1063/1.4994161.
- [37] A. Kleinschmidt et al. “Intense, directed neutron beams from a laser-driven neutron source at PHELIX”. In: *Physics of Plasmas* 25.5 (May 2018), p. 053101. DOI: 10.1063/1.5006613.
- [38] I. Pomerantz et al. “Ultrashort Pulsed Neutron Source”. In: *Physical Review Letters* 113.18 (Oct. 2014). DOI: 10.1103/physrevlett.113.184801.
- [39] D. P. Higginson et al. “Temporal Narrowing of Neutrons Produced by High-Intensity Short-Pulse Lasers”. In: *Physical Review Letters* 115.5 (July 2015). DOI: 10.1103/physrevlett.115.054802.
- [40] Y. Wu. “Neutron production from thermonuclear reactions in laser-generated plasmas”. In: *Physics of Plasmas* 27, 022708 (2020) (Jan. 10, 2019). DOI: 10.1063/1.5126411. arXiv: <http://arxiv.org/abs/1901.08979v2> [physics.plasm-ph].
- [41] S. Le Pape et al. “Fusion Energy Output Greater than the Kinetic Energy of an Imploding Shell at the National Ignition Facility”. In: *Physical Review Letters* 120.24 (June 2018). DOI: 10.1103/physrevlett.120.245003.
- [42] T. Ma et al. “Thin Shell, High Velocity Inertial Confinement Fusion Implosions on the National Ignition Facility”. In: *Physical Review Letters* 114.14 (Apr. 2015). DOI: 10.1103/physrevlett.114.145004.
- [43] R. E. Olson et al. “First Liquid Layer Inertial Confinement Fusion Implosions at the National Ignition Facility”. In: *Physical Review Letters* 117.24 (Dec. 2016). DOI: 10.1103/physrevlett.117.245001.
- [44] O. A. Hurricane et al. “Fuel gain exceeding unity in an inertially confined fusion implosion”. In: *Nature* 506.7488 (Feb. 2014), pp. 343–348. DOI: 10.1038/nature13008.
- [45] Ch. J. Cerjan et al. “Dynamic high energy density plasma environments at the National Ignition Facility for nuclear science research”. In: *Journal of Physics G: Nuclear and Particle Physics* 45.3 (Feb. 2018), p. 033003. DOI: 10.1088/1361-6471/aa8693.

- [46] S. Kar et al. “Beamed neutron emission driven by laser accelerated light ions”. In: *New Journal of Physics* 18.5 (Apr. 2016), p. 053002. doi: 10.1088/1367-2630/18/5/053002.
- [47] F. Negoita et al. “Laser driven nuclear physics at ELI-NP”. In: *Romanian Reports in Physics* 68.Supple (2016), S37–S144.
- [48] I. Pomerantz. *Laser Generation of Neutrons: Science and Applications*. Presentation at ELI-NP summer school 2015. 2015. URL: [http://www.eli-np.ro/2015-summer-school/presentations/23.09/Pomerantz\\_Eli-NP-Summer-school-2015.pdf](http://www.eli-np.ro/2015-summer-school/presentations/23.09/Pomerantz_Eli-NP-Summer-school-2015.pdf).
- [49] P. Hill and Y. Wu. “Exploring laser-driven neutron sources for neutron capture cascades and the production of neutron-rich isotopes”. In: (Apr. 5, 2020). arXiv: 2004.07953v1 [nucl-th].
- [50] D.A. Brown et al. “ENDF/B-VIII.0: The 8th Major Release of the Nuclear Reaction Data Library with CIELO-project Cross Sections, New Standards and Thermal Scattering Data”. In: *Nuclear Data Sheets* 148 (Feb. 2018), pp. 1–142. doi: 10.1016/j.nds.2018.02.001.
- [51] A. J. Koning and D. Rochman. “Modern Nuclear Data Evaluation with the TALYS Code System”. In: *Nuclear Data Sheets* 113.12 (Dec. 2012), pp. 2841–2934. doi: 10.1016/j.nds.2012.11.002.
- [52] T. Rauscher and F.-K. Thielemann. “Tables of Nuclear Cross Sections and Reaction Rates: An Addendum to the Paper “Astrophysical Reaction Rates from Statistical Model Calculations””. In: *Atomic Data and Nuclear Data Tables* 79.1 (Sept. 2001), pp. 47–64. doi: 10.1006/adnd.2001.0863.
- [53] T. Rauscher and F.-K. Thielemann. “Astrophysical Reaction Rates From Statistical Model Calculations”. In: *Atomic Data and Nuclear Data Tables* 75.1-2 (May 2000), pp. 1–351. doi: 10.1006/adnd.2000.0834.
- [54] T. Mayer-Kuckuk. *Kernphysik Eine Einfuhrung*. B.G. Teubner, 1984. ISBN: 3-519-33021-0.
- [55] D. J. Hughes. *Neutron Cross Sections*. Ed. by J. V. Dunworth R. A. Charpie. Pergamon Press, 1957.
- [56] A. J. Koning, S. Hilaire, and S. Goriely. *TALYS-1.95. A Nuclear Reaction Programm. User Manual*. First Edition. Dec. 2019.
- [57] A. Deltuva and A. C. Fonseca. “Four-nucleon scattering: Ab initio calculations in momentum space”. In: *Physical Review C* 75.1 (Jan. 2007). doi: 10.1103/physrevc.75.014005.
- [58] P. Navrátil et al. “Unified ab initio approaches to nuclear structure and reactions”. In: *Physica Scripta* 91.5 (Apr. 2016), p. 053002. doi: 10.1088/0031-8949/91/5/053002.
- [59] H. Feshbach. *Theoretical Nuclear Physics, Nuclear Reactions (Theoretical Nuclear Physics Vol. 2) (Volume 2)*. Wiley-VCH, 1992. ISBN: 0-471-05750-9.
- [60] K. Bethge, G. Walter, and B. Wiedemann. *Kernphysik*. Springer Berlin Heidelberg, 2008. doi: 10.1007/978-3-540-74567-9.
- [61] N. Bohr. “Neutron Capture and Nuclear Constitution”. In: *Nature* 137.3461 (Feb. 1936), pp. 344–348. doi: 10.1038/137344a0.

## Bibliography

- [62] US Department of Energy. *DOE Fundamentals Handbook-Nuclear Physics and Reactor Theory*. Tech. rep. Technical Report, 1993.
- [63] Y. Xu et al. “Systematic study of neutron capture including the compound, pre-equilibrium, and direct mechanisms”. In: *Physical Review C* 90.2 (Aug. 2014). DOI: 10.1103/physrevc.90.024604.
- [64] A. J. Koning et al. “TENDL: Complete Nuclear Data Library for Innovative Nuclear Science and Technology”. In: *Nuclear Data Sheets* 155 (Jan. 2019), pp. 1–55. DOI: 10.1016/j.nds.2019.01.002.
- [65] A. J. Koning, D. Rochman, and J. Ch. Sublet. *TENDL-2019*. Dec. 2019. URL: [https://tendl.web.psi.ch/tendl\\_2019/tendl2019.html](https://tendl.web.psi.ch/tendl_2019/tendl2019.html).
- [66] T. Rauscher. *HTML interface of the NON-SMOKER database*. 2018. URL: <https://nuastro.org/nonsmoker.html>.
- [67] A. Trkov and D. A. Brown. *ENDF-6 formats manual: Data formats and procedures for the evaluated nuclear data files*. Tech. rep. Brookhaven National Lab.(BNL), Upton, NY (United States), 2018.
- [68] A.D. Carlson et al. “Evaluation of the Neutron Data Standards”. In: *Nuclear Data Sheets* 148 (Feb. 2018), pp. 143–188. DOI: 10.1016/j.nds.2018.02.002.
- [69] D. Rochman A. J. Koning. *TENDL-2015*. Jan. 2016. URL: [https://tendl.web.psi.ch/tendl\\_2015/tendl2015.html](https://tendl.web.psi.ch/tendl_2015/tendl2015.html).
- [70] *PREPRO 2018 Home Page*. International Atomic Energy Agency - Nuclear Data Services. June 2018. URL: <https://www-nds.iaea.org/public/endl/prepro2018/>.
- [71] Dermott E. Cullen. *PREPRO 2018*. Nuclear Data Section, IAEA. June 2018.
- [72] P. Möller et al. “Nuclear Ground-State Masses and Deformations”. In: *Atomic Data and Nuclear Data Tables* 59.2 (Mar. 1995), pp. 185–381. DOI: 10.1006/adnd.1995.1002.
- [73] J. M. Pearson, R. C. Nayak, and S. Goriely. “Nuclear mass formula with Bogolyubov-enhanced shell-quenching: application to r-process”. In: *Physics Letters B* 387.3 (Oct. 1996), pp. 455–459. DOI: 10.1016/0370-2693(96)01071-4.
- [74] T. Rauscher. “Relevant energy ranges for astrophysical reaction rates”. In: *Physical Review C* 81.4 (Apr. 2010). DOI: 10.1103/physrevc.81.045807.
- [75] W. Hauser and H. Feshbach. “The Inelastic Scattering of Neutrons”. In: *Physical Review* 87.2 (July 1952), pp. 366–373. DOI: 10.1103/physrev.87.366.
- [76] H. Feshbach. “The Optical Model and Its Justification”. In: *Annual Review of Nuclear Science* 8.1 (Dec. 1958), pp. 49–104. DOI: 10.1146/annurev.ns.08.120158.000405.
- [77] J.-P. Jeukenne, A. Lejeune, and C. Mahaux. “Optical-model potential in finite nuclei from Reid’s hard core interaction”. In: *Physical Review C* 16.1 (July 1977), pp. 80–96. DOI: 10.1103/physrevc.16.80.
- [78] L. McFadden and G.R. Satchler. “Optical-model analysis of the scattering of 24.7 MeV alpha particles”. In: *Nuclear Physics* 84.1 (Aug. 1966), pp. 177–200. DOI: 10.1016/0029-5582(66)90441-x.
- [79] R. B. Firestone et al. “The 8th edition of the Table of Isotopes”. In: *Proceedings of the 9th International Symposium on Capture gamma-ray spectroscopy and related topics*. V. 2. 1997.

- [80] J.A. Holmes et al. “Tables of thermonuclear-reaction-rate data for neutron-induced reactions on heavy nuclei”. In: *Atomic Data and Nuclear Data Tables* 18.4 (Oct. 1976), pp. 305–412. doi: 10.1016/0092-640x(76)90011-5.
- [81] A. C. Larsen et al. “Novel techniques for constraining neutron-capture rates relevant for r-process heavy-element nucleosynthesis”. In: *Progress in Particle and Nuclear Physics* (2019).
- [82] A. Gilbert and A. G. W. Cameron. “A COMPOSITE NUCLEAR-LEVEL DENSITY FORMULA WITH SHELL CORRECTIONS”. In: *Canadian Journal of Physics* 43.8 (Aug. 1965), pp. 1446–1496. doi: 10.1139/p65-139.
- [83] T. Rauscher, F.-K. Thielemann, and K.-L. Kratz. “Nuclear level density and the determination of thermonuclear rates for astrophysics”. In: *Physical Review C* 56.3 (Sept. 1997), pp. 1613–1625. doi: 10.1103/physrevc.56.1613.
- [84] Z. Y. Bao et al. “Neutron Cross Sections for Nucleosynthesis Studies”. In: *Atomic Data and Nuclear Data Tables* 76.1 (Sept. 2000), pp. 70–154. doi: 10.1006/adnd.2000.0838.
- [85] R. Capote et al. “RIPL – Reference Input Parameter Library for Calculation of Nuclear Reactions and Nuclear Data Evaluations”. In: *Nuclear Data Sheets* 110.12 (Dec. 2009), pp. 3107–3214. doi: 10.1016/j.nds.2009.10.004.
- [86] G. Audi, A.H. Wapstra, and C. Thibault. “The Ame2003 atomic mass evaluation”. In: *Nuclear Physics A* 729.1 (Dec. 2003), pp. 337–676. doi: 10.1016/j.nucphysa.2003.11.003.
- [87] S. Goriely, F. Tondeur, and J.M. Pearson. “A Hartree–Fock Nuclear Mass Table”. In: *Atomic Data and Nuclear Data Tables* 77.2 (Mar. 2001), pp. 311–381. doi: 10.1006/adnd.2000.0857.
- [88] A. J. Koning and J. P. Delaroche. “Local and global nucleon optical models from 1 keV to 200 MeV”. In: *Nuclear Physics A* 713.3-4 (2003), pp. 231–310.
- [89] E. Sh. Soukhovitskii et al. “Global coupled-channel optical potential for nucleon–actinide interaction from 1 keV to 200 MeV”. In: *Journal of Physics G: Nuclear and Particle Physics* 30.7 (May 2004), pp. 905–920. doi: 10.1088/0954-3899/30/7/007.
- [90] S. Watanabe. “High energy scattering of deuterons by complex nuclei”. In: *Nuclear Physics* 8 (Sept. 1958), pp. 484–492. doi: 10.1016/0029-5582(58)90180-9.
- [91] V. Avrigeanu, M. Avrigeanu, and C. Mănăilescu. “Further explorations of the-particle optical model potential at low energies for the mass range  $A \approx 45-209$ ”. In: *Physical Review C* 90.4 (Oct. 2014). doi: 10.1103/physrevc.90.044612.
- [92] G. R. Satchler. *Introduction to Nuclear Reactions*. Palgrave Macmillan UK, 1990. doi: 10.1007/978-1-349-20531-8.
- [93] T. Tamura. “Analyses of the Scattering of Nuclear Particles by Collective Nuclei in Terms of the Coupled-Channel Calculation”. In: *Reviews of Modern Physics* 37.4 (Oct. 1965), pp. 679–708. doi: 10.1103/revmodphys.37.679.
- [94] S. Goriely, S. Hilaire, and A. J. Koning. “Improved predictions of nuclear reaction rates with the TALYS reaction code for astrophysical applications”. In: *Astronomy & Astrophysics* 487.2 (June 2008), pp. 767–774. doi: 10.1051/0004-6361:20078825.

## Bibliography

- [95] Yi Xu and S. Goriely. “Systematic study of direct neutron capture”. In: *Physical Review C* 86.4 (Oct. 2012). doi: 10.1103/physrevc.86.045801.
- [96] A. J. Koning, S. Hilaire, and S. Goriely. “Global and local level density models”. In: *Nuclear Physics A* 810.1-4 (Sept. 2008), pp. 13–76. doi: 10.1016/j.nuclphysa.2008.06.005.
- [97] J. Kopecky and M. Uhl. “Test of gamma-ray strength functions in nuclear reaction model calculations”. In: *Physical Review C* 41.5 (May 1990), pp. 1941–1955. doi: 10.1103/physrevc.41.1941.
- [98] S. Pal. “Dynamical features of nuclear fission”. In: *Pramana* 85.2 (July 2015), pp. 251–266. doi: 10.1007/s12043-015-1040-6.
- [99] P. A. Moldauer. “Statistics and the average cross section”. In: *Nuclear Physics A* 344.2 (Aug. 1980), pp. 185–195. doi: 10.1016/0375-9474(80)90671-5.
- [100] T. Kawano, R. Capote, and S. Hilaire. “Statistical Hauser-Feshbach theory with width fluctuation correction including direct reaction channels for neutron induced reaction at low energies”. In: (Apr. 28, 2016). doi: 10.1103/PhysRevC.94.014612. arXiv: 1604.08635v1 [nucl-th].
- [101] A. J. Koning and M. C. Duijvestijn. “A global pre-equilibrium analysis from 7 to 200 MeV based on the optical model potential”. In: *Nuclear Physics A* 744 (Nov. 2004), pp. 15–76. doi: 10.1016/j.nuclphysa.2004.08.013.
- [102] C. Kalbach. “Preequilibrium reactions with complex particle channels”. In: *Physical Review C* 71.3 (Mar. 2005). doi: 10.1103/physrevc.71.034606.
- [103] S. F. Mughabghab. *Atlas of Neutron Resonances*. Elsevier, 2018. doi: 10.1016/c2015-0-00524-x.
- [104] H. E. Suess and H. C. Urey. “Abundances of the Elements”. In: *Reviews of Modern Physics* 28.1 (Jan. 1956), pp. 53–74. doi: 10.1103/revmodphys.28.53.
- [105] D. D. Clayton. *Principles of Stellar Evolution and Nucleosynthesis*. University Of Chicago Press, 1984.
- [106] U. Ratzel et al. “Nucleosynthesis at the termination point of the process”. In: *Physical Review C* 70.6 (Dec. 2004). doi: 10.1103/physrevc.70.065803.
- [107] L. Neufcourt et al. “Neutron drip line in the Ca region from Bayesian model averaging”. In: *Phys. Rev. Lett.* 122, 062502 (2019) (Jan. 22, 2019). doi: 10.1103/PhysRevLett.122.062502. arXiv: <http://arxiv.org/abs/1901.07632v2> [nucl-th].
- [108] I. Iben and A. Renzini. “Asymptotic Giant Branch Evolution and Beyond”. In: *Annual Review of Astronomy and Astrophysics* 21.1 (Sept. 1983), pp. 271–342. doi: 10.1146/annurev.aa.21.090183.001415.
- [109] D. Hollowell and I. Iben Jr. “Nucleosynthesis of solar system material in a low-mass, low-metallicity asymptotic giant branch star”. In: *The Astrophysical Journal* 333 (1988), pp. L25–L28.
- [110] J. C. Lattanzio. “S-process nucleosynthesis on the asymptotic giant branch”. In: *Publications of the Astronomical Society of Australia* 10.2 (1992), pp. 99–103.

- [111] M. Lugaro et al. “Current hot questions on the r-process in AGB stars”. In: *Journal of Physics: Conference Series* 665 (Jan. 2016), p. 012021. DOI: 10.1088/1742-6596/665/1/012021.
- [112] M. R. Mumpower et al. “The impact of individual nuclear properties on r-process nucleosynthesis”. In: *Progress in Particle and Nuclear Physics* 86 (2016), pp. 86–126.
- [113] B. Pfeiffer et al. “Nuclear structure studies for the astrophysical r-process”. In: *Nuclear Physics A* 693.1-2 (2001), pp. 282–324.
- [114] J. J. Cowan and F.-K. Thielemann. “R-Process Nucleosynthesis in Supernovae”. In: *Physics Today* 57.10 (Oct. 2004), pp. 47–53. DOI: 10.1063/1.1825268.
- [115] I. Dillmann and Y. A. Litvinov. “r-Process nucleosynthesis: Present status and future experiments at the FRS and ESR”. In: *Progress in Particle and Nuclear Physics* 66.2 (Apr. 2011), pp. 358–362. DOI: 10.1016/j.pnpnp.2011.01.034.
- [116] A. G. W. Cameron, J. J. Cowan, and J. W. Truran. “The waiting point approximation in r-process calculations”. In: *Astrophysics and Space Science* 91.2 (1983), pp. 235–243.
- [117] R. Baruah, K. Duorah, and H. L. Duorah. “Rapid neutron capture process in supernovae and chemical element formation”. In: *Journal of Astrophysics and Astronomy* 30.3-4 (2009), pp. 165–175.
- [118] A. Arcones and G. Martínez-Pinedo. “Dynamical r-process studies within the neutrino-driven wind scenario and its sensitivity to the nuclear physics input”. In: *Physical Review C* 83.4 (2011), p. 045809.
- [119] J. Beun et al. “Neutrinos, Fission Cycling, and the r-process”. In: *arXiv preprint astro-ph/0607180* (2006).
- [120] K.-L. Kratz et al. “Nuclear structure studies at ISOLDE and their impact on the astrophysical r-process”. In: *Hyperfine Interactions* 129.1-4 (2000), pp. 185–221.
- [121] C. Sneden et al. “The Extremely Metal-poor, Neutron Capture-rich Star CS 22892-052: A Comprehensive Abundance Analysis”. In: *The Astrophysical Journal* 591.2 (July 2003), pp. 936–953. DOI: 10.1086/375491.
- [122] B. S. Meyer. “The r-, s-, and p-Processes in Nucleosynthesis”. In: *Annual Review of Astronomy and Astrophysics* 32.1 (Sept. 1994), pp. 153–190. DOI: 10.1146/annurev.aa.32.090194.001101.
- [123] I. V. Panov and H.-Th. Janka. “On the dynamics of proto-neutron star winds and r-process nucleosynthesis”. In: *Astronomy & Astrophysics* 494.3 (Dec. 2008), pp. 829–844. DOI: 10.1051/0004-6361:200810292.
- [124] S. E. Woosley et al. “The r-process and neutrino-heated supernova ejecta”. In: *The Astrophysical Journal* 433 (1994), pp. 229–246.
- [125] A. Arcones, H.-Th. Janka, and L. Scheek. “Nucleosynthesis-relevant conditions in neutrino-driven supernova outflows”. In: *Astronomy & Astrophysics* 467.3 (Mar. 2007), pp. 1227–1248. DOI: 10.1051/0004-6361:20066983.
- [126] T. A. Thompson and A. ud-Doula. “High-entropy ejections from magnetized proto-neutron star winds: implications for heavy element nucleosynthesis”. In: *Monthly Notices of the Royal Astronomical Society* 476.4 (Feb. 2018), pp. 5502–5515. DOI: 10.1093/mnras/sty480.

## Bibliography

- [127] P. Mösta et al. “R-process Nucleosynthesis from Three-Dimensional Magnetorotational Core-Collapse Supernovae”. In: (Dec. 26, 2017). doi: 10.3847/1538-4357/aad6ec. arXiv: 1712.09370v1 [astro-ph.HE].
- [128] C. Freiburghaus, S. Rosswog, and F.-K. Thielemann. “R-process in neutron star mergers”. In: *The Astrophysical Journal Letters* 525.2 (1999), p. L121.
- [129] D. Argast et al. “Neutron star mergers versus core-collapse supernovae as dominant r-process sites in the early Galaxy”. In: *Astronomy & Astrophysics* 416.3 (2004), pp. 997–1011.
- [130] A. Frebel. “From Nuclei to the Cosmos: Tracing Heavy-Element Production with the Oldest Stars”. In: *Annual Review of Nuclear and Particle Science* 68 (2018), pp. 237–269.
- [131] K. Hotokezaka, T. Piran, and M. Paul. “Short-lived 244 Pu points to compact binary mergers as sites for heavy r-process nucleosynthesis”. In: *Nature Physics* 11.12 (2015), pp. 1042–1042.
- [132] B. P. Abbott et al. “GW170817: Observation of Gravitational Waves from a Binary Neutron Star Inspiral”. In: *Physical Review Letters* 119.16 (Oct. 2017). doi: 10.1103/physrevlett.119.161101.
- [133] S. Valenti et al. “The discovery of the electromagnetic counterpart of GW170817: kilonova AT 2017gfo/DLT17ck”. In: *The Astrophysical Journal Letters* 848.2 (2017), p. L24.
- [134] O. Korobkin et al. “On the astrophysical robustness of the neutron star merger r-process”. In: *Monthly Notices of the Royal Astronomical Society* 426.3 (Oct. 2012), pp. 1940–1949. doi: 10.1111/j.1365-2966.2012.21859.x.
- [135] S. Wanajo et al. “PRODUCTION OF ALL THE r-PROCESS NUCLIDES IN THE DYNAMICAL EJECTA OF NEUTRON STAR MERGERS”. In: *The Astrophysical Journal* 789.2 (June 2014), p. L39. doi: 10.1088/2041-8205/789/2/L39.
- [136] S. Goriely, A. Bauswein, and H.-T. Janka. “R-process nucleosynthesis in dynamically ejected matter of neutron star mergers”. In: *The Astrophysical Journal Letters* 738.2 (2011), p. L32.
- [137] *High Flux Isotope Reactor (HFIR). User Guide*. US Department of Energy. Nov. 2015.
- [138] P. E. Koehler. “Comparison of white neutron sources for nuclear astrophysics experiments using very small samples”. In: *Nuclear Instruments and Methods in Physics Research Section A: Accelerators, Spectrometers, Detectors and Associated Equipment* 460.2-3 (2001), pp. 352–361.
- [139] C. Weiß et al. “The new vertical neutron beam line at the CERN n\_TOF facility design and outlook on the performance”. In: *Nuclear Instruments and Methods in Physics Research Section A: Accelerators, Spectrometers, Detectors and Associated Equipment* 799 (Nov. 2015), pp. 90–98. doi: 10.1016/j.nima.2015.07.027.
- [140] L. Yin et al. “Monoenergetic and GeV ion acceleration from the laser breakout afterburner using ultrathin targets”. In: *Physics of Plasmas* 14.5 (May 2007), p. 056706. doi: 10.1063/1.2436857.
- [141] A. P. L. Robinson et al. “Radiation pressure acceleration of thin foils with circularly polarized laser pulses”. In: *New Journal of Physics* 10.1 (Jan. 2008), p. 013021. doi: 10.1088/1367-2630/10/1/013021.

- [142] A. Higginson et al. “Near-100 MeV protons via a laser-driven transparency-enhanced hybrid acceleration scheme”. In: *Nature Communications* 9.1 (Feb. 2018). DOI: 10.1038/s41467-018-03063-9.
- [143] J. C. Fernández et al. “Laser-plasmas in the relativistic-transparency regime: Science and applications”. In: *Physics of Plasmas* 24.5 (May 2017), p. 056702. DOI: 10.1063/1.4983991.
- [144] *ELI Nuclear Physics*. URL: <https://www.eli-np.ro/>.
- [145] O. Kum. “Development of easy-to-use interface for nuclear transmutation computing, VCINDER code”. In: *Nuclear Engineering and Technology* 50.1 (Feb. 2018), pp. 25–34. DOI: 10.1016/j.net.2017.10.007.
- [146] J.-Ch. Sublet et al. “FISPACT-II: An Advanced Simulation System for Activation, Transmutation and Material Modelling”. In: *Nuclear Data Sheets* 139 (Jan. 2017), pp. 77–137. DOI: 10.1016/j.nds.2017.01.002.
- [147] N. Klay et al. “Nuclear structure of Lu 176 and its astrophysical consequences. II. Lu 176, a thermometer for stellar helium burning”. In: *Physical Review C* 44.6 (1991), p. 2839.
- [148] F. Käppeler et al. “The s-process branchings at W-185 and Re-186”. In: *The Astrophysical Journal* 366 (1991), pp. 605–616.
- [149] N. Vassh et al. “Using excitation-energy dependent fission yields to identify key fissioning nuclei in r-process nucleosynthesis”. In: *Journal of Physics G: Nuclear and Particle Physics* 46.6 (2019), p. 065202.
- [150] P. O. Strom, G. R. Grant, and A. C. Pappas. “Independent Yields of 124Sb and 126Sb in Thermal Neutron Induced Fission and their Implication on the Empirical Z p Function”. In: *Canadian Journal of Chemistry* 43.9 (1965), pp. 2493–2507.
- [151] N. Imanishi, I. Fujiwara, and T. Nishi. “Independent isomer yields of Sb and Te isotopes in thermal-neutron fission of 233U, 235U and 239Pu”. In: *Nuclear Physics A* 263.1 (1976), pp. 141–149.
- [152] T. J. Gray et al. “Early Signal of Emerging Nuclear Collectivity in Neutron-Rich Sb 129”. In: *Physical Review Letters* 124.3 (2020), p. 032502.
- [153] W. M. Haynes, ed. *CRC Handbook of Chemistry and Physics 2016-2017: A Ready-reference Book of Chemical and Physical Data*. 97th ed. William M. Haynes, David R. Lide, and Thomas J. Bruno, 2016.
- [154] *Periodic Table*. Royal Society of Chemistry. URL: <http://www.rsc.org/periodic-table>.
- [155] D. L. Clark et al. “The Chemistry of the Actinide and Transactinide Elements”. In: *Springer* 2 (2006), pp. 813–1264.